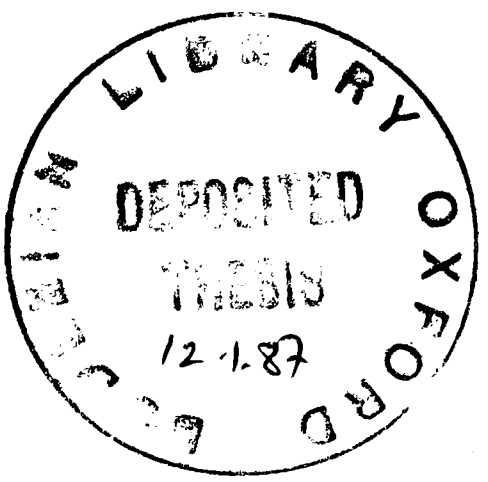
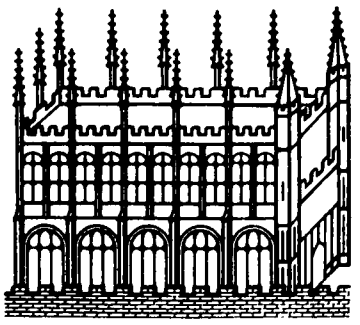
A Study of the γ-rays from the Self-Conjugate Nuclei ^{64}Ge and ^{48}Cr using n-γ coincidence techniques

Stanley Seong Ling Ooi
Keble College



A thesis submitted in partial fulfillment of the requirements
for the degree of Doctor of Philosophy
in the University of Oxford
May 1986



Bodleian Library

The copyright of this thesis belongs to the author.
Use made of it must be properly acknowledged.
Quotation from it in published work requires the prior
written consent of the author.

Readers must sign their name in the space below to
show that they accept these conditions. They are
asked to add their permanent address.

Please complete this section in capital letters:

Name and address	Signature	Date

to pop & mom

Hos successus alit : possunt quia posse videntur
— Virgil (70-19 B.C.)

CONTENTS

Abstract iv
Preface v
List of Figure Captions viii

1. Introduction 1

2. Theoretical Considerations & Motivation 4
2.1 Introduction *4*
2.2 A Review of Shell Effects and Potential Energy Surfaces *6*
2.3 CASCADE *10*
2.4 ^{48}Cr *13*
2.4.1 ^{48}Cr – A Synopsis *13*
2.4.2 Choice of Reaction to form ^{48}Cr *14*
2.4.3 CASCADE Analysis for ^{48}Cr *15*
2.5 ^{64}Ge *16*
2.5.1 Models of ^{64}Ge & PES calculations *16*
2.5.2 Choice of Reaction to make ^{64}Ge *18*
2.5.3 CASCADE Analysis for ^{64}Ge *20*

3. Experimental Details 22
3.1 Introduction - Design of a pure *n*-multiplicity detector *22*
3.2 'ningles' *24*
3.3 The Neutron Detector *24*
3.4 Neutron-Gamma Discrimination *26*
3.4.1 Time-of-Flight *26*
3.4.2 Pulse Shape Discriminator (Freiburg box) *27*
3.4.3 *Composite* Pulse Shape Discriminator *28*
3.5 Electronics *28*
3.6 Layout of the Experiment *29*
3.7 Data Collection & On-line Analysis *31*
3.8 Performance Tests on the Neutron Wall *33*
3.8.1 Timing resolution (& Neutron flight path) *33*
3.8.2 Detector Efficiency *34*
3.8.3 Figure of Merit *35*
3.9 PSD-TOF plots *36*
3.10 Off-line Analysis *37*

4. Chromium-48 38
4.1 Introduction *38*
4.2 Experimental Details *39*
4.3 Results & Analysis *41*
4.3.1 Excitation Function *41*
4.3.2 Neutron Gating *42*
a) Total 2n spectrum 44
b) 2n spectrum with non-adjacent detectors 45
c) Ratio of 2n to 1n peaks 45
4.3.3 γ-γ Sort and Coincidence Spectra *46*
4.3.3.1 ^{48}Cr Band Structure *47*
a) Ground State Band (gsb) *47*
b) Side Band *48*
c) A New Transition in ^{48}Cr *49*
4.3.3.2 Background Lines *49*
4.3.3.3 γ-ray Intensities *50*
4.3.3.4 n-γ-γ Coincidence Spectra *50*
4.3.4 Conclusion *51*
4.4 Discussion *52*

5. Germanium-64 54
5.1 Introduction *54*
5.2 Kinematic Focusing and the Inverse Reaction *56*
5.3 Excitation Function *59*
5.3.1 Experimental Details *59*
5.3.2 Analysis - Excitation Function *60*
5.4 Relative Cross-sections *62*
5.4.1 Absolute Cross-sections *66*
5.5 ^{64}Ge β-decay *68*
5.5.1 Relative Cross-sections *68*
5.6 ^{64}Ge Reaction Study *72*
5.6.1 Experimental Details *73*
5.6.2 Results & Analysis *75*
5.6.3 Relative Intensities of the Reaction Lines *84*
5.6.4 Summary *86*
5.7 Conclusion *87*

6. Conclusion 94

Appendices 96

Appendix I - Coulomb Excitation *96*
I.1 Introduction *96*
I.2 Iron-56 *96*
I.3 Gold-197 *97*
I.4 Some Useful Formulae *98*
Appendix II - The Neutron Wall *100*
II.1 Setting up the Neutron Wall *100*
II.2 The Neutron Wall at a glance *101*
II.3 Setting up the Composite PSD *101*
II.4 Setting up the Freiburg PSD *103*
Appendix III - Pulse Shape Discrimination with Liquid Scintillators *104*
III.1 Liquid Scintillators *104*
III.2 Freiburg Pulse Shape Discriminator - *modus operandi* *106*
Appendix IV - The Sorting Routine *107*
IV.1 A Sorting Language **SOL** *107*
IV.2 An Example **SOL** Programme *110*
IV.3 Syntax of **SOL** *112*
Appendix V - CASCADE input *113*
Appendix VI - List of Runs *116*

References 118

ABSTRACT

A Study of the γ-rays from the Self-Conjugate Nuclei ^{64}Ge and ^{48}Cr using n-γ coincidence techniques

Stanley Seong Ling Ooi, Keble College, Oxford

Submitted for the degree of Doctor of Philosophy

Trinity Term 1986

A neutron multiplicity detector system has been developed to study weak pure neutron evaporation channels from heavy-ion reactions. Such a system allows us to study nuclei far away from the line of β-stability — in particular, self-conjugate nuclei where the shell-effects for protons and neutrons are in phase and their combined effects may drive the nucleus towards superdeformation. The system consists of a *neutron wall* — 4 large quadrant neutron detectors and a small central detector — with 4 large volume Ge(Li) γ-ray detectors positioned as close as possible to the target. Neutron-gamma coincidences were recorded and neutron multiplicity events could be extracted from the data. Rejection of gamma-ray events in the neutron detectors was achieved by time-of-flight and pulse shape discrimination methods. A surface barrier detector at 0° allowed a further rejection of charged particle events — especially events which feature neutrons as well.

The system was tested with the reaction ^{27}Al(^{24}Mg, $2np\gamma$)^{48}Cr at 62 MeV and a 1347 keV γ-ray transition was discovered. This has been shown to be the γ-decay of a new 8408 keV level in ^{48}Cr.

Gamma-rays from ^{64}Ge, a nucleus predicted to have a superdeformed ground state shape, were investigated using the reaction ^{12}C(^{54}Fe, $2n\gamma$)^{64}Ge at 150 MeV beam energy. The first excited state was found to be 901.6±0.5 keV and the systematics of the region suggest a spin and parity of 2^+. With this energy for the first 2^+ state, the prediction of superdeformation can be ruled out. Nevertheless, this is the heaviest N=Z nucleus to be studied by in-beam γ-ray spectroscopy and this observation of pure neutron evaporation from a very neutron deficient compound nucleus is potentially important for observing heavier exotic self-conjugate systems.

PREFACE

Physics is common sense made difficult

For those of you who are interested in seeing whether you are mentioned in this thesis, I suggest you look at the end of this preface where the names are listed out and for the (even fewer) ones who are reading this thesis for the physics, start at Chapter 1 — this preface contains nothing more than some *random jottings of a demented physicist.* It's perhaps politic at this point to apologize to J.A. for the blatant plagiarization in chapter 1 of her catch-phrase but good opening lines are so hard to find. I confess to having a predilection for using words which I don't quite understand and a predisposition for using words I can't spell. I have endeavoured to curb this habit while writing this thesis and I sincerely hope that the physics will get through to the reader relatively unharmed. Liberally sprinkled throughout this thesis are quotes in *italics.* The shrewd and well-informed reader will instantly recognize the wit of L.C.† — from A. in W. and T. the L.G. They seem to summarize some of the chapters so well. The quote for this preface is, I hastily add, not from the same source. I must apologize for my grammer (or lack of it) and my tenses although my 'proof-readers' have assiduously tried to ensure that I write in some form of recognizable English. On a good day, I have been known to change the tense 5 times [EFG] in one sentence. I believe this is the current record at Oxford. The production of this thesis has certainly employed the *state-of-the-art* technology — GKS for the plots, TEX and a laser printer for the text, laser photocopier of the b. + w. pages and a coloured p. for the c. p. I hope that the contents will live up to this.

I have to thank Raoul Davie and David Pringle for much assistance during the last legs of my writing up — proof-reading my final drafts, providing cheerful conversations and keeping me relatively sane. I have also enjoyed Ian McArthur's company during these troubled times and I have to thank him for the many pleasant conversations that took my mind off the cares of writing up. Thanks, too, to Serena for ringing me up every day — much to the consternation of her bank manager.

Finally, I should like to thank the people listed below for making my spell at Oxford a most agreeable one and the writing of this thesis a much pleasanter task than it would otherwise have been. As I thumb through my Roget's for choice adjectives to describe these splendid creatures, the phrase that comes to mind is that they are all *terrific hons.* So w.o. much f.a., let me proceed with the details...

---

† The slower ones will still be wondering who L.C. is.

Very many thanks to:

- ◇ Prof. K.W.Allen for extending to me the hospitality of a first class laboratory (and its attendent facilities).
- ◇ David Sinclair, my supervisor, who has been an invaluable guide and mentor over the past four years.
- ◇ Russel Betts for supervising me while DS was away down a mine shaft.
- ◇ Keith Fifield, an antipodean *hon*, without whom the 8408 keV state in ^{48}Cr would not have been discovered (by me at any rate).
- ◇ Elspeth Garman, David Pringle, Raoul Davie and Serena Hesmondhalgh for proof-reading my drafts — wading through the split infinitives and future imperfect tenses with remorseless tenacity — they deserve a special vote of thanks.
- ◇ Alicia Kucharska, for her splendid company throughout my stay at Oxford and for countless delicious dinners with her and her fiancé.
- ◇ David Pringle, John Vermeer, Tim Shaw and Richard Baldock for v. many useful discussion sessions: JV for helping me understand the intricacies of Coulex and DP for nuclear physics in general.
- ◇ Peter Barratt and Dominic Aitken for building the PSD's and for allowing me to use their splendid CAD system for my diagrams.
- ◇ Tom Brock for v. interesting discussions on bit-slice processors, Macro-11 and the subtleties of BNF.
- ◇ Simon Towers, Neil Geddes and Phil Bull, erstwhile particle physicists (not everyone is perfect), for their jovial company.
- ◇ Susan Allcock, Raoul Davie and Paul Keeling for stoically sharing the same office as me and a special thanks to RD for very many useful and stimulating discussions on nuclear physics in that office.
- ◇ Arthur Smith for some amusing conversations and Nina Poffé for much help during my preliminary runs and for her pleasant company.
- ◇ the men at the wheels of the FT — our level one boys — Messrs. A.Aitken, J.Early, R.Hole, R.Hopkins, F.Kelly and the late N.Walters for providing excellent company and incomparable support during my 25 runs.
- ◇ Dick Hyder for running a tiptop accelerator and suffering silently as I kept breaking the FT by running at 10 MV.
- ◇ the lads in the OEG workshop, lead by Colin Graham, for knocking up something from nothing and in a shorter time than it took — consistently.
- ◇ the 'snap-chaps' viz. Messrs. P.Flint, M.E.Osman and C.W.Band for the excellent photographs included in this thesis.
- ◇ Paul Leyland for teaching me how to pronounce 'unixes' and Clive Rodgers for being an exceptionally sympathetic employer during my stint as a quasi-employee of the Clarendon Laboratory across the road.
- ◇ Ian McArthur for being a close friend, a good computer manager and a superb drinking partner.
- ◇ Serena for providing a shoulder to cry on in times of tension and stress (which was every other day) and for providing a fathomless source of encouragement

and reassuarance that was so desparately vital to me; and accumulating a vast telephone bill in the process.

- ◇ My sister Siu for providing good food and excellent shelter when I needed to run away from the slings and arrows of outrageous physics.
- ◇ Pop and Mom, for remembering me in their prayers and for much needed love, encouragement and support and to whom I humbly dedicate this thesis.

I should also like to thank some *hons* that are based further afield, namely

- ◇ Kim Lister, of Manchester, for many useful discussion sessions.
- ◇ Dr. P.Betz, Prof. Röpke and the chaps in the Fakultät fur Physik in Freiburg for supplying the design of their PSD as well as a working prototype (that works).
- ◇ Dr. N.Schmal at the University of Köln, for providing me with a preprint of his ^{64}Ga level scheme.

Finally, I would like to express gratitude to the Science and Engineering Research Council for financial support for two years of my research work.

S.S.L.O

Oxford, 1986

LIST OF FIGURE CAPTIONS

The page numbers on the far right indicate the page following which the figures can be found.

Figures for CHAPTER 2

2.1 PES plots : (a) ^{64}Ge (b) ^{48}Cr 8
2.2 Shell Effects vs. ϵ and (N,Z) contour maps 8
2.3 Single particle spectrum for axially symmetric HO potential 9
2.4 Single particle spectrum for modified oscillator potential 9
2.5 Schematic diagram for fusion-evaporation reaction 11
2.6 Spin distribution in a compound nucleus 11
2.7 E vs. J(J+1) plot for ^{48}Cr 13
2.8 CASCADE excitation functions for ^{24}Mg + ^{27}Al 15
2.9 CASCADE E vs. J for ^{48}Cr 15
2.10 CASCADE excitation functions for ^{12}C + ^{54}Fe in (a) one plot
(b) separate plots 21

Figures for Chapter 3

3.1 End view of Neutron Wall 25
3.2 PSD spectra with (a) Freiburg and (b) *Composite* PSD's 27
3.3 Electronic block diagram of the *composite* PSD 28
3.4 Electronic block diagram of the system 28
3.5 Overall block diagram of the system 28
3.6 Typical TOF spectrum 29
3.7 Layouts of the experiments (L1...L5) 29
3.8 Router spectrum 31
3.9 TOF spectra for (a) 65 cm and (b) 35 cm flight paths 34
3.10 E_n (lab.) vs. θ plot for various n centre-of-mass energies 34
3.11 (a) Singles and (b) 1n-gated (TOF) spectra 36
3.12 1n-gated (TOF & PSD) spectrum 36
3.13 PSD-TOF plot 36

Plates for Chapter 3

3.1 Isometric view of the target mount 30
3.2 Side view of the target mount 30
3.3 Front view of the target mount 30
3.4 Back view of the Neutron Wall 31
3.5 Side view of the n-γ detection system 31
3.6 Top view of the target chamber 31

List of Figure Captions

Figures for Chapter 4

4.1 PSD-TOF plot 40
4.2 Yield curve of γ-ray peaks & CASCADE excitation functions 41
4.3 CASCADE cross-section for ^{24}Mg + ^{27}Al at 62 MeV 42
4.4 (a) Singles and (b) n-gated γ-ray spectra 43
4.5 (a) $2n$-gated and (b) $(2n - 1n)$-gated spectra 43
4.6 (a) $2n$-(non adj.)-gated and (b) $(2n - 1n)$-gated spectra 43
4.7 Ratio of selected peaks in $2n$ and $1n$-gated spectra 45
4.8 ^{48}Cr level scheme 47
4.9 γ-γ-coincidence spectra 47
4.10 Sum of gsb γ-γ-coincidence spectra 49
4.11 88 keV coincidence spectra 49
4.12 271 keV coincidence spectra 49
4.13 Intensity of peaks in the coincidence spectra 50
4.14 n-γ-γ-coincidence spectra 50
4.15 Sum of gsb n-γ-γ-coincidence spectra 50
4.16 Experimental and shell model states in ^{48}Cr 53
4.17 E vs. J(J+1) plots for ^{48}Cr , ^{46}Ti and ^{50}Cr 53

Figures for Chapter 5

5.1 Singles γ-ray spectrum : ^{12}C + ^{54}Fe at 35 MeV 57
5.2 Singles γ-ray spectrum : ^{54}Fe + ^{12}C at 150 MeV 57
5.3 n-gated spectrum : ^{12}C + ^{54}Fe at 35 MeV 57
5.4 E_n (lab.) vs. θ plot for evaporated n's in Fe-C & C-Fe reactions 57
5.5 Effective solid angle subtended by n-wall as a function of target-n-wall distance 57
5.6 Electronic block diagram for Compton suppressor 60
5.7 Yield curves for the reaction ^{12}C + ^{54}Fe 61
5.8 Ge(Li) efficiency curve with a ^{152}Eu source 62
5.9 Singles spectrum showing Coulomb excitation lines 67
5.10 ^{64}Ge decay scheme. 68
5.11 Beam cycle of the β-decay experiment 68
5.12 Activity spectrum for the β-decay experiment (5 hrs. coll. time) 68
5.13 Activity spectrum for the β-decay experiment (16 hrs. coll. time) 68
5.14 (a) $1p$ and (b) $0p$ γ-ray spectra 74
5.15 ^{64}Ga level scheme 75
5.16 (a) Singles and (b) $1n$-gated spectra 75
5.17 Singles spectrum for γ-ray catalogue 76
5.18 $1n$-gated spectrum for γ-ray catalogue 76
5.19 $1n0p$-gated spectrum for γ-ray catalogue 76
5.20 $2n$-gated spectrum for γ-ray catalogue 76
5.21 $2n0p$-gated spectrum for γ-ray catalogue 76
5.22 Ratio of selected peaks in $1n1p$ and $1n0p$-gated spectra 79
5.23 (a) $1n0p$ (b) $1n1p$ and (c) $1n0p - const. \times 1n1p + const.$ spectra 79
5.24 Expanded section of fig. 5.23 79
5.25 Subtracted spectra $(1n0p - 1n1p)$ normalized to (a) 128 keV and (b) 367 keV pn lines 80

5.26 (a) $2n$ and (b) $1n$ spectra 81
5.27 (a) $2n0p$ (b) $1n0p$ and (c) $2n0p - const. \times 1n0p + const.$ spectra 81
5.28 (a) $2n0p$ (b) $2n1p$ and (c) $2n0p - const. \times 2n1p + const.$ spectra 81
5.29 (a) $2n0p$ (b) $2n1p$ and (c) $2n0p - const. \times 2n1p + const.$ spectra (non-adj. n-detectors) 81
5.30 (a) $1n0p$ (b) $1n1p$ and (c) $1n0p - const. \times 1n1p + const.$ spectra (Run 20) 82
5.31 (a) $2n1p$ and (b) $2n0p$-gated spectra (Run 24) 82
5.32 Sequence of spectra showing steps in data reduction 82
5.33 Comparing CASCADE and experimental cross-sections 87
5.34 Four possible placements of the 902 keV γ-ray transition (other than a g.s. transition to the 1st. excited state) 89
5.35 Subtracted spectrum (from fig. 5.23) 92
5.36 Systematics of the 2_1^+ states in the A=60 mass region 92
5.37 Systematics of the first 4 excited states in the Ge isotopes 92
5.38 As for fig. 5.23 but with the high energy region shown 92

Figures for Appendix I

I.1 $d\sigma/d\Omega$ vs. θ plot for the Coulomb excitation of ^{56}Fe 96
I.2 Classical f_{E2} function 97

Plate for Appendix II

II.2 Front panel of the Freiburg PSD 103

Figures for Appendix III

III.1 Ionization in a scintillator caused by a heavily ionizing charged particle ... 104
III.2 Ionization in a scintillator caused by an electron 106
III.3 Light output from a scintillator as a function of time 106
III.4 Output from an integrator showing difference between n and γ-ray signals from a scintillator 106
III.5 Dynode chain for the photomultipliers 106
III.6 Electronic block diagram for the Freiburg PSD 106
III.7 Freiburg PSD spectra for (a) a neutron and (b) a γ-ray source 106

Figures for Appendix V

V.1 Input cards to CASCADE 114
V.2 Typical CASCADE output 115
V.3 Pictorial representation of the variation in the CASCADE cross-sections as the input parameters are changed 115

1

CHAPTER 1

Introduction

"Begin at the beginning," the King said gravely,

"and go on till you come to the end; then stop."

It is a truth universally acknowledged that the nucleons in a nucleus can be considered as moving in an averaged potential from which an inhomogeneous energy level density distribution is obtained which groups the nuclear energy levels into distinct shells. However, the bulk properties of nuclei e.g. binding energies, are better described by considering the nucleus as a liquid drop. In this approach, the nuclear level density is a smoothly varying function of energy and no shell structure exists. In order to determine the nuclear *shape*, the total energy of the nucleus as a function of the shape parameters (e.g. quadrupole deformation parameter) has to be found. The shape of the nucleus is then determined by minimizing the energy with respect to these shape degrees of freedom. The total energy can be considered as a sum of a liquid drop term and a correction term which accounts for the grouping of the nuclear levels into shells. The positions of these energy levels vary with deformation and shell closures may occur at different deformations for different nucleon numbers. A nucleus achieves greater stability with a closed shell

configuration and so may assume a deformed shape to obtain such a configuration. In self-conjugate nuclei, these shell effects occur simultaneously for both protons and neutrons. Hence, if the shell effects have a preference for a deformed shape, the neutron and proton components may reinforce each other to drive the nucleus towards large deformation. Thus, self-conjugate nuclei are a natural place to look for superdeformation.

Our knowledge of N=Z nuclei stops abruptly at ^{60}Zn, which has been made via two proton transfer on a stable target [MIL67]. In this thesis, we report the first advance in 18 years in this experimental field with the measurement of the energy of the first excited state in ^{64}Ge. There are many predictions for the shape of ^{64}Ge — ranging from a superdeformed to a spherical but soft shape i.e. where there is no well defined energy minimum with respect to the shape parameters. This suggests that the driving influence of the shell effects is very finely balanced and that the predicted shape is very sensitive to the parameterizations of the nuclear shape used in the different models. So, an experimental measurement of the shape is very important for testing these different models. One way of doing this is by using γ-ray spectroscopy of the low-lying states. For instance, the energy of the first 2^+ state is commonly used as the simplest criterion for nuclear deformation.

There have been several unsuccessful attempts by other workers [SCH84, SUG79] to study this nucleus. The curvature of the valley of stability makes this nucleus difficult to study as the cross-section for its production is very small. However, as ^{64}Ge lies on the neutron deficient side of the valley, if we choose a heavy-ion reaction that populates this nucleus via pure neutron evaporation, all the other channels (except ones which feature pure neutron evaporation) can be suppressed by rejecting charged particle related events and accepting only pure neutron events. Thus, a very weak evaporation channel can be extracted from a large background of charged particle evaporation channels.

This thesis describes the design, development and implementation of a *npγ*-detection system for the study of weak pure neutron evaporation channels from a

fusion-evaporation reaction. The neutron detector consisted of five separate units which allowed the neutron multiplicity of an event to be determined. With this system, we achieved a 100:1 rejection ratio for charged particle events and were able to pick out a weak $2n$ channel ($\sim$ 0.2 % of the total cross-section†) from the reaction ^{54}Fe (^{12}C,$2n\gamma$) ^{64}Ge. In order to test the neutron multiplicity filter of the system, the reaction ^{24}Mg + ^{27}Al, was chosen because the suppression of the $2pn$ channel (37 % of the total cross-section†) in favour of the $p2n$ channel (5 % of the total cross-section†) served as a test of the performance of the system. The $p2n$ channel populates states in ^{48}Cr which is another self-conjugate nucleus and interesting in its own right. ^{48}Cr is a mid-shell ($f_{7/2}$ shell) nucleus and may be expected to show considerable collectivity and be deformed in its ground state. In this nucleus only states up to spin 10 were known and this reaction was also used to populate the high-spin states in an attempt to extend our knowledge of the band structure in this nucleus.

This thesis has been laid out as follows : Chapter 2 describes the *microscopic-macroscopic* model of Strutinksy from which the various shapes for ^{64}Ge were deduced. It was clear that a specially designed detection system was required to study this very neutron deficient nucleus. ^{48}Cr was chosen to test the performance of this system and a brief background description of this nucleus, as well as ^{64}Ge, is given and justification is given for the choice of the reactions. Chapter 3 describes the neutron detection system developed and used for our investigations. The results of the performance tests on the system are also given in chapter 3. The analyses of the ^{48}Cr and ^{64}Ge experiments are then considered separately in chapters 4 and 5 respectively. Finally, a brief conclusion of the results of the experiments is given in chapter 6.

---

† Using an evaporation code, CASCADE (see §2.3).

CHAPTER 2

Theoretical Considerations & Motivation

"Why, sometimes I've believed as many as six impossible things before breakfast"

2.1 Introduction

From general theoretical considerations, nuclei with N and Z in the middle of a shell are expected to show considerable collectivity and may be deformed in their ground states. Closed shell nuclei are spherical in their ground state but in nuclei away from closed shells, the valence nucleons polarize the core and this results in a non-spherical shape. The extent of this deformation varies from nucleus to nucleus but general trends are observed. For example, in the rare-earth region ($A = 140 - 180$), the nuclei have fairly large deformed ground state shapes (with a quadrupole deformation parameter $\epsilon \approx 0.3$). In some special cases, *superdeformation* may occur. If the nuclear shape is approximated by an ellipsoid, then we define the term *superdeformation* to correspond to a 2:1 ratio of the major and minor axes which is equivalent to an ϵ of 0.6. These superdeformed shapes have been observed in light nuclei (e.g. ^{8}Be and ^{12}C) which feature this as their ground state

shape and also in the the heavier mass region (A > 200), where the fission isomers exhibit such a shape. However, in the intermediate mass region (A ≈ 60 – 100), no superdeformed ground state shape has been observed experimentally although theoretical predictions have been made for the existence of such shapes. It should be pointed out that although superdeformed ground state shapes have not been observed, the observation of superdeformed shapes for high-spin states have been proposed. A case in point is ^{48}Cr where a study of the ^{24}Mg + ^{24}Mg reaction has been shown to produce very strong and narrow resonances [BET84, ZUR83] which can be understood in terms of high-spin (I ≈ 32) superdeformed ($\epsilon \approx 1.0$) states in ^{48}Cr being populated by the reaction. The calculations predicting superdeformation employ the *microscopic-macroscopic* model to determine the equilibrium shape of a nucleus. In this chapter, a brief résumé of this model is given and ^{64}Ge is shown to be a possible superdeformed nucleus from such an approach although several other calculations predict a far less extreme shape.

The other nucleus investigated in this work is ^{48}Cr. The reaction chosen to populate this nucleus was ^{27}Al (^{24}Mg, $2np\gamma$) ^{48}Cr. As it is a $2n$-related channel, and the theoretical predictions of its cross-section shows that it forms ~ 5 % of the total cross-section, this reaction allowed us to investigate the behaviour of the neutron multiplicity detection system under moderately favourable conditions. A parallel purpose of this experiment was to extend our knowledge of the states in this nucleus. ^{48}Cr is in the middle of the $f_{7/2}$ shell and, as a result, should show strong collective behaviour and be deformed (although not necessarily superdeformed) in its ground state but previous work has shown that it does not exhibit the rotational behaviour expected of a deformed nucleus. Further knowledge of the excited states and the bands they form in this nucleus was therefore expected to shed more light on the structure of this nucleus.

In order to populate the excited states in both these nuclei, heavy ion fusion-evaporation reactions were used. An n-γ detection system was developed to detect γ-rays in coincidence with the evaporated neutrons thereby enhancing n-related

events. It consisted of several independent sectors and acted as a multiplicity filter for the neutron events.

An evaporation code, CASCADE, was used to study the cross-sections of the exit channels from the many possible reactions. From this, the optimum projectile-target combination to produce the nucleus of interest was chosen. A brief description of the statistical model used by this code is given and possible inaccuracies of the code, as well as its sensitivity to the input parameters, is discussed.

2.2 A Review of Shell Effects and Potential Energy Surfaces

In this section a simple derivation of the shell correction energy is given and the use of this approach in producing Potential Energy Surfaces (PES) to determine the equilibrium deformation(s) of nuclei is discussed. The approach we have adopted is after Ring and Schuck [RIN80].

The Schrödinger Equation of a many-body system with A nucleons is given by

$$\hat{H}|\Psi> = E|\Psi> \qquad \text{where} \qquad <\mathbf{r}|\Psi> = \Phi(\mathbf{r}(1),...,\mathbf{r}(A)) \tag{2.1}$$

The Hamiltonian is given by the sum over the kinetic energy terms $T(k)$ and the nucleon-nucleon interaction $W(k,l)$ for all pairs of nucleons

$$\hat{H} = \sum_{k=1}^{A} \hat{T}(k) + \sum_{k<l}^{A} \widehat{W}(k,l) \tag{2.2}$$

The shell model approach is adopted which considers the nucleus as a collection of nucleons moving in an average field. Thus, a single-particle potential $U(k,A)$ is introduced, the form of which will depend on the number of nucleons:

$$\hat{H} = \sum_{k=1}^{A} \{\hat{T}(k) + \hat{U}(k,A)\} + \underbrace{\{\sum \widehat{W}(k,l) - \sum \hat{U}(k,A)\}}_{\text{"residual interaction"}} \tag{2.3}$$

$$= \sum_{k=1}^{A} \hat{e}(k,A) + \hat{V}_{residual} \tag{2.4}$$

The shell model energy, E_{sm}, of the nucleus, ignoring $\hat{V}_{residual}$, is

$$E_{sm} =< \Psi|\hat{H}|\Psi >= \sum_{k=1}^{A} e_k(A) \tag{2.5}$$

We find that summing up these single-particle energies, e_k, does not reproduce the absolute nuclear binding energies. This is because the binding energies are bulk properties of nuclei and these are not well represented by the shell model. However, these binding energies are observed to consist of a smoothly varying function with an oscillatory part that reflects the bunching of the nuclear energy levels into shells. The potential energy can be considered as a sum of two parts:

$$E_{PE} = E_{osc} + E_{LDM} \tag{2.6}$$

where E_{osc} is the oscillatory part and E_{LDM} is the smoothly varying liquid drop energy. Strutinsky proposed [STR67, STR68] that E_{osc} could be calculated from the shell model while taking E_{LDM} from the liquid drop model. Thus, the shell model energy, E_{sm}, has to be divided into a smooth and an oscillatory part.

$$E_{sm} = \sum_{k=1}^{A} e_k = E_{osc} + < E_{sm} > \tag{2.7}$$

where $< E_{sm} >$ is the smooth (averaged) variation of E with A. Hence

$$E_{PE} = E_{LDM} + [E_{sm} - < E_{sm} >] \tag{2.8}$$

The energy is thus divided up into a macroscopic term, E_{LDM}, which changes smoothly over the periodic table and a shell-correction energy $[E_{sm} - < E_{sm} >]$ which accounts for microscopic variations from nucleus to nucleus. Thus

$$E_{PE} = E_{macro} + E_{shell} \tag{2.9}$$

$$\text{where} \qquad \mathrm{E_{shell}} = \sum_{i}^{A} e_i - \langle \sum_{i}^{A} e_i \rangle \tag{2.10}$$

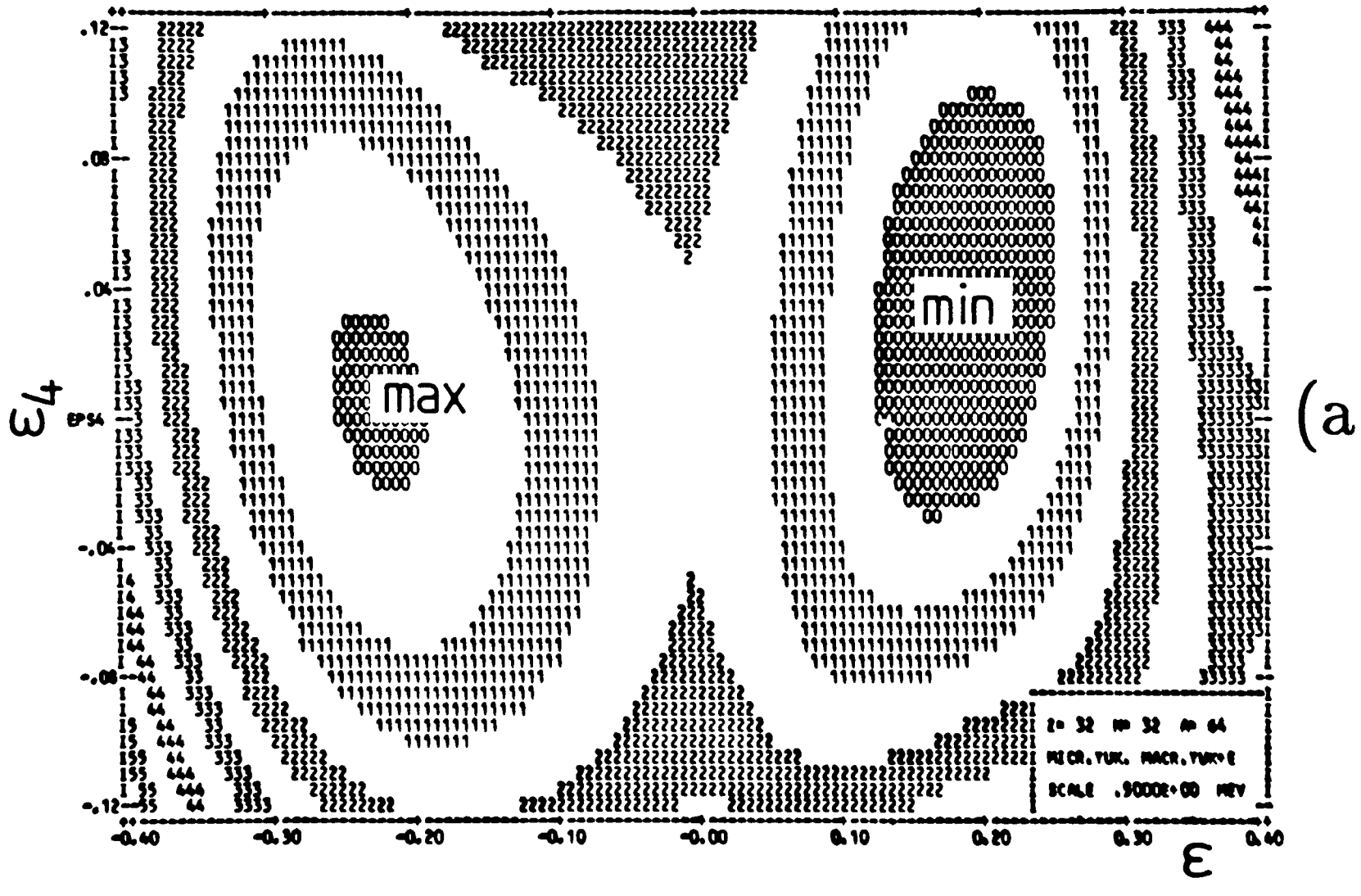
The pairing energy, E_{pair} can also be added in a similar fashion. We must remember that the liquid drop term already contains the smoothly varying part of E_{pair} and so only the oscillatory part should be added

$$E_{PE} = E_{LDM} + [E_{sm} - < E_{sm} >] + [E_{pair} - < E_{pair} >] \qquad (2.11)$$

From this *microscopic-macroscopic* approach, the equilibrium deformation of a nucleus can be determined. Each term can be expressed as a function of shape parameters [BOL72] and so by minimizing the energy with respect to these shape degrees of freedom, the equilibrium shape can be found. The results of these calculations are often presented as *Potential Energy Surface* plots. In these diagrams, the potential energy is plotted against two shape degrees of freedom (usually ϵ and γ) and these values for the minimum in a PES plot specify the equilibrium shape of the nucleus. Two such plots are shown in fig. 2.1. Part (a) is the PES plot for ^{64}Ge [MOL81]. The shape parameters used here are ϵ, the quadrupole deformation parameter, and ϵ_4, the hexadecapole deformation parameter. Part (b) shows the PES plot for ^{48}Cr [LAR76] and this time, the shape parameters are ϵ and γ, the axial asymmetry parameter.

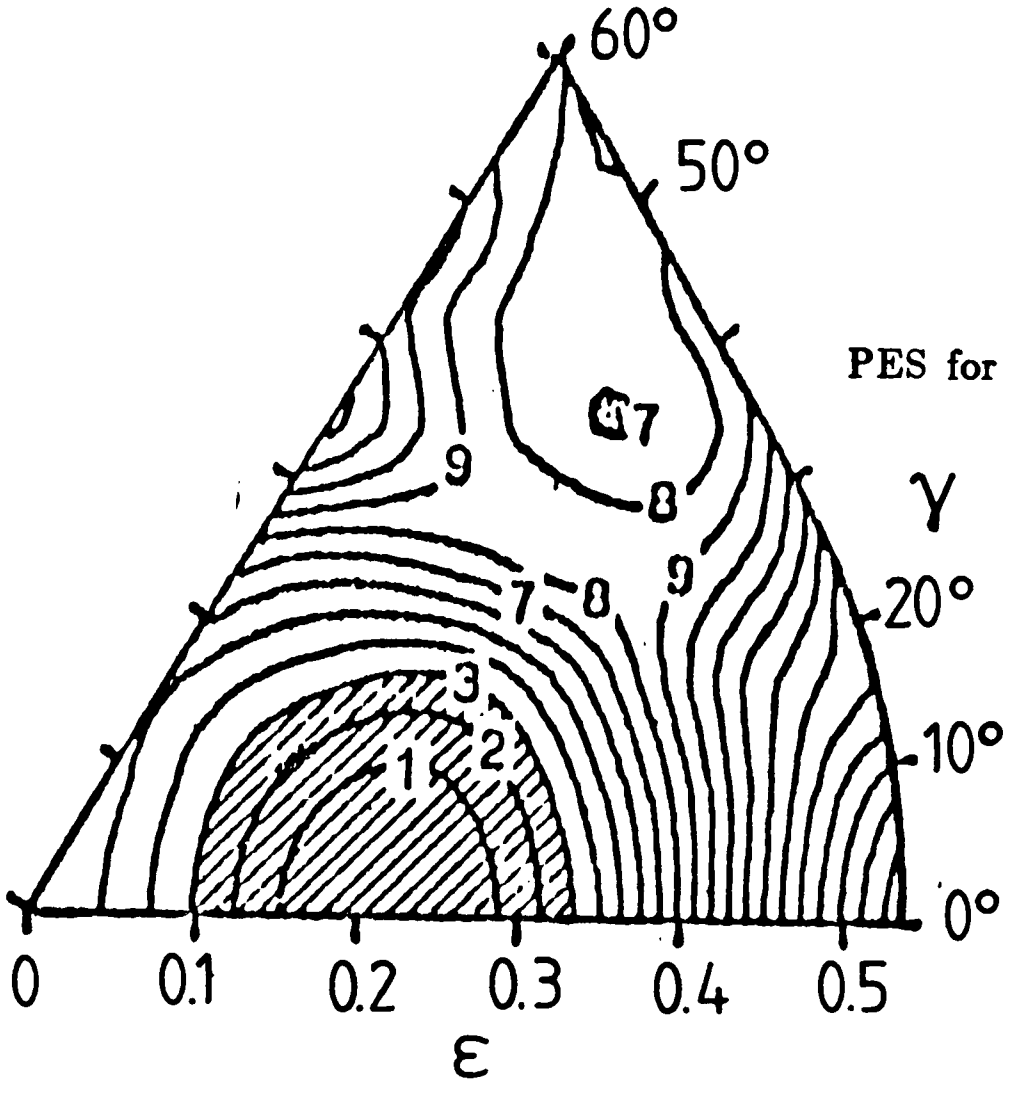
A survey of the periodic table can be made by plotting the potential energy as a function of the proton (or neutron) number and one shape parameter (usually ϵ). A 'contour map' is obtained in which well-defined valleys and ridges occur. Fig. 2.2 shows, for example, such a map for shell and pairing corrections. As with ordinary contour maps, the valleys correspond to stable equilibria. For a given nucleon number, the nucleus will attempt to attain minimum energy and may adopt a deformed shape to do so. We see that for $\epsilon = 0$, there are well-defined minima at the magic numbers 8, 20, 50, 82 and 126. However, minima also exist for $\epsilon \neq 0$ and these may cause the nucleus to prefer a deformed ground state. A detailed account of this method and its comparison with selected nuclei can be found in a paper by Ragnarsson, Nilsson and Sheline [RAG78].

PES for ^{64}Ge



(a)

PES for ^{48}Cr



(b)

Fig.2.1 : Potential Energy Surface plots. (a) ^{64}Ge from [MOL81]; the minimum corresponds to $\epsilon \approx 0.2$ and $\epsilon_4 \approx 0.04$. (b) ^{48}Cr from [LAR76]; it predicts a deformed prolate rotor with $\epsilon \approx 0.21$.

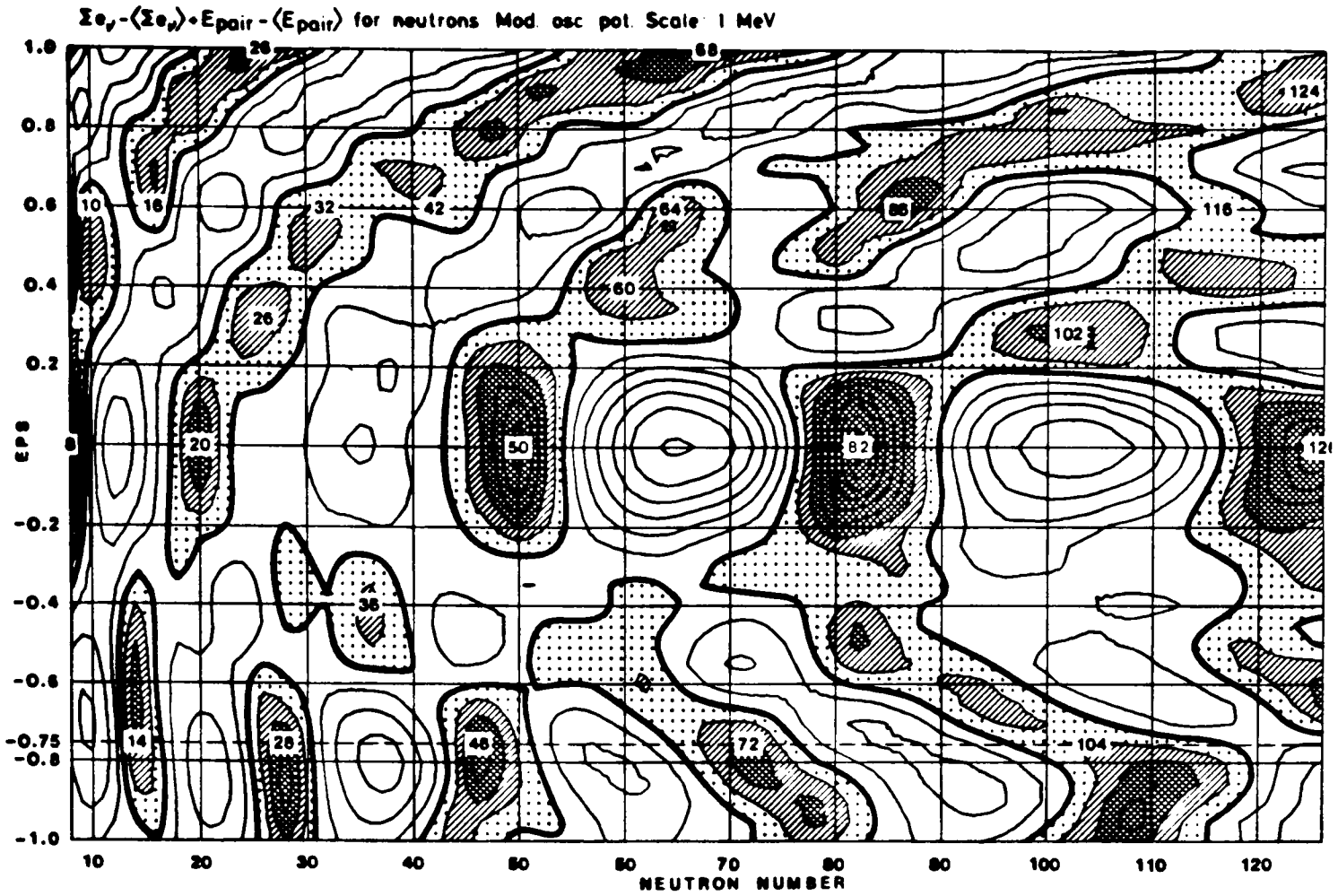


Fig.2.2 : 'Contour maps' of shell and pairing corrections for neutrons and protons. The top figure shows the corrections as a function of neutron number and ϵ, the quadrupole deformation parameter. The bottom figure is a similar plot for protons. Both figures have been taken from [RAG78].

For the axially symmetric harmonic oscillator potential, gaps between the levels appear at well-defined ratios of the frequencies of the oscillator well (fig. 2.3) As the energy of the levels vary with deformation, in certain cases, a nucleus may find it energetically advantageous to adopt a deformed shape. The minima in the contour plots above are analogous to the shell gaps seen in the figure†.

By replacing the harmonic oscillator with a more realistic potential (e.g. modified oscillator), the plot of energy levels versus deformation becomes, not surprisingly, more complicated and we are left with the familiar Nilsson diagrams as shown in fig. 2.4

In summary, the shell correction energy allows us to quantify the degree of stability of a nucleus for different shapes and hence allows us to calculate the equilibrium shape of a nucleus. By studying the behaviour of the shell correction energy as a function of ϵ and N (or Z), shell closures at large deformations are observed. With a harmonic oscillator potential, the first sign of shell structure reappears (the first appearance being the shell structure observed for spherical nuclei) at a 2:1 axis ratio which we have defined to correspond to a superdeformed shape. In the above calculations, the liquid drop term, of course, has to be considered as it also depends on the deformation parameters. In this term, we have the surface and Coulomb energies which tend to hold together and pull apart the nucleus respectively. Table 2.1 shows the magnitudes of the surface and Coulomb terms at zero deformation for various mass numbers. We see that the surface energy, E_S, is larger than the Coulomb energy, E_C, and dominates the lower and intermediate mass region. In the heavier mass region, E_C is of the same order-of-magnitude as E_S and their effects cancel each other. For light masses, where E_S is still moderately small, shell effects ($\sim 5 - 10$ MeV from [MYE60, MYE66]) can have a significant impact on the potential energy and in the heavier mass region, where E_S and E_C cancel each other, shell effects again play an important role. However, in the intermediate

† For the contour plots, a modified oscillator potential was used.

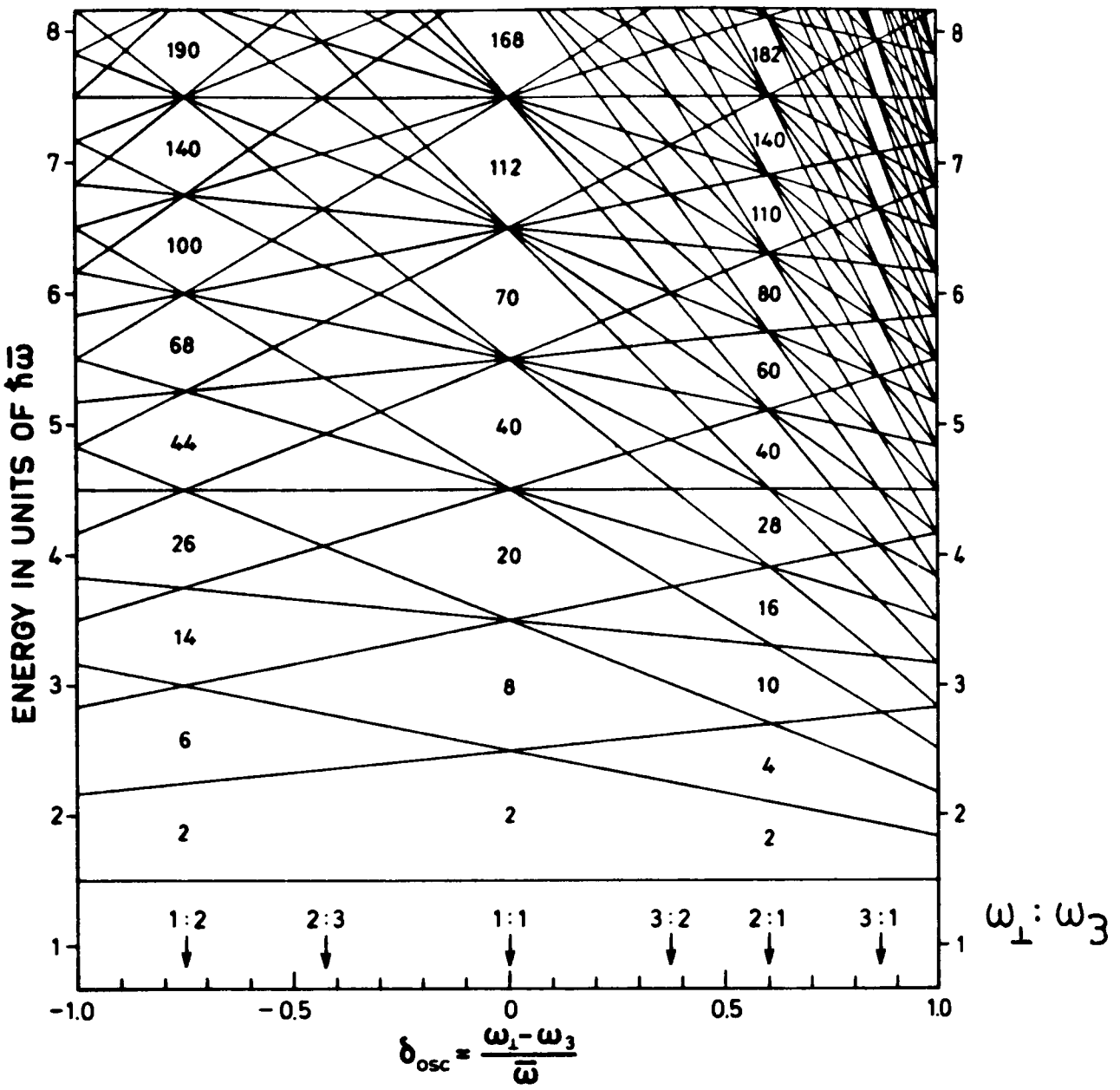


Fig.2.3 : Single particle spectrum for axially symmetric harmonic oscillator potential [BOH75].

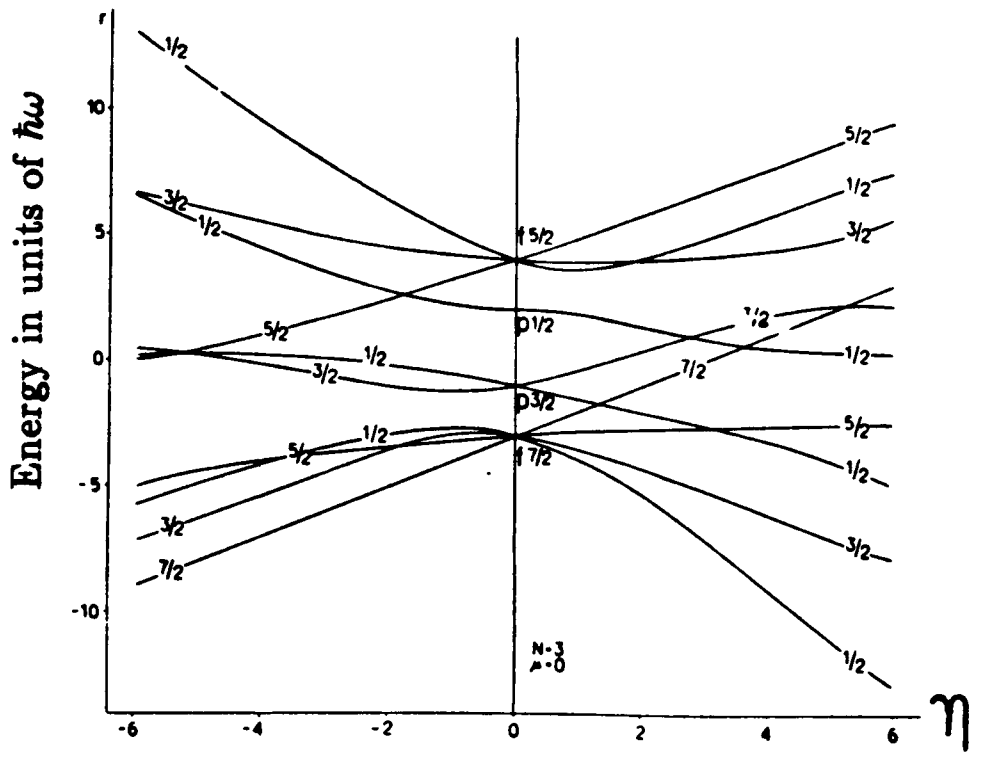


Fig.2.4 : Single particle spectrum for a modified oscillator potential [NIL55].

mass region, where E_S is the dominant term, the shell effects may be considerably weakened by this surface term which favours a spherical shape.

A	N	Z	E_S	E_C
10	5	5	86	8
40	20	20	217	84
80	40	40	345	266
100	54	44	400	299
208	126	82	652	814

Table 2.1 : Surface (E_S) and Coulomb (E_C) energies (in MeV) for different mass regions.

2.3 CASCADE

In order to select a suitable reaction to produce the nuclei of interest in reasonable abundance, we resorted to a statistical model code for determining the cross-sections of the many evaporation channels. In a compound nuclear reaction, the projectile and target fuse together to form a compound nucleus (CN) in an excited state which then decays by the emission of light particles. The probabilities for emission of these light particles depend on their transmission probabilities and the level densities in the initial and final nucleus and can be calculated from the Hauser-Feshbach formula [HAU52]. As the level densities are quite large and as we are dealing with a many-body system, statistical methods can be applied in analysing the system. In the statistical model, the CN is assumed to have been formed in statistical equilibrium with respect to all degrees of freedom. This means that the CN is initially 'equilibrated' (i.e it loses all knowledge of its formation process) and all the decay channels that are open (unless closed due to Coulomb or

centrifugal barriers) are equally probable. The only factors governing the probability of decay are the level densities and the barrier penetrabilities of the particles. Fig. 2.5 shows schematically the formation and decay of the CN. The cross-section for production of the CN with spin J and parity π is given by [THO64]

$$\sigma(j_p, j_t; J, E) = \frac{\lambda^2}{4\pi} \frac{2J+1}{(2j_p+1)(2j_t+1)} \sum_{j=|j_p-j_t|}^{j_p+j_t} \sum_{l=|J-j|}^{J+j} T_l(E) \qquad (2.12)$$

where j_p and j_t are the projectile and target spins respectively and the vector sum of these give the channel spin, j. This channel spin couples with the orbital angular momentum, l, to form the spin, J, in the CN. λ is the deBroglie wavelength of the relative motion and T_l is the transmission coefficient for the l^{th} partial wave of the incident particle and is given by the Fermi distribution

$$T_l = \frac{1}{1+\exp[-(l-l_o)/d]} \qquad (2.13)$$

where l_o defines the maximum angular momentum brought into the system and d is the diffuseness parameter. In the simple case where the projectile and target spins are zero ($j_t = j_p = 0$ and $J = l$), we have $\sigma \sim (2l+1)T_l$ and this distribution is shown in fig. 2.6

The decay of the CN depends on the barrier penetrability of the emitted particle as well as the level densities in the initial and final nucleus. The decay width for emitting a particle x and leaving a residual nucleus with spin j_r, parity π_r at an excitation energy E_r is

$$\Gamma_x(\epsilon_x) = \frac{\rho_r(E_r, j_r, \pi_r)}{2\pi\rho(E, J, \pi)} \sum_{j'=|j_r-s_x|}^{j_r+s_x} \sum_{l'=|J-j'|}^{J+j'} T_l^x(\epsilon_x) d\epsilon_x \qquad (2.14)$$

where ϵ_x, s_x and l' are the kinetic energy, spin and orbital angular momentum respectively of the evaporated particle and j' is the channel spin. The ρ's are the level densities in the initial and final nuclei and may be obtained from the Fermi Gas Model [GIL65]. The transmission coefficient T_l^x is calculated from the optical model.

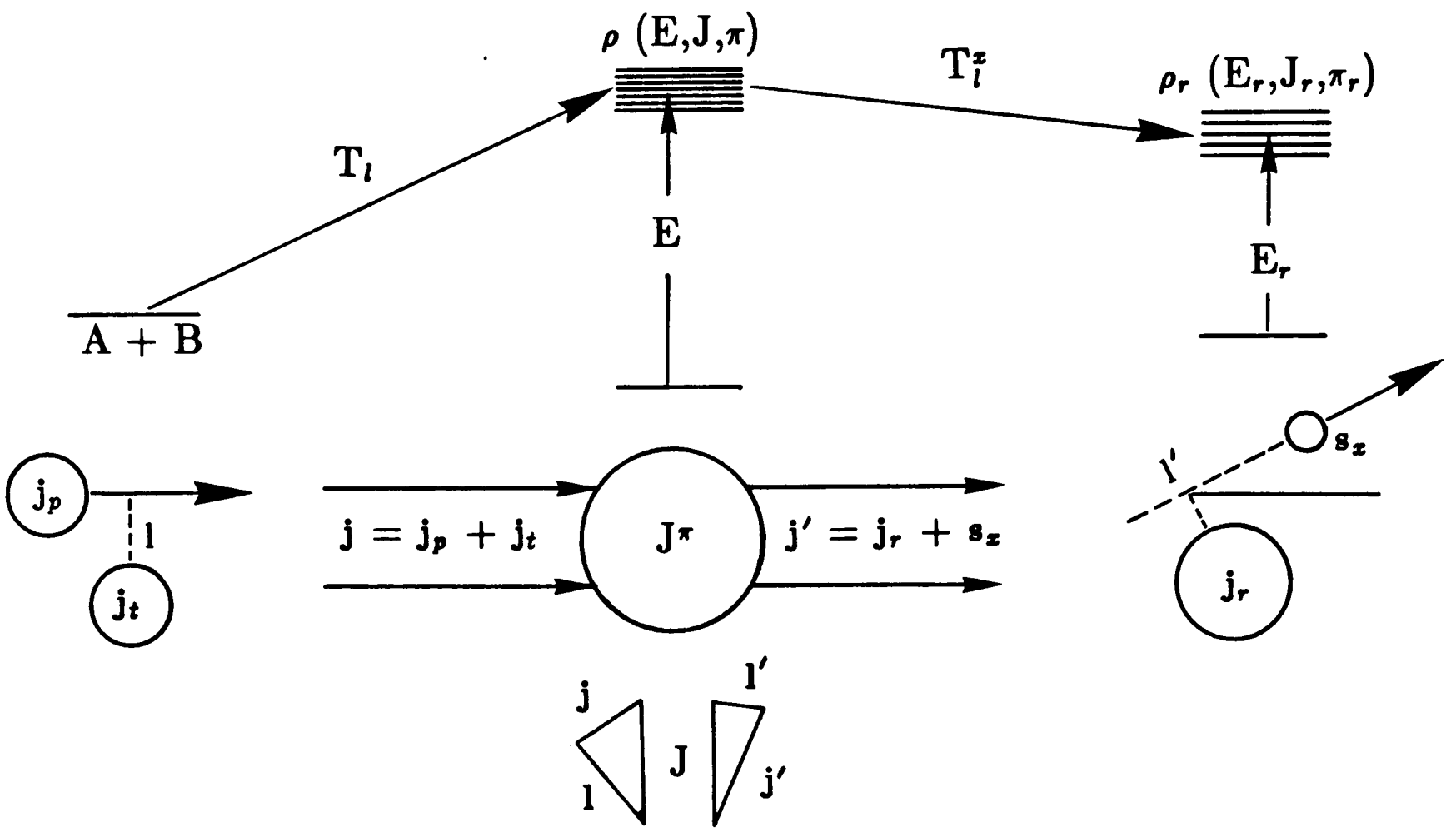


Fig.2.5 : Schematic diagram showing a fusion-evaporation reaction.

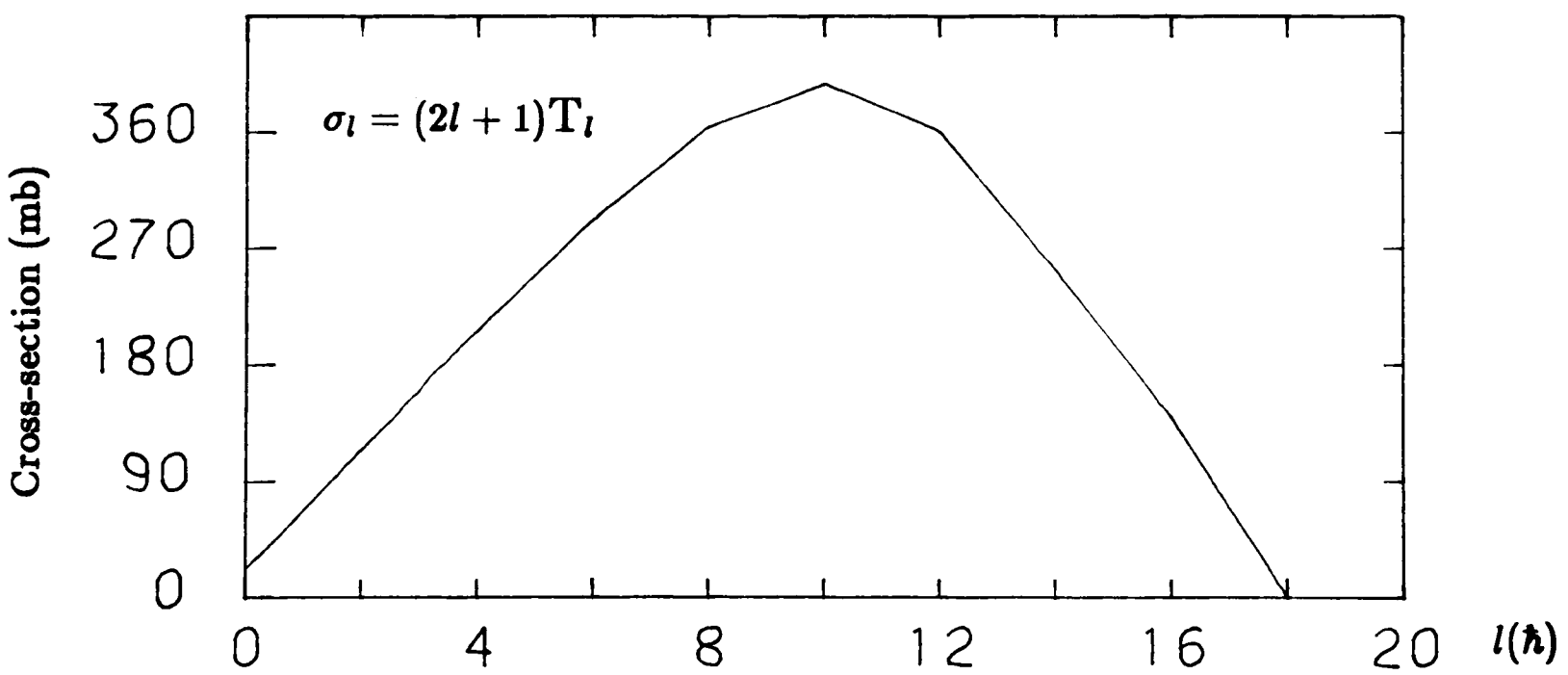


Fig.2.6 : Distribution of angular momentum brought into the compound nucleus with spin 0 target and projectile (^{54}Fe + ^{12}C at 150 MeV).

If the nucleus is still sufficiently hot after the evaporation of one particle, it will continue to emit particles until the available energy drops below the different particle evaporation thresholds. At this stage, the nucleus de-excites by the emission of γ-rays. The decay width for the γ-rays is of a similar form to the particle widths [PUH77a].

Several computer codes exist which perform the above calculations iteratively to determine the cross-sections for producing the various residual nuclei. The code chosen was CASCADE [PUH77a]. Apart from the advantage of having it in executable form on our VAX 11/780, this code has been applied with reasonable success to many nuclei in the fp-shell [PUH77a, PUH77b, CAN79]. The code contains several input parameters (see Appendix V) which specify the level densities, the fusion cross-section and various cut-offs imposed by the program. Default values are used by the program in the absence of an input value and these default values are listed in the documentation with the program [PUH79]. In our calculations, these default values were used but we also investigated the effects of changing these values on the cross-sections obtained. In Appendix V, table V.2 shows the cross-sections calculated using different input parameters. Fig. V.3 is a pictorial representation of this table and shows the percentage change from the default cross-sections. We see that the cross-sections vary by no more than a factor of two and as we were interested in order-of-magnitude estimates of the cross-sections, this accuracy was quite adequate for our purposes.

2.4 ^{48}Cr

2.4.1 ^{48}Cr – A Synopsis

The self-conjugate nucleus $^{48}_{24}Cr_{24}$ has 8 particles in the $f_{7/2}$ shell. With these many particles outside a closed-shell, their anisotropic orbits will tend to drive the nucleus away from spherical symmetry and deform the nucleus [RAI50]. The Potential Energy Surface (PES) plot for ^{48}Cr is shown in fig. 2.1(b) and we see that this plot predicts the nucleus to have a prolate deformed ground-state shape [LAR76]. For a shell-model analysis in the $f_{7/2}$ shell, this nucleus provides a rigorous test as it is in the middle of the shell and therefore has the most complex shell model configuration.

In the early and mid-70's, the first γ-ray spectroscopic studies of this nucleus were undertaken using heavy-ion (HI) evaporation reactions [KUT73,HAA75]. Before this, the only information was from $2p$ transfer and pickup reactions ([SHE72] and references in [KUT73]). This was followed by other HI-evaporation experiments [EKS79,HAN79] which allowed a level scheme (up to 7 Mev in excitation and 10^+ in spin) for states produced in HI-induced reactions to be constructed. The spin and parity assignments of 10^+ for the state at 7066 keV are still uncertain. These investigations showed that no well-defined rotational band is observed in ^{48}Cr. Fig. 2.7 shows a plot of the energy of the levels against $J(J+1)$ and shows that a rotational band built on the 2^+ state is a possibility but the energy of the states depart from ideal rotational behaviour above the 6^+ state. Shell model calculations in the $f_{7/2}$ shell have been used in an attempt to understand these levels observed [EKS79]. This has been reasonably successful but in ^{48}Cr, states up to I=16 are possible with the $(1f_{7/2})^8$ configurations and these high-spin states have yet to be studied. A knowledge of more levels in ^{48}Cr would thus allow us to apply a more rigorous test to the shell model predictions.

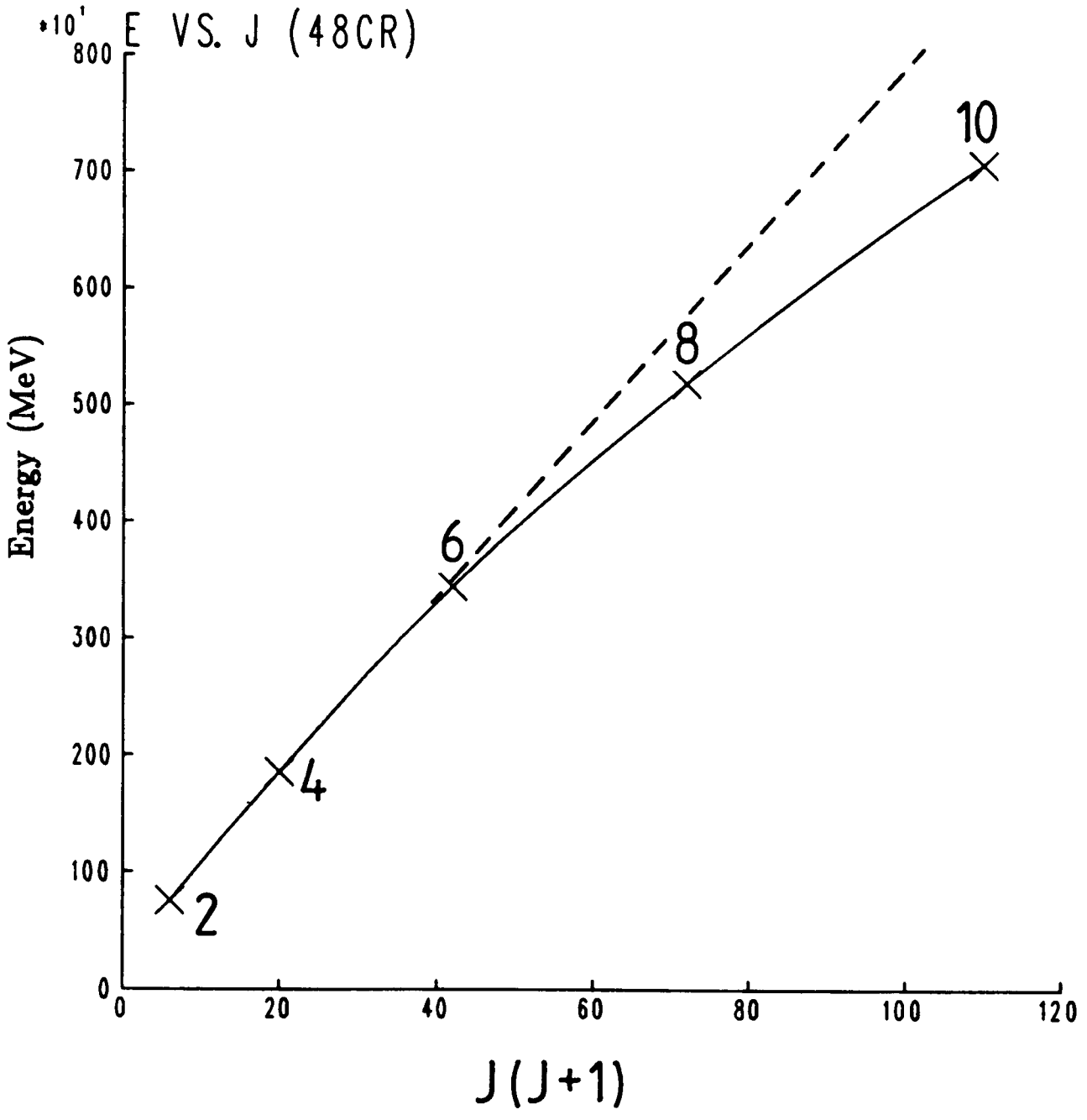


Fig.2.7 : Energies of the states in the main band in ^{48}Cr against J(J+1). The dotted line shows the trend expected for an ideal rotational band built on the 2^+ level.

To this end, the ^{48}Cr experiment described in this thesis used a reaction that was chosen to bring in as much angular momentum as possible in order to populate the high-spin states in ^{48}Cr.

2.4.2 Choice of Reaction to form ^{48}Cr

Previous HI-evaporation studies of this nucleus have used the reactions listed in table 2.2. The energies quoted are values at which the majority of the data were taken.

Reaction	Energy(1) (MeV)	Reference	$E_x^{CN(2)}$ (MeV)	$l_m^{(3)}$ ($\hbar$)
$^{40}_{20}$Ca($^{10}_{5}$B,$pn\gamma$)	22.5	[HAN79]	37.8	7.1
	24	[EKS79]	39.0	8.7
	25	[KUT73]	39.8	9.6
$^{34}_{16}$S($^{16}_{8}$O,$2n\gamma$)	34	[HAA75]	38.7	10.4
$^{36}_{18}$Ar($^{14}_{7}$N,$pn\gamma$)	33	[EKS79]	39.0	11.0
$^{27}_{13}$Al($^{24}_{12}$Mg,$p2n\gamma$)	62	[present work]	50	18.5

Table 2.2 : HI reactions used to date for the study of gamma rays from ^{48}Cr.
(1) Projectile energy in the laboratory frame
(2) Excitation energy in the compound nucleus.
(3) Maximum angular momentum brought into the compound nucleus [COH74].

The ^{27}Al(^{24}Mg,$p2n\gamma$)^{48}Cr reaction was chosen for its relatively simple target requirements and for the large angular momentum the ^{24}Mg brought into the system. The dominant decay in this reaction was expected to be the $2pn$ channel leading to ^{48}V (see next section). As a major part of the work described in this thesis involved the design and development of a neutron multiplicity detector, the added advantage of the above reaction was that ^{48}Cr was produced via a $p2n$ channel. Furthermore, γ-rays from a large contaminant $2pn$ channel had to be suppressed. This allowed the performance of the system to be tested under strict (but not extreme) experimental conditions.

2.4.3 CASCADE Analysis for ^{48}Cr

The evaporation code, CASCADE, as described in section 2.3, was used to determine the optimum bombarding energy needed to maximize the yield of ^{48}Cr. Calculations were made with energies just above the Coulomb barrier where the few particle evaporation channels were dominant. The input parameters to the code were the default* values and the cross-sections obtained are shown in fig. 2.8. The $p2n$ channel (^{48}Cr) is almost an order of magnitude lower in cross-section than the $2pn$ channel (^{48}V) but is, nevertheless, reasonably large (~30 mb). This disparity in the $2n$: $1n$ cross-sections was used to test the $2n$ detection efficiency of the n-multiplicity detection system against a large $1n$ background (a similar situation situation was expected for ^{64}Ge – see section 2.5.3). The formation cross-section of ^{48}Cr peaks at about 58 – 62 MeV and at this energy, the cross-section is still larger than the other $2n$-related channel, $2p2n$, making ^{47}V. A bombarding energy of ~60 MeV is thus the optimum value predicted by the evaporation code.

Fig. 2.9 shows the CASCADE population matrix for the residual nucleus, ^{48}Cr, after $p2n$ evaporation. This is a two-dimensional plot of the cross-sections (calculated by the code) for populating the states of energy E and spin J in ^{48}Cr after particle evaporation. We see that states with spins up to ~14 $\hbar$ can be populated but that most of the strength is expected to populate states with spins of about $11 - 12$ $\hbar$. A search was performed to find other possible reactions that might have brought in more angular momentum but none with a convenient target and projectile was found. A larger bombarding energy would have brought in more angular momentum but the cross-section for producing ^{48}Cr would have been intolerably small.

---

* see Appendix V

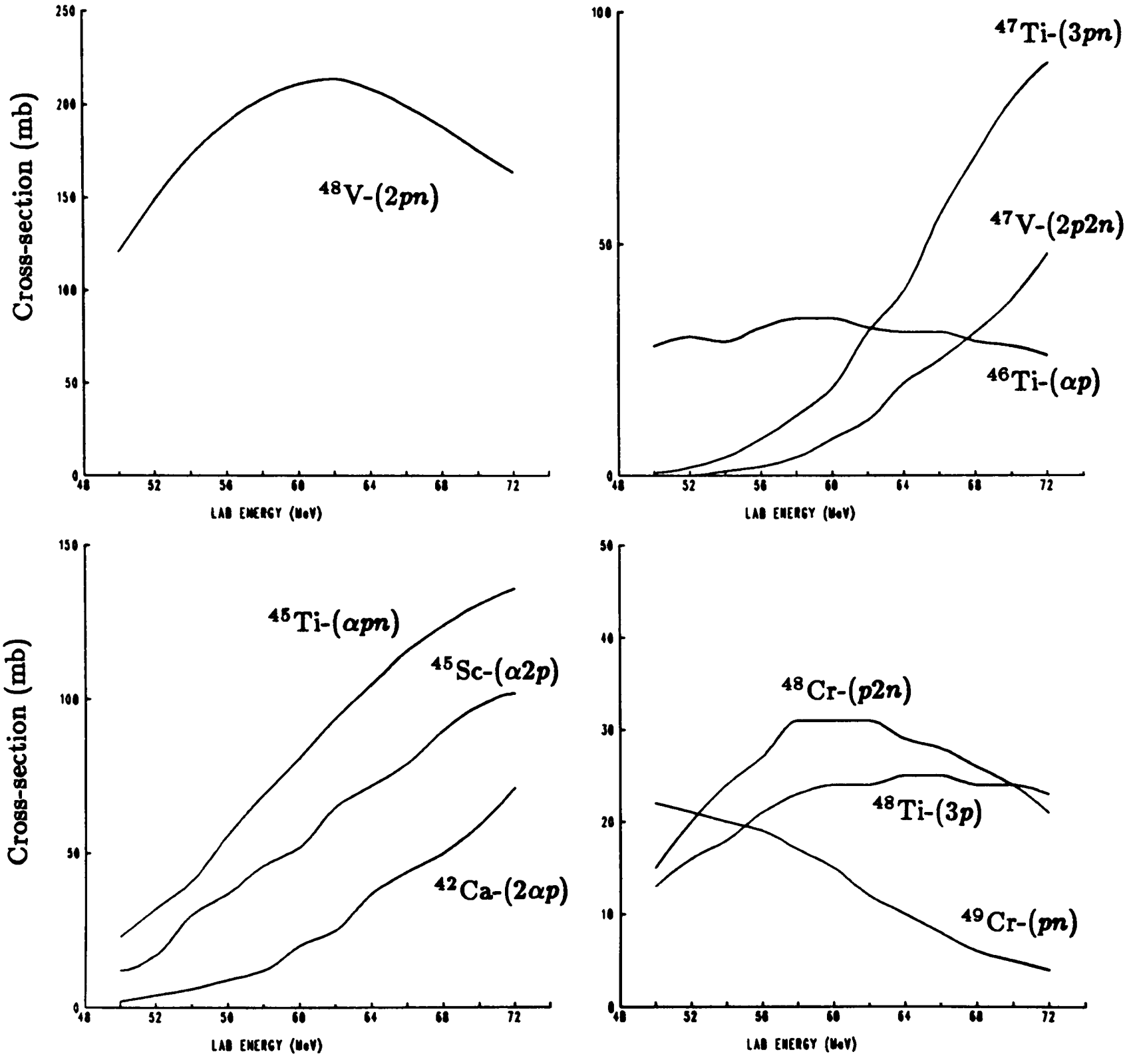
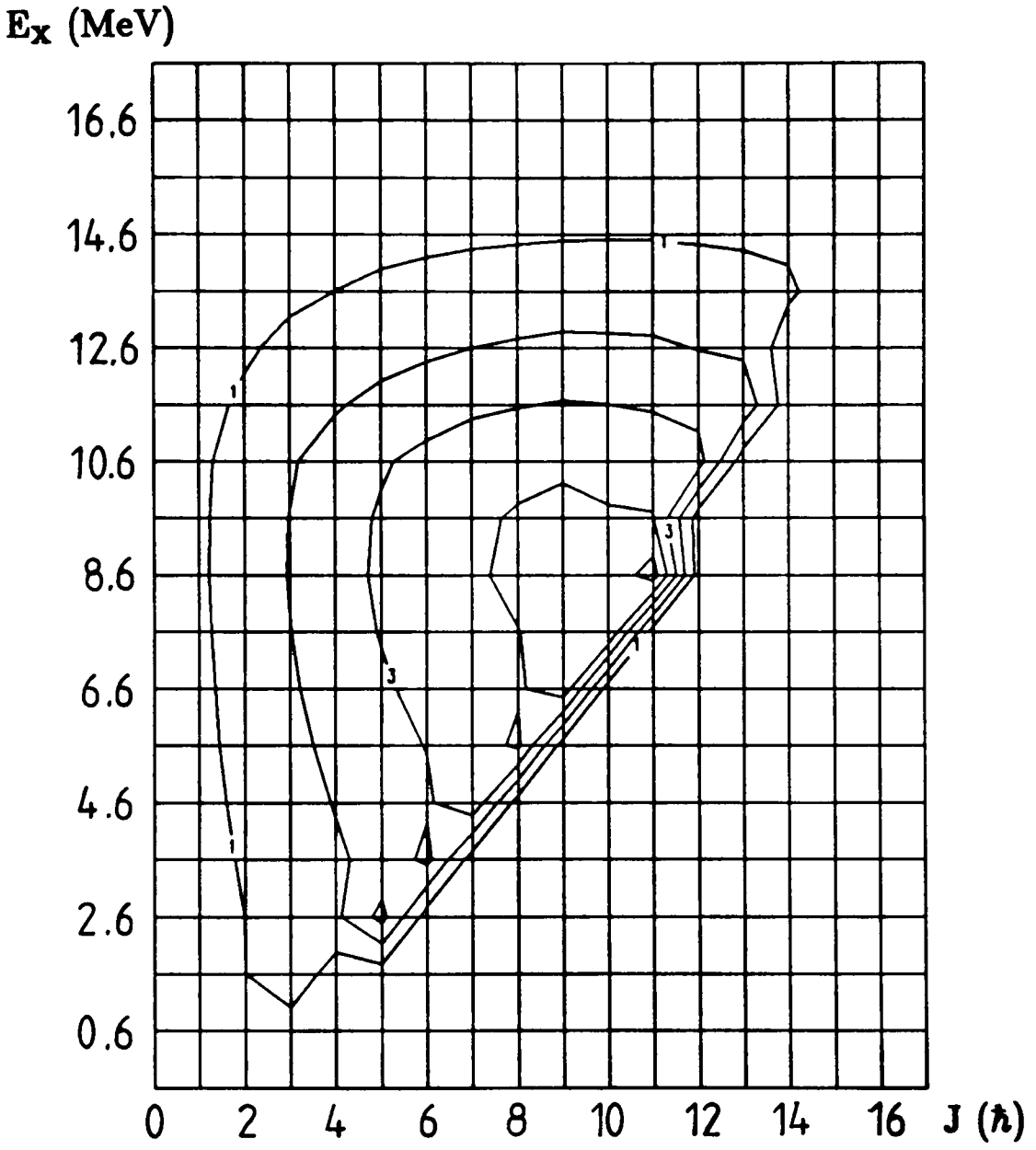


Fig.2.8 : CASCADE cross-sections for ^{48}Cr. ($Al^{27} + Mg^{24}$)



CONTOUR KEY	
1	84.4
2	253.2
3	422.0
4	590.8
5	759.6

micro-barns

Fig.2.9 : Population matrix of ^{48}Cr as predicted by CASCADE.

2.5 ^{64}Ge

2.5.1 Models of ^{64}Ge & PES calculations

There was some speculation in the mid 70's [SHE76] that the ground state of ^{64}Ge was superdeformed. For an axially symmetric potential, this implies a value of at least 0.6 for the quadrupole deformation parameter, ϵ [LOB70 for the definition of ϵ]. If ^{64}Ge is superdeformed, it will be the first instance of such a shape for the ground state in the intermediate mass region (A $\sim$ 60 to 100).

Using the approach of section 2.2, the total potential energy of a nucleus can be subdivided into a liquid drop (LD) term and a shell correction term, the former of which is a sum over the volume, surface, Coulomb and other terms [KUM66]. The shape of the nucleus will depend essentially on the surface term (which will favour a spherical shape), the Coulomb term (which is repulsive and will therefore distort the nucleus) and the shell effects (the outcome of which will depend on the Nilsson level density at the particular deformation). A pairing correction term also has to be added. This term will be negative if the level density near the Fermi level is high as more pairs can then interact. This is in opposition to shell effects which tend to favour lower level densities (i.e. a shell gap). However, shell effects are larger than pairing corrections [BOL72] and so they determine the trends of the corrections to the liquid drop energy.

In the intermediate mass region, the influence of shell effects is far less pronounced. This is because the surface term in the LD energy is dominant compared with the shell effects. The LD parameters have yet to be determined experimentally (by fitting the LD parameters to experimental masses) in this region . If the liquid drop energy is neglected as a first approximation, the shell and pairing corrections for different masses at different deformations can be calculated. This is shown in fig. 2.2 and there is a suggestion of a stable equilibrium at $\epsilon \simeq 0.6$ for N=Z=32, which was pointed out by Sheline [SHE76]. The calculation performed to obtain

these two plots used a realistic (modified oscillator as opposed to a harmonic oscillator) potential and shows N=Z=32 to be a closed shell for prolate 2:1 ($\epsilon = 0.6$) shapes. This ratio corresponds to a superdeformed shape, as defined above. Later calculations by Ragnarsson, Nilsson and Sheline [RAG78] showed ^{64}Ge to be less deformed but with a greater degree of γ-deformation hence forming a triaxial shape. These calculations included the γ degree of freedom which showed the opening up of a shell gap in the Nilsson plot for N=Z=32 for $\epsilon = 0.3, \epsilon_4 = 0.08$ and $\gamma = 35°$.

More recently, a more complete calculation, with a greater number of shape parameters, was performed [RAG84]. This predicted a far softer nucleus with almost no deformation. Other workers [MOL81, BEN84], using the same technique but with a Yukawa-plus-exponential potential (instead a LD potential) for the macroscopic term, produced a mildly deformed ($\epsilon = 0.2$) nucleus with a small hexadecapole deformation ($\epsilon_4 = 0.04$). The PES of this calculation is shown in fig. 2.1(a). This new potential has far more correction terms in it that account for the finite range of nuclear forces and the Coulomb diffuseness [MOL81].

However, the calculations, although probably good for indicating the general trends of a region, fall short of a precise (and consistent) prediction for the shape of an individual nucleus. Each calculation differs from the others by the inclusion of more (or different) parameters to the potential used. The many different predictions obtained indicate that the minimum in the PES plot is sensitive to the parameterization of the potential and the shape degrees of freedom used. The simple model with a realistic potential but only one shape parameter, ϵ, predicts the ground state of ^{64}Ge to be superdeformed. Hence, it was of great interest to test this prediction and see how well this simple treatment performed. For stable isotopes, the magnitude of nuclear deformation can be determined by Coulomb excitation of nuclear levels or hyperfine splitting measurements of the atomic spectrum. This is not possible for unstable isotopes and, instead, a knowledge of transition rates provides a similar insight. Historically, the energy of the first 2^+ state has been used as a yardstick for determining the degree of deformation of a nucleus. The

observation of a well-defined rotational band is even better (!) except that for ^{64}Ge, where the cross-section is expected to be small (see next section), we can hope, at best, to measure the energy of the first one or two excited states. Assuming that only the first excited state is observed, we can employ the empirical relationship [GRO62] between the energy of the first 2^+ state and the B(E2;2→0) to calculate the deformation parameter as given by [STE72]

$$\epsilon^2 \approx \frac{1176}{A^{7/3}E(2^+)[\mathrm{MeV}]} \tag{2.15}$$

This formula was derived assuming an axially deformed nucleus. Such a simplistic model may not accurately represent the nuclear shape and also if the first 2^+ state is a collective vibrational state, then ϵ does not have much meaning. Nevertheless, equation 2.15 is useful in providing an approximation of the deformation parameter of a nucleus if only the energy of the first 2^+ state is known. However, we should always bear in mind the generalizations made in its derivation. Using equation 2.15 and assuming a superdeformed shape ($\epsilon = 0.6$) for A=64, the first excited state is expected to be at about 200 keV.

Our knowledge of the spectra of even-even N=Z nuclei stops at ^{60}Zn. In self-conjugate nuclei, the protons and neutrons occupy the same orbitals. Therefore, neutron and proton shell effects are in phase and are expected to reinforce each other. If the shell effects have a preference for a deformed shape, then a coherent combination of both the neutron and proton shell effects may drive the nucleus towards superdeformation. The study of γ-rays from ^{64}Ge would thus shed light on what still remains a little known region of the periodic table.

2.5.2 Choice of Reaction to make ^{64}Ge

As ^{64}Ge is some distance away from the β-stable line, the cross-section is very small for populating the states of this nucleus. The lack of suitable projectiles and targets made transfer reactions inappropriate and so a heavy-ion evaporation reaction had to be used. As ^{64}Ge is on the proton-rich side of the line of stability,

charged particles are preferentially boiled off. The cross-section predicted by CASCADE for different projectile-target combinations and various exit channels making ^{64}Ge are almost zero. The reaction which was chosen gave the largest calculated cross-section and is a ^{12}C-^{54}Fe combination producing ^{64}Ge via a $2n$ channel. In this reaction, a large background of charged particle channels was expected. However, most of the γ-rays from these contaminant channels were removed by our n-γ detection system. This projectile-target combination has the added advantage of having been used before to successfully produce ^{64}Ge [DAV73].

2.5.3 CASCADE Analysis for ^{64}Ge

Calculations were carried out with projectile energies just above the Coulomb barrier. These energies were chosen because larger incident energies would have opened up more unwanted evaporation channels. The cross-sections of the various exit channels are listed in table 2.3 and are plotted in fig. 2.10. The CASCADE input parameters used were the default values (see Appendix V).

Energy (lab)	Energy (cm)	$2p$ ^{64}Zn	$2pn$ ^{63}Zn	$3p$ ^{63}Cu	αp ^{61}Cu	pn ^{64}Ga	αn ^{61}Zn	$p2n$ ^{63}Ga	$2n$ ^{64}Ge
(MeV)	(MeV)	(mb)	(mb)	(mb)	(mb)	(mb)	(mb)	(mb)	(mb)
30	24.5	76	6	5	30	46	3.3	0	0.2
31	25.4	98	13	10	43	60	5.3	0	0.4
32	26.2	110	24	19	55	70	7.1	0	0.5
33	27.0	124	34	25	66	80	8.9	0	0.7
34	27.8	130	55	34	78	79	10.7	0.4	0.7
35	28.6	120	75	49	79	73	11.6	0.8	0.7
36	29.4	114	102	62	85	68	12.5	1.0	0.9
37	30.2	110	125	72	95	68	12.8	1.9	0.8
38	31.1	101	148	86	100	64	13.6	3.1	0.7
39	31.9	99	183	80	104	55	14.4	4.3	0.6
40	32.7	83	195	103	106	50	13.3	6.2	0.5

Table 2.3 : Cross-sections for the various decay channels of $^{12}C + {}^{54}Fe \rightarrow {}^{66}Ge$. Energies given are for the incident energy in the laboratory (lab) and centre-of-mass (cm) frames. The Coulomb barrier is at 25.7 MeV in the centre-of-mass frame.

We see from this table and fig. 2.10 that the optimum range at which to run the experiment is between 32 and 38 MeV (laboratory frame). A larger bombarding energy simply opens up more contaminant channels while a lower bombarding energy is below the Coulomb barrier. The largest channel is the $2p$ channel and so we expect the singles spectrum to be dominated by the γ-rays from ^{64}Zn. The $1n$-related channels are about two orders of magnitude larger than the $2n$ channel. The cross-scattering of neutrons between detectors means that the breakthrough of

these channels into the $2n$-gated γ-ray spectrum is inevitable and steps have to be taken to reduce this breakthrough. There are very few $2n$-related channels. The cross-section for the $\alpha 2n$ channel is zero throughout the energy range and so that leaves the $2n(^{64}\mathrm{Ge})$ and $p2n(^{63}\mathrm{Ga})$ channels with finite cross-sections. Nothing is known about the energy spectrum of ^{63}Ga and so this is a possible source of concern. In order to remove these unwanted channels to obtain a γ-ray spectrum of true $2n$ events, a pure neutron multiplicity detection system is required which satisfies the following criteria:–

1) removes charged particle channels.
2) removes $1n$-related channels e.g. pn, αn, & $2pn$
3) removes $2n$-(charged particle) channels e.g. $p2n$

The design and development of such a system is described in the next chapter.

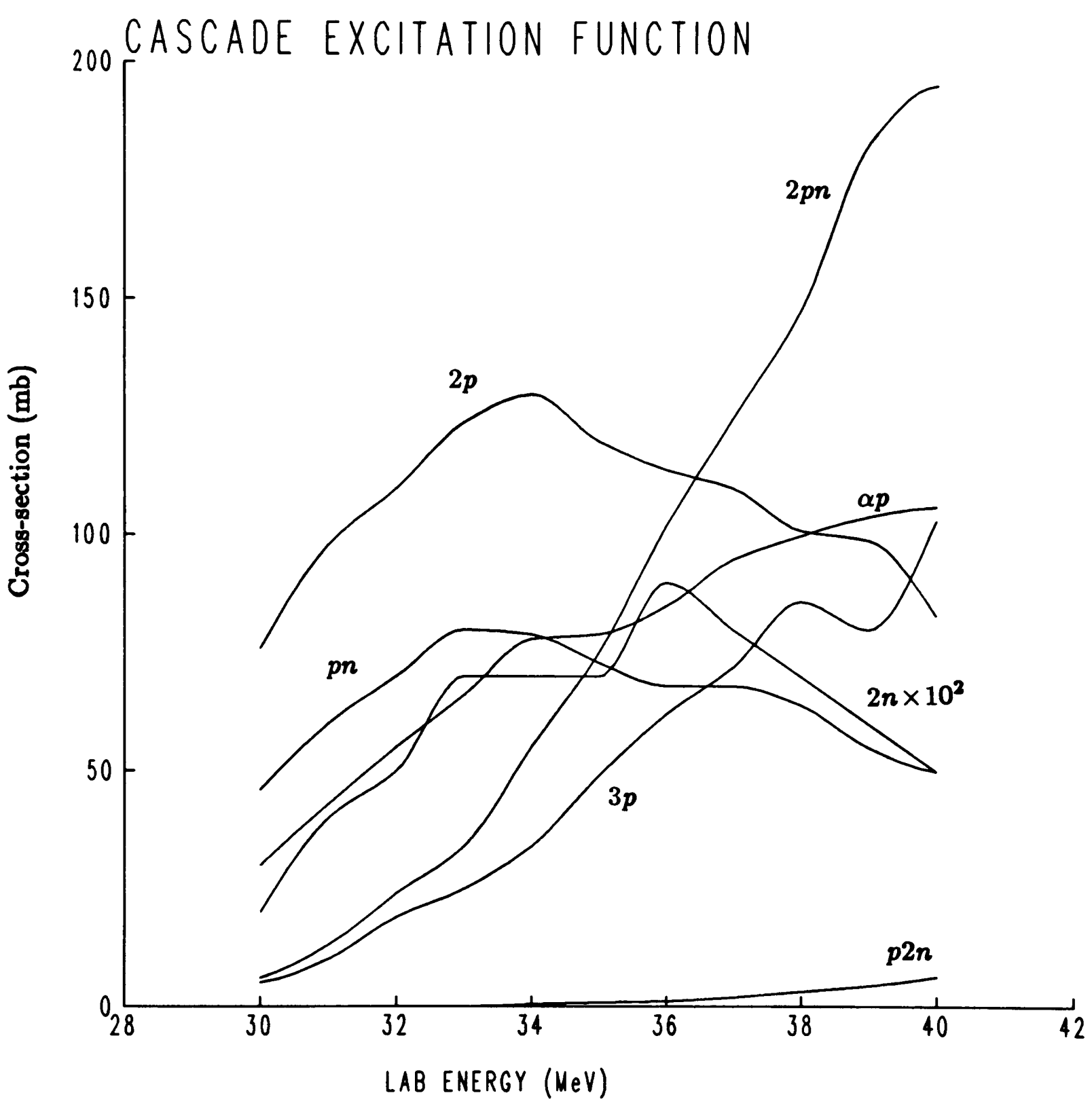


Fig.2.10 (a) : CASCADE cross-sections for $^{12}C + ^{54}Fe$.

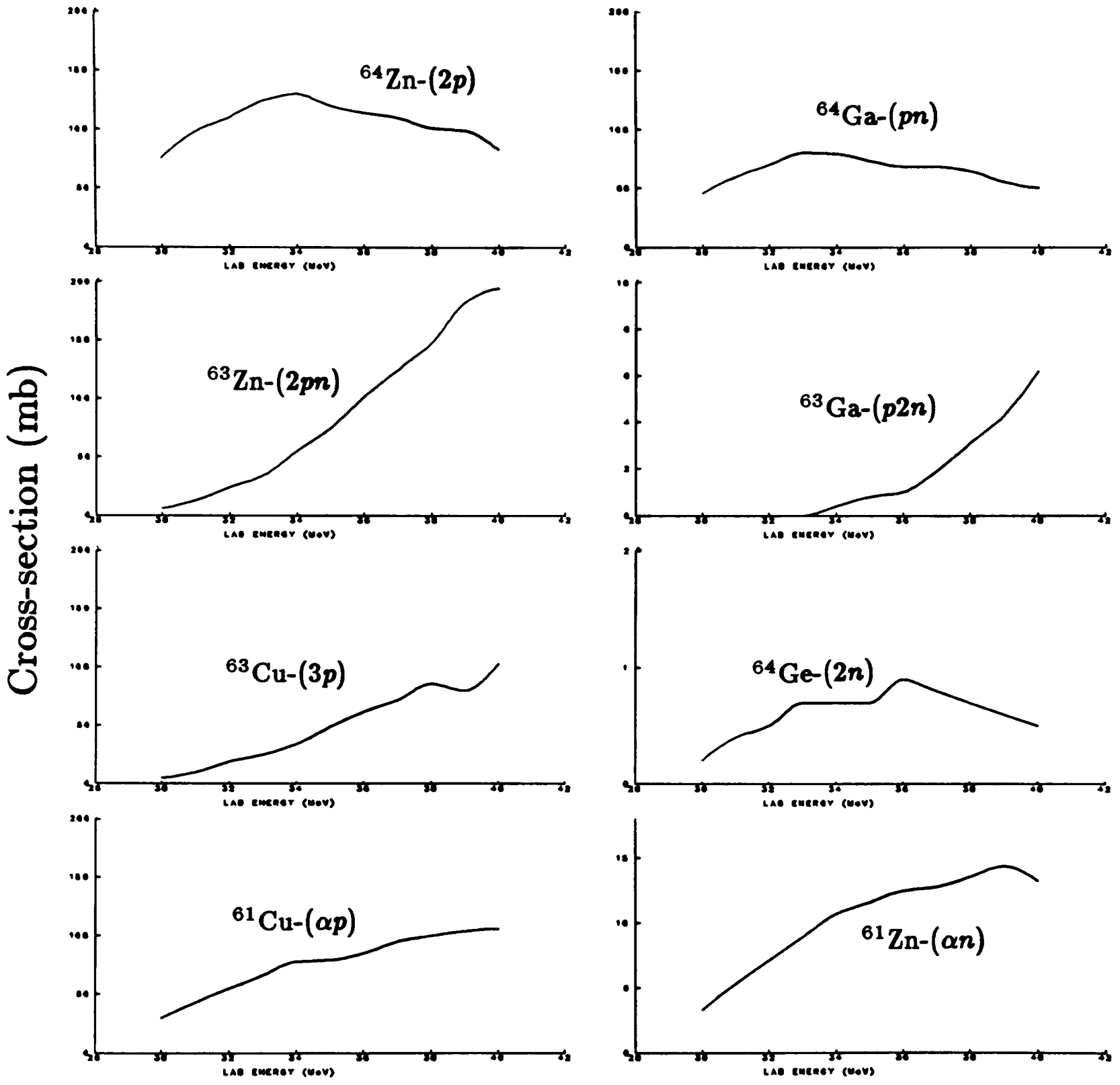


Fig.2.10 (b) : CASCADE cross-sections for $^{12}C + ^{54}Fe$.

3

CHAPTER 3

Experimental Details

"No, no!", said the Queen, "sentence first

— verdict afterwards"

3.1 Introduction - Design of a pure n-multiplicity detector

All the experiments described in this thesis were performed using the Folded-Tandem accelerator at the Nuclear Physics Laboratory in Oxford. In this chapter, we address ourselves to the design and subsequent development of a detection system capable of detecting weak pure neutron evaporation channels in a background of predominantly charged particle events. The reaction considered here is the ^{54}Fe(^{12}C,$2n\gamma$) reaction producing ^{64}Ge. As the channel of interest is the $2n$ channel, the determination of the n-multiplicity of an event provides useful additional information in identifying the γ-rays from this channel. This can be done by having an array of neutron detectors and sorting the data for events in which two detectors fire. In principle, this gating should suppress the $1n$ channel but scattering of neutrons from one detector into another usually means a certain amount of $1n$

events break through into the $2n$ spectrum. For our reaction, the $1n$ channel is negligible but the pn channel is predicted by CASCADE to be two orders of magnitude larger than the $2n$ channel. However, this channel can be suppressed by detecting charged particles from the experiment. Events which feature charged particles are rejected thus enhancing pure neutron channels. This vetoing also suppresses the other two large contaminant channels viz. αn and $2pn$. Furthermore, the insidious $p2n$ channel is considerably reduced by this approach. A 4π charged particle detector is the ideal solution but for practical purposes, a more modest approach must be adopted. These specifications were used as guide-lines in designing the experimental apparatus. In the following sections, a detailed description of each component of the system is presented and discussed. To detect such a weak channel meant that the neutron detectors had to be efficient and reliable. The neutron detectors were also sensitive to γ-rays and the method by which neutrons and γ-ray signals in the neutron detector are differentiated is discussed. Standard Nuclear Instrument Modules (NIM) were used for the amplification, shaping and timing of the signals and the electronic block diagram for these modules is presented. Several experimental arrangements were tried for the experiments and the schematic arrangements of these experiments are also presented. The off-line reduction of the data to extract the $2n$ events was achieved by using a sorting language, **SOL**, which allowed fairly complex logical manipulations to be performed on the data. The elements of this sorting language are given but a detailed description of it is left to appendix IV. Finally, the performance of the whole system in-beam is presented and discussed.

3.2 'ningles'

"When I make a word do a lot of work like that,"
said Humpty Dumpty, "I always pay it extra."

The neutron detector used in these experiments was sensitive to both neutrons and γ-rays. n-γ discrimination was not performed *in situ* but pulse shape and time-of-flight information were collected and written onto magnetic tape. The separation between neutron and gamma-ray events was done by software gates during off-line sorting since this allowed a more flexible constraint to be imposed. However, not all the signals from the experiment were recorded. In order to reduce the data rate, 'singles' γ-ray signals from the Ge(Li) detectors which were not in coincidence with any signal in the neutron detectors were rejected. All γ-ray signals recorded onto magnetic tape were thus in coincidence with at least one event in a neutron detector but the event in the neutron detector could have been due to either a γ-ray or a neutron. The spectrum thus obtained was half-way between a pure singles spectrum and an n-gated spectrum and will, for the sake of convenience, be termed 'ningles' in this thesis.

3.3 The Neutron Detector

A large liquid scintillator was used to detect the neutrons. This was an existing detector [CAR72, JOH71] which was modified to suit the needs of the experiments performed for this thesis. The modification was essentially an increase in the thickness of the detector to improve its neutron detection efficiency. The detector was in the shape of a cylinder 35 cm in radius and 16 cm thick with a hole of 8 cm radius in the centre. It was divided into independent quadrants, each of which was viewed by two 11 cm diameter Mullard XP1040 photomultiplier tubes. The central

hole was filled by a smaller (125 mm × 125 mm) cylindrical, encapsulated liquid scintillator. Fig. 3.1 shows the end view of this neutron 'wall' (consisting of the five neutron detectors). The dotted lines show the extent of the quadrant tanks. The detector was supported by a metal frame which was attached to a base plate with wheels in a track so the target-detector distance could be adjusted easily. The centre of the neutron wall was at the height of the centre of the beam line. All five detectors were filled with NE213†, a liquid scintillator which has good pulse shape properties. This means that the shape of the scintillation pulse was different for neutron induced events and gamma-ray induced events and this difference was used to separate the two types of events. Essentially, the light output from a liquid scintillator can be regarded as having a prompt and a delayed component and the ratio of these two components reflects the nature of the event. Neutron events have a larger delayed component in their light output and so have a different pulse shape from a γ-ray event. This is described further in Appendix III.

A simple formula for the efficiency at zero bias‡ of a liquid scintillator is given by [BAT61]

$$\epsilon = 1 - \exp(-n_H \sigma_H d)$$

where n_H is the number of hydrogen atoms/bn-cm of scintillator (0.05 atoms/bn-cm for NE213†), σ_H is the *n-p* cross-section and d is the mean thickness of the scintillator. An efficiency of ~53 % was calculated for the neutron detector in the ^{64}Ge experiment (using a ^{54}Fe beam on a ^{12}C target), assuming a neutron energy of approximately 4 MeV in the laboratory frame (calculated using CASCADE) and an *n-p* cross-section of 1.9 barns [HUG55]. Although a thicker scintillator would have resulted in a larger detection efficiency, this would have created problems with light collection in a larger tank with a subsequent deterioration of the timing resolution of the detector. Self-absorption effects in a larger scintillator would also have come

† Nuclear Enterprises Ltd., Beenham, Reading, Brochure 126P, 1980.

‡ where the bias level corresponds to the minimum neutron energy that can be detected.

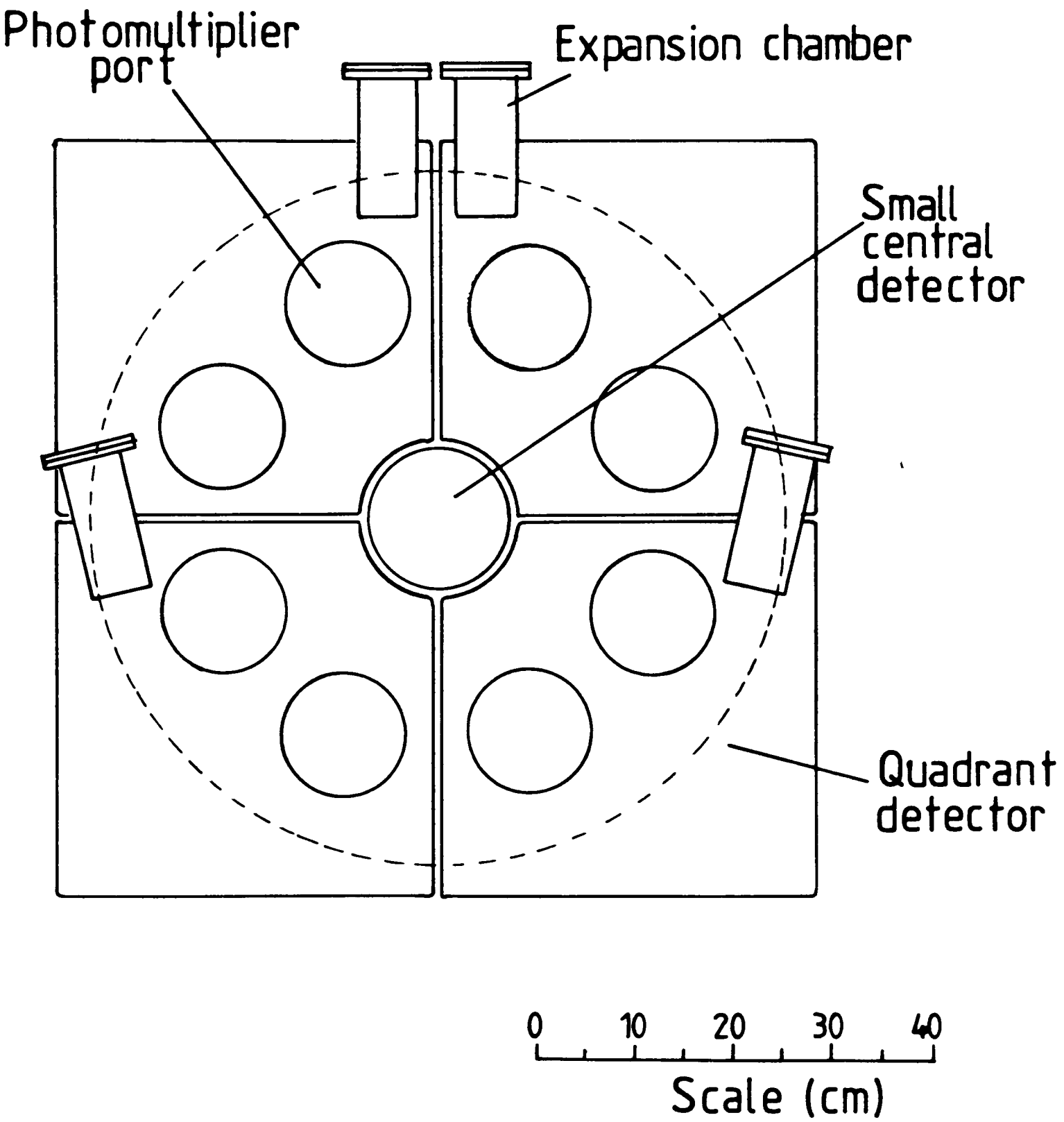


Fig.3.1 : End view of the Neutron Wall showing the four quadrant detectors (the extent of each tank is shown by the dotted line) and the small central detector.

into play [WAK69]. As it was, the time taken for a 4 MeV neutron to travel the thickness of the detector (16 cm) was calculated to be 5.7 ns.

The timing signals from the neutron detectors were taken off the anode of the photomultipliers. A fast coincidence (20 ns) was required between each pair of phototubes attached to a quadrant detector. This served to reduce the tube noise (dark current) of the photomultipliers. The positive dynode signals were used for pulse shape discrimination using standard NIM modules as described below. However, the Pulse Shape Discriminator units (PSD) were fed by the negative signals from the anode.

3.4 Neutron-Gamma Discrimination

With a large volume scintillator, the light collected from different parts of the scintillator arrive at the photomultiplier at different times. This distorts the pulse shape and makes the difference in pulse shape between a neutron and a γ-ray event much harder to distinguish so that commercial PSD's, which work well with smaller scintillators, were found not to work with our detectors. An interim solution was reached by using a *composite* PSD (that used standard NIM modules) instead of a custom-built PSD. Eventually, a PSD was found which worked with the large volume detectors used in the experiments. TOF n-γ discrimination was also used for n-γ discrimination and both TOF and pulse shape discrimination were used together to improve the n-γ discrimination. All these methods will be described below.

3.4.1 Time-of-Flight

Neutrons and gamma rays can be differentiated by measuring the time taken to traverse a set distance. This is normally done by using a pulsed beam which

provides a useful zero time signal (see chapter IV.A of ref. [MAR60]). However, with a DC beam, the γ-rays from the reaction can be used to provide the initial pulse to the timing circuit. This is possible provided short time intervals can be measured with precision, which requires a resolving time of the circuits of $\sim 10^{-9}$ sec. (chapter V.Q of ref. [MAR60]) and this was achieved here with fast logic boxes. Timing signals were taken from the Ge(Li) detector and the scintillator — the time difference was converted to a voltage by a time-to-amplitude converter (TAC). The beam current was sufficiently low (~5 enA) so that random coincidence rates were at an acceptable level (30 cts/s). This is demonstrated by the TOF spectrum in section 8 where the background channels have very few counts. As the counting rates in the neutron detectors (~3 kcts/s) were much lower than in the Ge(Li) detectors (~10 kcts/s), the timing of the TAC was started by the n-detector and stopped by a delayed Ge(Li) timing signal. The TOF technique proved simple to use and provided reasonable n-γ separation as is shown below. A disadvantage of TOF discrimination was that the neutron detectors were necessarily placed some distance (~60 cm) away from the target and this reduced the solid angle subtended by the detector at the target.

3.4.2 Pulse Shape Discriminator (Freiburg box)

The pulse shape discriminator (PSD) used was based on a Freiburg design [BET74]. This unit accepted negative signals from the anode of the phototube and the circuit essentially determined the decay time of the input signal and converted this information into two timing signals (one 'start' and one 'stop' signal) which were channelled into a TAC. Five such boxes were constructed and they were found to work well with the large volume scintillators that were used. TOF information was still collected during the experiments as this, in conjunction with the pulse shape information, was used to provide a clean neutron gated spectrum, as will be explained later. These Freiburg units were used mainly in the ^{48}Cr experiment. A typical PSD spectrum is shown in fig. 3.2(a) with the n and γ peaks labelled.

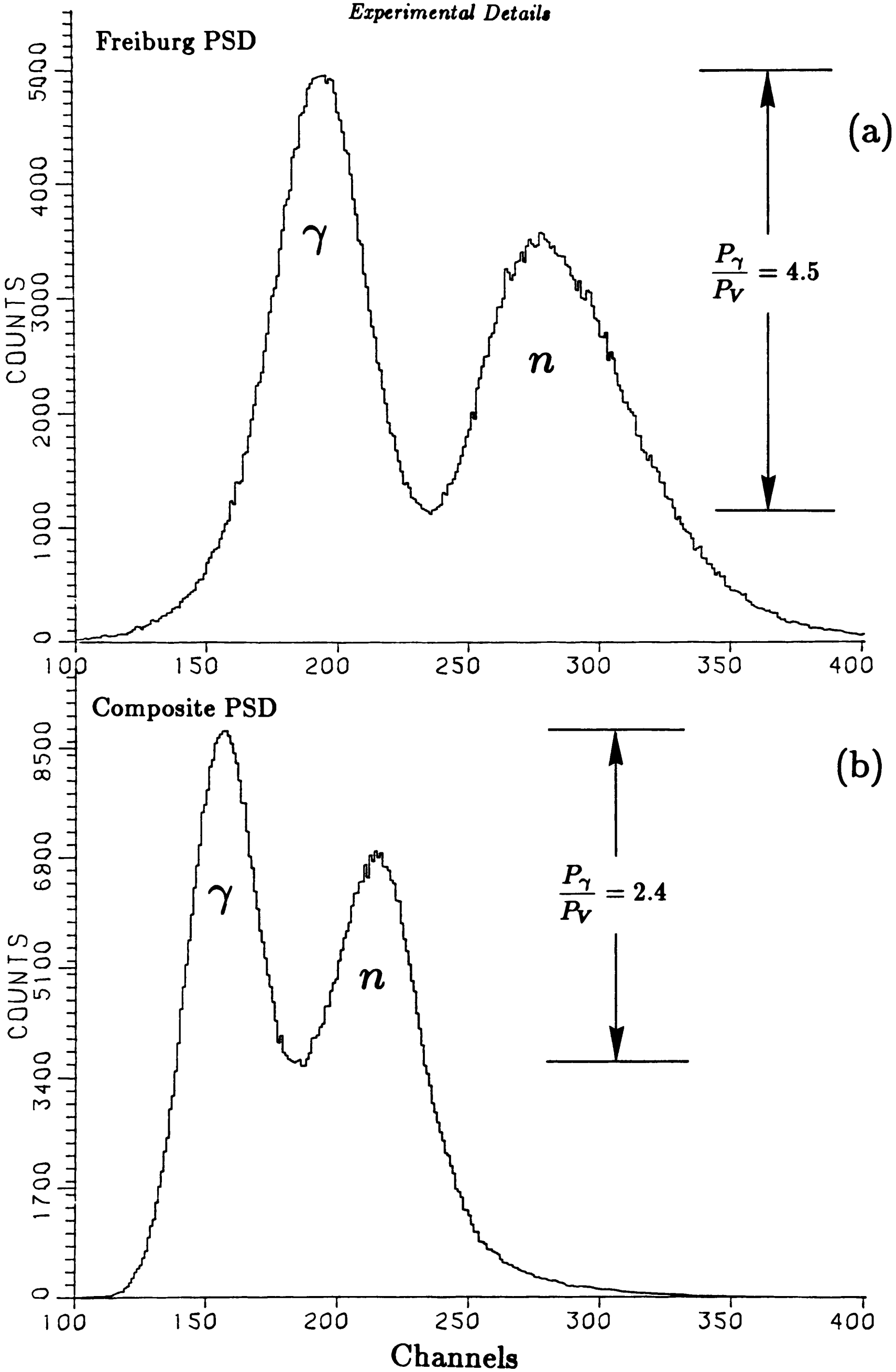


Fig.3.2 : PSD spectra: (a) spectrum obtained using the Freiburg PSD (b) spectrum obtained with the *composite* PSD. The gamma peak to valley ratios are shown.

3.4.3 *Composite* Pulse Shape Discriminator

Before the Freiburg boxes were constructed, a *composite* PSD was assembled out of standard NIM units as shown in fig. 3.3. To use these units, a positive signal was required which was derived from the dynode of the photomultiplier. The exponential decay of the positive input signal (A) was converted to a bipolar signal (B), the cross-over time being dependent on the decay time. This is a slightly unorthodox use of the Timing Filter Amplifier but the short decay time (~few ns) of the input pulse means that the output signal undershoots and results in a bipolar signal. This cross-over point was picked up by the constant fraction unit (C) and the time difference between this and the leading edge of the pulse (D) was converted into a TAC pulse (E). This is a well known technique and has been reported elsewhere (e.g. [GED68]). Fig. 3.2(b) shows a typical spectrum obtained by this method. Four out of five PSD's used in the ^{64}Ge experiment were based on this method. The fifth PSD used was a Freiburg PSD.

3.5 Electronics

Fast logic units were vital for achieving the timing accuracy required to perform TOF measurements and pulse shape discrimination with standard NIM modules. Fig. 3.4 shows the schematic layout of the electronics. For clarity, the circuits of only one Ge(Li) and one neutron detector are shown. The TOF circuit is shown in the dotted box and consisted of a start timing signal from the n-detector and a stop timing signal from a Ge(Li) detector. The Logic Unit shown in the TOF circuit was used as a fan-in for the 4 Ge(Li) detector timing signals. Associated with each n-detector was a TOF circuit as shown in fig. 3.5. As n-γ coincidences between any Ge(Li) and any n detector were required, all the Ge(Li) timing signals were OR*ed* together in the Logic Unit (as shown in the TOF circuit in fig. 3.4). This was then

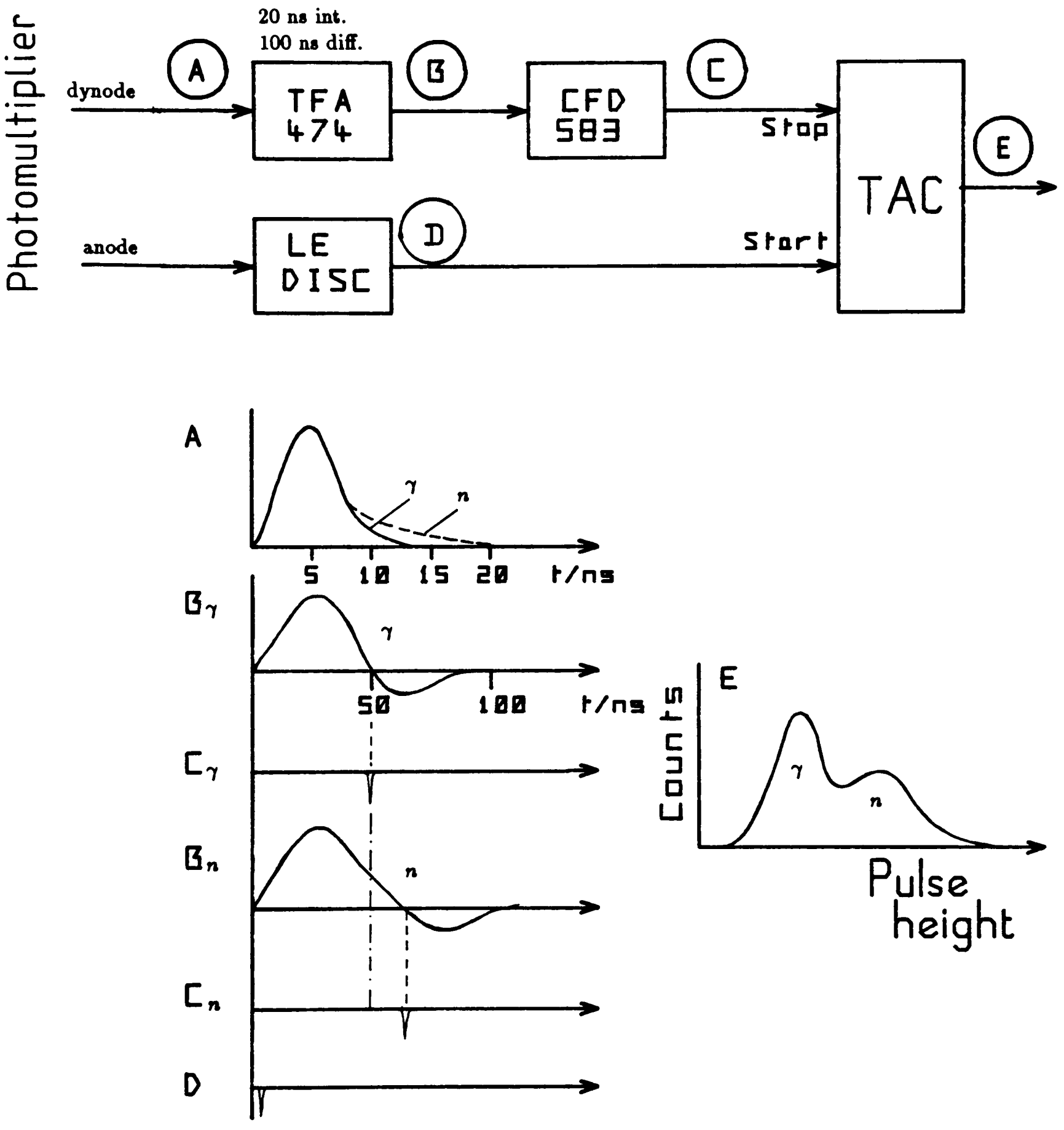


Fig.3.3 : *Composite* Pulse Shape Discriminator built out of standard NIM modules. The graphs in the lower half of the figure show signals expected at the points labelled A,B,C,etc. in the electronic block diagram. At points B and C, the signals due to n's and γ's are shown separately.

KEY TO FIGURE 3.4

The following figure is an electronic block diagram of the experiment. Listed below is a key explaining the acronymns used in the figure. The PSD's used were either the custom-built Freiburg PSD's or the PSD based on conventional NIM modules. For clarity, the TOF circuit has been separated from the other units by a dotted line.

a	- anode output of the photomultiplier.
AD811	- 8-channel CAMAC Analog-to-Digital Converter [Ortec AD811].
ADC	- Analog-to-Digital Converter [Tennelc TC205A].
ADD	- 50Ω adder.
CFD	- Constant Fraction Discriminator [Ortec 583].
COINC	- Coincidence Unit [Oxford IF-3].
d	- dynode output of the photomultiplier.
FAN OUT	- Digital Fan Out [Oxford].
DELAY	- Delay box.
DISC	- Leading-Edge Discriminator [LeCroy 4608].
DLY AMP	- Delay Amplifier [Ortec 427].
g1...g4	- Ge(Li) timing signals.
GeLi	- Germanium (lithium-drifted) gamma-ray detector.
G&D	- Gate and Delay Generator [Ortec 416A].
LA	- Linear Amplifier.
LU=n	- Coincidence Logic Unit (n=coincidence level) [Phillips 755].
MLU	- Multiplicity Logic Unit [LeCroy 380A].
N	- One quadrant of the Neutron Wall (Norman).
n1...n5	- Neutron Detectors.
n5	- Little Neutron Detector (Norman Jr.).
PM	- Photomultipliers [Mullard XP1040].
PSD	- Pulse Shape Discriminator [Freiburg design-Oxford built or *Composite* PSD (see text)].
Router	- CAMAC router unit [Oxford].
SB	- Silicon Surface-Barrier Detector.
TAC	- Time-to-Amplitude Converter [Ortec 467, Ortec 437A].
TFA	- Timing Filter Amplifier [Ortec 474, Ortec 454].
11/60	- DEC PDP11/60 minicomputer.

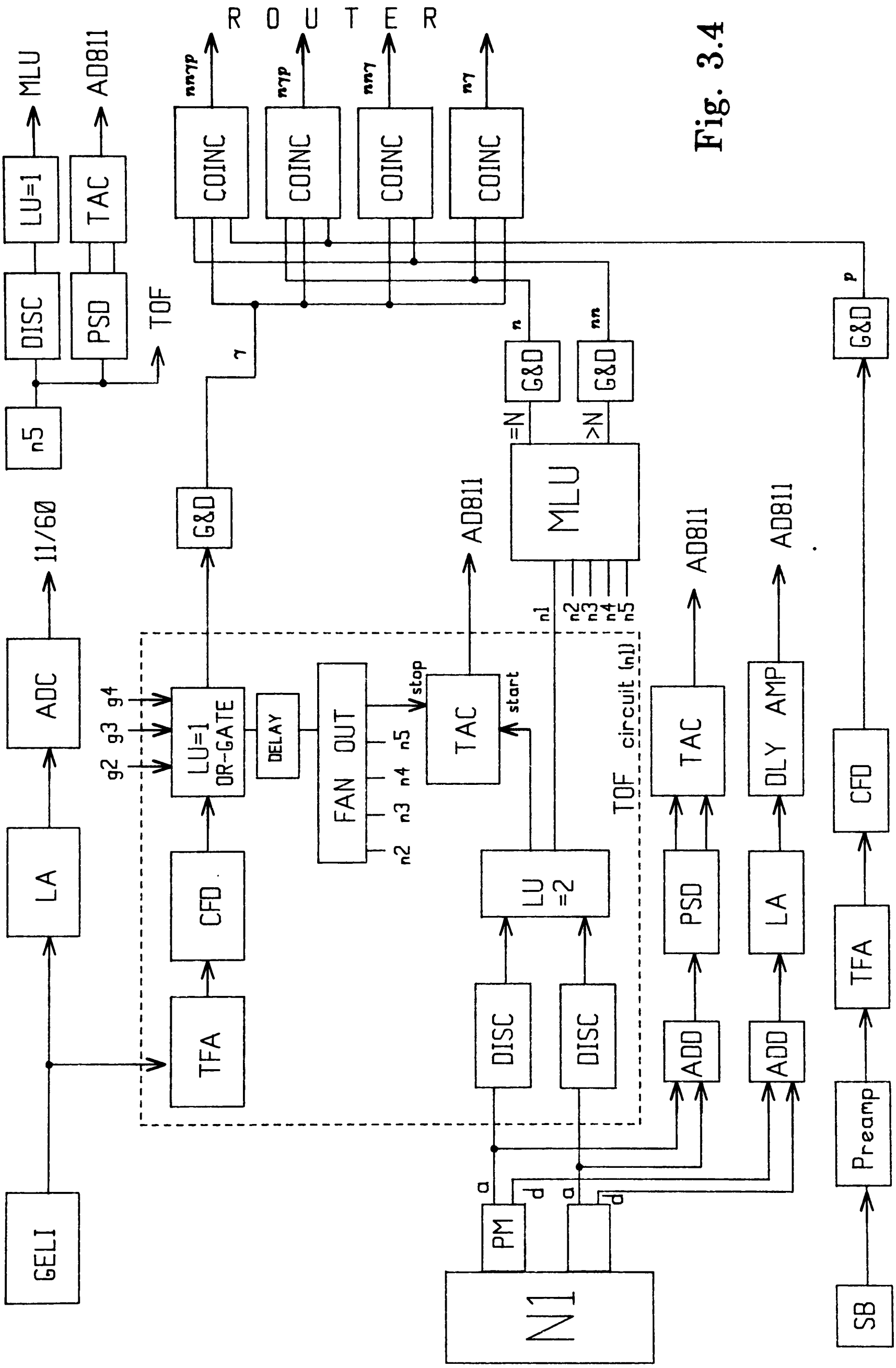

ROUTER
COINC
COINC
COINC
COINC
MLU
AD811
LU=1
TAC
DISC
PSD
TOF
n5
11/60
ADC
LA
GELI
G&D
G&D
G&D
G&D
=N
>N
MLU
AD811
AD811
AD811
LU=1
OR-GATE
DELAY
FAN OUT
stop
start
TAC
CFD
TFA
g2 g3 g4
n2 n3 n4 n5
n1
n2
n3
n4
n5
TOF circuit (n1)
LU
=2
DISC
DISC
TAC
PSD
ADD
DLY AMP
LA
ADD
CFD
TFA
Preamp
SB
PM
N1
a
d
a
d
p

Fig. 3.4

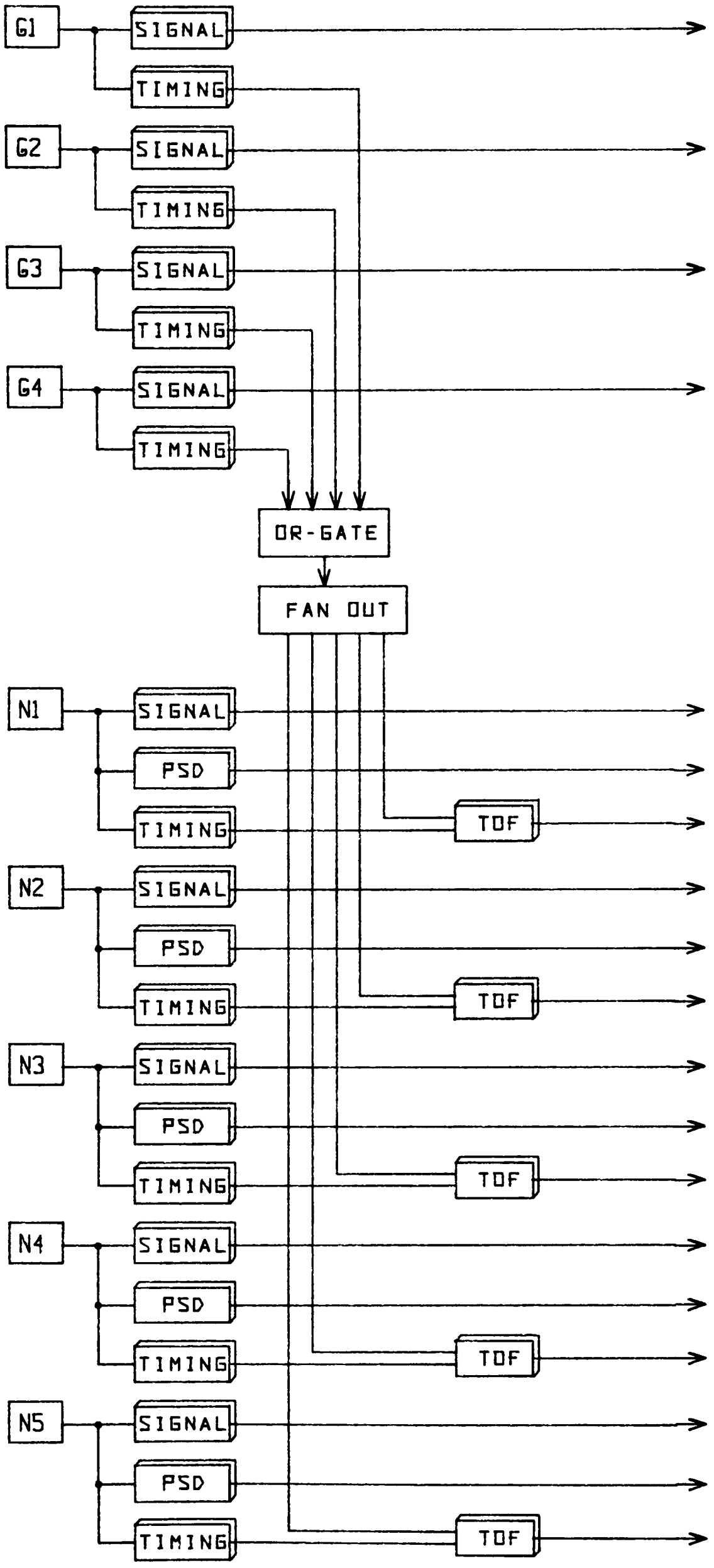


Fig.3.5 : Overall block diagram for the electronics.

fed into a fan-out to generate the timing signals to strobe the five separate TOF circuits. The photomultipliers were run negatively to reduce the distortion on the signal. If a photomultiplier is driven with a positive bias, the anode will be at a high potential, thus necessitating the use of a decoupling capacitor. However, if the bias is negative, then the anode will be at ground potential and so the capacitor can be removed thus reducing the possible distortion on the anode signals. This is important as any distortion of the anode signal would reduce the effectiveness of the Freiburg PSD circuits. The timing signals from the neutron detectors were fed into the TOF circuits. These signals were also fed into a multiplicity logic unit from which two signals were derived corresponding to $=$N and $\geq$N events where N was set to 2. Events in which one (or more) neutron detector fired, in slow coincidence (400ns) with one (or more) gamma ray detector, were accepted and recorded.

A partially depleted silicon surface barrier detector (0.9 mm thick and $\approx$ 115 mm^2 in area) was used in some of the experiments and the timing signal from this detector was collected in slow coincidence (400 ns) with the n-γ events. The presence of this signal indicated the detection of a charged particle in an event. Four logic signals were thus derived from the electronics which corresponded to the four possible combinations of detector signals viz. γnp, γnnp, γn and γnn.

3.6 Layout of the Experiment

The neutron detector was placed some distance away from the target so that the flight path was long enough for TOF n-γ discrimination to work. Fig. 3.6 shows a typical TOF spectrum for a detector-target distance of 83 cm.

The Ge(Li) detectors were placed around and as close to the target as possible. Several geometries were tried and are shown in figs. 3.7. Referring to these figures, in L1 and L2, $n5$ and $n6$ were $23 \times 23 \times 8$ cm plastic scintillators which achieved n-γ

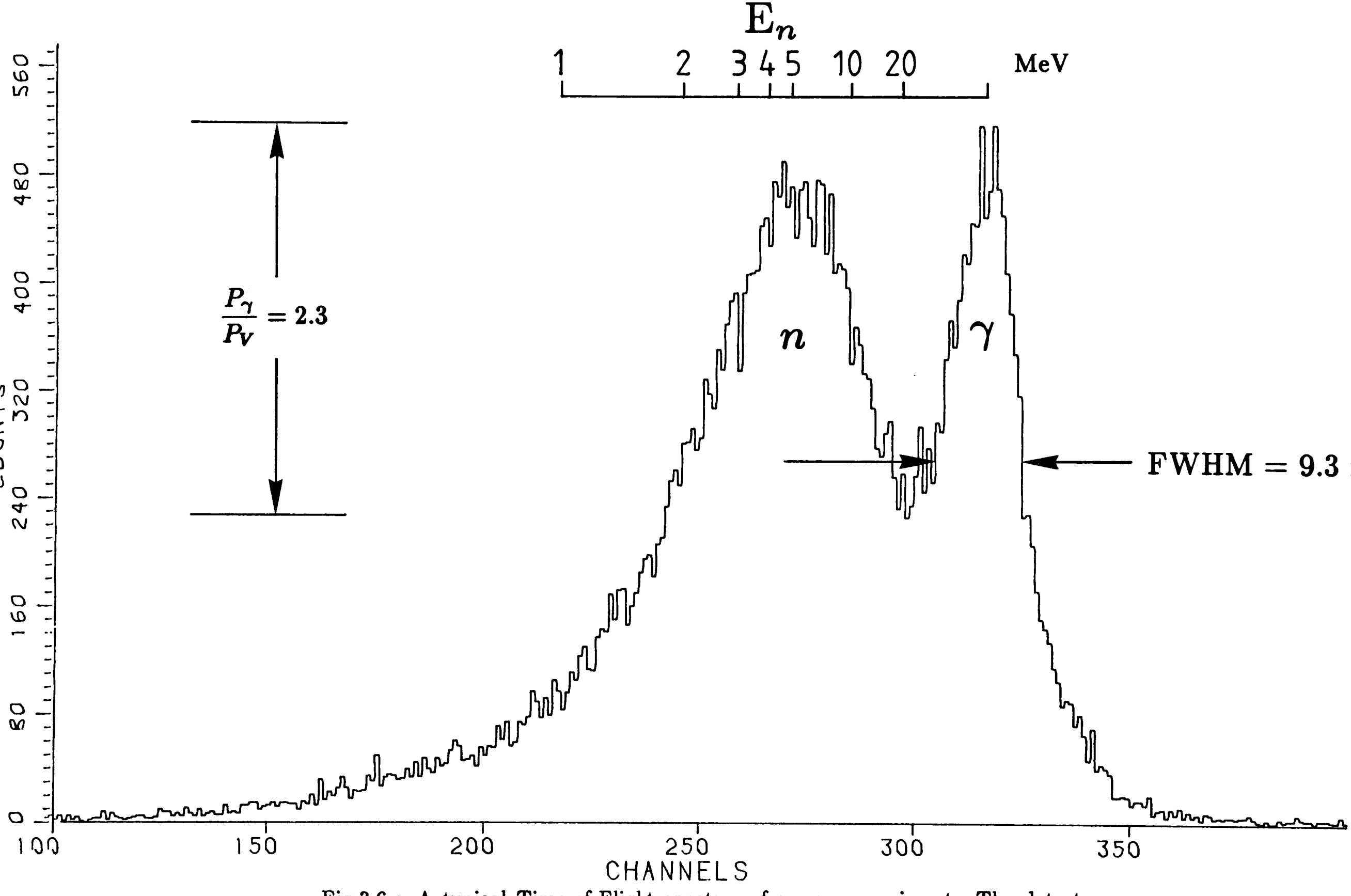


Fig.3.6 : A typical Time-of-Flight spectrum from an experiment. The detector-target distance was 83 cm and the spectrum was obtained from a $^{54}Fe + ^{12}C$ run at 150 MeV incident beam energy.

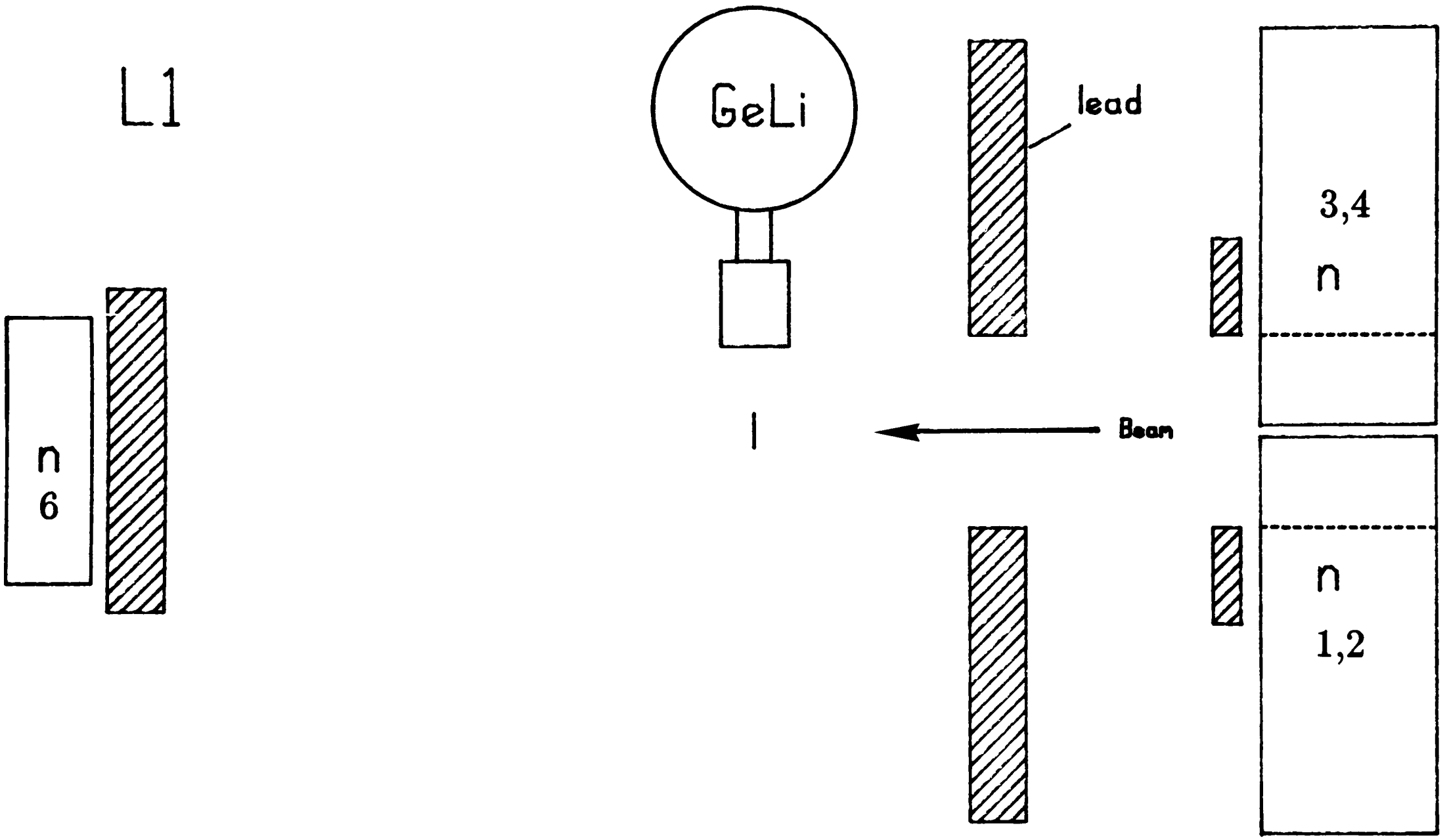


Fig.3.7 : This figure and the following figures show the five different layouts that have been used in the course of the ^{64}Ge experiments. See the text for a detailed description of each.

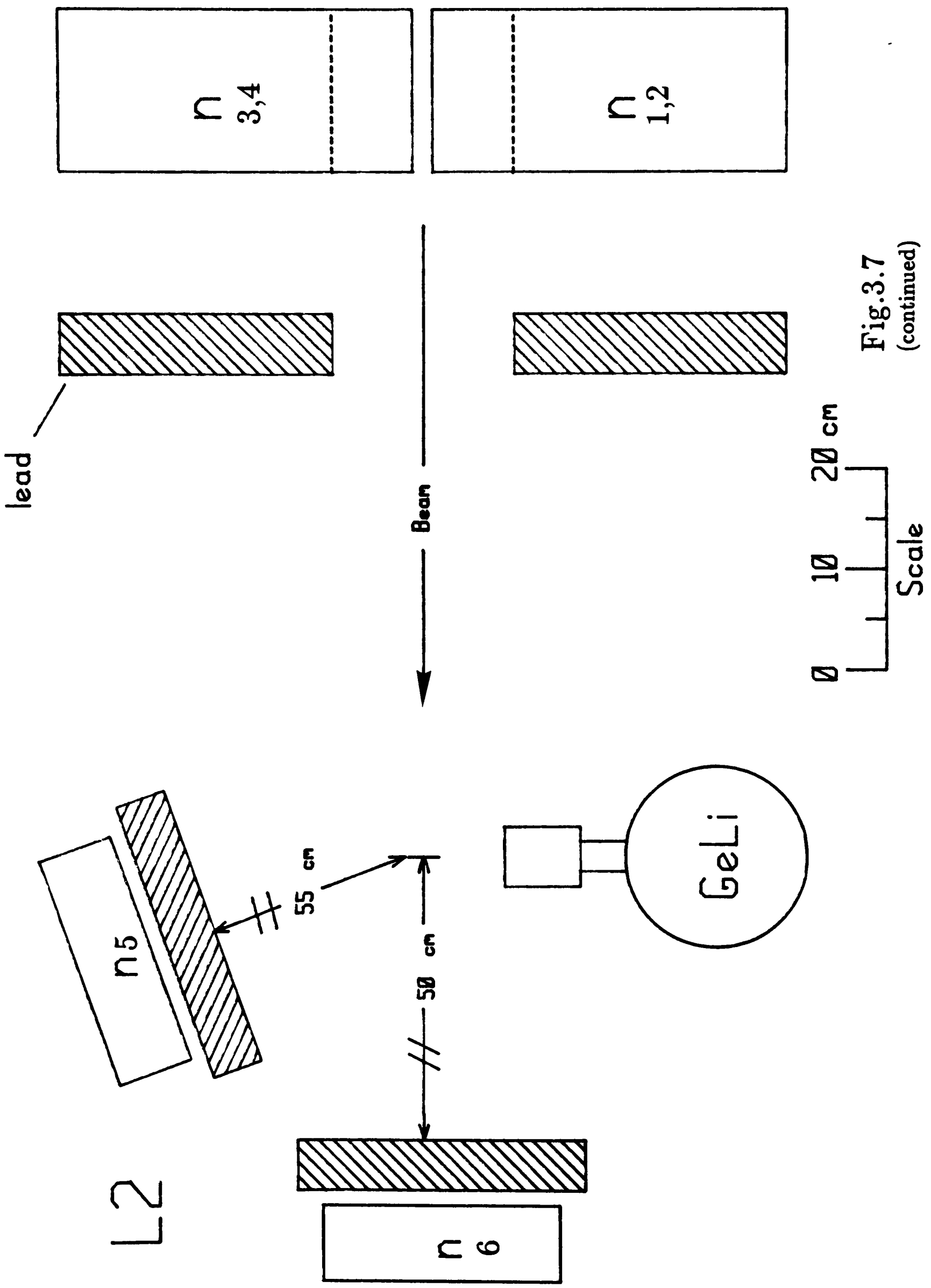


Fig.3.7
(continued)

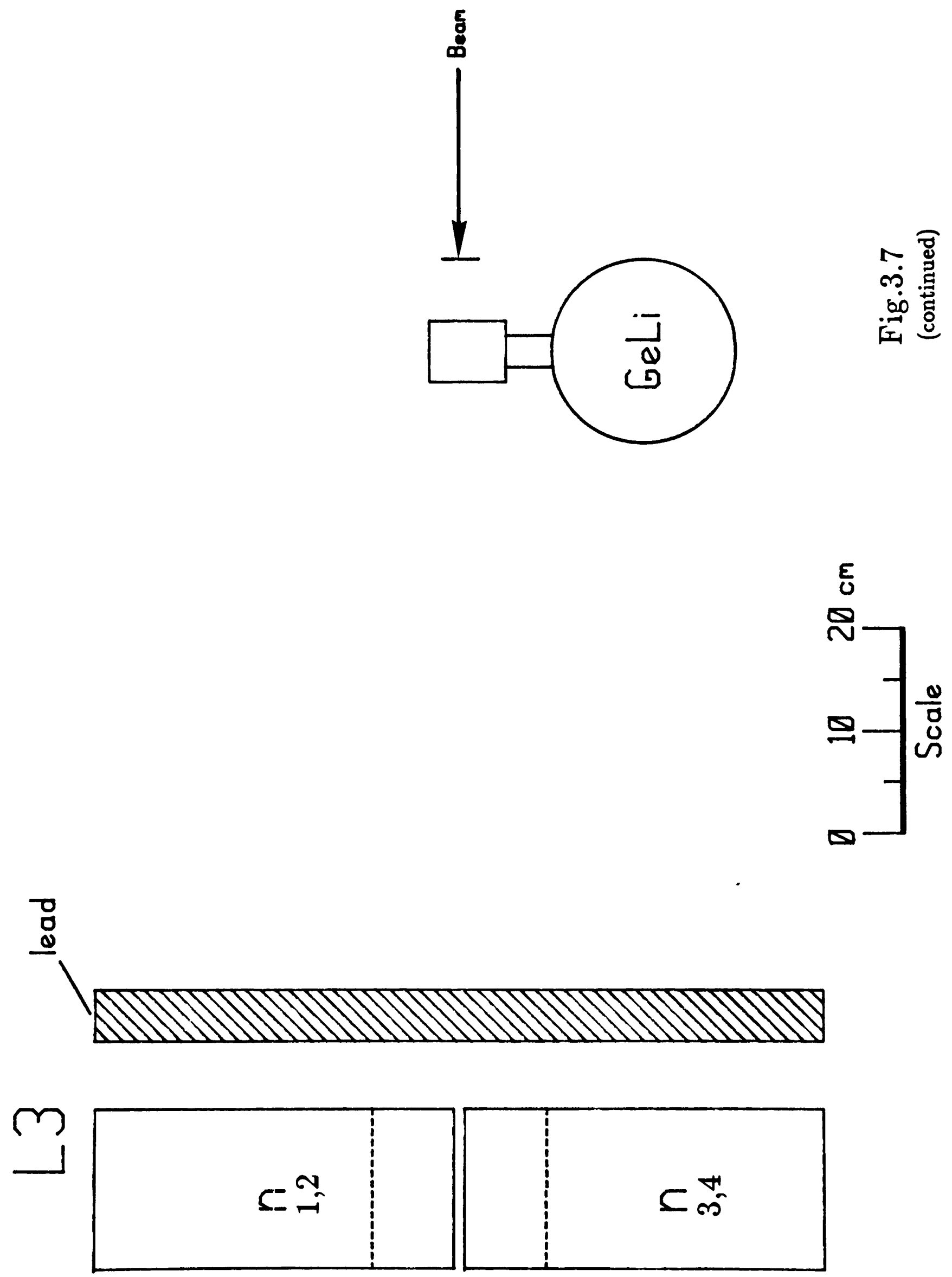


Fig.3.7
(continued)

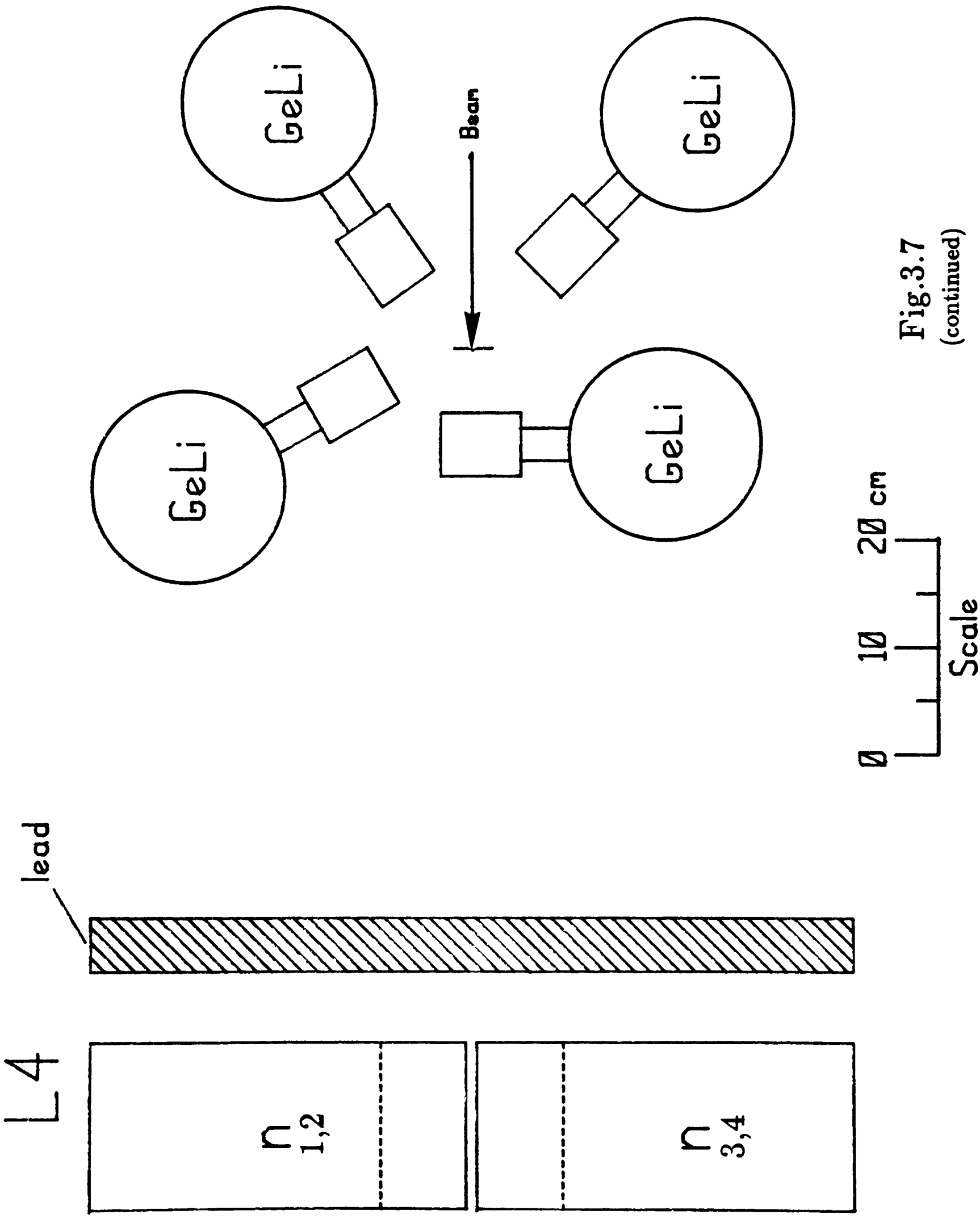


Fig.3.7
(continued)

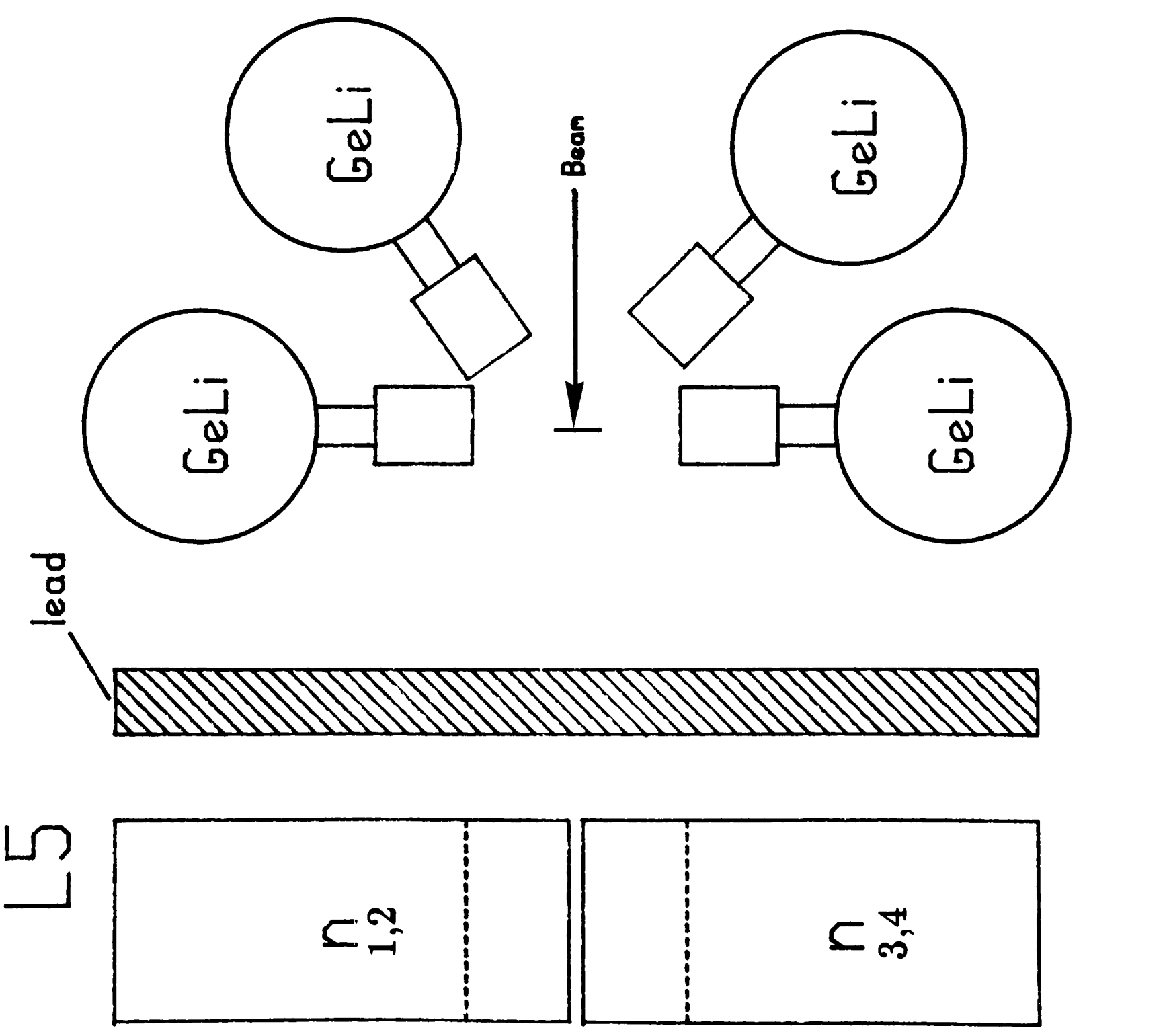


Fig.3.7
(continued)

discrimination solely through TOF. Although only a few of the geometries eventually proved useful (see Chapters 4 and 5), the others have been included to show the geometries that did not prove as fruitful. Layouts L1 and L2 were used for the ^{12}C + ^{54}Fe experiments. The forward-backward orientation of the neutron detectors was an attempt to remove cross-scattering of the neutrons between detectors. However, the background lines from reactions of carbon on the light impurities were a severe problem and to overcome this, the inverse reaction was used instead (see Chapter 5). The plastic scintillators were therefore abandoned when the large neutron detectors were repositioned downstream as the kinematics of the reaction showed that the majority of the neutrons would be focused into these large detectors. L3 to L5 were the layouts used for most of the data-taking runs on ^{64}Ge (see Chapter 5). For the ^{48}Cr experiment, the layout used was L5.

As mentioned before, a surface barrier (SB) detector was used to reject charged particle related events. This detector (0.9 mm thick and $\approx$ 115 mm^2 in area) was placed about 2 mm behind the target to subtend as large a solid angle as possible. This SB detector was mounted on a slab of acetal ($13 \times 4 \times 1.4$ cm thick) which was attached to the lid of the target chamber. Plates 3.1 to 3.3 show the target mount used. The target was placed on top the SB detector but insulated from it by a thin sheet (10 thousandths of an inch) of PTFE. A 6 cm diameter tantalum disc with a 10 mm dia. hole was positioned on top of the target to secure it against the SB detector. This disc was not insulated from the target and so a lead was taken off it for the target current. Approximately 6 mm away, another 6 cm dia. tantalum disc with a 8 mm dia. hole served as a collimator. A lead was also taken off this disc to monitor the collimator current. Both these leads were connected to BNC feed-throughs on the lid of the target chamber.

Gamma radiation from the target which reached the neutron detector was attenuated by placing a 6 cm thick lead wall in front of the detector. Tests were carried out with a 10 mCi Am-Be neutron source to determine the effects of a lead

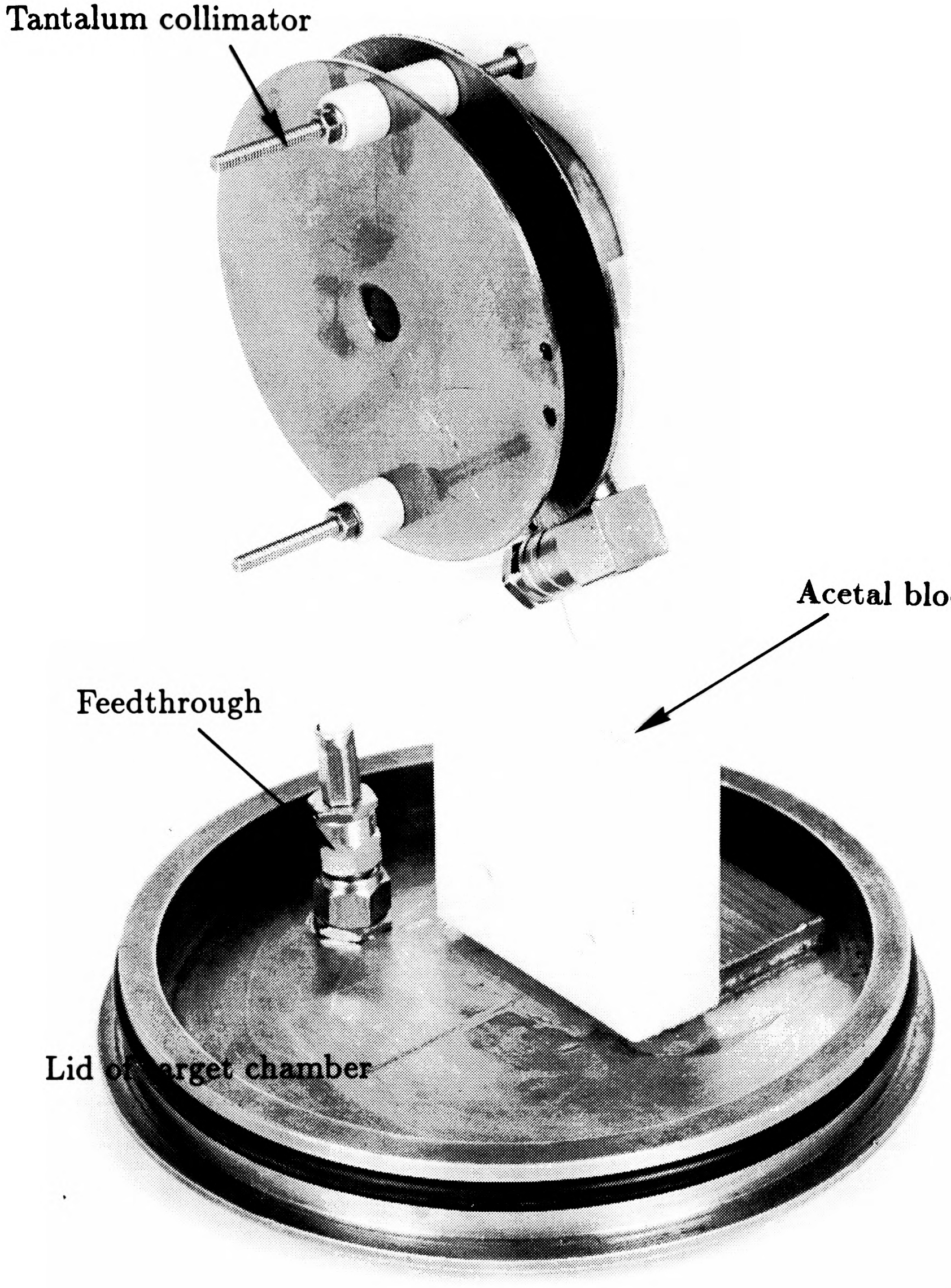
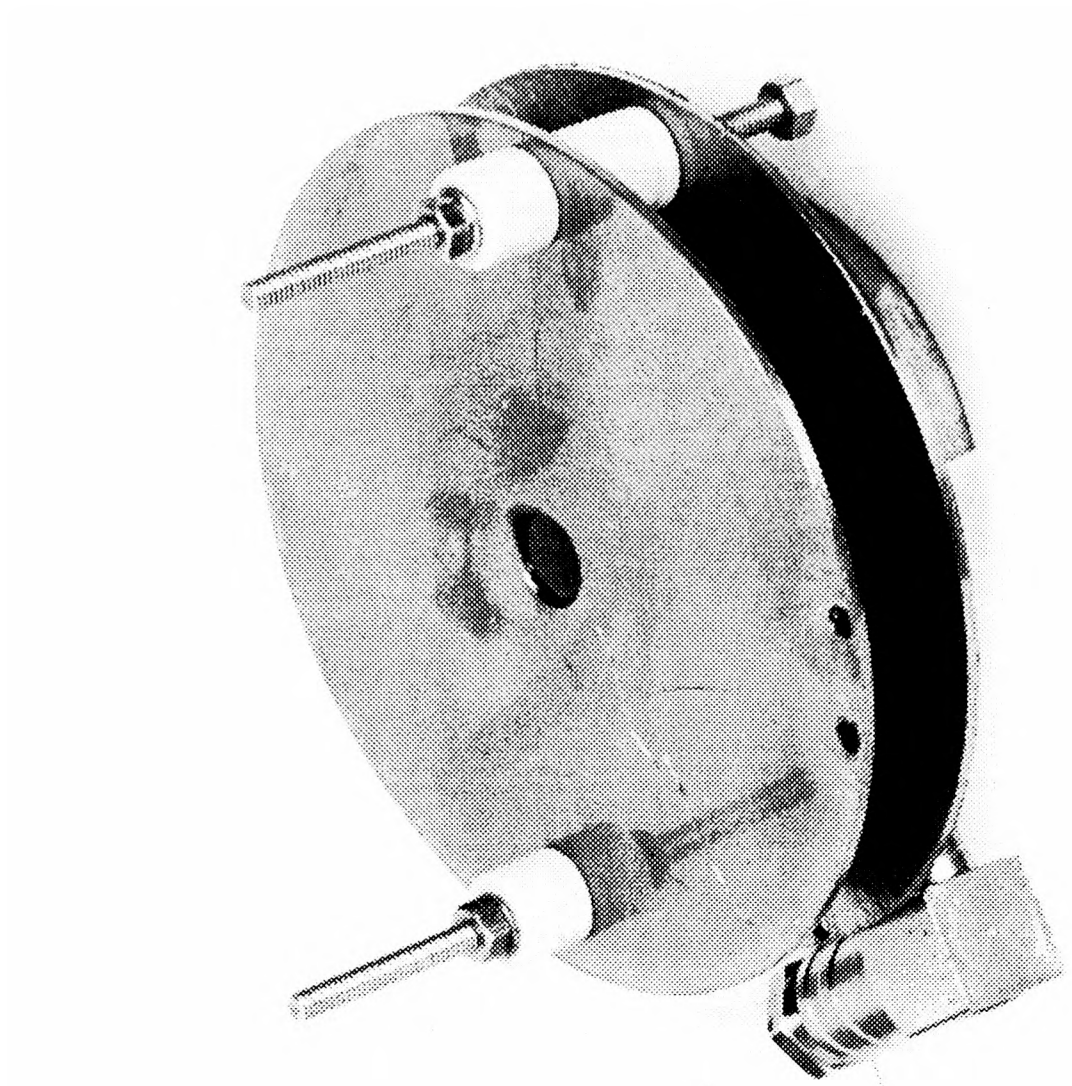


Plate 3.1 : Target Mount - Isometric View





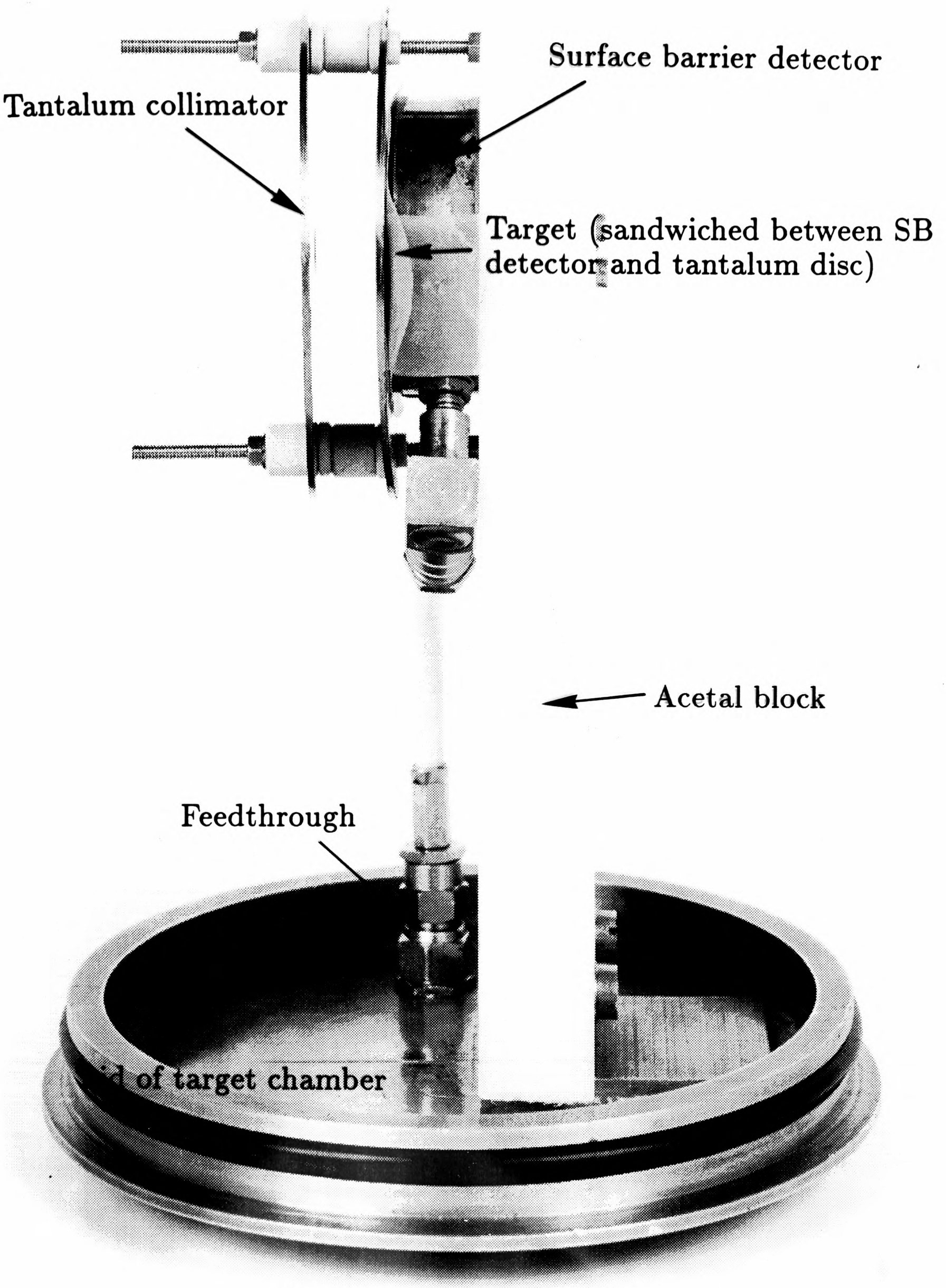
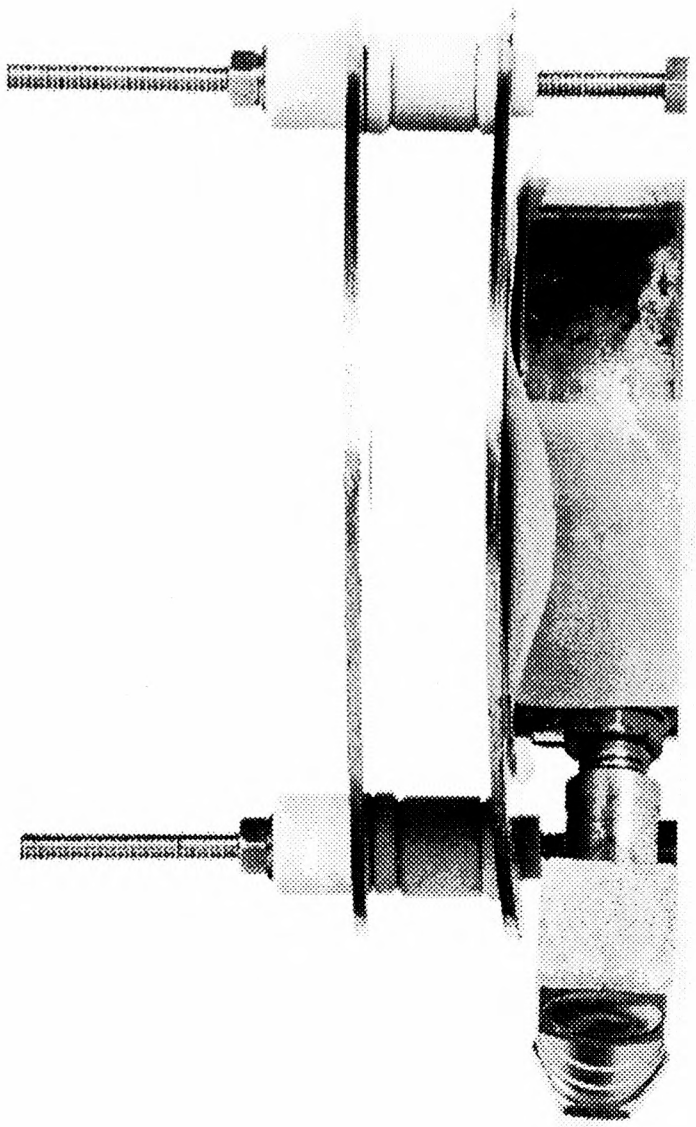
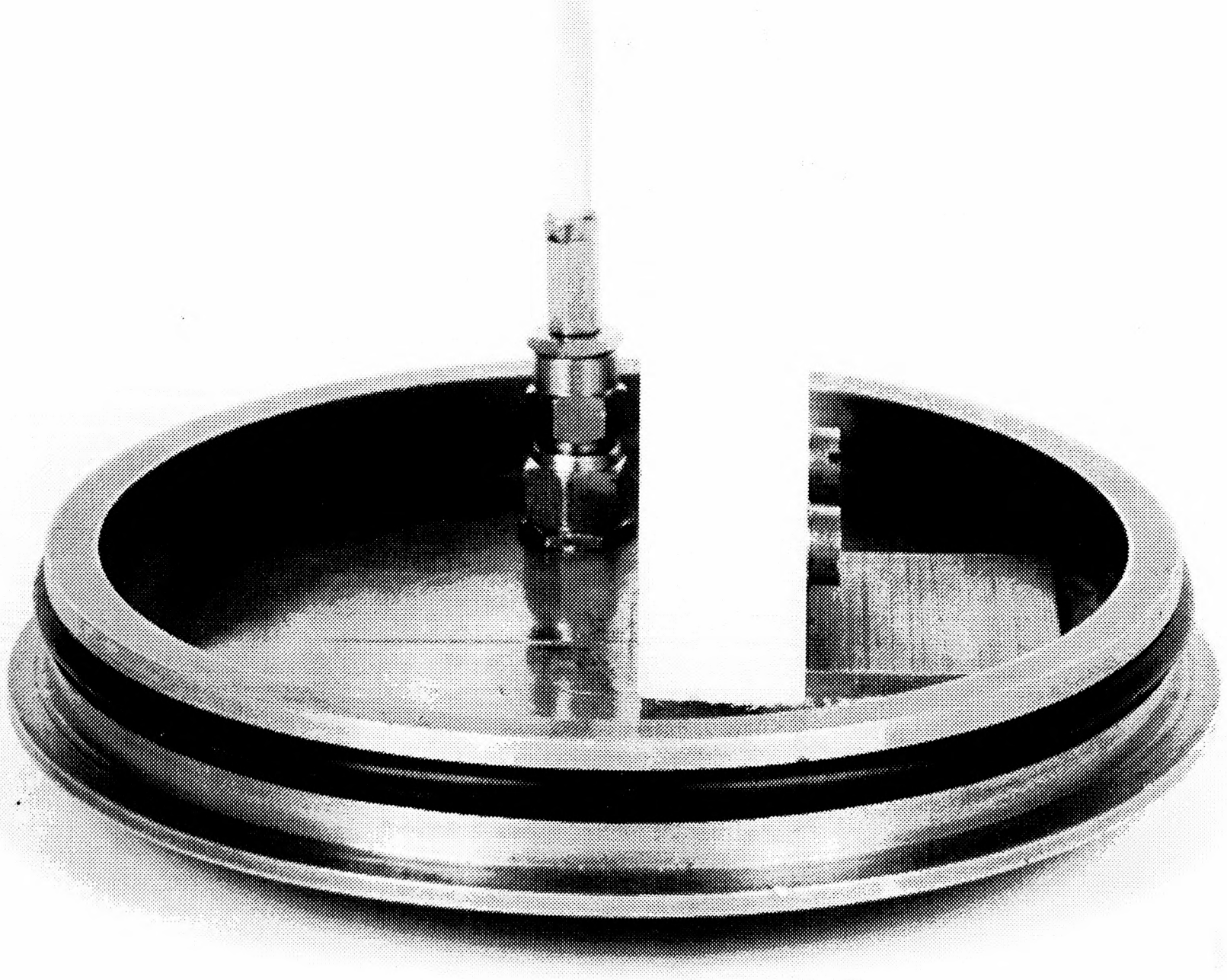


Plate 3.2 : Target Mount - Side View





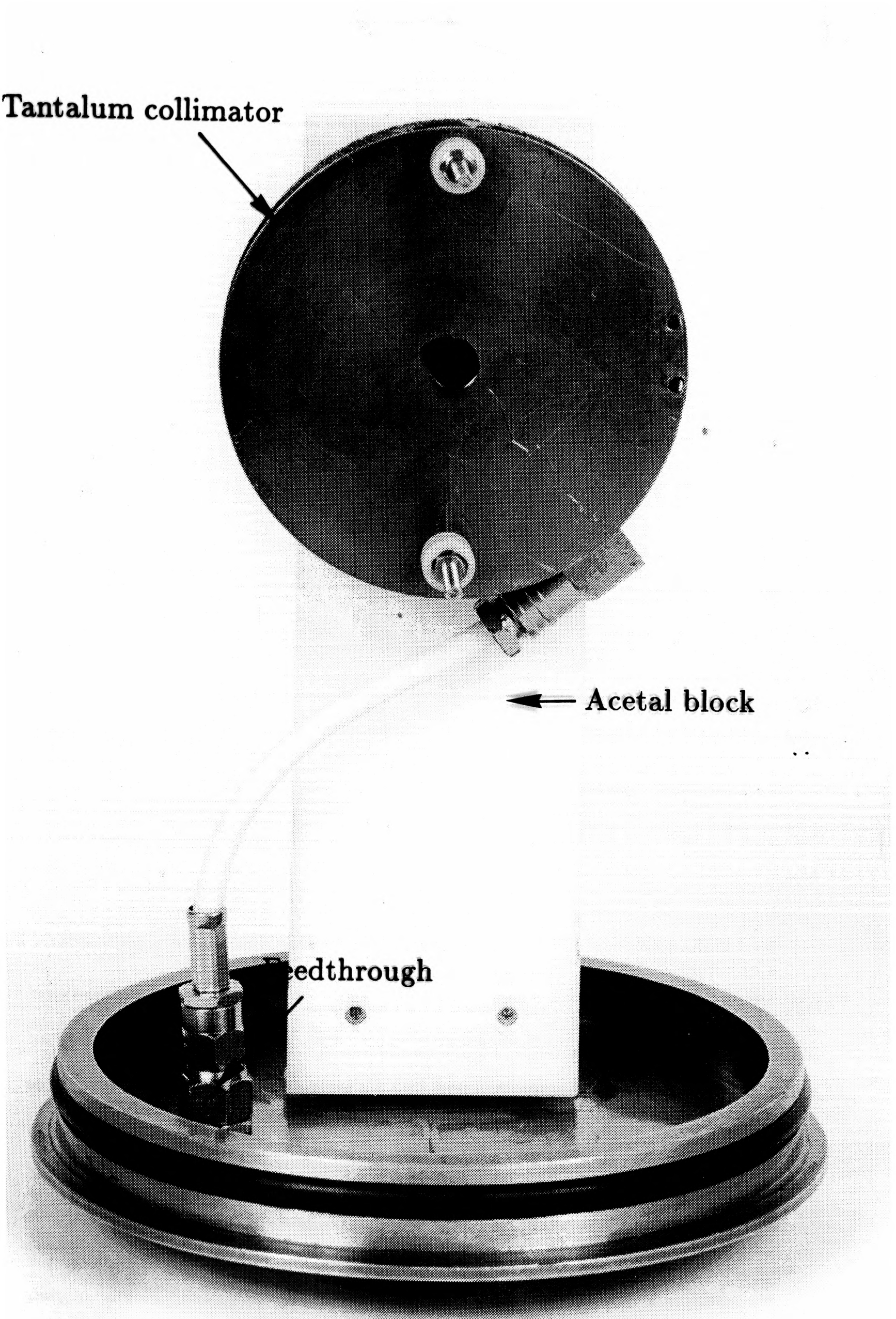
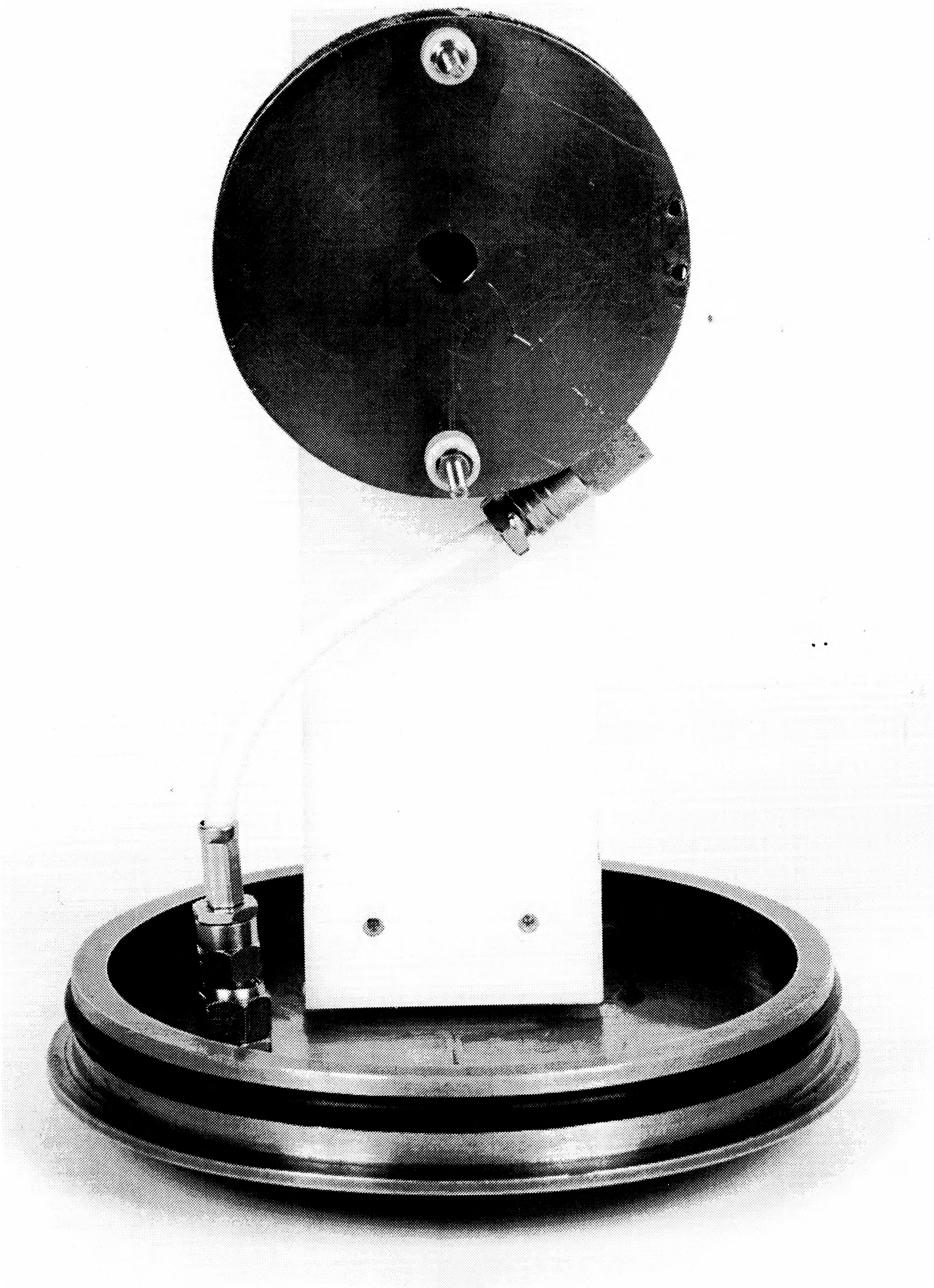


Plate 3.3 : Target Mount - Front View

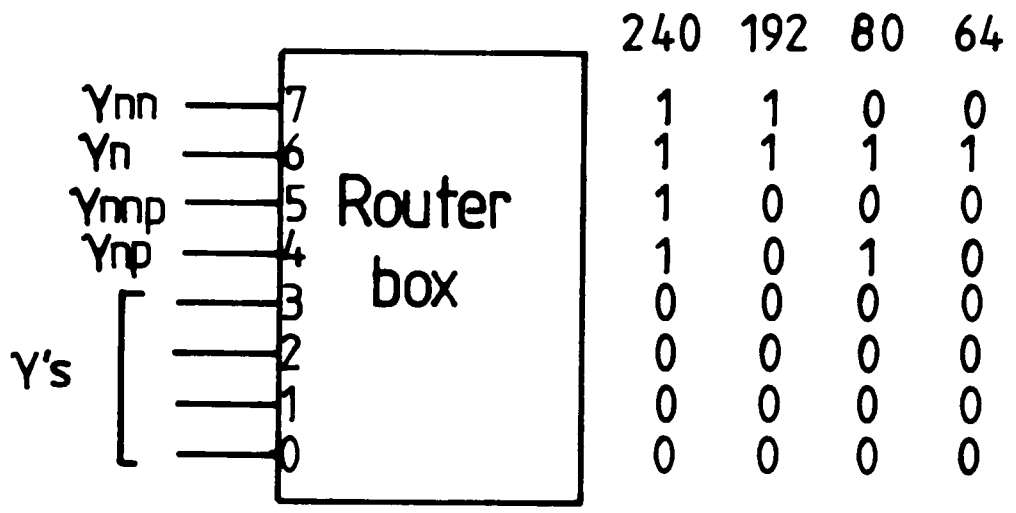


wall on the neutrons and γ-rays. A TOF spectrum was obtained between a NaI† and the neutron detectors with the source placed next to the NaI. The neutron to gamma peak ratio of the TOF spectrum with a 6 cm thick lead wall was 3.6 while the same ratio without a wall was 0.8. The γ-ray intensity was thus significantly reduced by the presence of the lead wall. The attenuation of the γ-rays , of course, depends on their energy and the figures quoted here are averaged values (over the whole NaI spectrum with a range from ~0.2 to 4 MeV γ-rays). Plates 3.4 to 3.5 show different views of the entire system.

3.7 Data Collection & On-line Analysis

A PDP 11/60 minicomputer was used for data acquisition. Data were read into the computer via CAMAC [IEE75]. An Oxford Nuclear Physics Laboratory built CAMAC interrupt encoder, which could handle up to 8 positive logic signals, was employed to handle the input signals from the experiment. Each input signal initiated an interrupt service routine that read the appropriate analog-to-digital convertor or input register in the CAMAC crate. The encoder (or router box) also put out a pre-set pattern of software controlled logic pulses (both positive and negative) for use as strobes. In cases of simultaneous multiple inputs, the interrupt encoder obeyed a hardwired priority scheme where the input with the highest priority (in this case, the highest numbered input) was serviced. The inputs to the interrupt encoder were thus arranged so that the events with the lowest rate (e.g. $2n$ events) had the highest priority. Fig. 3.8 shows that γnn events, which had the lowest rate had the highest priority (input 7) while the more prolific γnp events had lower priority (input 4). The input signals formed a bit pattern (table

† A Ge(Li) detector was not used due to the high flux of neutrons from the neutron source.



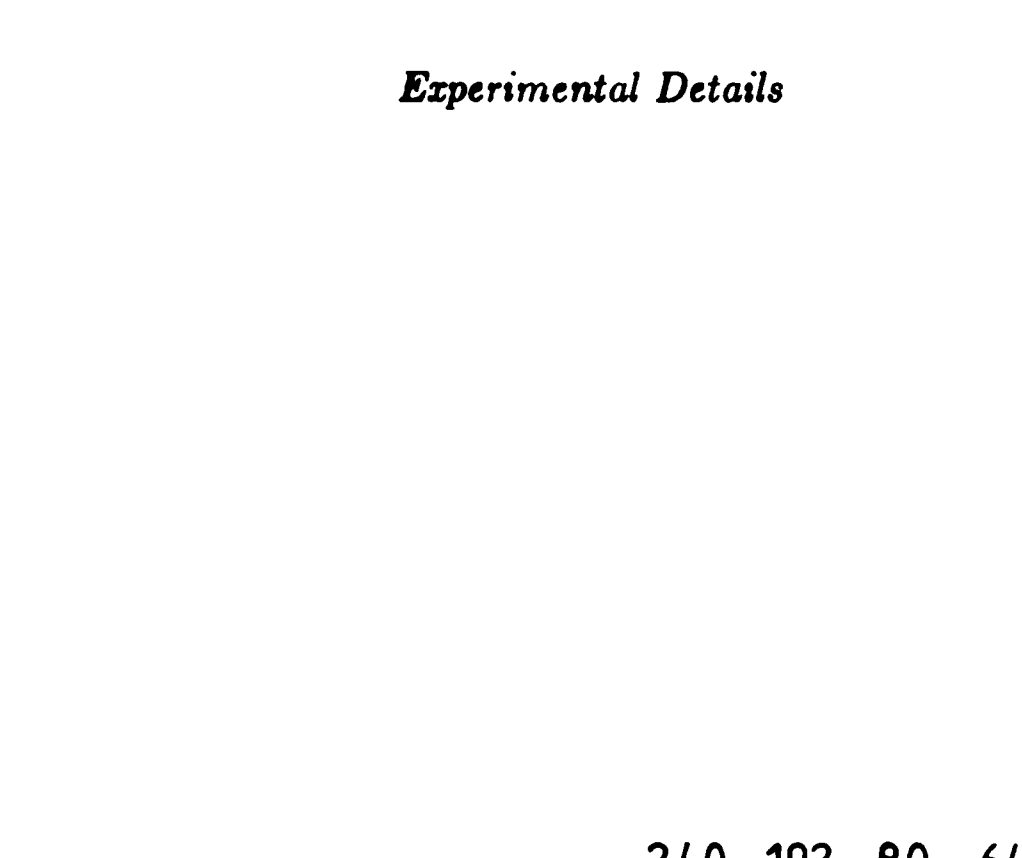


Fig.3.8 : Router spectrum showing channels incremented according to the multiplicity of the event. The top half of the figure shows the various inputs to the router box and the bit pattern obtained.

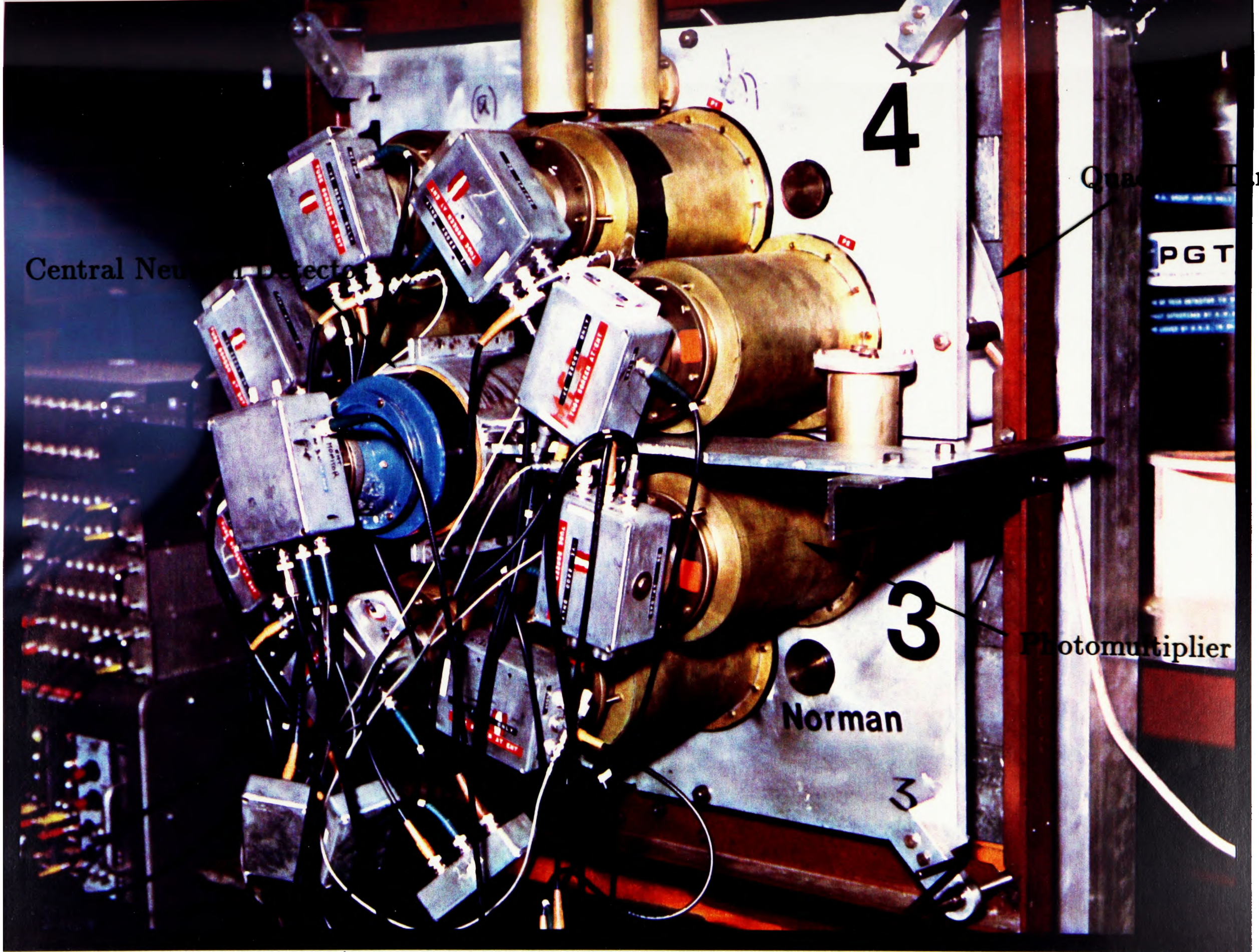


Plate 3.4 : Back view of Neutron Wall

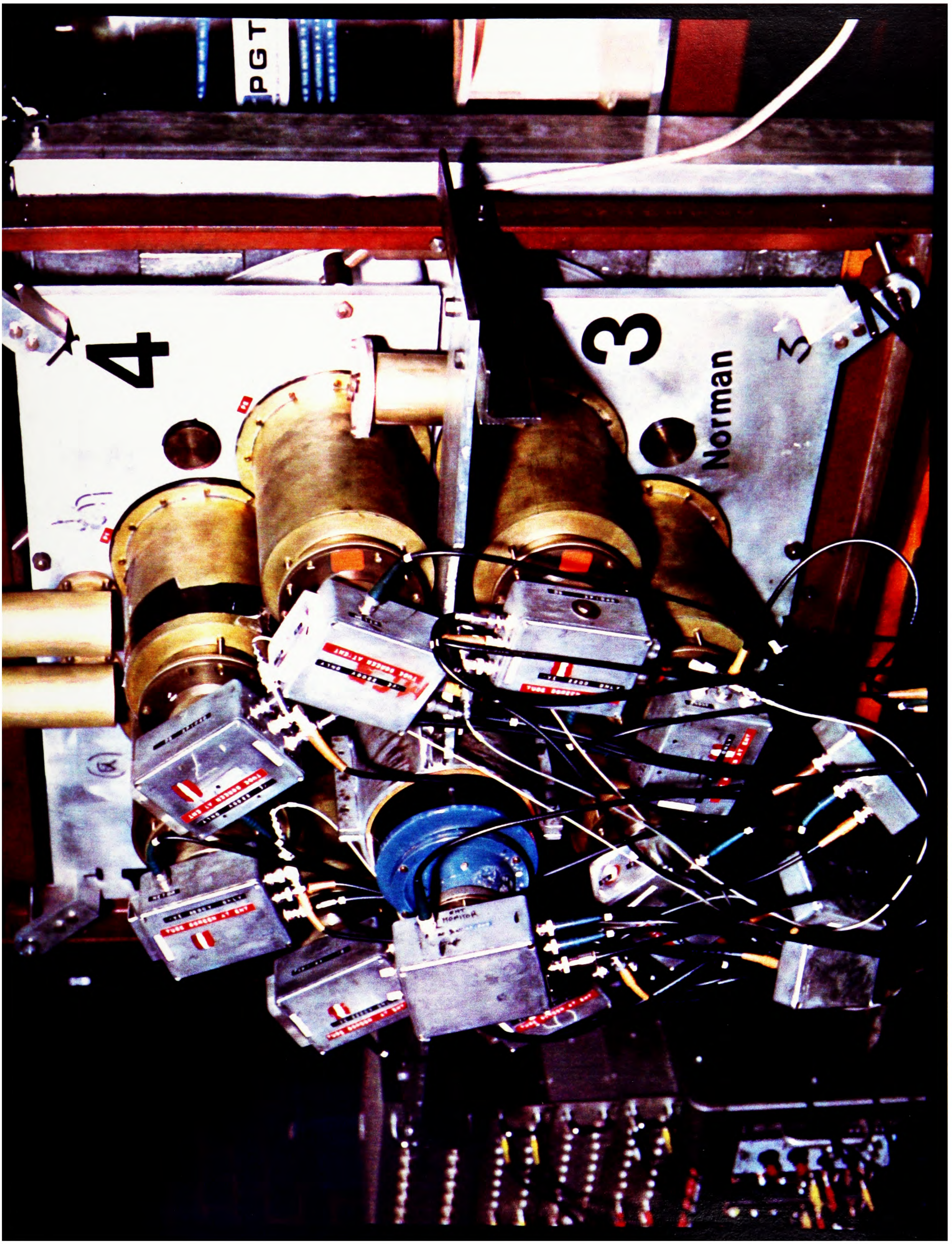


Plate 3.4 : Back view of Neutron Wall

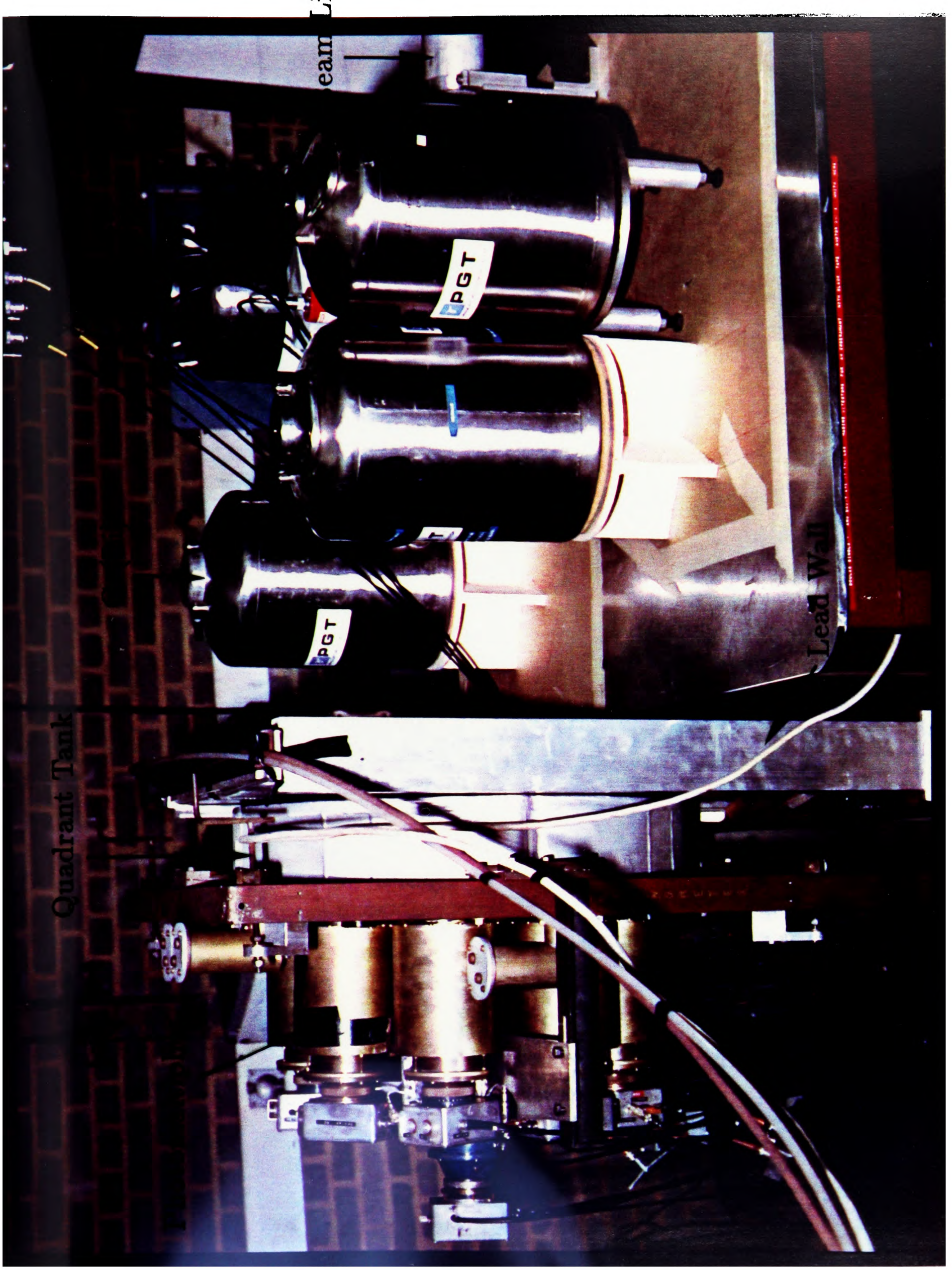


Plate 3.5 : Side view of Neutron-Gamma Detection System

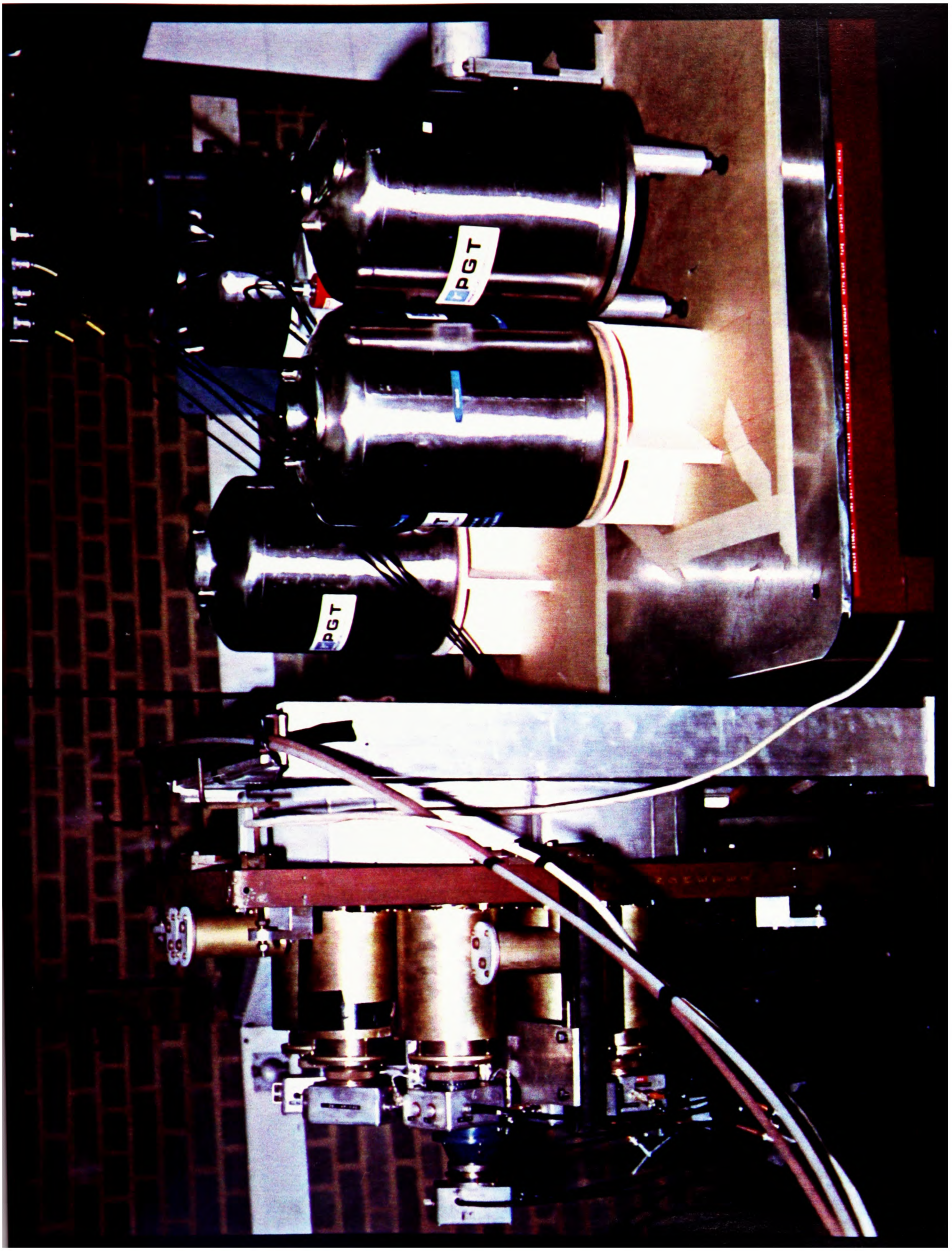


Plate 3.5 : Side view of Neutron-Gamma Detection System

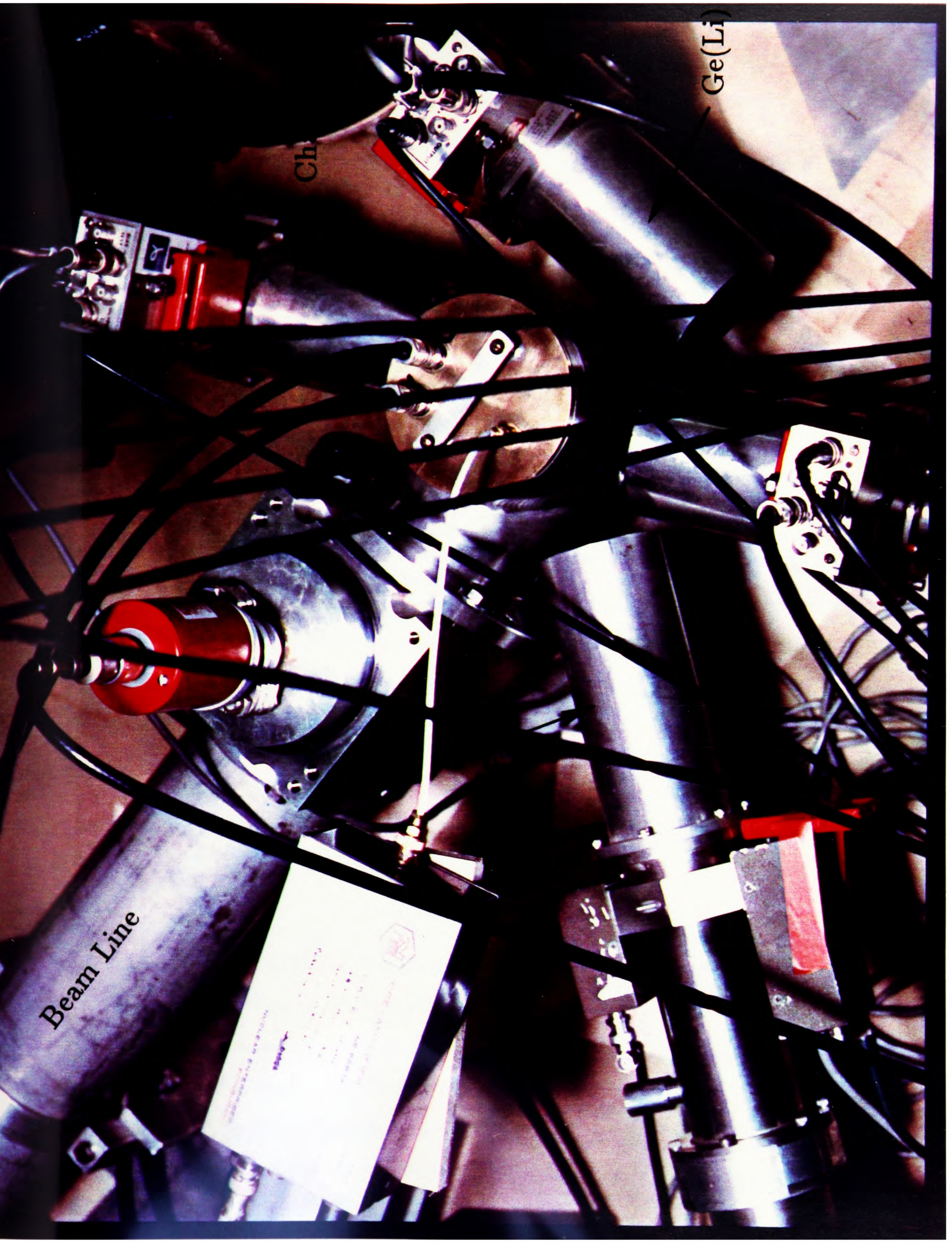


Plate 3.6 : Top view of Target Chamber and Ge(Li) detectors

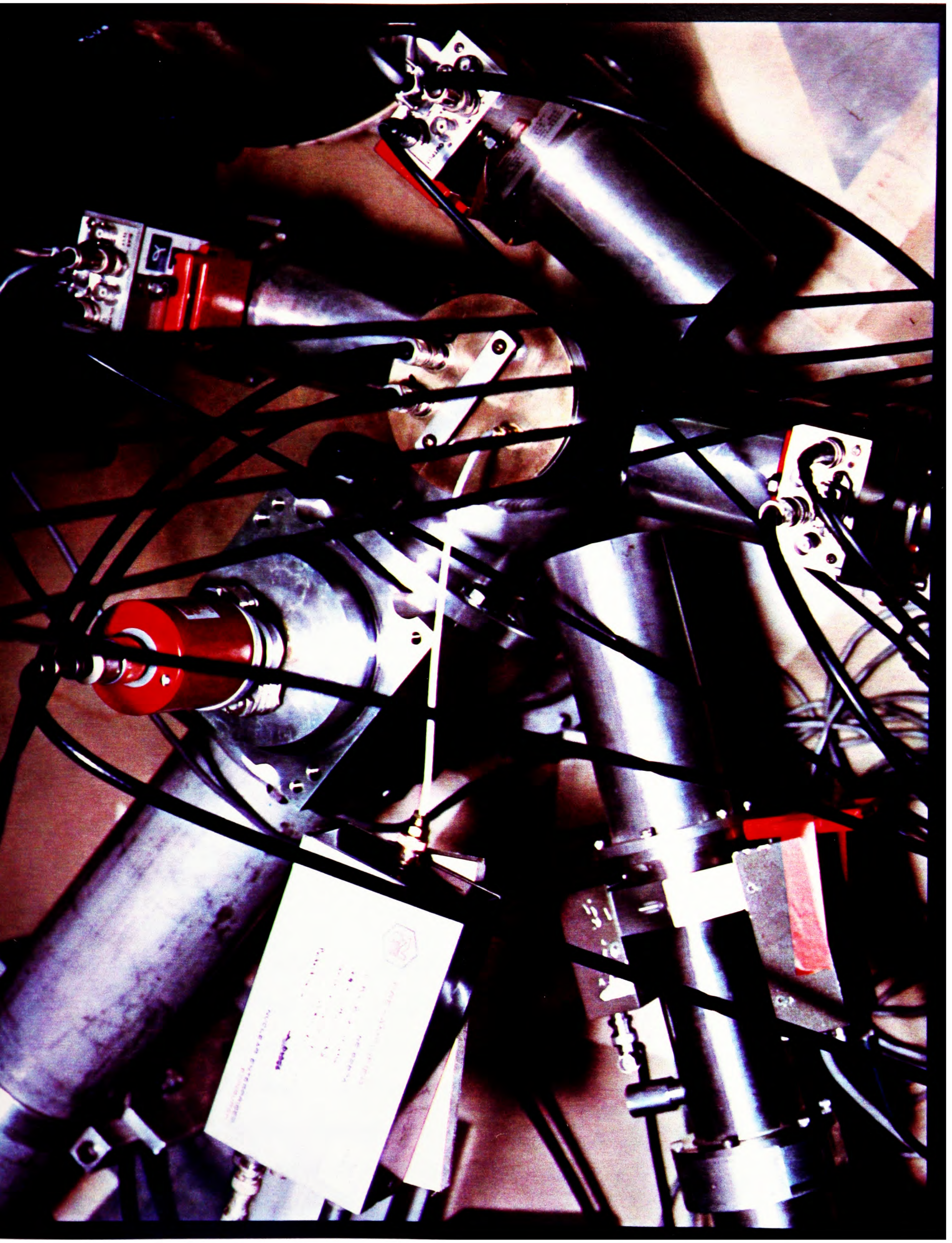


Plate 3.6 : Top view of Target Chamber and Ge(Li) detectors

3.1) which was read and written onto magnetic tape so that the multiplicity of an event could be determined during subsequent off-line analysis. In runs which included the surface-barrier detector, the logic signal from this device was read into the computer in the same way, as shown in table 3.1.

Bit pattern (bit number)								Sum	Event
7	6	5	4	3	2	1	0		
0	1	0	0	0	0	0	0	64	$1n0p$
0	1	0	1	0	0	0	0	80	$1n1p$
1	1	0	0	0	0	0	0	192	$2n0p$
1	1	1	1	0	0	0	0	240	$2n1p$

Table 3.1 : Typical input bit patterns and the resulting words obtained (see fig.3.8 for the type of input corresponding to each bit).

The first 4 bits (0-3) of the bit pattern were used to identify singles events (for the 4 Ge(Li) detectors) but were frequently disabled to reduce the dead-time of the ADC's. Bits 4 to 7 corresponded to

Bit 4 : γnp

Bit 5 : γnnp

Bit 6 : γn

Bit 7 : γnn

As can be seen from table 3.1, both γn and γnn signals were received from $2n$ events. This was a feature of the multiplicity logic unit used in the experiment. The bit pattern was written as a 16-bit word onto tape and during play-back, it was used to produce event identification spectra such as the one shown in fig. 3.8. Setting windows on these channels thus enabled the various coincidence events to be sorted. Data were recorded event-by-event into tape and 20 parameters were written for each event (Table 3.2)

Parameter	Input signal
0-4	time-of-flight TAC's
5-9	pulse shape TAC's
10-14	n signal pulse height
15-18	Ge(Li) 1 $\rightarrow$ Ge(Li) 4
19	router bit pattern

Table 3.2 : Parameters written onto magnetic tape

In order to cope with the volume of data collected, the on-line data analysis program on the PDP 11/60, GENDAT [COO78], was modified to allow data to be transferred to a VAX 11/780 via a DEC DMC-11 Synchronous Communications Line Interface. Once on the VAX, the data were written onto tape in high-density (6250 bpi) format. A certain number of events were lost during the dead time when data were being transferred to the VAX but adequate buffering of the data ensured that these constituted no more than 1% of the total number of events.

3.8 Performance Tests on the Neutron Wall

In this section, data from a few experiments are presented to show the performance of the system under experimental conditions. Two special points of interest were the timing resolution achieved (important for TOF) and the overall efficiency for detecting neutrons. These will be considered separately.

3.8.1 Timing Resolution (& Neutron flight path)

A typical TOF spectrum, with the n and γ peaks labelled, was shown in fig. 3.6. This spectrum was calibrated by inserting a known delay in the path of the stop signal to the TAC and noting the resulting shift in the peak positions. This gives a

FWHM of the γ-ray peak of $\sim$9 ns. The n energies from $^{54}Fe + ^{12}C$ were expected to peak at 500 keV in the centre-of-mass frame, which corresponds to 4.3 MeV in the laboratory frame and fig. 3.6 shows that this agrees with the experimental results.

The choice of the flight path length (between the target and the neutron detectors) was invariably a compromise between high efficiency and good n-γ separation of the TOF peaks. Fig. 3.9(a) shows a TOF spectrum for a flight path of 65 cm while fig. 3.9(b) was obtained with a flight path of 30 cm. It can be seen that the latter flight path was too short for TOF n-γ discrimination and here, the PSD's were used instead (see section 9). Neutrons with centre-of-mass energies $\leq$ 500 keV were focused into a cone of semi-angle 31° by the kinematics of the reaction. Fig. 3.10 shows the variation of laboratory energy of evaporated neutrons against the laboratory angle of emission of the neutrons. A flight path of 65 cm was used during the early runs which provided as large a solid angle as possible (semi-angle = 29°) while maintaining a reasonable n-γ separation for the TOF spectrum (as shown in fig. 3.9). In later runs where the emphasis on n-γ discrimination was placed on PSD's, the neutron detectors were positioned much closer to the target (30 cm).

3.8.2 Detector Efficiency

The efficiency of the neutron wall was measured during several experiments and the data obtained have been summarized in table 3.3. For γ-rays from n-related channels, the ratio of the intensity of the peak in a n-gated spectrum to that in the singles spectrum is a measure of the efficiency. The efficiencies given in table 3.3 were calculated in this way and have been averaged over several γ-rays . A $2n$ channel has been included for comparison. The increased efficiency for detecting two neutrons is given by

$$\epsilon_{2n} = 2\epsilon(1-\epsilon) + \epsilon^2$$

$$\epsilon = \text{efficiency for detecting one } n$$

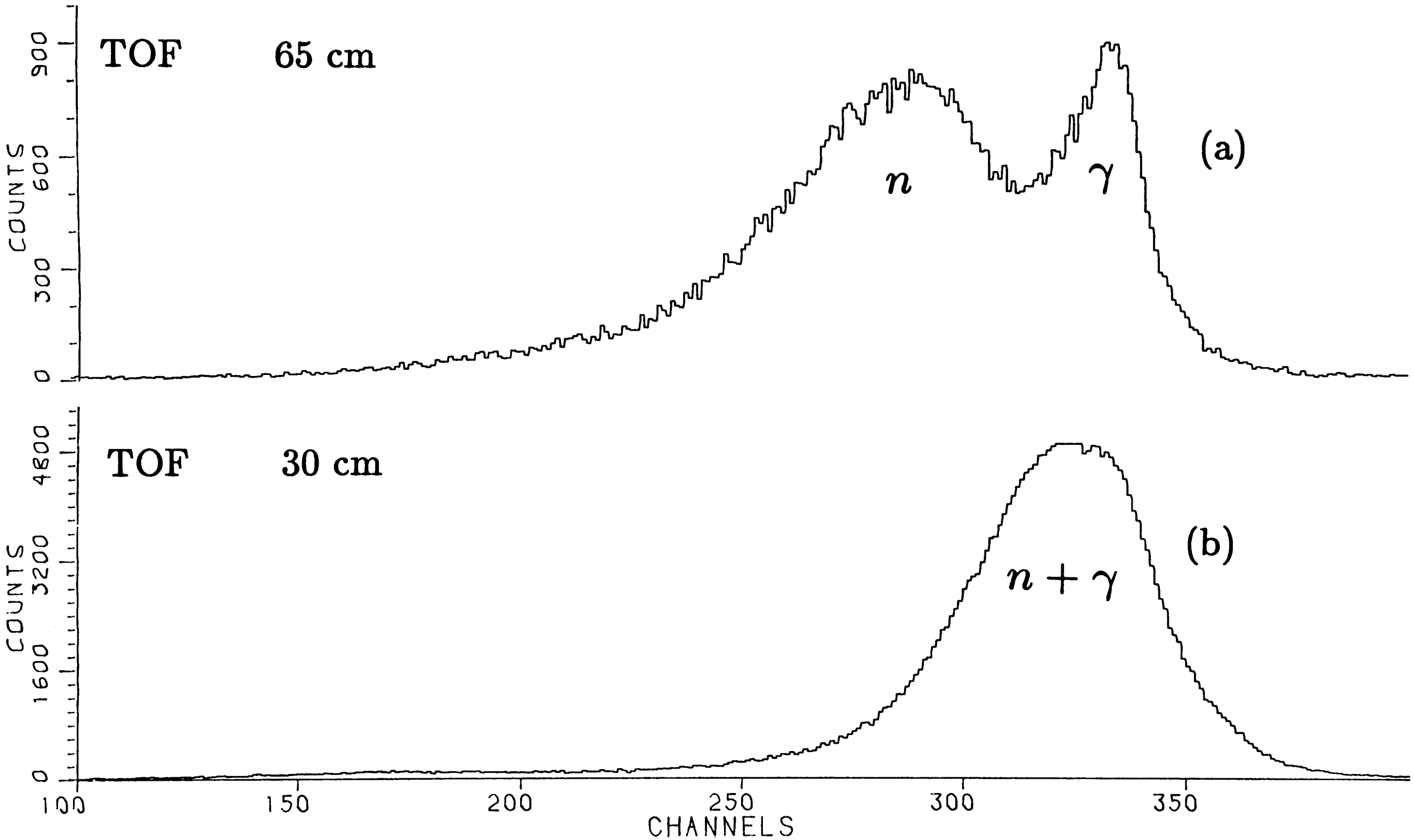


Fig.3.9 : Time-of-flight spectra between a Ge(Li) and the neutron wall with the reaction $^{54}Fe + ^{12}C$. The neutron and gamma peaks are as labelled. The flight paths were of different lengths: (a) 65 cm and (b) 30 cm.

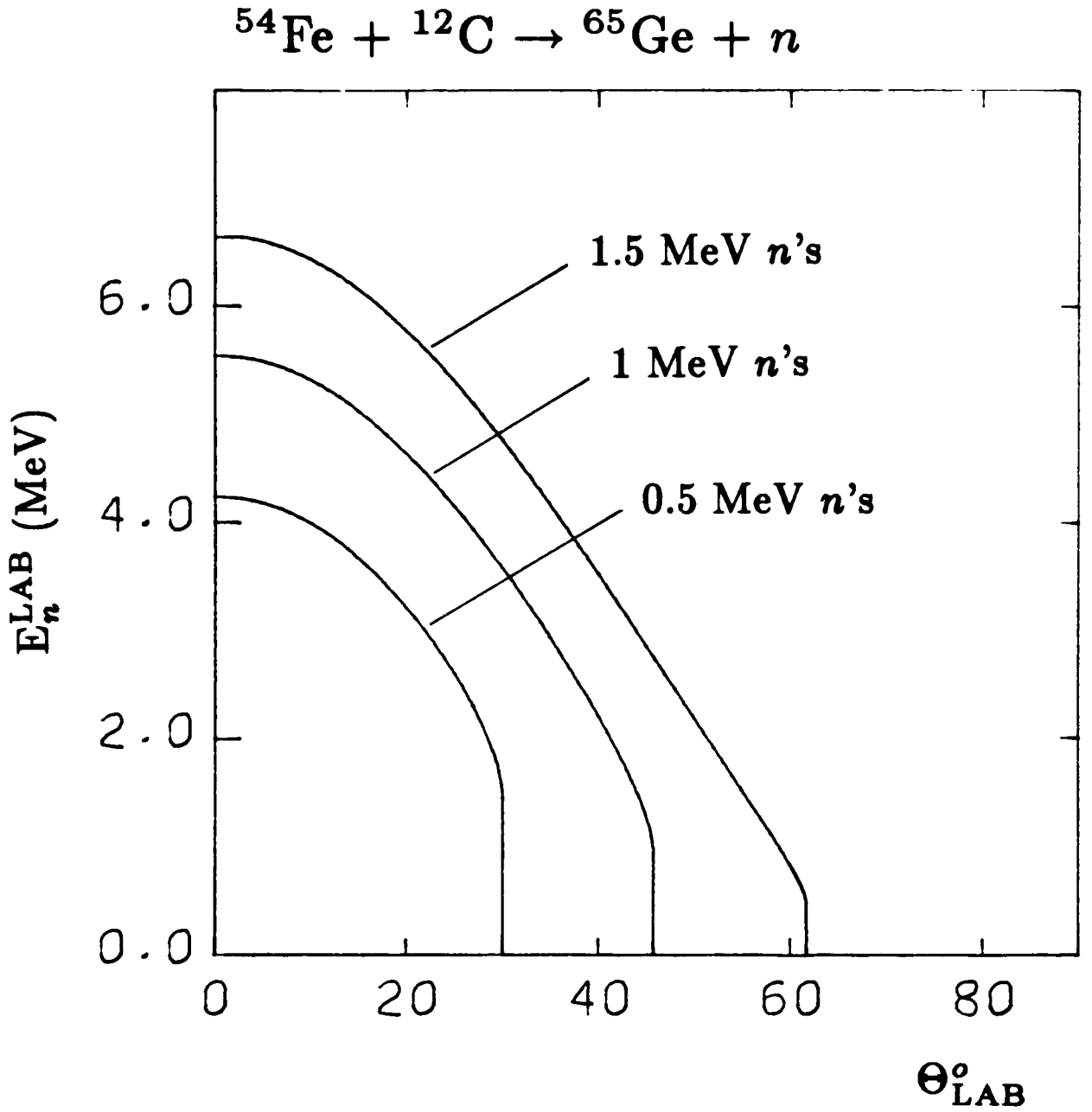


Fig.3.10 : Laboratory energy of evaporated neutrons against the laboratory angle of emission from simple kinematics. The 3 curves correspond to 3 different evaporation energies of the neutrons in the centre-of-mass frame.

Reaction	Chan.	E_n(MeV)[1]	d(cm)[2]	Ω(st)[3]	n-γ disc.[4]	Eff. (%)[5]
$^{54}Fe + ^{12}C$	pn	4.3	72	0.7	TOF	6.8(4)
$^{54}Fe + ^{12}C$	pn	4.3	30	4.3	PSD	12.6(5)
$^{24}Mg + ^{27}Al$	$2pn$	2	30	4.3	PSD	8.0(2)
$^{24}Mg + ^{27}Al$	$p2n$[6]	2	30	4.3	PSD	15.6(6)

Table 3.3 : Neutron wall efficiencies measured during different experiments. The different parameters of the experiments have also been included.
(1) Energy of n in laboratory frame from CASCADE calculations.
(2) Distance between target and neutron wall.
(3) Solid angle subtended by the n-wall at the target.
(4) Main method of n-γ discrimination used.
(5) Efficiency = (counts in peak in n-gated spectrum)/singles peak $\times$ 100.
(6) $2n$ channel included for comparison. n energy here is the energy of the first n.

where the first term is the efficiency for detecting one of the two neutrons while the second term is the efficiency for detecting both neutrons. Using $\epsilon = 8$ % gives a value of 15.4 %, in good agreement with the experimental value (of the ***p2n*** channel). The efficiency for the ^{54}Fe + ^{12}C reaction was slightly higher than for the ^{24}Mg + ^{27}Al reaction due to kinematic focusing and the larger neutron energy of the former, which made the neutrons easier to detect.

3.8.3 Figure of Merit

A figure of merit, M, after Kalyna and Taylor [KAL70] (see also [BRI72]), can be used to provide a quantitative measure of the effectiveness of the n-γ discrimination of a system. M is given by $M = S/(W_n + W_\gamma)$ where S = separation of the neutron peak (fwhm = W_n) and the gamma-ray peak (fwhm = W_γ). Table 3.4 gives the figure of merit for the many n-γ discrimination systems employed in this thesis. For comparison, the value quoted by Kalyna and Taylor for an 8" diameter by 1" thick (0.8 litres) NE213 scintillator is also included. Our values are slightly lower, but this is to be expected as we have a much larger (14.6 litres per quadrant) and thicker (6") scintillator.

Type of n-γ discrimination	Figure of Merit M
TOF	0.64
Freiburg PSD	0.74
Composite PSD	0.68
KT PSD	0.81

Table 3.4 : Figure of merits for the different methods employed to discriminate n's from γ's. The entry for KT PSD has been included for comparison (see text).

3.9 PSD-TOF plots

Initially, before the Freiburg PSD's had been constructed, the main method by which n-γ discrimination was achieved was through TOF. The *Composite* PSD's were set up but were not reliable enough on their own. Setting these PSD's up was a time-consuming process as the behaviour of the various NIM modules varied from unit to unit and there were many parameters to be adjusted (e.g. CF threshold, CF walk, TFA shaping times and pulse amplitudes), each of which was very sensitive to the setting of the others. TOF information was thus initially used for n-γ discrimination. But some breakthrough of non-neutron events was still observed as can be seen in fig. 3.11 where the ^{56}Fe Coulomb excitation line is evident in the n-gated spectrum. However, demanding a PSD n-gated condition as well removed this line (fig. 3.12). We see here that the 850 keV line from ^{64}Ga, which overlapped the breakthrough of the Coulomb excitation line in the previous spectrum, stands out clearly. Thus, the data were sorted using both TOF and PSD to obtain cleaner spectra. The pulse shape parameter plotted against TOF shows two distinct peaks corresponding to n's and γ's (fig. 3.13). Gates on PSD as well as TOF would then select the n peak, leaving out the γ peak and randoms. Alternatively, a two-dimensional polygonal window could be set around the n peak in the two-dimensional PSD-TOF spectrum to be more selective in the gating. The latter approach was adopted during the analysis of the ^{64}Ge data where both the cleanliness and the statistical quality of the spectrum were of paramount importance. Although fig. 3.13 may suggest that PSD n-γ discrimination alone was adequate, the *composite* PSD's were not entirely reliable and so a double-check was made by employing both methods. With the advent of the Freiburg PSD's, n-γ discrimination was achieved entirely by pulse shape discrimination. TOF information was still collected as this allowed us to impose stricter limits on neutron events thereby obtaining very clean neutron gated spectra.

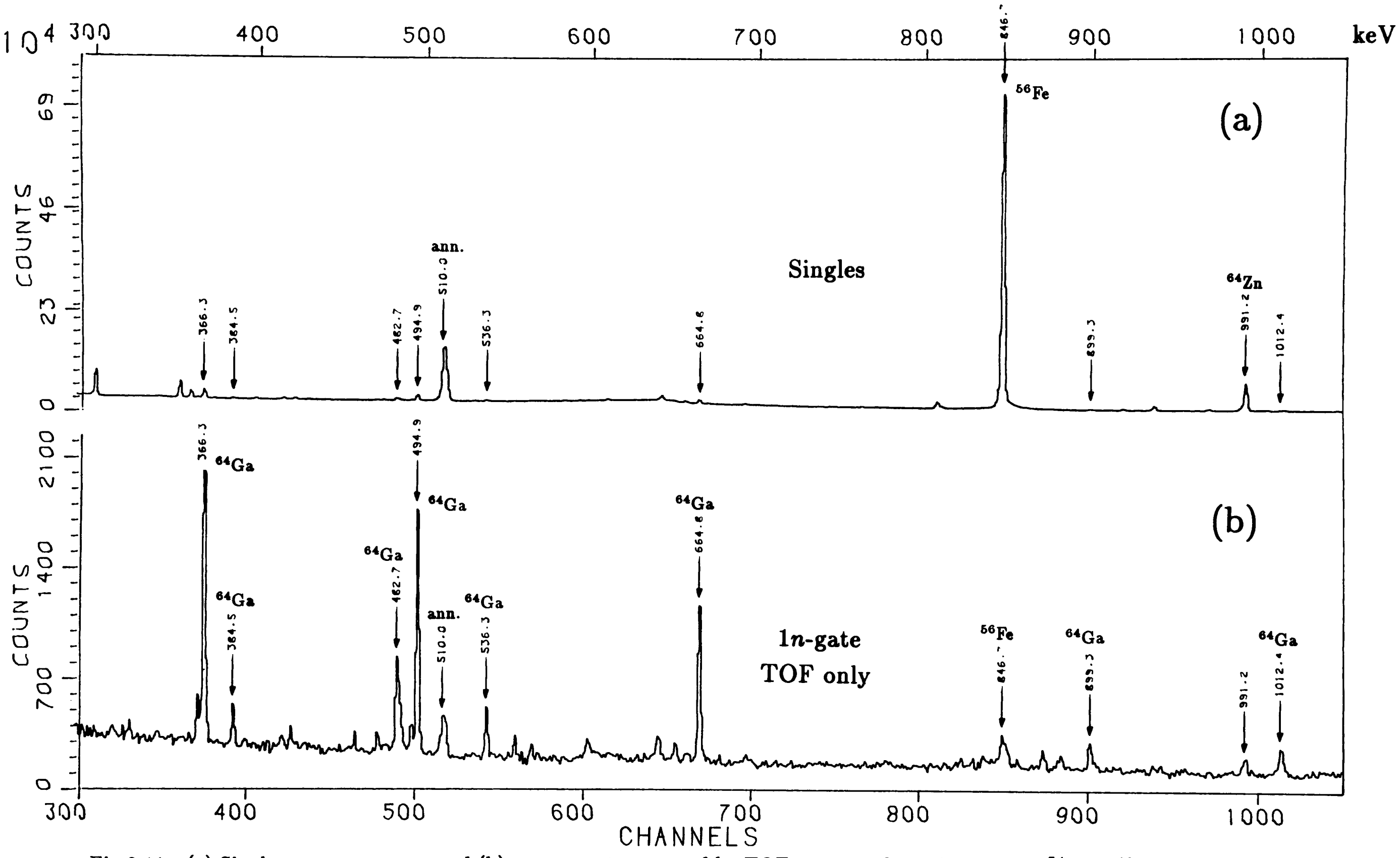


Fig.3.11 : (a) Singles γ-ray spectrum and (b) γ-ray spectrum gated by TOF neutrons from the reaction $^{54}Fe + ^{12}C$. The presence of the 847 keV Coulomb excitation line from the backing ^{56}Fe is clearly visible. Spectrum (b) should be compared with the spectrum on the following page where this line disappears when the spectrum is gated by both the TOF and PSD signals.

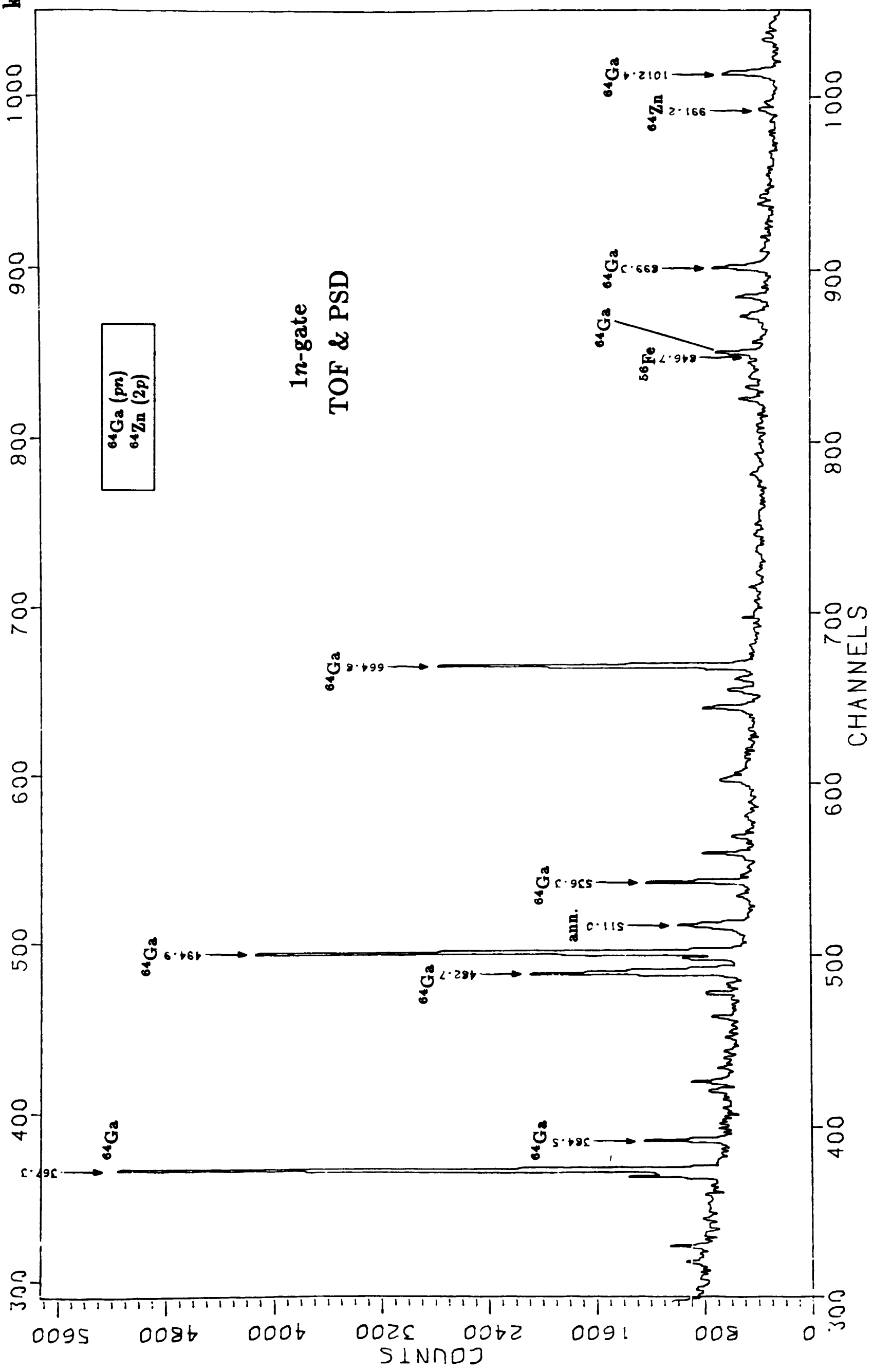


Fig.3.12 : γ-ray spectrum gated by neutrons satisfying TOF and PSD windows from the reaction ^{54}Fe + ^{12}C.

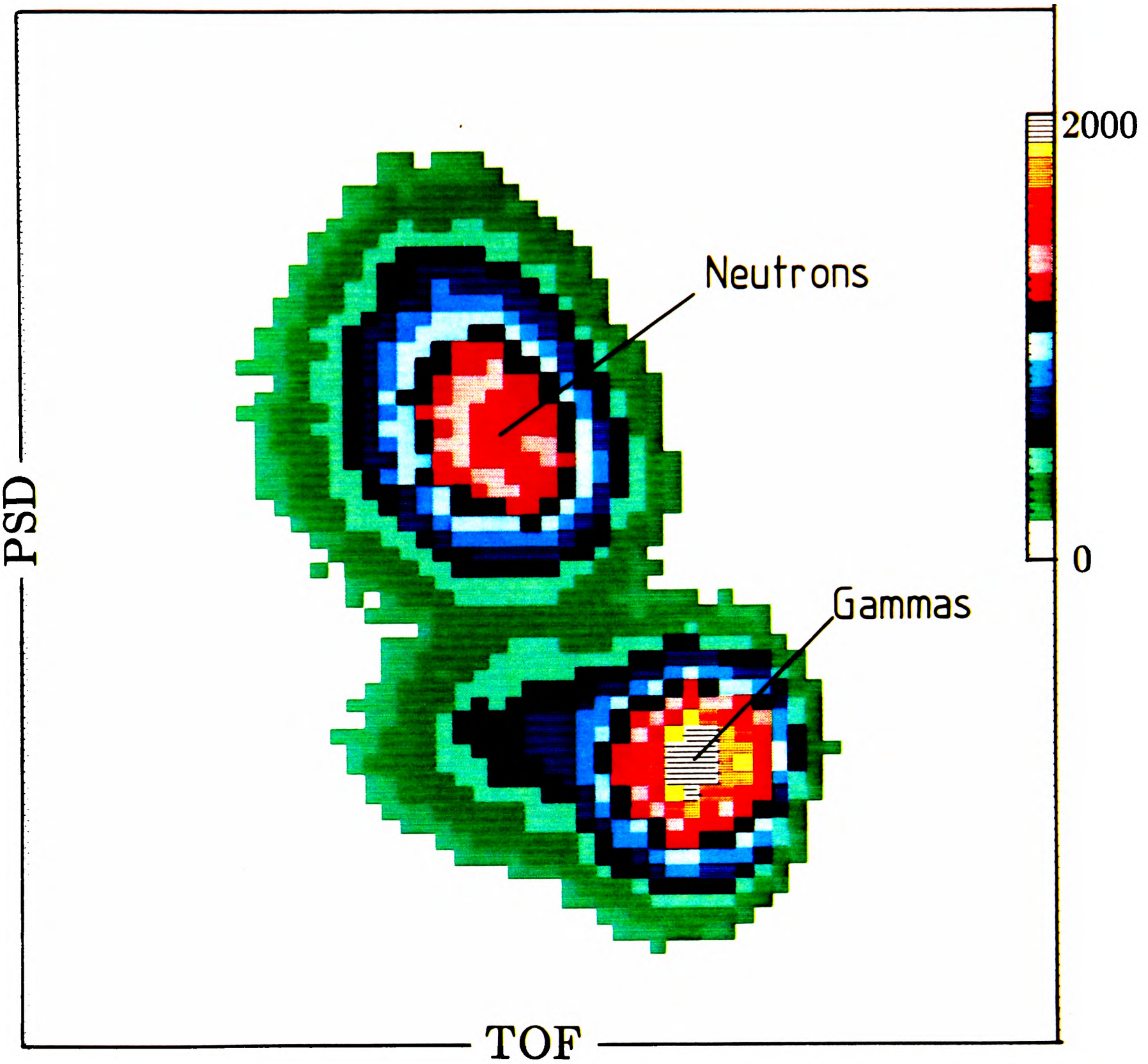


Fig.3.13 : PSD-TOF plot showing two distinct peaks corresponding to neutron and γ-ray events. A two-dimensional window set on the neutron peak was used to selectively pick out neutron coincidence events.

3.10 Off-line Analysis

In order to reduce the data and extract spectra gated by neutrons with or without protons, a method was required in which the different logical relationships could be handled in a flexible manner. To this end, a general purpose sorting language **SOL** was defined which allowed fairly complex logical operations to be performed with the data. For instance, this allowed a gate to be set on (say) $2n0p$ events, $1n1p$ events or even $2n0p$ events where the two neutrons were detected in non-adjacent detectors. A detailed description and user's guide to this language is given in Appendix IV. Throughout this thesis, where appropriate, **SOL** programmes will be included after a spectrum to show the precise logical operations performed to obtain the spectrum in question.

All the analyses were performed on a VAX 11/780 using a general purpose data acquisition program GENDAT. This program was significantly modified to incorporate the **SOL** interpreters and miscellaneous analysis tools such as peak search routines and polynomial calibration routines. Bit manipulation of the data was also incorporated in the program. This was useful as the router pattern was stored as a 16 bit word where each bit corresponded to the multiplicity of an event (i.e. whether it was $1n0p$, $1n1p$, etc...). It was thus possible to test individual bits and then sort the data accordingly. Two-dimensional windows could also be set and the analysis of the ^{64}Ge runs used this feature to obtain clean n-gated spectra with good statistics.

4

CHAPTER 4

Chromium-48

"I'll tell thee everything I can;

There's little to relate."

4.1 Introduction

In this chapter, the experimental investigation of $^{48}_{24}$Cr is discussed. As ^{48}Cr is in the middle of the $1f_{7/2}$ shell, it has the most complex $f_{7/2}$ shell model configuration. Thus, it provides a rigorous test for various shell model techniques. With the $(1f_{7/2})^8$ configuration, it is possible to build states up to $I = 16$ and, before these experiments were performed, states up to only 10^+ were known. The motivation, then, was to populate the high spin states and observe their γ-decays. The reaction chosen to study this nucleus, ^{27}Al(^{24}Mg,$p2n\gamma$)^{48}Cr, also has a reasonably large cross-section† (compared with the ^{64}Ge cross-section discussed in the next chapter) for the evaporation of two neutrons (and a proton) and so could be used to test the performance of the neutron wall under reasonably favourable conditions.

† 5.3 % of the total fusion cross-section by CASCADE.

The general experimental arrangement has been described in chapter 3 but some of the details were changed for this experiment and these differences are discussed in section 2 of this chapter. A transition from a new level in ^{48}Cr has been observed and the placement of this state in the level scheme of ^{48}Cr is presented in section 3. During the experiment, n-γ and γ-γ events were collected. They were analysed separately to provide corroborating evidence for the assignment of the observed γ-rays to the decay of various nuclei and the subsequent placement of these γ-rays in the decay schemes of these nuclei. These data are presented and discussed in section 3. Finally, in section 4, the updated level scheme of ^{48}Cr is considered and compared with shell model predictions.

In this chapter, the term *1n-event* is used fairly loosely and should be taken to mean events in which at least one neutron is present which may or may not have been accompanied by charged particles. Where appropriate, the sorting programmes used to generate a particular spectrum are included. These are on the pages following the relevant spectra and are labelled with the same figure number but with the extension '.SOL' after the number. Also, where appropriate, the channel through which a nucleus is made is included in parenthesis after the name e.g. ^{48}Cr($p2n$). Unless otherwise stated, the γ-ray energies given in the figures indicate the value at the maximum of the peak. The energies quoted in the text are all centroid values and so there may be a small discrepancy between these two values.

4.2 Experimental Details

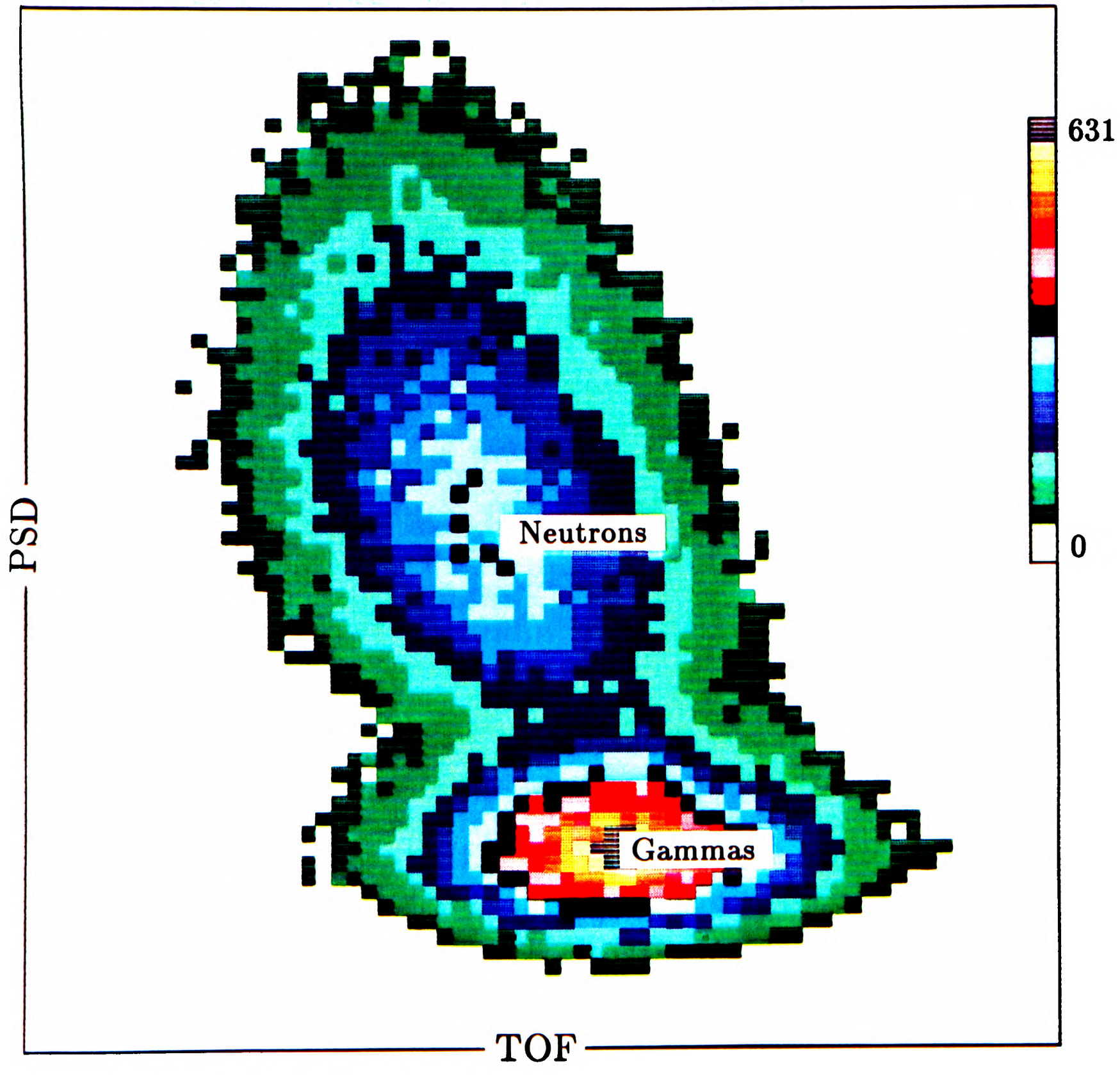
The general arrangement of the experiment was as described in §3.6 viz. a neutron wall downstream and 4 Ge(Li) detectors positioned around and as close as possible to the target. In order to do so, two Ge(Li) detectors were located at 90° to the beam axis with the remaining two at the backward angles of 123° and 127°. The

plan of this arrangement is shown in L5 of §3.6 The neutron wall was placed 30 cm away from the target. Although this prevented effective n-γ discrimination by TOF, all 5 neutron detector signals were fed into Pulse Shape Discriminators (PSD) which enabled the necessary n-γ discrimination to be achieved. The resolution obtained using a PSD-TOF plot is shown in fig. 4.1. It can be seen that the resolution in the PSD direction was quite adequate for a clean n-γ separation.

The target mount consisted of a target holder connected to one end of a thin cylindrical rod that was attached at the other end to the lid of the chamber. This assembly was insulated from the chamber and could be rotated about the axis. To reduce the attenuation of γ-rays through the target, the target was positioned at 60° to the beam axis

A ^{24}Mg beam, with laboratory energies between 60 and 72 MeV (inclusive) was used to bombard a target of 250 μg/cm^2 ^{27}Al on 18.9 mg/cm^2 gold backing. Data were collected event-by-event onto high-density tape via a DMC-11 interface, as was explained in §3.7. At each energy, approximately $2\frac{1}{2}$ million events were recorded and from these data, yield curves for several γ-rays were determined. The main data collecting run was performed at 62 MeV and a total of 68 hours beam time was used with $\sim 6 \times 10^7$ events collected onto tape. The lowest common denominator of an event was a *ningle* event‡. In other words, if a γ-ray was detected in coincidence with a signal (whether γ or n) from one neutron detector, all the ADC's were strobed and the parameters read were written onto tape. Higher multiplicity events were similarly recorded. Singles events in the Ge(Li) detectors were stored in memory and written to disc at the end of each sequence (which lasted ~4 hours).

‡ For the definition of '*ningle*', see §3.2.



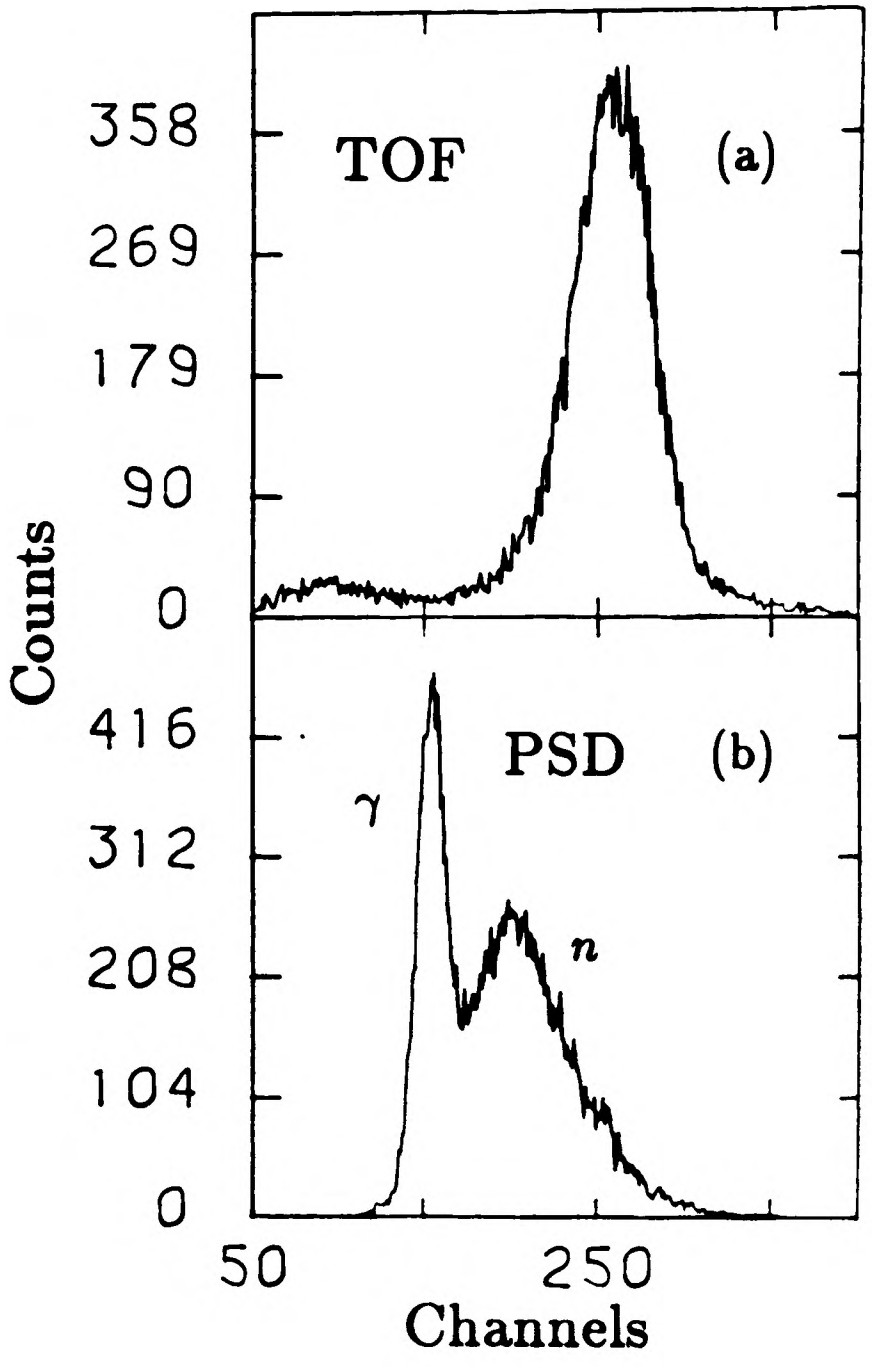


Fig.4.1 : PSD-TOF plot. The spectra shown on the right are the (a) TOF and (b) PSD plots.

4.3 Results & Analysis

4.3.1 Excitation Function

CASCADE predictions (§2.4.3) show a slowly varying yield for the reaction ^{27}Al(^{24}Mg,2np)^{48}Cr for incident energies ranging from just above the Coulomb barrier, 51.5 MeV (laboratory frame), to 72 MeV with a maximum at approximately 60 MeV (see fig. 2.8). The excitation functions for various outgoing channels from the reaction were determined for energies between 60 MeV and 72 MeV (with a step size of, typically, 2 MeV). The yield of the γ-rays of interest was normalized to the 279 keV line from the Coulomb excitation of the gold backing. The integrated cross-section for the Coulomb excitation of the gold was calculated and its variation over the energy range corrected for (see Appendix I). Fig. 4.2(a) shows the excitation function of the 751 keV γ-ray from $^{48}_{24}$Cr$_{24}$. This is the transition from the first excited state to the ground state and as all the known γ-decay chains pass through this level, this transition reflects the total yield of the nucleus. Fig. 4.2(b) shows the CASCADE cross-section for the production of this nucleus. The excitation functions of two strong γ-ray lines in $^{48}_{23}$V$_{25}$ and $^{45}_{22}$Ti$_{23}$ are also presented (Fig. 4.2(c) for the 627 keV transition in ^{48}V and fig. 4.2(e) for the 744 keV transition in ^{45}Ti). Their respective CASCADE cross-sections have also been included for comparison. In these two nuclei the decay schemes are complex (due to the odd number of nucleons) and although the transitions each represent a sizeable portion of the γ-decay strength, they do not reflect the total yield of the nucleus. We see, nevertheless, the (general) trend calculated by CASCADE borne out by experimental evidence.

To populate states with high spins, it is necessary to bring into the compound nucleus as much angular momentum, and hence energy, as possible. However, figs. 4.2(a) & (b) show that the cross-section for the production of ^{48}Cr decreases with increasing bombarding energies above 58 MeV. The yield of the 1106 keV line (^{48}Cr;

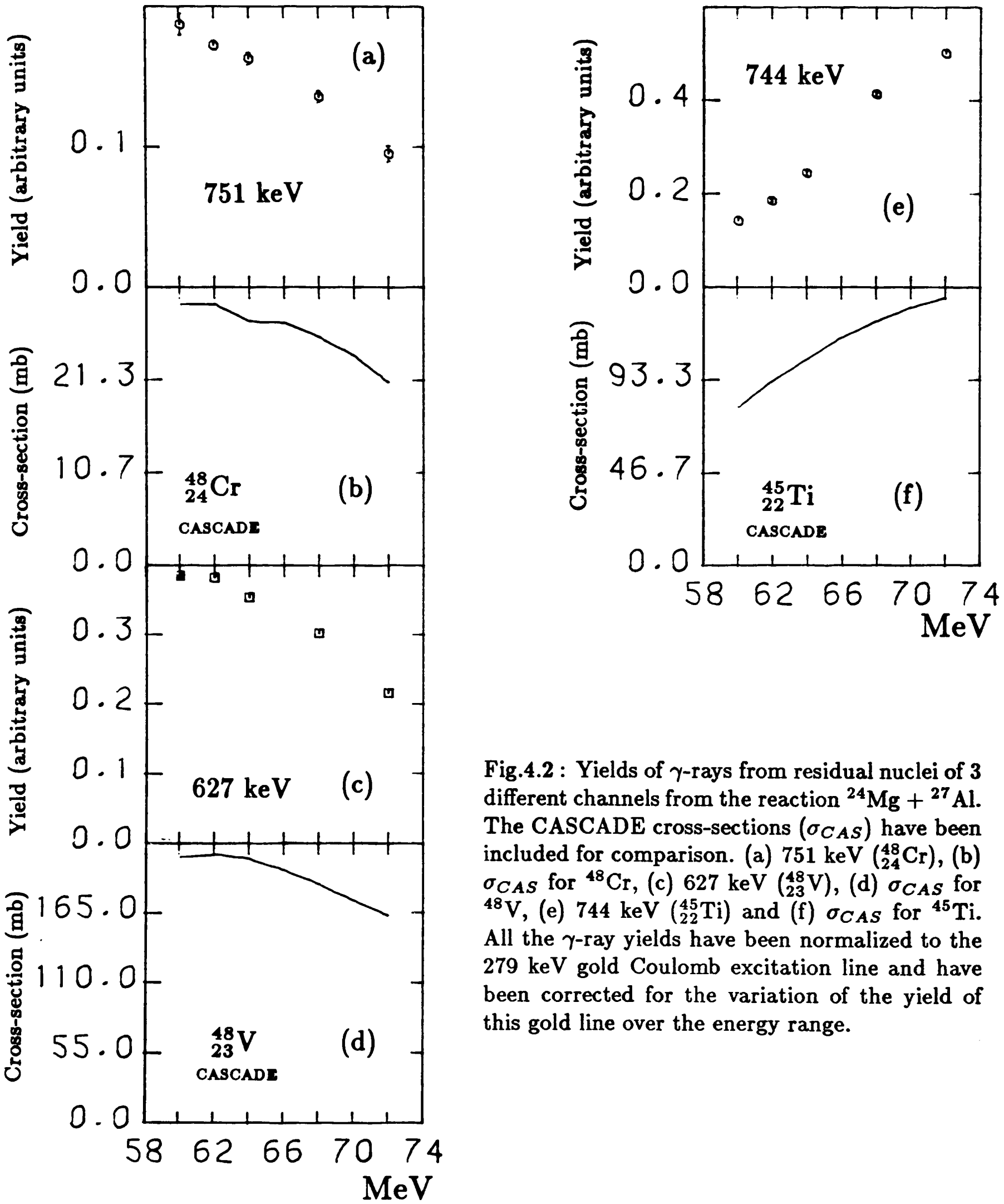


Fig.4.2 : Yields of γ-rays from residual nuclei of 3 different channels from the reaction ^{24}Mg + ^{27}Al. The CASCADE cross-sections (σ_{CAS}) have been included for comparison. (a) 751 keV ($^{48}_{24}$Cr), (b) σ_{CAS} for ^{48}Cr, (c) 627 keV ($^{48}_{23}$V), (d) σ_{CAS} for ^{48}V, (e) 744 keV ($^{45}_{22}$Ti) and (f) σ_{CAS} for ^{45}Ti. All the γ-ray yields have been normalized to the 279 keV gold Coulomb excitation line and have been corrected for the variation of the yield of this gold line over the energy range.

4+ → 2+) relative to the 751 keV line (^{48}Cr; 2+ → 0+) was monitored. Table 4.1 shows this ratio, as well as the relative intensity of the 751 keV line with respect to the 627 keV line from ^{48}V. From this table, we see that the variation is only ~15 % over the energy range of 60 to 72 MeV and so the choice of energy was not a crucial issue. A bombarding energy of 62 MeV was chosen. The CASCADE cross-sections for the various evaporation channels at this energy is given in fig. 4.3 and we see that ^{48}Cr is a reasonably strong channel and accounts for over 5 % of the total fusion cross-section.

E_{lab} MeV	I(4→2)/I(2→0)(1)	I(751 keV)/I(627 kev)(2) $\times 10^{-2}$
60	0.45(2)	5.5 (1)
62	0.47(1)	5.17(7)
64	0.48(2)	5.18(9)
68	0.52(2)	4.6 (1)
72	0.53(4)	4.7 (2)

Table 4.1 : Ratios monitored during the excitation function experiment show variation of yield of ^{48}Cr lines ~15 % over the energy range 60 to 72 MeV.
(1) Ratio of the 4→2 transition to the 2→0 transition in ^{48}Cr
(2) Ratio of the 2→0 transition in ^{48}Cr to the 6→4 ground state transition in ^{48}V.

4.3.2 Neutron Gating

The four Ge(Li) detectors used in this experiment were gain-matched and their efficiency curves determined with a ^{152}Eu source immediately after the experiment. These curves were found to be similar and in order to improve the statistics, the spectra analysed and presented below are the sum of the γ-ray spectra from all four Ge(Li)'s. As the nucleus of interest, ^{48}Cr, was made through a $p2n$ channel, sorting on neutron coincidence events helped remove unwanted lines e.g. Coulomb

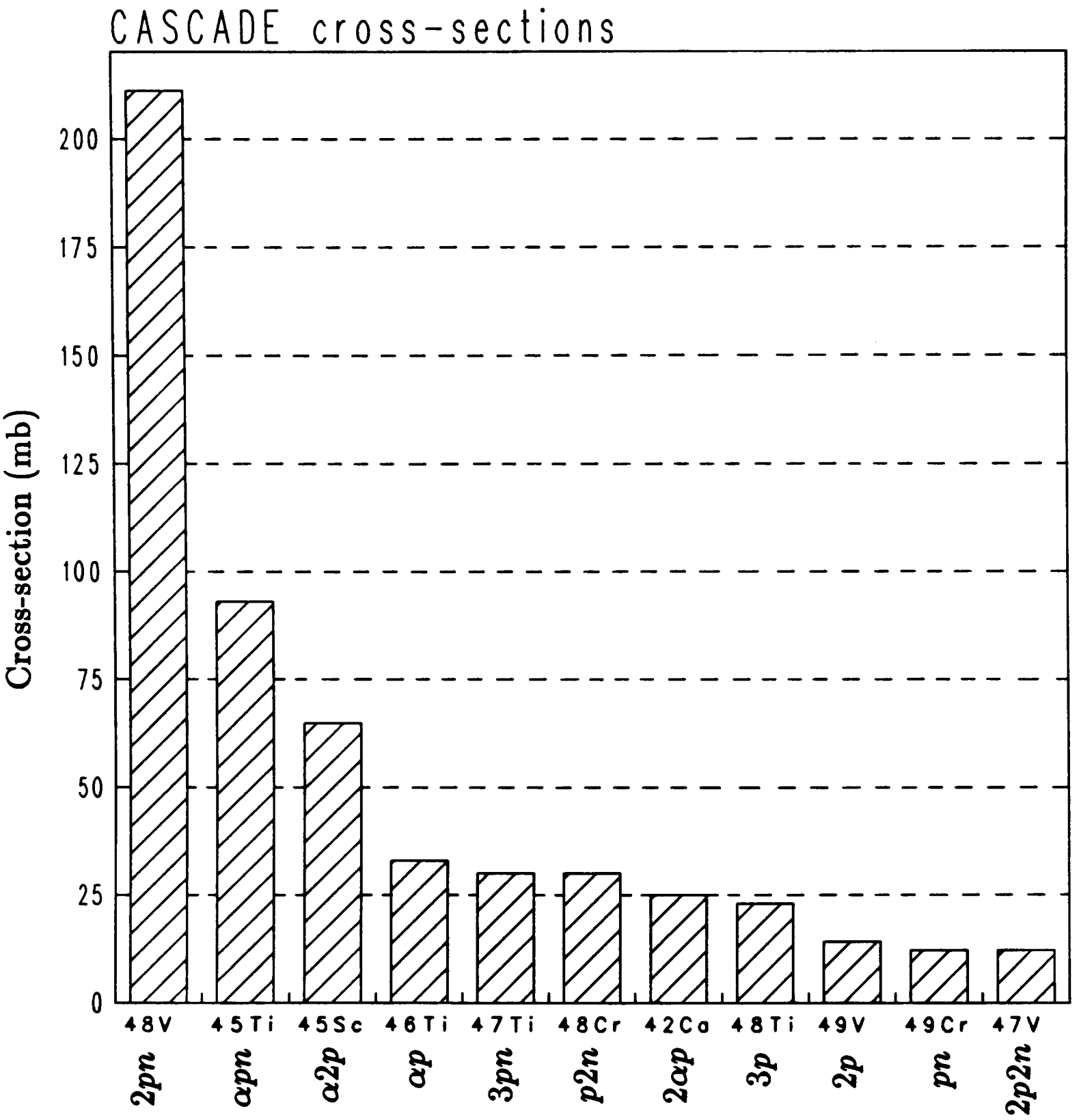


Fig.4.3 : CASCADE cross-sections for the major evaporation channels from the reaction ^{24}Mg + ^{27}Al at 62 MeV.

excitation (Coulex) lines and lines from charged-particle-only channels. This is clearly shown in fig. 4.4 where we see the 279 and 547 keV gold Coulex lines in the singles spectrum (part (a)) effectively suppressed in the n-gated spectrum (part (b)). The lines from the charged-particle-only channels viz. $^{45}_{21}$Sc ($\alpha 2p$), $^{46}_{22}$Ti (αp) and $^{48}_{22}$Ti ($3p$) have also been removed by the n-gate. In order to enhance the ^{48}Cr ($p2n$) lines over the other lines (which come in coincidence with one neutron only) the data were sorted for $2n\gamma$ events. Fig. 4.5(a) shows the γ-ray spectrum of events in which neutrons in any two (or more) neutron detectors were detected in coincidence with a γ-ray. It can be seen that many $1n$ lines (especially ^{48}V($2pn$)) are present in this $2n$ spectrum. These *pseudo*-$2n$ events are the result of neutrons scattering off one detector into another. It should be possible to remove these breakthrough peaks by subtracting off a (suitably normalized) $1n$ spectrum from the $2n$ spectrum. Part (b) of the figure shows such a subtracted spectrum, where the $1n$-spectrum, normalized to the 628 keV line (one of the largest $2pn$ peaks) in the $2n$ spectrum, has been subtracted from the $2n$ spectrum. The peaks in this subtracted spectrum should be indicative of true $2n$ events and not simply of $1n$ breakthrough. If the cross-talk between n-detectors is to be reduced further, we can sort for events in which the two neutrons triggered non-adjacent detectors and this is shown in fig. 4.6(a) with part (b) being the subtracted spectrum as before.

We have to be careful in subtracting spectra normalized to a chosen γ-ray line in a spectrum. This is because the n energies for different channels (e.g. pn,$2pn$,$3pn$,...) are different. Neutrons in channels with fewer particles will, on average, be evaporated with more energy. Higher energy neutrons have a greater probability of causing the *pseudo*-$2n$ events mentioned above as the scattered neutron will still be energetic enough to be detected. So, the breakthrough of the $1nxp$ channel into the $2n$ spectrum is largest, on average, for the smallest value of x. If the spectra are normalized to a pn line, then the $2pn$,$3pn$,... lines will be over-subtracted. As the $2pn$ lines dominate the spectrum, it is sensible to use a $2pn$ line for normalization

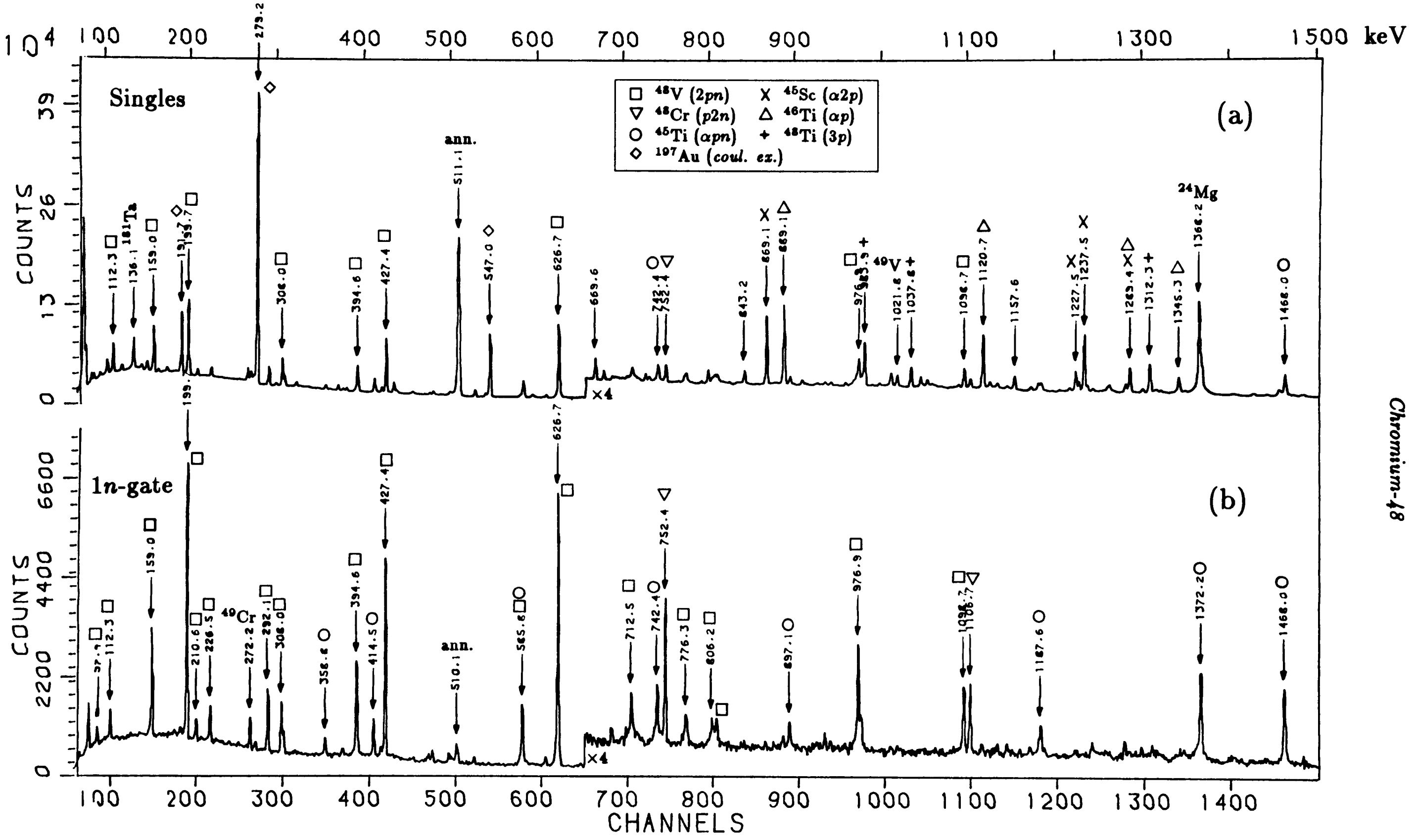


Fig.4.4 : (a) singles γ-ray spectrum and (b) n-gated γ-ray spectrum from the reaction ^{24}Mg + ^{27}Al at 62 MeV.

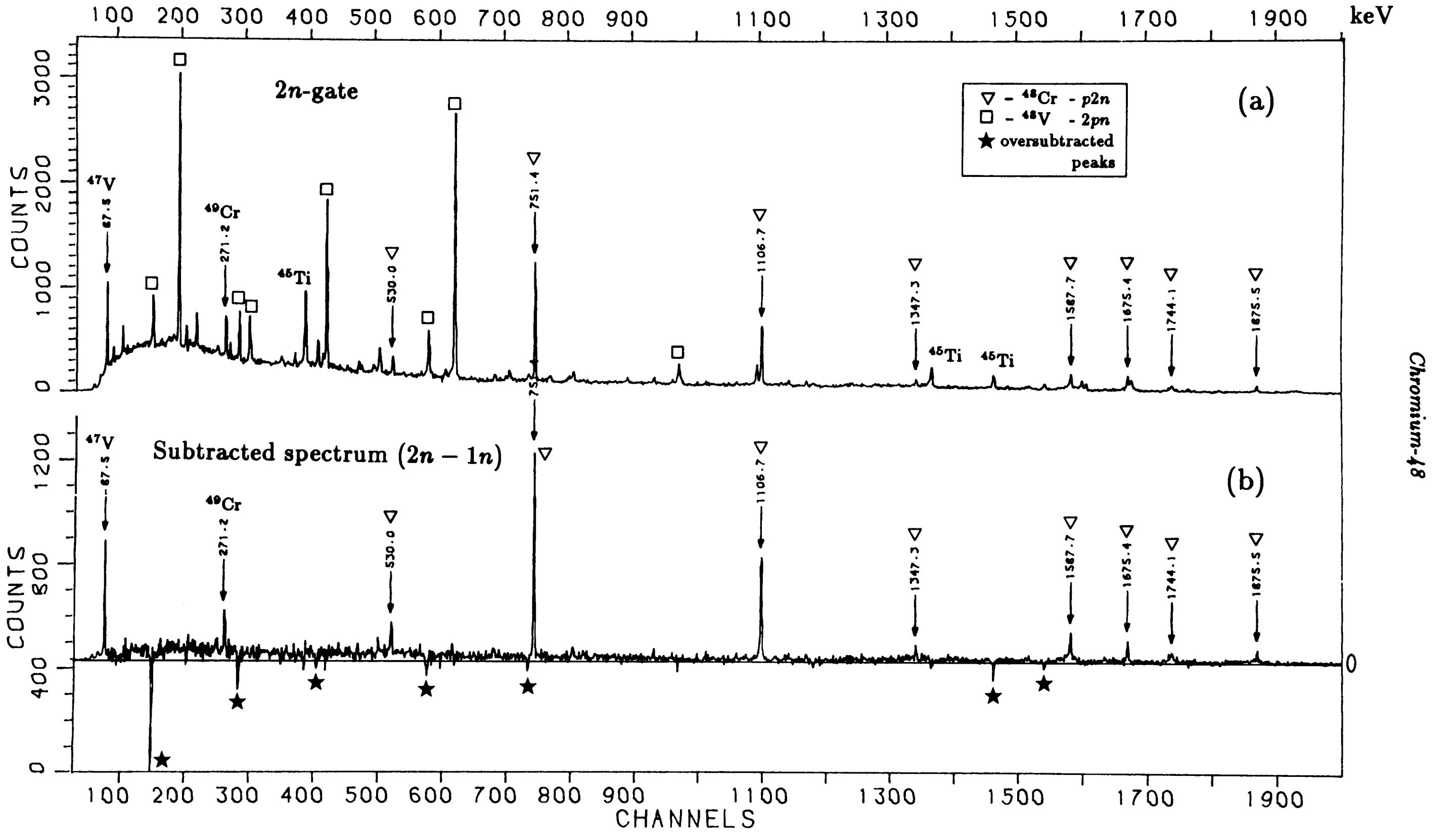


Fig.4.5 : (a) γ-rays in coincidence with two neutrons in any two n-detectors. (b) The above $2n$ spectrum with the $1n$ spectrum (normalized to the 628 keV line) subtracted from it. The oversubtracted peaks labelled ★ are discussed in the text.

```
001  !
002  !     Sort programme to look for 1n and 2n channel
003  !     Window 0 - PSD1
004  !     Window 1 - PSD2
005  !     Window 2 - PSD3
006  !     Window 3 - PSD4
007  !     Window 4 - PSD5
008  !     Window 5 - 2n event
009  !
010   TITLE S707
011   OR 0 1 2 3 4 R0              !check that it's 1n
012   IF R0
013       INC 0 P15 0 1            !GAMMA 1
014       INC 1 P16 0 1            !GAMMA 2
015       INC 2 P17 0 1            !GAMMA 3
016       INC 3 P18 0 1            !GAMMA 4
017   ENDIF
018   IF 5                         !check for 2 ningles
019     AND 0 1 R1
020     AND 0 2 R2
021     AND 0 3 R3
022     AND 0 4 R4
023     AND 1 2 R5
024     AND 1 3 R6
025     AND 1 4 R7
026     AND 2 3 R8
027     AND 2 4 R9
028     AND 3 4 R10
029     OR R1 R2 R3 R4 R5 R6 R7 R9 R9 R10 R11      !any 2n event
030     IF R11
031       INC 4 P15 0 1            !GAMMA 1
032       INC 5 P16 0 1            !GAMMA 2
033       INC 6 P17 0 1            !GAMMA 3
034       INC 7 P18 0 1            !GAMMA 4
035    ENDIF
036   ENDIF
037   END
```

Fig.4.5.SOL : Sorting programme for 1*n* and 2*n*-gated spectra.

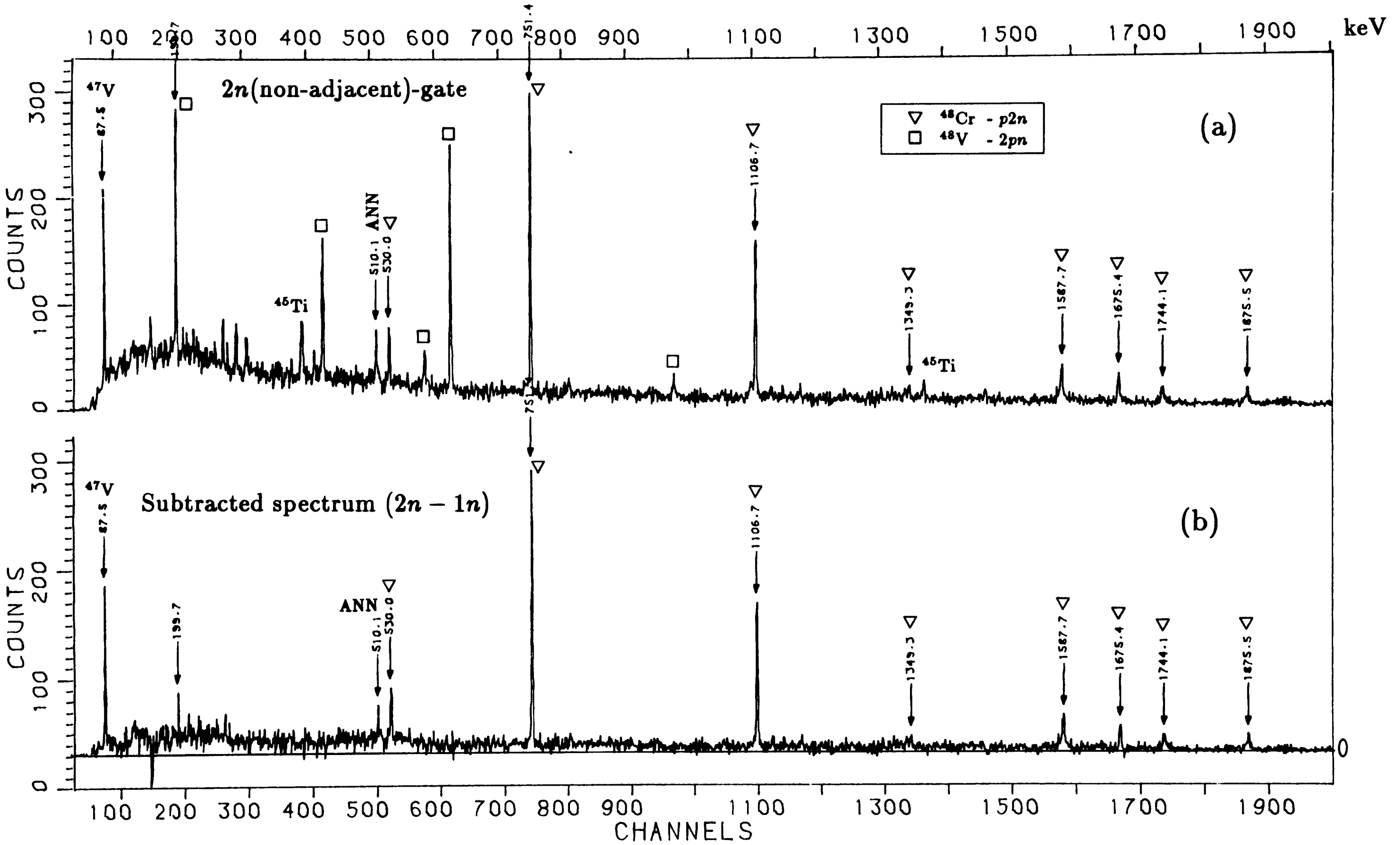


Fig.4.6 : (a) γ-rays in coincidence with two neutrons detected in two non-adjacent n-detectors. (b) The above $2n$ spectrum with the $1n$ spectrum (normalized to the 628 keV line) subtracted from it.

```
001  !
002  !     Sort programme to look for NON-ADJ 1n channel
003  !     ( with and without the little neutron detector )
004  !
005  !     Window 0 - PSD1
006  !     Window 1 - PSD2
007  !     Window 2 - PSD3
008  !     Window 3 - PSD4
009  !     Window 4 - PSD5
010  !     Window 5 - 2n event
011  !
012   TITLE S718
013   OR 0 1 2 3 4 R0              !check that it's 1n
014   IF R0
015    IF 5                        !check for 2 ningles
016      AND 0 2 R1
017      AND 1 3 R2
018      AND 0 4 R3
019      AND 1 4 R4
020      AND 2 4 R5
021      AND 3 4 R6
022      OR R1 R2 R11               !2 neutron event
023      IF R11                     ! ignore little Norman Jr.
024       INC 0 P15 0 1             !GAMMA 1
025       INC 1 P16 0 1             !GAMMA 2
026       INC 2 P17 0 1             !GAMMA 3
027       INC 3 P18 0 1             !GAMMA 4
028      ENDIF
029      OR R1 R2 R3 R4 R5 R6 R12      !Here, we include Norman Jr.
030      IF R12
031       INC 4 P15 0 1             !GAMMA 1
032       INC 5 P16 0 1             !GAMMA 2
033       INC 6 P17 0 1             !GAMMA 3
034       INC 7 P18 0 1             !GAMMA 4
035      ENDIF
036    ENDIF
037   ENDIF
038   END
```

Fig.4.6.SOL : Sorting programme for $2n$-(non adj.)-gated spectra.

in the present case. However, we must bear in mind the possibility of some *pn* lines under-subtracting and breaking through, and these must be taken into account.

In the rest of this section, the γ-ray peaks observed in the *n*-gated spectra will be identified. No attempt will be made to fit these γ-rays to any level scheme of the identified nuclei as this will be done in the next section in the light of the γ-γ data.

a) Total 2n spectrum — Fig. 4.5

Fig. 4.5(a) shows the γ-ray spectrum obtained by gating on any $2n$ signal i.e. neutron signals from any two detectors. Even though the spectrum has a fairly substantial breakthrough of the $1n$ channel (due to cross-scattering of the neutrons), the subtracted spectrum (fig. 4.5(b)) has only 10 prominent lines:-

88 keV γ-ray

This line is from the γ-decay of the first excited state in $^{47}_{23}$V ($2p2n$). This assignment is confirmed by the γ-γ coincidence spectra.

271 keV γ-ray

The 271 keV γ-ray is the transition from the first excited state in ^{49}Cr (pn) to its ground state. The presence of this peak is due to the under-subtraction of the *pn* peaks as mentioned above. Further evidence for this assignment is gained by comparing this spectrum with the spectrum of the γ-rays in coincidence with neutrons detected in non-adjacent detectors (fig. 4.6 and below). In the latter spectrum, the line has disappeared. This assignment is confirmed by the coincidence data.

530, 751, 1106, 1586, 1674, 1743 and 1875 keV γ-rays

These are known transitions in ^{48}Cr ($p2n$) and correspond to almost all (a line at 1343 keV, reported in [HAN79] was not seen) of the lines identified in HI-evaporation reactions [KUT73, HAA75, EKS79, HAN79]. These assignments agree with those from the γ-γ data.

1347 keV γ-ray

This is a new γ-ray which has not been observed in previous work. The $2n$-gated data suggest a $2n$ component in the evaporation channel but no assignment can be made on this basis because it may be a $^{47}_{23}$V ($2p2n$) line – although it does not correspond to any known transition there – or a breakthrough γ-ray as is the case for the 271 keV γ-ray line. However, the γ-γ data can be used to identify the source of this γ-ray , as is discussed below.

The over-subtracted peaks (shown by ★) correspond to γ-ray energies of 160 keV (^{47}Ti; $3pn$) and 293, 415, 587, 743, 1468 and 1546 keV (^{45}Ti; αpn). In these cases, the neutron energies were reduced because more energy was taken up by the evaporating charged particles so they (the neutrons) had smaller cross-scattering cross-sections, as mentioned previously. This smaller cross-scattering probability was reflected in a lower breakthrough into the $2n$ spectrum. The γ-γ data support these assignments.

b) 2n spectrum with non-adjacent detectors — Fig.4.6

Here, the $2n$ signals were only accepted from non-adjacent detectors. The $2n$ lines are still evident in the subtracted spectrum (part (b)). but with the poorer statistics, the evidence for a line at 1347 keV line is not as convincing as before. A 199 keV line has also appeared but this is statistical and the result of the subtraction of the strong 199 keV (^{48}V; $2pn$) line. We see that the over-subtracted peaks observed before in the previous section from ^{47}Ti($3pn$) and ^{45}Ti(αpn) have been considerably reduced. This shows that the non-adjacent detector requirement has reduced the $1n$ cross-talk in the neutron detectors.

c) Ratio of 2n to 1n peaks

An alternative method for determining the true $2n$ lines is to take the ratio of the peaks in the $2n$ and $1n$ spectra (fig. 4.7). The $2n$ data were taken from a $2n$-spectrum gated by signals from any two neutron detectors. This shows, again,

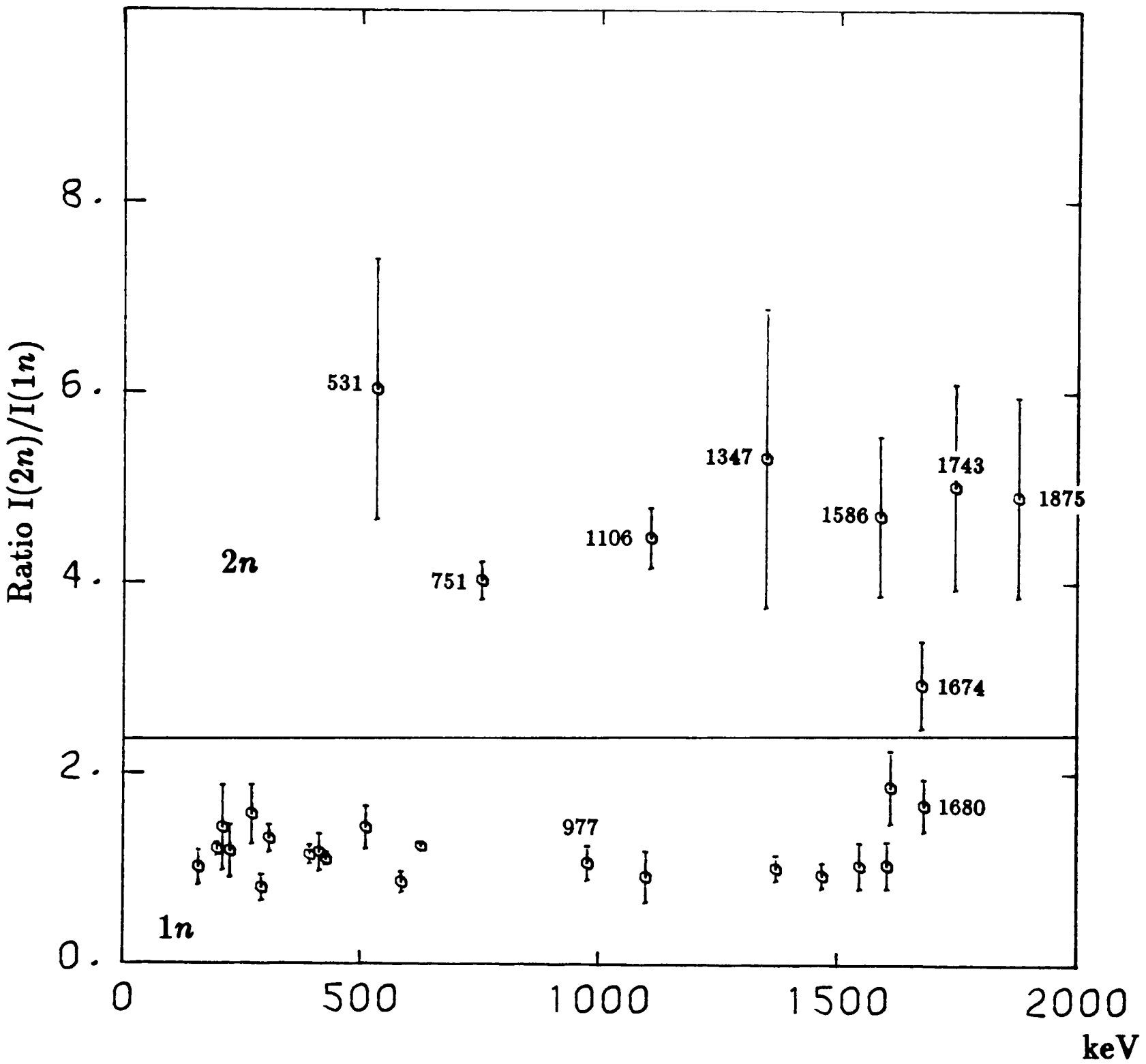


Fig.4.7 : Ratio of the intensities of selected peaks in the $2n$ γ-ray spectrum to the intensities in the $1n$ γ-ray spectrum. The line separating the true $2n$ from the $1n$ peaks has been drawn mainly to guide the eye.

the clear separation of the ^{48}Cr ($p2n$) lines from the $1n$-lines and indicates that the new 1347 keV line belongs to ^{48}Cr.

4.3.3 γ-γ Sort and Coincidence Spectra

The γ-ray data were also sorted into a two-dimensional matrix of size 2048 by 2048 channels. For each event, there were four γ-ray energies corresponding to the four different Ge(Li) detectors. Thus, 12 possible γ-γ plots were possible for each event ($^4P_2$=12) and so 12 two-dimensional (2d) arrays should have been, in principle, be used. The limited memory size of the analysis computer prevented this approach (194 Mbytes of memory would have been required). Instead, just one 2d array was used and the 12 possible permutations were used to update this i.e. this 2d array obtained was the sum of the 12 possible 2d arrays. This was permissible as the Ge(Li) detectors had been gain-matched and their efficiency curves were similar. Doppler shifts in the backward Ge(Li) detectors were not found to be significant enough to create a problem. Hence, a symmetric matrix, M(x,y), was obtained which was used to generate the coincidence spectra. For example, the coincidence spectrum, f(x), for a γ-ray energy $(E, E+\Delta E)$ is given by

$$f(x) = \sum_{y=E}^{E+\Delta E} M(x,y)$$

where y is the channel number corresponding to the energy E. In this section, a spectrum '*gated*' by a γ-ray implies such a projection. It must be made clear that the γ-γ sorts here are slightly different from the conventional γ-γ sort in so far as all the γ-rays come in coincidence with a signal from the neutron wall i.e. where the projection of the whole γ-γ matrix in a conventional γ-γ sort is the *singles* spectrum, in this case, it is a *ningles* spectrum (see §3.2).

The coincidence spectra discussed below were obtained by gating on the γ-ray of interest and subtracting off a background spectrum gated on the neighbouring background (over the same number of channels). A constant level was usually

added before subtraction to avoid negative counts in the subtracted spectrum. In each figure, the true zero is indicated on the right-hand axis.

The γ-γ data were used either to decide on or confirm the many channel assignments made using the neutron gated data for the γ-ray lines observed.

4.3.3.1 ^{48}Cr Band Structure

All the known levels of ^{48}Cr that have been populated in previous studies [KUT73, HAA75, EKS79, HAN79] by HI-evaporation reactions are shown in fig. 4.8 [EKS79,HAN79]. The coincidence spectra from gates on the various transitions obtained in this work are shown in figs. 4.9 (a) – (h).

a) Ground State Band (gsb)

The coincidence spectra of transitions in the main gsb are shown in fig. 4.9 parts (a) to (e) and table 4.2 lists the transitions involved.

E_γ/keV	Transition	Figure
751	$2^+ \rightarrow 0^+$	4.9(a)
1106	$4^+ \rightarrow 2^+$	4.9(b)
1586	$6^+ \rightarrow 4^+$	4.9(c)
1743	$8^+ \rightarrow 6^+$	4.9(d)
1875	$(10^+) \rightarrow 8^+$	4.9(e)

Table 4.2 : List of transitions shown in fig. 4.9.

Figs. 4.9(a) and (b) are the coincidence spectra of the 751 and 1106 keV transitions respectively and show these two γ-rays in coincidence with one another and with the other transitions in ^{48}Cr. The level at 3532 keV is isomeric with a lifetime of 3.6±1 ns [EKS79] and, indeed, the 531 and 1675 keV lines show little of the Doppler broadening ($\Delta E/E \approx 0.006$) seen in the other lines. The 1347 keV

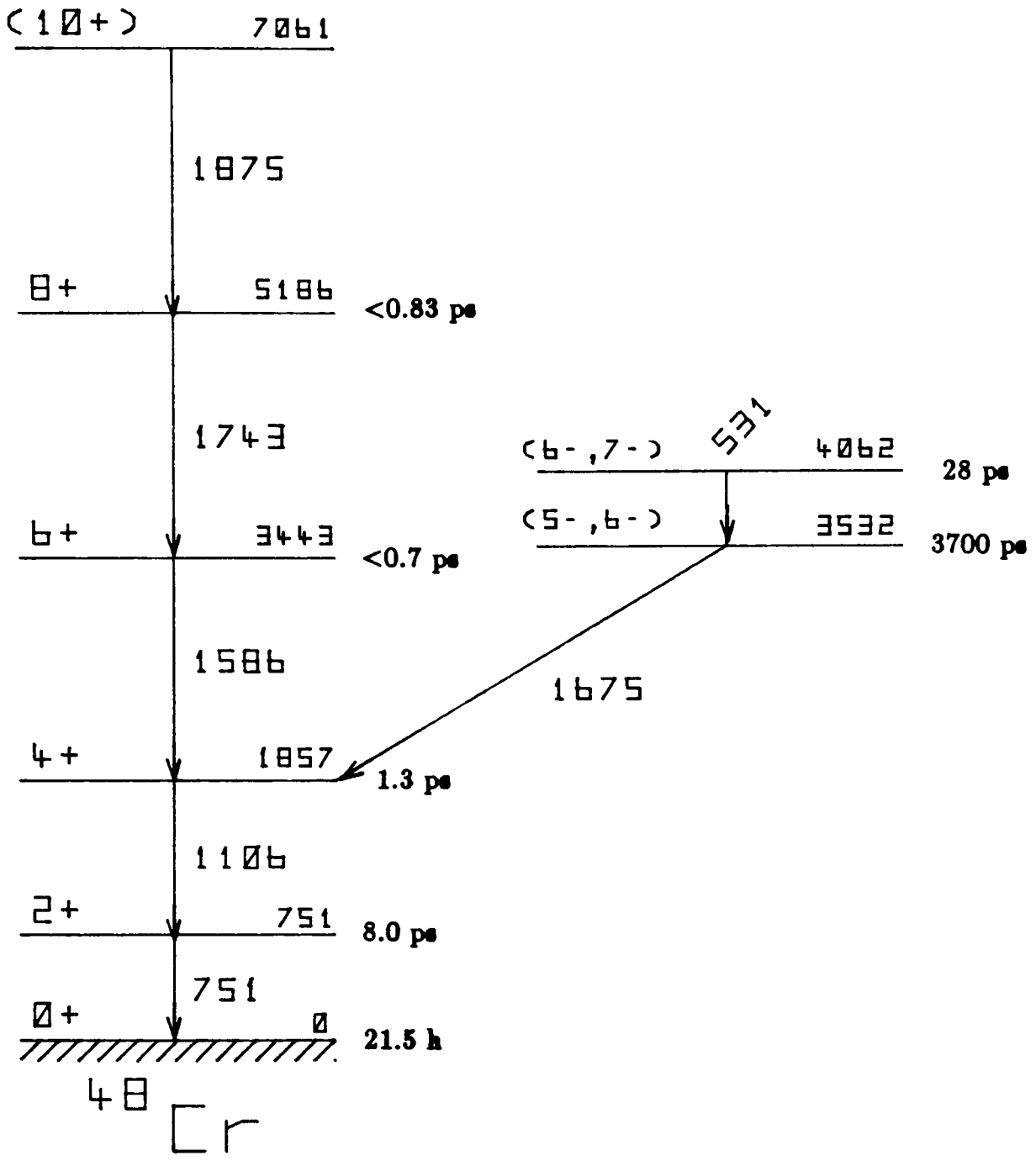


Fig.4.8 : ^{48}Cr level scheme. All the energies quoted are in keV. Certain levels have their half-lives included as well and these come from Nucl. Data Sheets **45** (1985). The spins and parities of the 3532 and 4062 keV levels come from [EKS79] and [HAN79] who quote values of $(5^-,6^-)$ and $(6^-,7^-)$ respectively for the two levels.

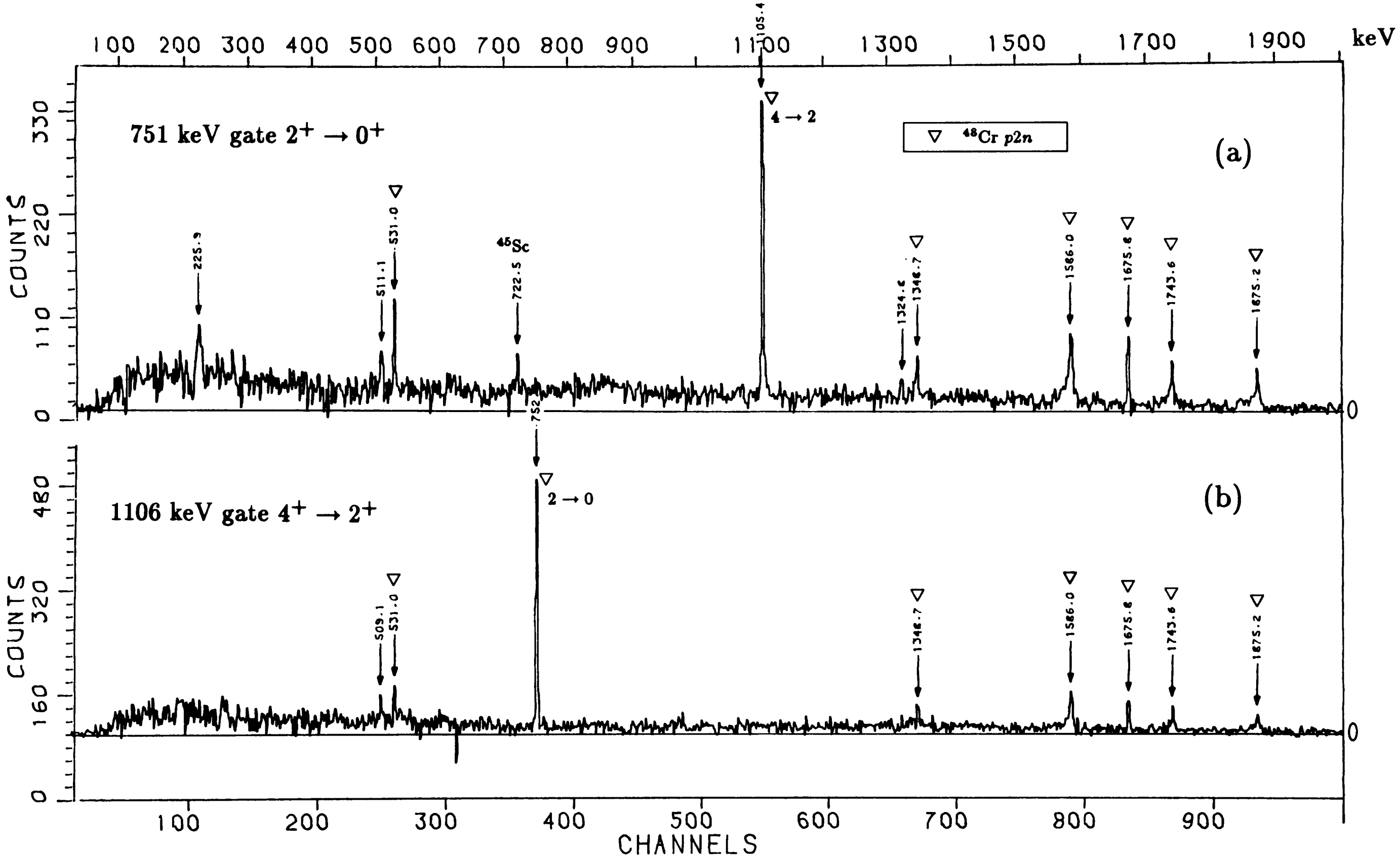


Fig.4.9 : Background subtracted coincidence spectra from the γ-γ data. The plots correspond to the following γ-rays : (a) 751 keV (b) 1106 keV (c) 1586 keV (d) 1743 keV (e) 1875 keV (f) 1347 keV (g) 530 keV and (h) 1674 keV. A constant level was added to show the oversubtraction but the true zero is indicated.

line in (a) arises from coincidence with a 752 keV γ-ray from ^{45}Sc [ROG69]. The 1324 keV γ-ray peak is a possible transition in ^{48}Cr. The unsubtracted coincidence spectrum of this line shows the presence of the 751 and 1106 keV lines but no peaks are observed in the corresponding subtracted spectrum. The evidence is weak and this assignment is tentative.

Figs. 4.9(c), (d) and (e) show the coincidence spectra of the 1586, 1743 and 1875 keV γ-rays. The γ-rays seen here are in agreement with the ^{48}Cr level scheme (fig. 4.8). The 751 and 1106 keV lines are prominent features while the 531 and 1675 keV peaks do not appear at all as these two γ-rays feed the main cascade at the 1857 keV (4^+) level and so will not be in coincidence with the other γ-rays of the main band above the 4^+ level. Again, the 1347 keV peak comes up strongly in these spectra. In the 1586 keV coincidence spectrum, two other transitions, 870 and 1237 keV are observed. These come from the ^{45}Sc ($\alpha 2p$) channel which produces a γ-ray (1586.2 keV)† that is very close in energy to the ^{48}Cr transition used as the gate.

b) Side Band

The two states in this side band were independently discovered by Hansen *et al* [HAN79] and Ekström *et al* [EKS79]. Although they disagreed on the actual spin of the states (see figure caption of fig. 4.8), they both agreed on the (negative) parity of these levels. The coincidence spectra gated by the γ-ray transitions (530 and 1674 keV) from these two states are shown in fig.4.9(g) and (h). The statistics of these spectra are poor but they support the placements of these γ-rays by the other workers. No new transitions are observed to allow us to extend this band upwards. A 1343 keV transition, from a tentative level at 4875 keV to the 3532 keV level, proposed by Hansen *et al* [HAN79], is not seen. With the higher energy and larger angular momentum brought into compound nucleus in the present reaction

† Nucl. Data Sheets **40**, 149 (1983).

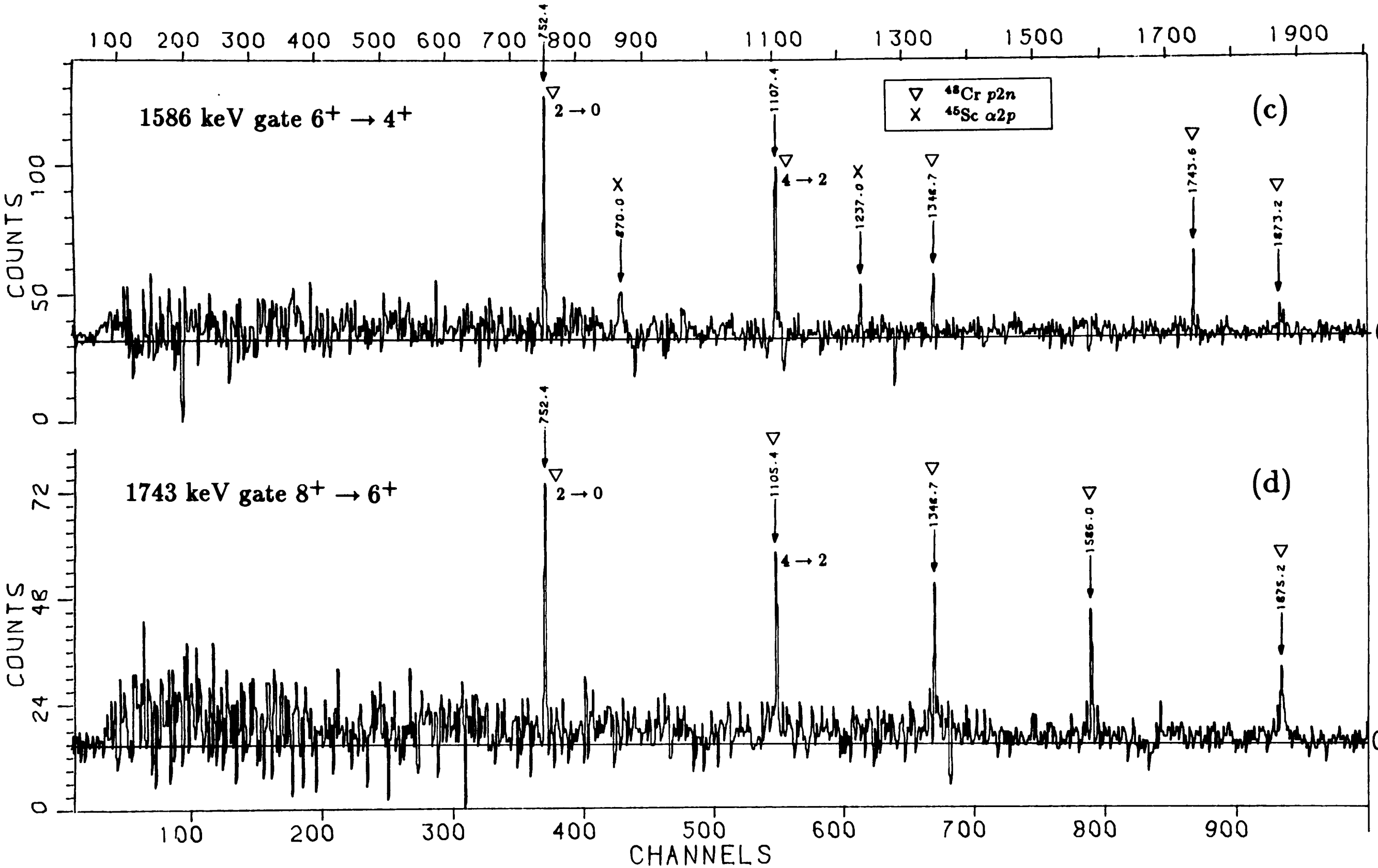


Fig.4.9 : Background subtracted coincidence spectra from the γ-γ data. The plots correspond to the following γ-rays : (a) 751 keV (b) 1106 keV (c) 1586 keV (d) 1743 keV (e) 1875 keV (f) 1347 keV (g) 530 keV and (h) 1674 keV. A constant level was added to show the oversubtraction but the true zero is indicated.

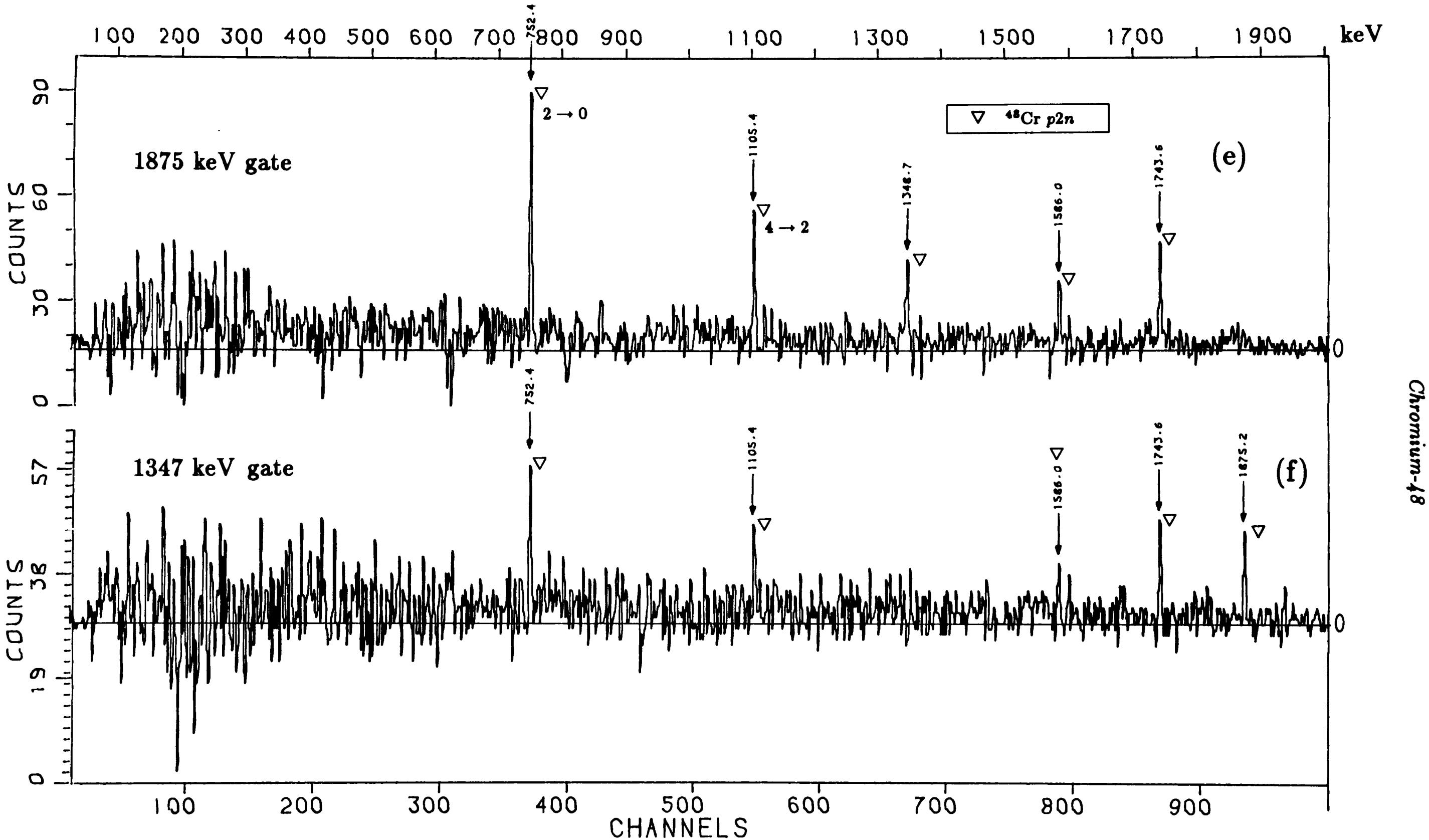


Fig.4.9 : Background subtracted coincidence spectra from the γ-γ data. The plots correspond to the following γ-rays : (a) 751 keV (b) 1106 keV (c) 1586 keV (d) 1743 keV (e) 1875 keV (f) 1347 keV (g) 530 keV and (h) 1674 keV. A constant level was added to show the oversubtraction but the true zero is indicated.

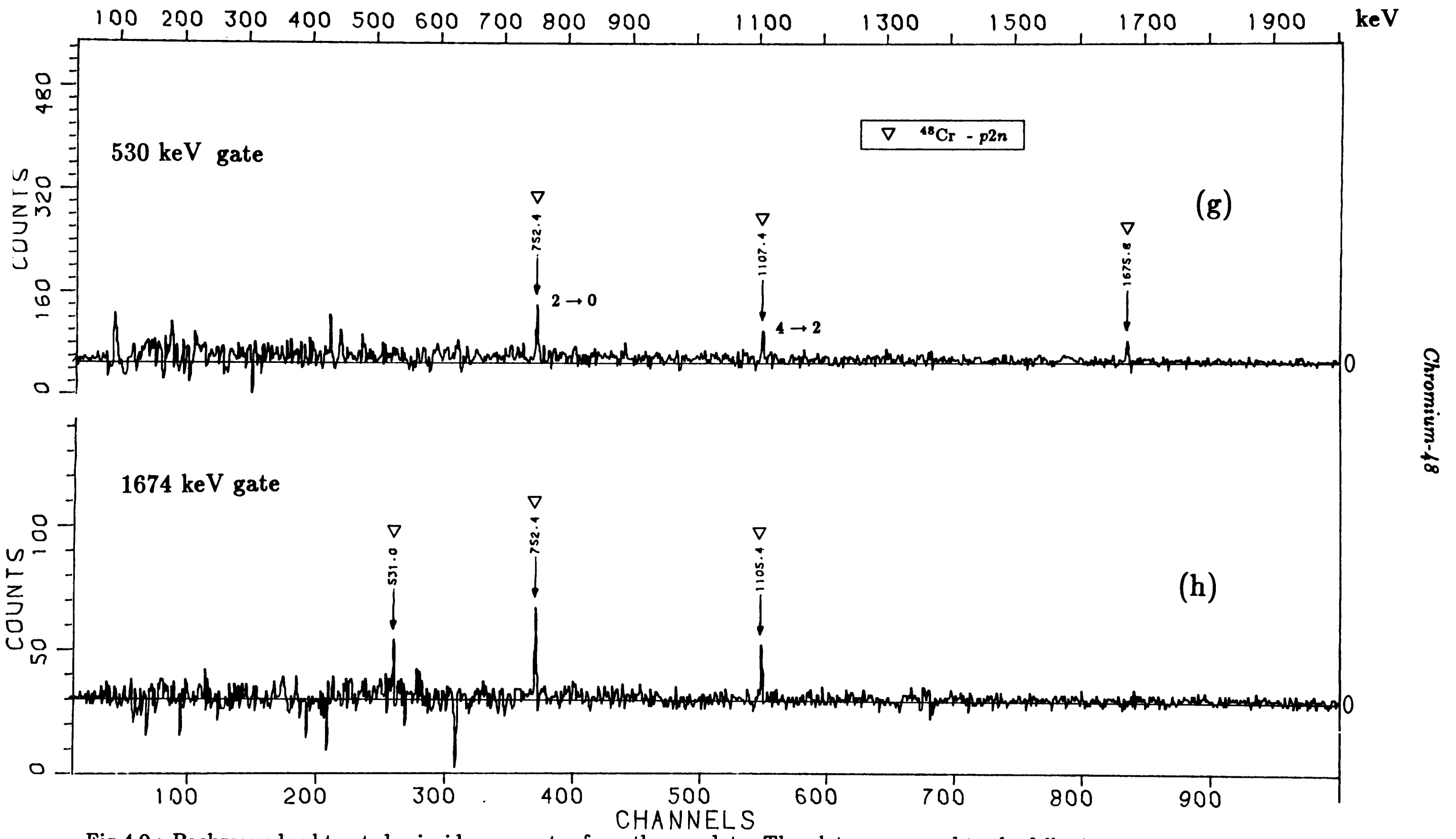


Fig.4.9 : Background subtracted coincidence spectra from the γ-γ data. The plots correspond to the following γ-rays : (a) 751 keV (b) 1106 keV (c) 1586 keV (d) 1743 keV (e) 1875 keV (f) 1347 keV (g) 530 keV and (h) 1674 keV. A constant level was added to show the oversubtraction but the true zero is indicated.

(see Table 2.2), we would have expected to see this transition and its noticeable absence suggests a mis-identification of this γ-ray by Hansen *et al.*

c) A New Transition in ^{48}Cr

A 1347 keV γ-ray is seen in coincidence with all of the known transitions in the main band of ^{48}Cr but does not appear in coincidence with either the 530 or the 1674 keV lines. Fig. 4.10 shows the sum of the coincidence spectra from the first 5 transitions of the main band. The lines are sharp and well-defined and the figure shows that, apart from the 1347 keV line, no new line is seen. The coincidence spectrum of the 1347 keV line (fig. 4.9(f)) again shows this γ-ray to be in coincidence with all the other γ-rays in the gsb.

4.3.3.2 Background Lines

Here, we present the coincidence spectra of the 88 and 271 keV γ-ray lines. These γ-rays were observed in the neutron gated spectra and were identified as γ-rays from channels other than the $p2n$ channel making ^{48}Cr. This is confirmed by the γ-γ coincidence spectra.

a) 88 keV γ-ray — Figs.4.11

The γ-γ data show this γ-ray to be in coincidence with the 1149 keV γ-ray from $^{47}_{23}$V ($2p2n$) which supports the assignment given in §4.3.2(a) that this γ-ray comes from ^{47}V. The 112 keV peak is a ^{48}V ($2pn$) line and is the result of random breakthrough due to the poor timing in the electronics for these low energy γ-rays. A study of the 112 keV coincidence spectrum as well as the coincidence spectra of lines in the 112 keV coincidence spectrum shows no reciprocal ^{47}V lines appearing in these spectra and so reinforces this claim.

b) 271 keV γ-ray — Figs.4.12

The 271 keV coincidence spectrum shows a large collection of $^{49}_{24}$Cr (pn) lines which supports the proposal in §4.3.2(a) that this γ-ray originates from ^{49}Cr. This

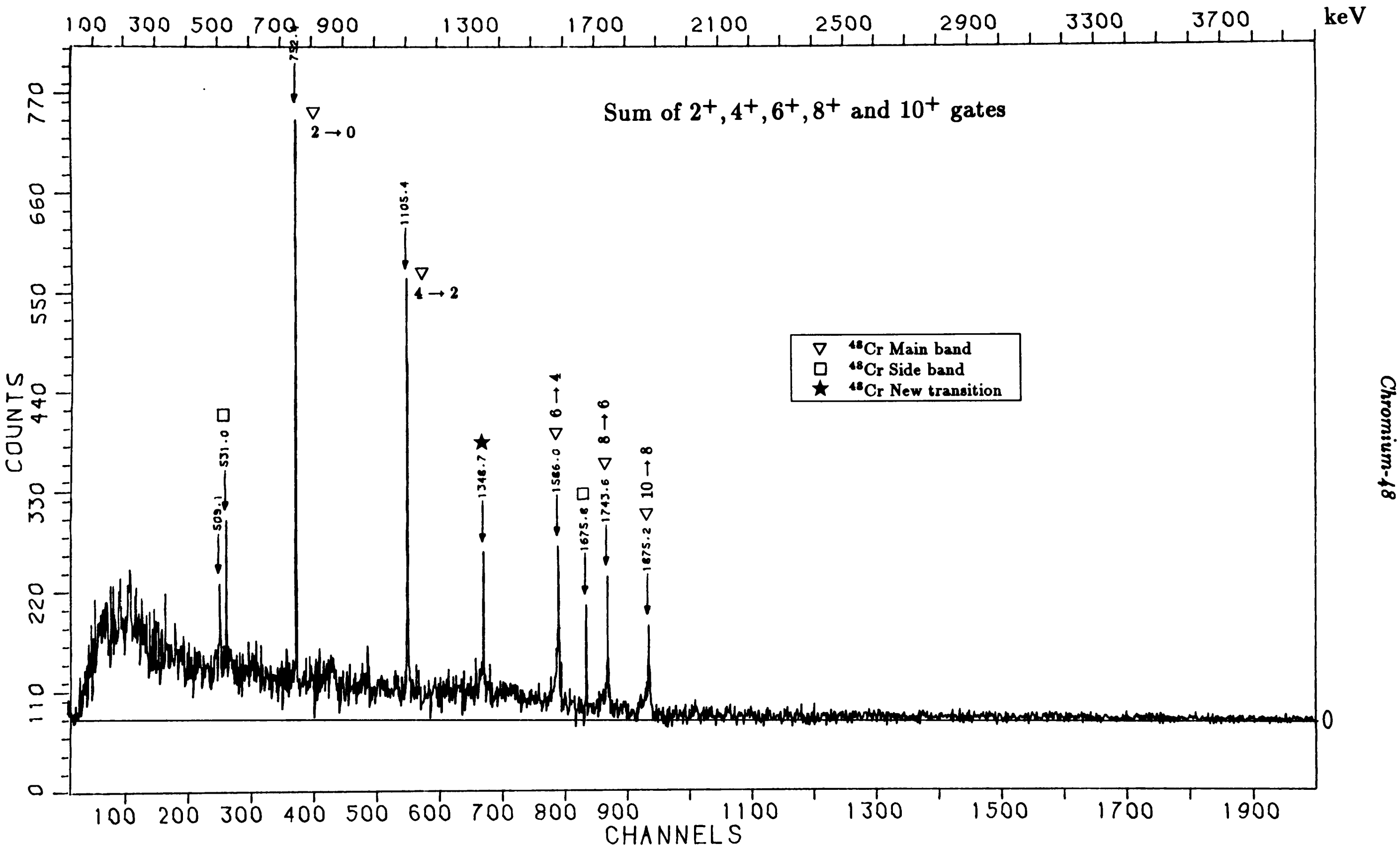


Fig.4.10 : The sum of the coincidence spectra of the γ-rays from the first 5 transitions in the gsb of ^{48}Cr.

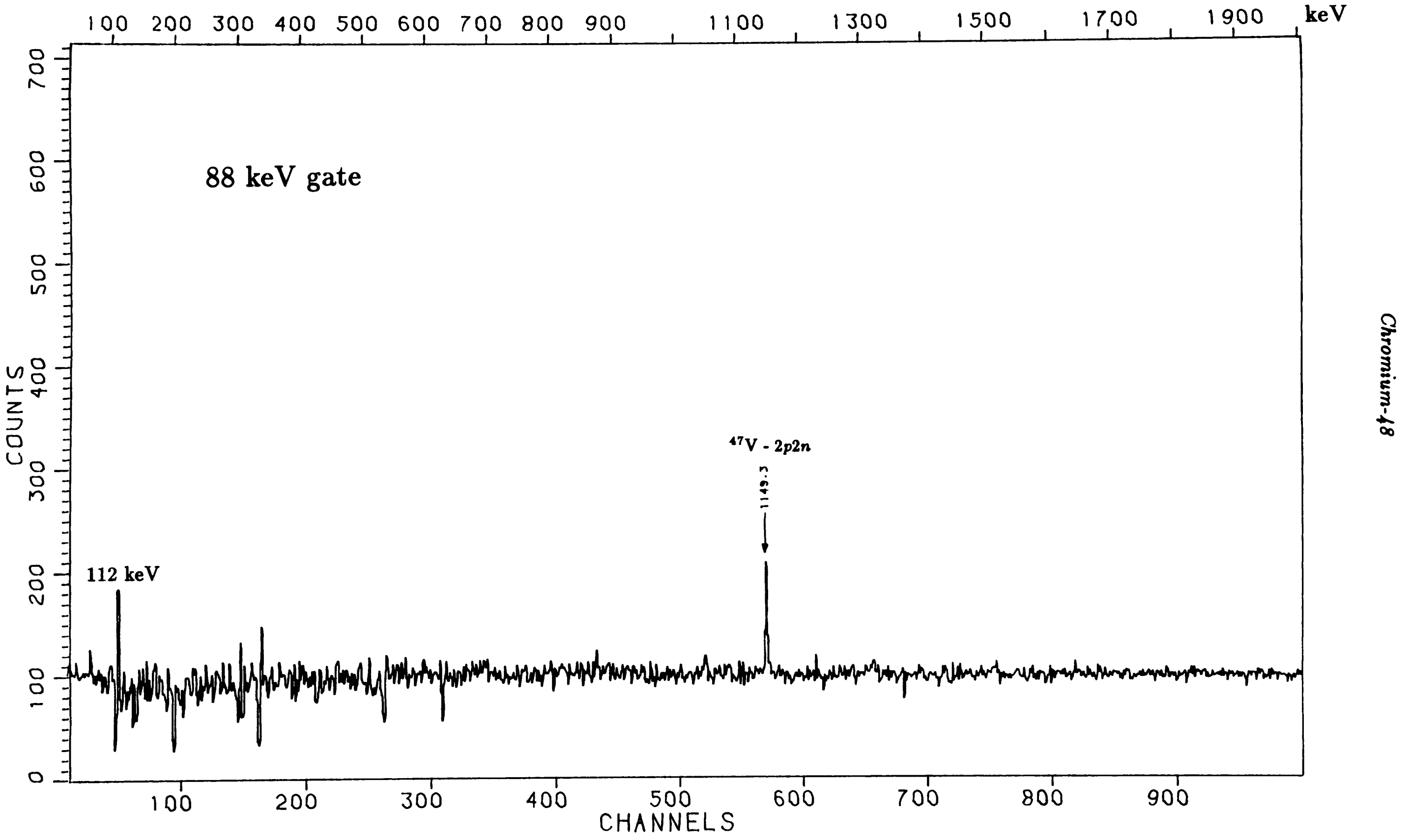


Fig.4.11 : Coincidence spectrum gated on the 88 keV line.

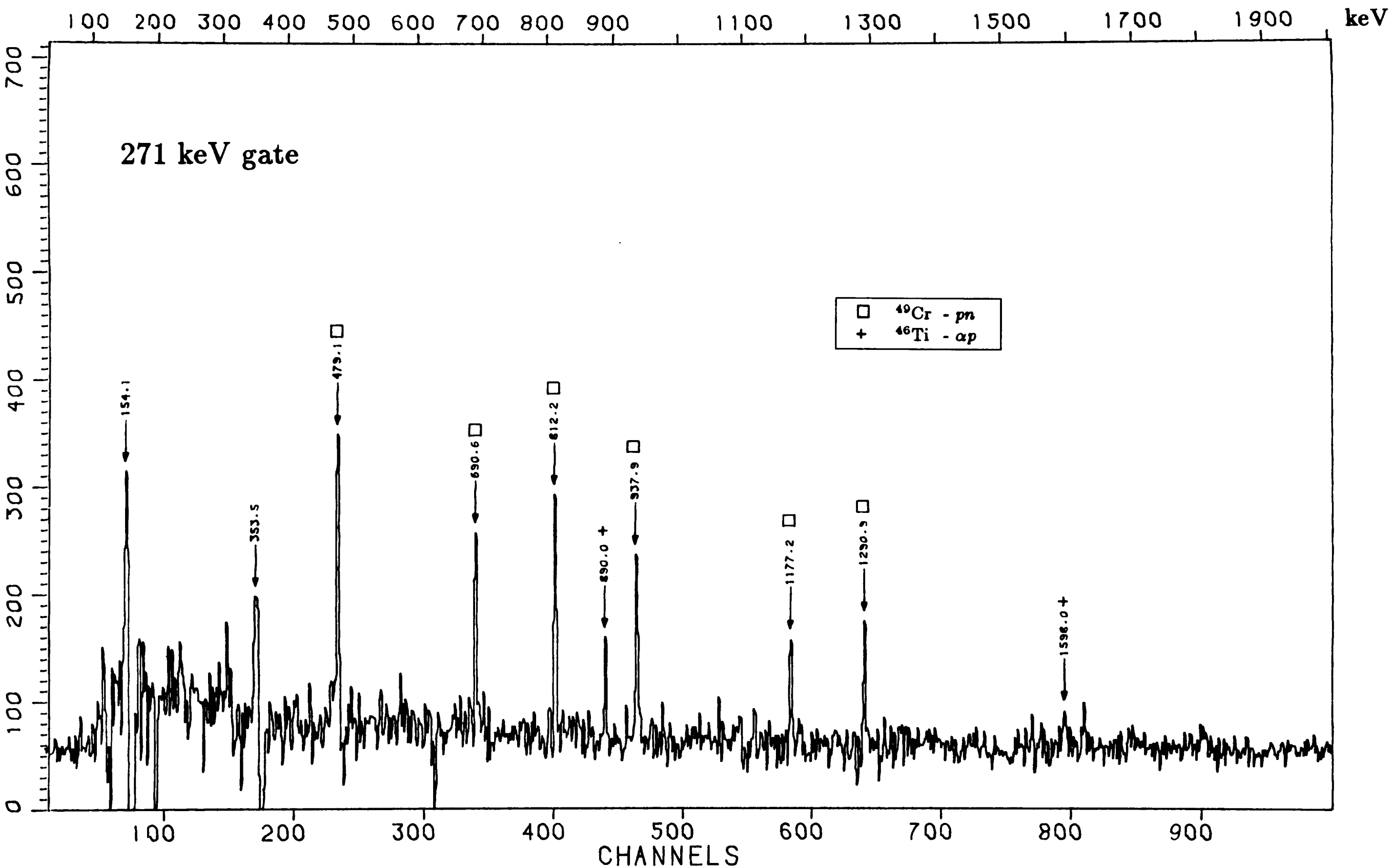


Fig.4.12 : Coincidence spectrum gated on the 271 kev line.

γ-ray is also present as a high-lying transition in $^{46}_{22}$Ti (αp) [FOR76] and we see lines from ^{46}Ti appearing in this spectrum. However, its presence in the $2n$-gated spectrum is entirely due to the breakthrough of the pn channel because (a) a 5 particle channel† is unlikely at this energy and (b) the intensities of the other ^{46}Ti lines were found to be significantly reduced by neutron gating (fig. 4.4).

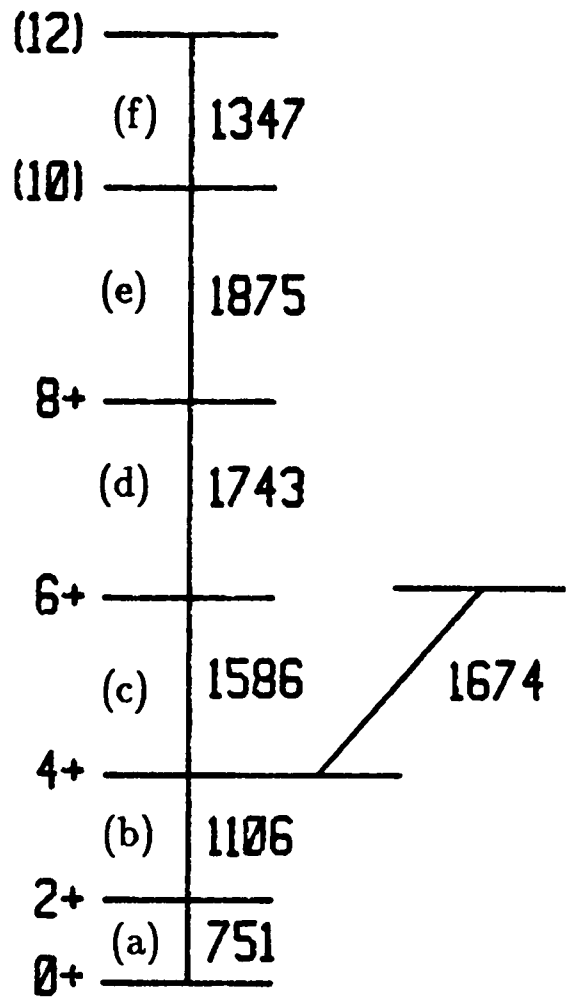
4.3.3.3 γ-ray Intensities

The intensities of the γ-rays in the γ-γ coincidence data were measured and corrected for the Ge(Li) γ-ray detection efficiency. The intensities of the γ peaks in figs. 4.9(a) – (f) are shown in figs. 4.13(a) – (f) respectively. In (a) and (b), the significantly larger intensities of the 751 and 1106 keV peaks are consistent with the side feeding of the 1857 keV level by the 3532 keV state. As we move up the band, the intensities of the γ-ray transitions decrease. This is consistent with the statistical picture of compound nuclear de-excitation [HAL68] where members of the gsb, as well as being fed via the cascade through the band itself, are populated by statistical γ-rays. However, the error bars for the intensities gated on the higher transitions (i.e. parts (d) to (f)) are too large for such a trend to be confirmed.

4.3.3.4 n-γ-γ Coincidence Spectra

The data were also sorted into a 2d n-γ-γ array where only events in coincidence with at least one neutron were accepted. This served to remove the charged-particle-only γ-rays. Fig. 4.14 (a) to (h) show the coincidence spectra for γ-ray transitions in the gsb. We see that the peaks in the coincidence spectra shown in §4.3.3.1 have not been removed by the neutron gating. The statistics are poorer after the n-gating but the 1347 keV transition is still quite evident in the plots. In the 1586 keV coincidence spectrum (part (c)), the $^{45}_{21}$Sc ($\alpha 2p$) lines observed before have now

† if we consider the $3p2n$ channel for ^{46}Ti. The αp channel for ^{46}Ti would have been removed by the n-gating.



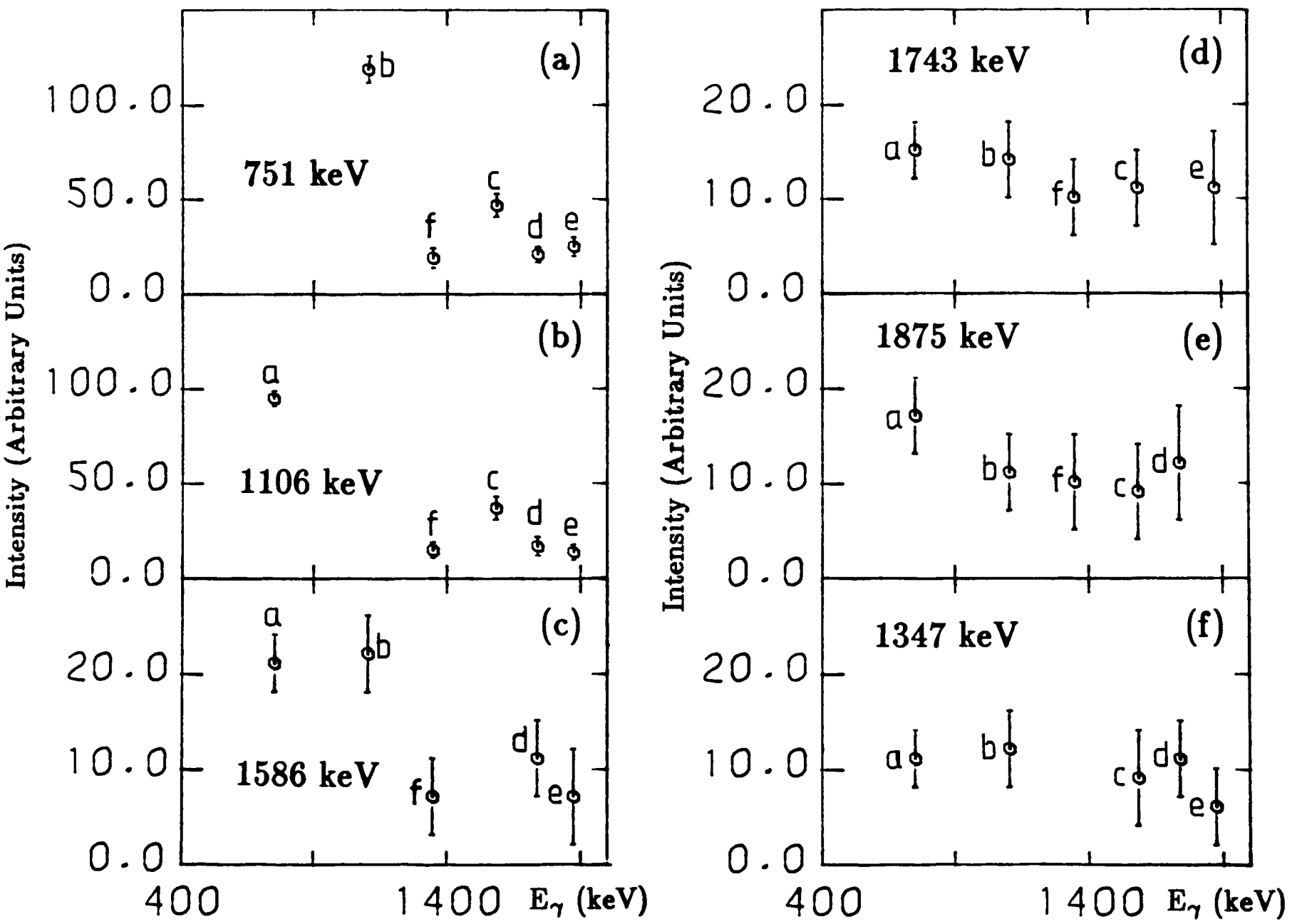


Fig.4.13 : Intensities of the peaks in the coincidence spectra of the gsb. The energy quoted in each figure is the energy gate for the respective coincidence spectrum and the schematic level diagram shows the position of the γ-ray in the band.

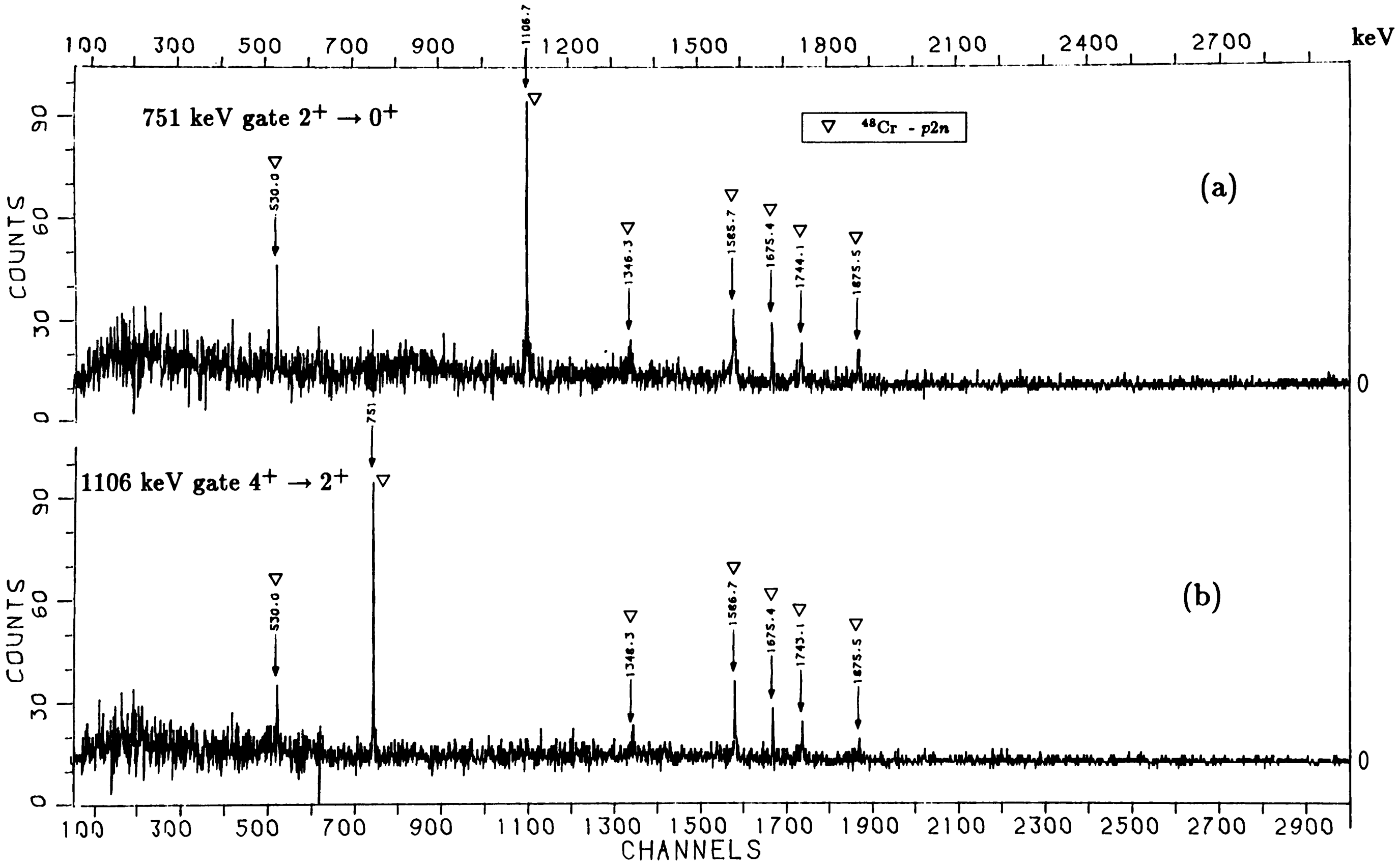


Fig.4.14 : Background subtracted coincidence spectra from the n-γ-γ data. The following plots correspond to the following γ-rays : (a) 751 keV (b) 1106 keV (c) 1586 keV (d) 1743 keV (e) 1875 keV (f) 1347 keV (g) 530 keV and (h) 1674 keV. A constant level was added to show the oversubtraction but the true zero is indicated.

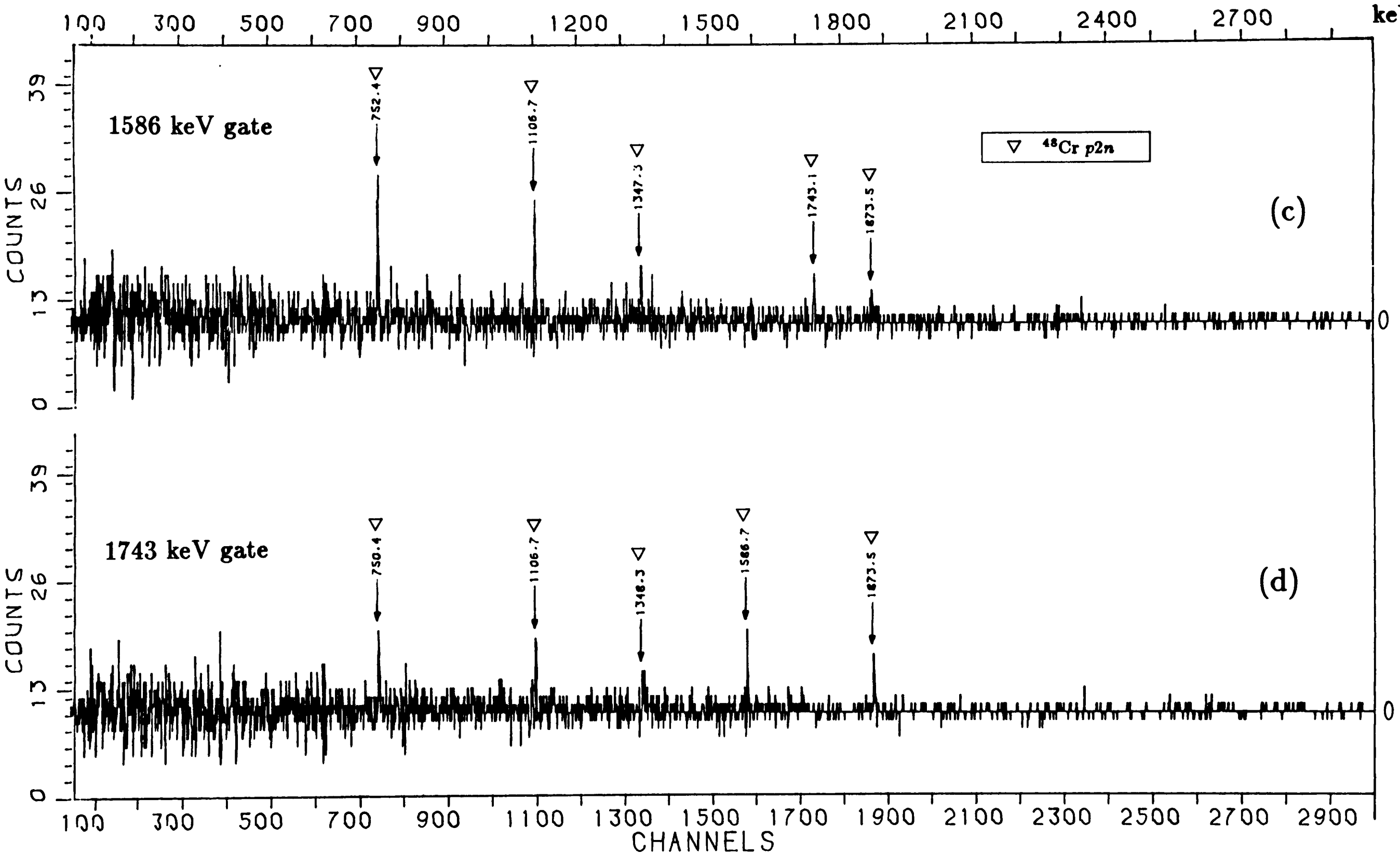


Fig.4.14 : Background subtracted coincidence spectra from the n-γ-γ data. The following plots correspond to the following γ-rays : (a) 751 keV (b) 1106 keV (c) 1586 keV (d) 1743 keV (e) 1875 keV (f) 1347 keV (g) 530 keV and (h) 1674 keV. A constant level was added to show the oversubtraction but the true zero is indicated.

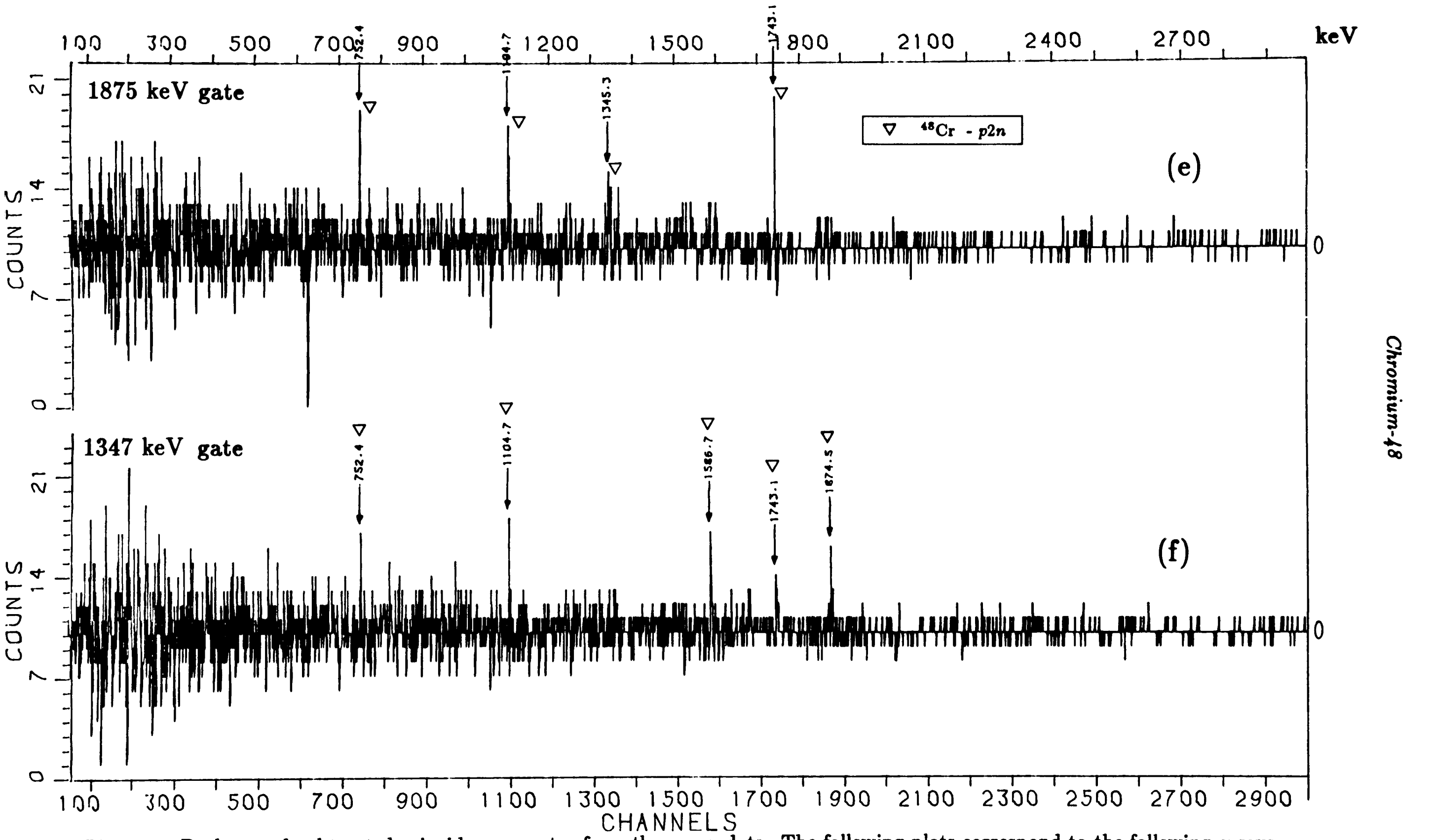


Fig.4.14 : Background subtracted coincidence spectra from the n-γ-γ data. The following plots correspond to the following γ-rays : (a) 751 keV (b) 1106 keV (c) 1586 keV (d) 1743 keV (e) 1875 keV (f) 1347 keV (g) 530 keV and (h) 1674 keV. A constant level was added to show the oversubtraction but the true zero is indicated.

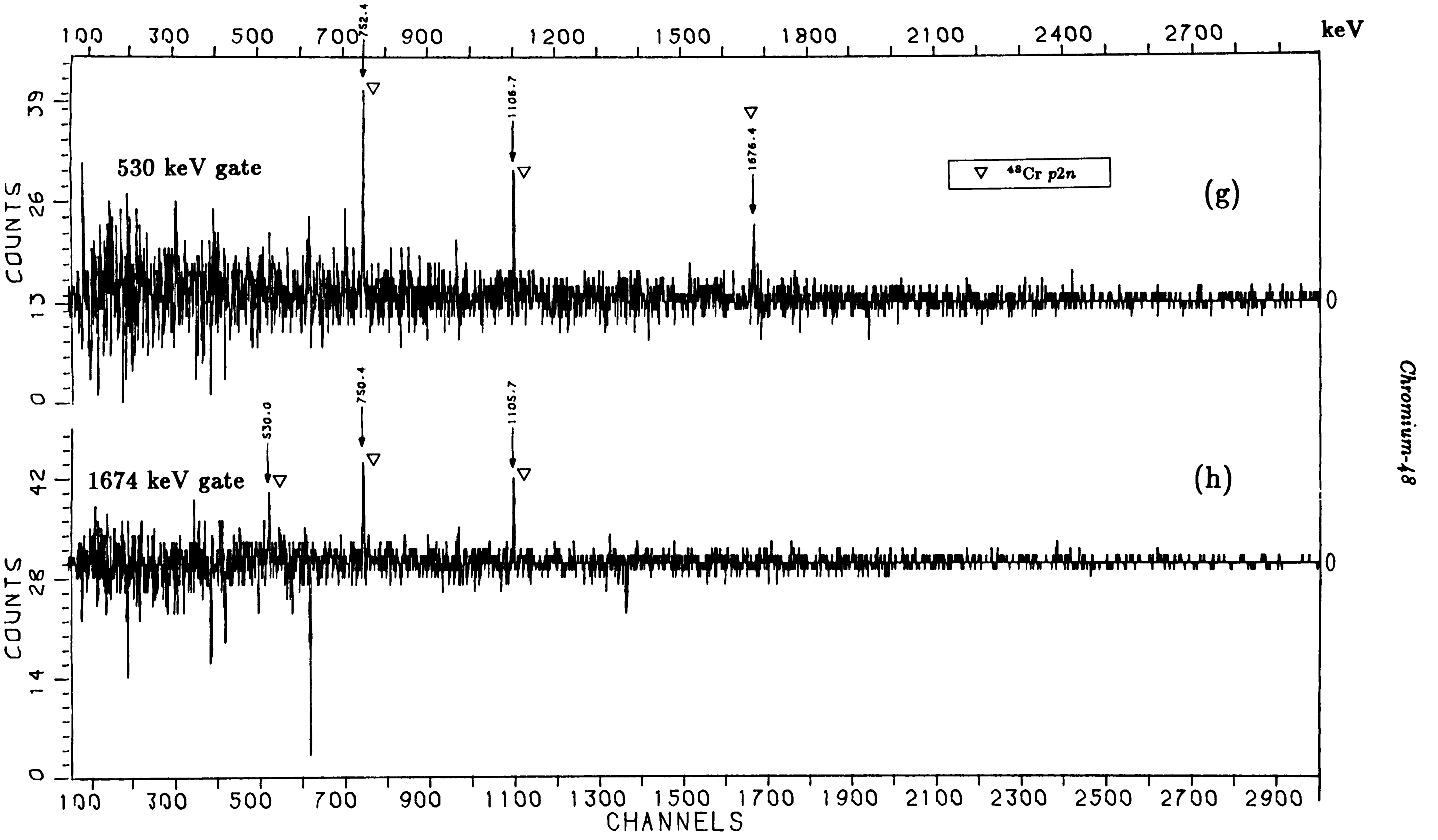


Fig.4.14 : Background subtracted coincidence spectra from the n-γ-γ data. The following plots correspond to the following γ-rays : (a) 751 keV (b) 1106 keV (c) 1586 keV (d) 1743 keV (e) 1875 keV (f) 1347 keV (g) 530 keV and (h) 1674 keV. A constant level was added to show the oversubtraction but the true zero is indicated.

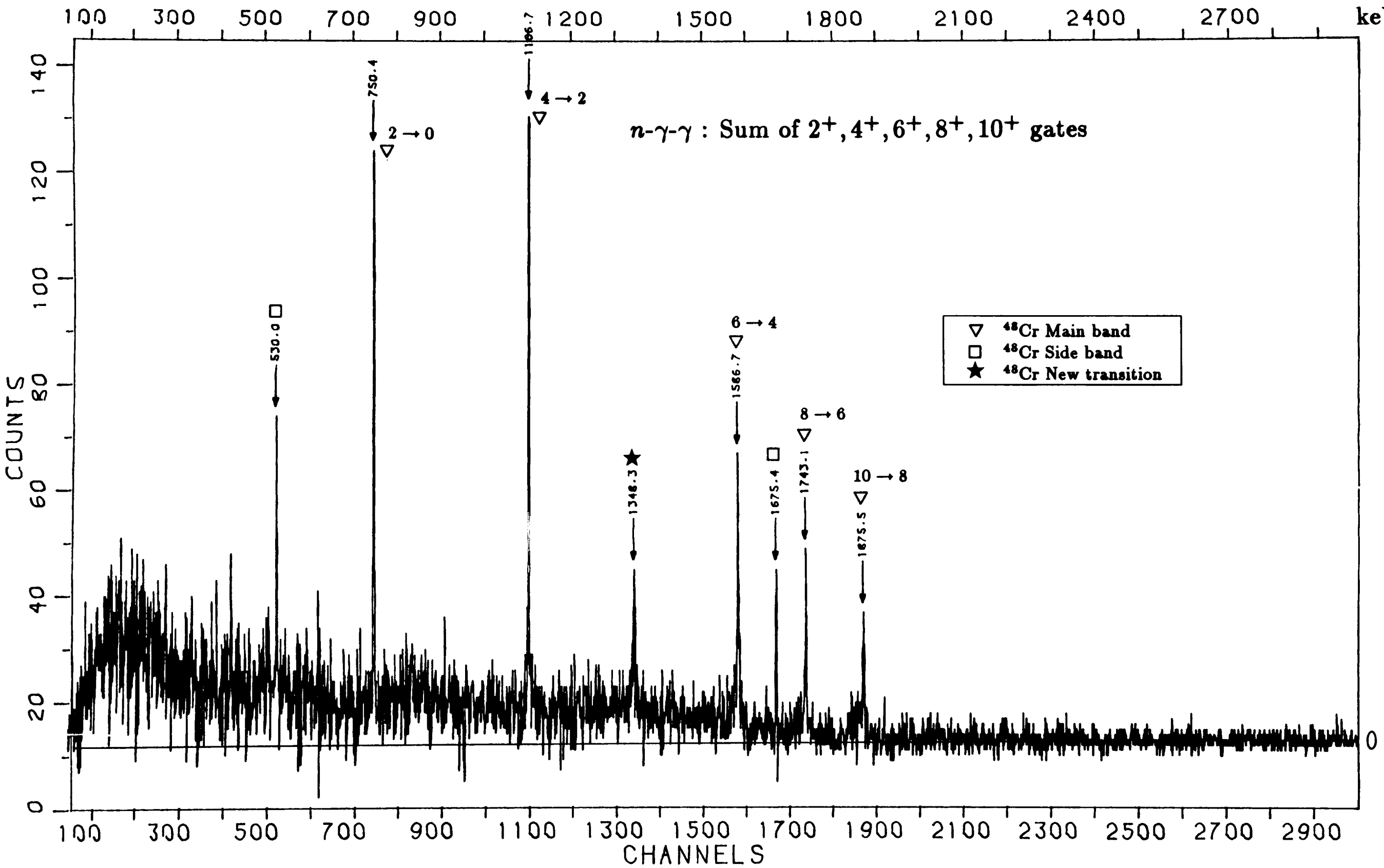


Fig.4.15 : Sum of the n-γ-γ coincidence spectra of the γ-rays from the first 5 transitions of the gsb in ^{48}Cr.

been removed by the n-gate. The sum of the coincidence spectra of the gsb is given in fig. 4.15 and again shows that, apart from the 1347 keV line, no new γ-ray lines are observed.

4.3.4 Conclusion

The level scheme in fig. 4.8 has been obtained through two independent sources [EKS79,HAN79] and is in agreement with the present data. As the 1347 keV line is seen in coincidence with all the γ-rays of the main band, the placement of this γ-ray above the 7061 keV level seems reasonable. No angular distribution data were taken and so no spin assignments could be made. The 7061 keV level, however, has had a spin and parity of 10^+ tentatively assigned to it by Ekström *et al* [EKS79] and Hansen *et al* [HAN79] where they derived this assignment from the excitation function of the line.

If the E2 cascade is assumed to continue past the 7061 keV level, then a 12^+ spin-parity assignment can be made to this new level at 8408 keV. This would explain the absence of this γ-ray in previous work, where the maximum angular momentum was approximately $11\hbar$ (Table 2.2).

In summary, this investigation has verified the level scheme proposed by previous workers as well as establishing a new level at 8408 keV in ^{48}Cr. The arguments are as follows:-

- n-n-γ data support a $2n$ related evaporation channel.
- γ-γ and n-γ-γ data show the γ-ray in coincidence with all the known γ-rays in the main gsb.
- If a spin of 12 is assumed for this state, then a consideration of the incident angular momenta of previous work explains its absence there.

The experiment has also shown that separation of $2n$-related from $1n$-related channels is possible with the neutron wall. The ratios of the peaks in the $2n$ spectrum to that in the $1n$ spectrum show that in the $2n$-gated spectrum, true $2n$

events are enhanced by a factor of 4 over the $1n$ breakthroughs. A similar separation can be expected for the ^{64}Ge experiment where the neutron energies (4.3 MeV†) are not too dissimilar from the ^{48}Cr neutron energies (3.9 MeV†).

4.4 Discussion

Our experiment has yielded a new state in ^{48}Cr. From the γ-γ data, the new γ-ray line observed was shown to connect this state with a known 7.06 MeV state hence making this transition part of the ground state band. No other transitions were observed. This nucleus has been compared with predictions from shell model calculations in the $f_{7/2}$ shell [HAA75, KUT73, EKS79]. Fig. 4.16 shows the experimental levels next to the shell model predictions from [KUT78]. The shell model calculation was carried out in the $f_{7/2}$ shell and the residual two-body interaction obtained by fits to the experimental spectrum of $^{42}_{21}$Sc. The side band consisting of the 3532 and 4062 keV levels are not considered here as these have been assigned as negative parity states by [HAN79] and [EKS79] (although they disagree on the spin assignments) and the model space does not provide states of this parity. The spin assignment of 10^+ to the 7061 keV level is still uncertain. If we consider the shell model predictions, they show that most of the transition strength goes through the even spin states and so we would expect an even spin for the new 8408 keV state. Let us assume that the spins and parities of the levels at 7061 and 8408 keV are 10^+ and 12^+ respectively. We can then plot the energies of the states against J(J+1) as shown in fig.4.17. Fig. 4.17 also shows similar plots for two neighbouring nuclei (^{46}Ti and ^{50}Cr). The shell model states using the ^{42}Sc interaction are shown in circles (o) in the plots and show that for ^{46}Ti and ^{50}Cr, the agreement with the

† calculated for the laboratory frame using n energies predicted by CASCADE and simple kinematics.

experimental states is much better than in ^{48}Cr. This can, perhaps, be understood if we note that ^{48}Cr has the lowest 2_1^+ state in the $f_{7/2}$ region [KUT73] and is therefore expected to show the largest degree of collectivity in this region. The truncated *fp* shell model space (to just the $f_{7/2}$ shell) may not be sufficient to account for this collectivity and the other half of the shell ($p_{3/2}$, $f_{5/2}$ and $p_{1/2}$) should be included to achieve the necessary configurations to do so. Fig. 4.17(d) shows the shell model states shifted up in energy to align the shell model and experimental 12^+ states. If the model space is extended to include the lower spin members of the *fp* shell, the configuration mixing will lower the low spin shell model states and we see from the figure that this will serve to reduce the gaps between the shell model and experimental levels. Nevertheless, the truncated space has worked remarkably well in predicting the experimental levels in this region.

We should also note that the absence of states above the 12^+ level may be explained by the 'up-bend' predicted by the shell model for the 12→14 transition. The efficiency of the Ge(Li) detectors would have been lower for these high energy γ-rays (see fig. 5.8) and so the intensity of the transition may be too weak to be observed. Furthermore, CASCADE calculations predict the cross-sections for populating the 14^+ and 16^+ states by our reaction to be very small (fig. 2.9).

In this experiment, only one more level has been added to our knowledge of ^{48}Cr and this precludes any major conclusions to be drawn. An assumption of 12^+ for the spin and parity of this state shows the shell model prediction in a favourable light. However, the transition rates of the higher lying transitions are not known and these should be measured to obtain a more reliable comparison with theory. We have not seen any extensions to the side band and a search with a more efficient γ-ray detection system (e.g. TESSA [TWI83]) may bring out more transitions in this side band and perhaps observe other side bands as well.

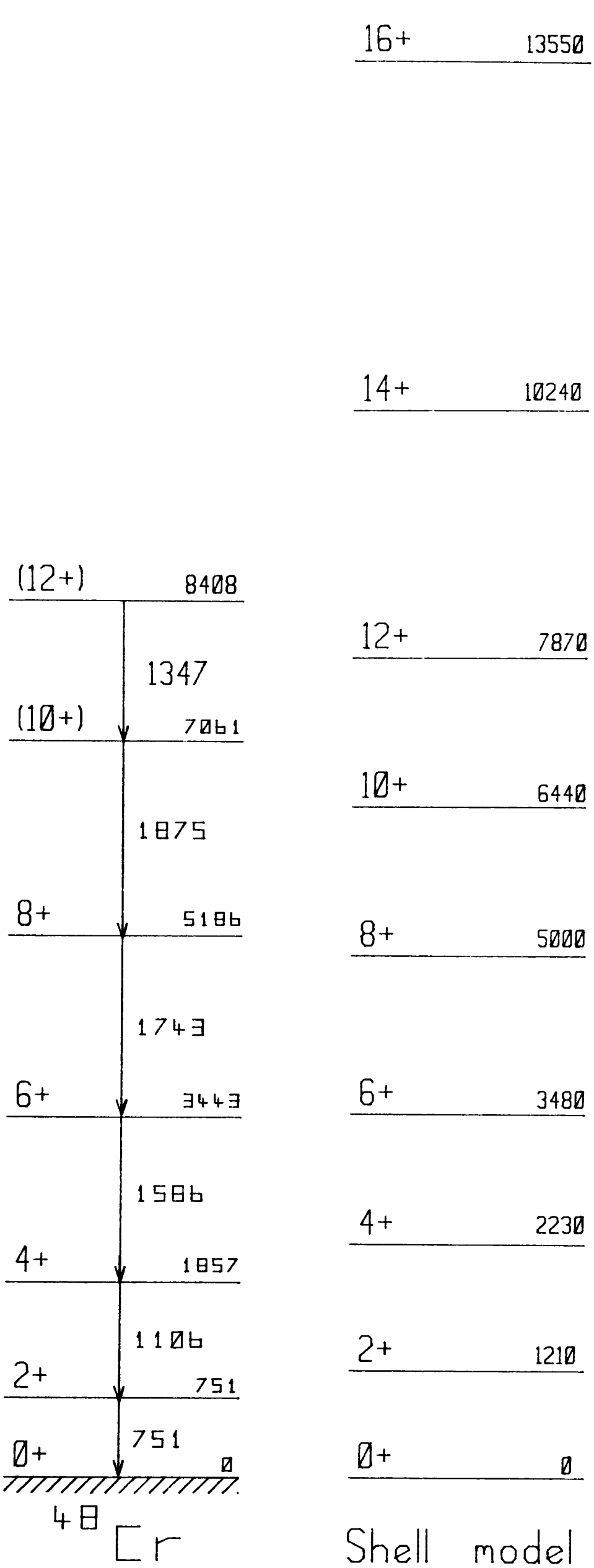


Fig.4.16 : Experimental levels in ^{48}Cr compared with shell model predictions from [KUT78].

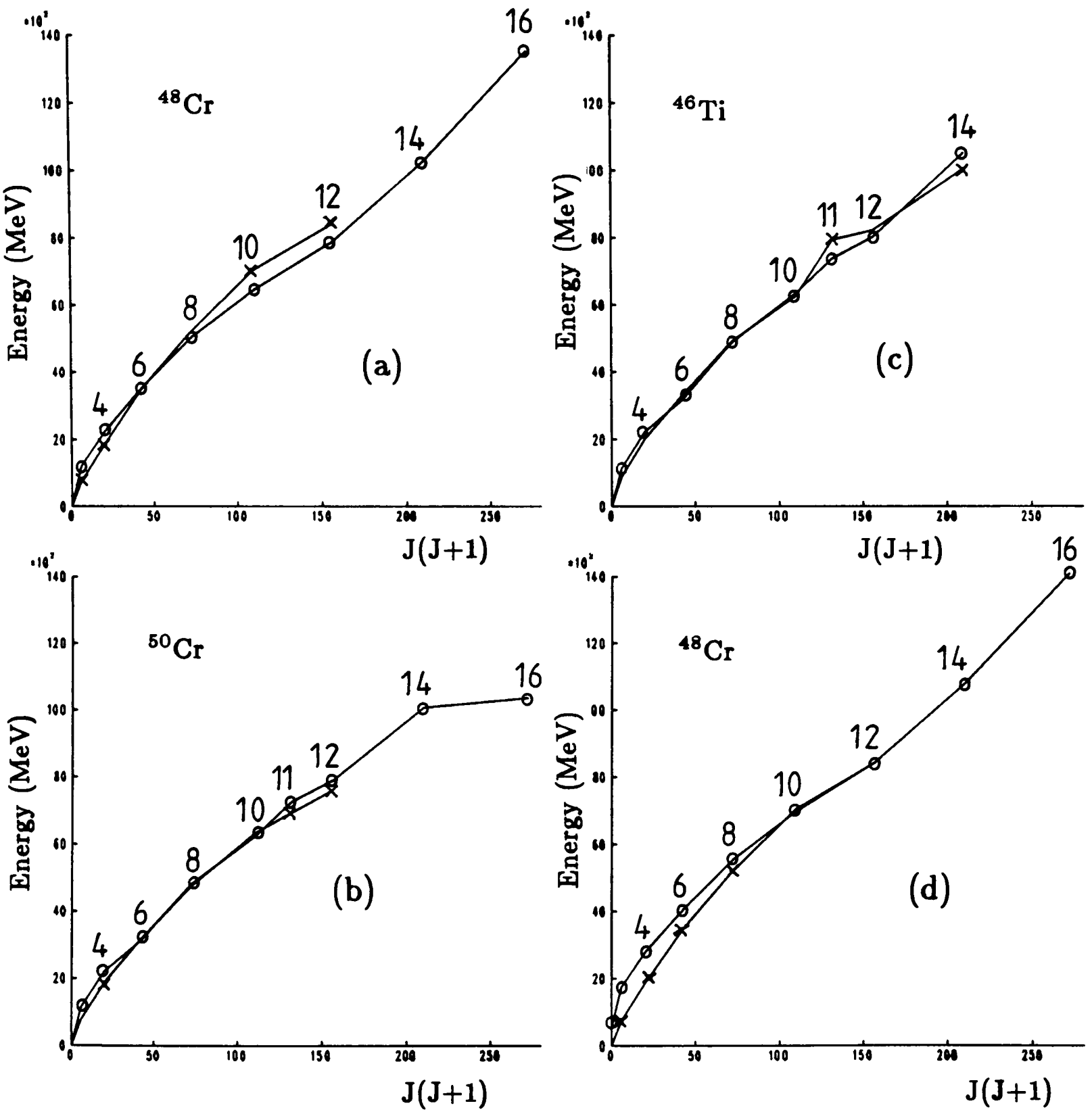


Fig.4.17 : Energy of states in (a) ^{48}Cr, (b) ^{50}Cr and (c) ^{46}Ti plotted against J(J+1). (d) shows the shell model states in (a) shifted up in energy to align the two 12^+ states.

5

CHAPTER 5

Germanium-64

"With a name like yours, you might be any shape, almost"

5.1 Introduction

The equilibrium shape of a nucleus depends on the interplay between shell effects and the liquid drop energy which serves to dampen the shape-driving effects of the former. In self-conjugate nuclei, as the neutrons and protons are in phase, we expect these shell effects to reinforce one another and, should they have a preference for large deformation, to drive the nucleus towards superdeformation. $^{64}_{32}$Ge was predicted to be such a superdeformed nucleus [SHE76]. The shape-driving influence of these shell effects is very finely balanced as can be seen from the many predictions of the shape of ^{64}Ge (see chapter 2). An experimental measurement of the shape was thus very important for testing these predictions and consequently the models employed for these predictions. The way chosen to do so was by the γ-ray spectroscopy of the low-lying states. A further incentive was that spectroscopic information on N=Z nuclei stopped at $^{60}_{32}$Zn and no information was available on ^{64}Ge,

the next even-even self-conjugate nucleus. In this chapter, an account of the search for, and the subsequent observation of, the first excited state in ^{64}Ge is given. The reaction ^{54}Fe(^{12}C,$2n\gamma$)^{64}Ge was chosen to produce ^{64}Ge. This projectile-target combination has been used successfully by other workers to make ^{64}Ge [DAV73] and was predicted by CASCADE to have the largest cross-section possible with a convenient projectile and target. The general arrangement of the experiment has been described in §3.6 but, wherever necessary, any modifications or enhancements to this layout is described in the appropriate sections. Using the conventional arrangement of a light projectile on a heavy target produced many contaminant nuclei from reactions on light impurities in the target. This is discussed in section 2 which also describes the circumnavigation of this problem by inverting the reaction. The excitation functions of several γ-rays from the reaction were obtained to confirm the CASCADE cross-sections of the dominant channels and thereby gain confidence in its predictions of cross-sections for the weaker channels. An experiment was also performed in which the singles spectrum was collected. From this spectrum, the relative intensities of the lines were obtained and the relative cross-sections of the pn and $2p$ channels deduced. From the results of this experiment, we were also able to calculate the absolute cross-sections of these channels. As the relative cross-section of the $2n$ channel is calculable from the n-wall data (see below), this experiment allowed us to determine the absolute cross-section of this channel.

The β-decay of ^{64}Ge was studied to provide the cross-section for the production of ^{64}Ge relative to the other nuclei. A knowledge of this cross-section allowed us to determine the practicability of the experiment. In section 6, the search for the first excited state in ^{64}Ge is detailed. A total of ~400 hours of beam time with the Oxford Folded-Tandem accelerator was used with $\sim 5 \times 10^7$ events collected in 3 separate experiments which had slightly different arrangements and used 2 different ^{12}C targets. Analyses of these experiments – as will be seen – show a consistent presence of a ^{64}Ge peak in their gated spectra. Finally, in section 7, the results of the analyses are reviewed and discussed. The shape of ^{64}Ge, vis-à-vis a superdeformed

shape, will also be considered. The evaporation code CASCADE has been used to guide us in the choice of reactions and reaction energies to use. The code has been used successfully in several *fp*-shell nuclei [PUH77a, PUH77b] and so was expected to give reasonable predictions (certainly within orders-of-magnitude) for the cross-sections in our case. In this chapter, CASCADE predictions are often included for comparison with the experimental results but it must be borne in mind that these have been generated with the default input values to the program (see Appendix V) and these comparisons should, on no account, be regarded as a rigorous test of the code.

5.2 Kinematic Focusing and the Inverse Reaction

Using a light beam on a heavy target poses a problem due to reactions of the beam on light impurities in the target. With a ^{12}C beam on a ^{54}Fe target, we may reasonably expect reactions on ^{12}C and ^{16}O in the target and also on any other target impurities lighter than ^{54}Fe. Table 5.1 shows the cross-sections predicted by CASCADE for ^{12}C on various nuclei at an energy of 35 MeV.

Reaction	σ_F	σ (n)	σ (pn)	σ $(2n)$
$^{12}C + ^{54}Fe$	420	–	73	0.7
$^{12}C + ^{12}C$	878	28	166	–
$^{12}C + ^{16}O$	851	11	175	–
$^{54}Fe + ^{16}O^{(1)}$	294	–	17	0.3

Table 5.1 : CASCADE cross-sections for a 35 MeV ^{12}C beam on various targets. σ_F is the fusion cross-section while the other columns give the cross-sections for a few n-related exit channels. All the cross-sections are in mb.
(1) $^{54}Fe + ^{16}O$ at 150 MeV has been included for comparison.

In the $^{12}C + ^{54}Fe$ experiment, γ-rays lines from reactions on carbon were, indeed, observed. If the reaction is inverted, we see from table 5.1 that the cross-section on a light impurity like oxygen is considerably reduced. Carbon, which was the main contaminant is now, of course, the target. The removal of contaminant reactions in the $^{54}Fe + ^{12}C$ case can be readily seen if we compare the singles spectrum from the $^{12}C + ^{54}Fe$ reaction (fig. 5.1) with that from the $^{54}Fe + ^{12}C$ reaction (fig. 5.2). The contaminant peaks in fig. 5.1 are clearly missing in the other singles spectrum. The presence of the large Coulomb excitation lines need not worry us as these are removed by neutron-gating. Fig. 5.3 shows the neutron-gated spectrum of the $^{12}C + ^{54}Fe$ reaction and shows the presence of lines from n-related channels from the contaminant reaction.

A second advantage of the inverted reaction is that the higher incident momentum kinematically focuses the evaporated neutrons into the neutron wall that is placed downstream. Fig. 5.4 shows the laboratory energy of one evaporated neutron against the laboratory angle of emission for the $^{12}C + ^{54}Fe$ (C-Fe) and $^{54}Fe + ^{12}C$ (Fe-C) reactions. (Here, and throughout this chapter, the order of the letters in the portmanteau 'C-Fe' will be taken to indicate the direction of the reaction). In the Fe-C reaction, the outgoing neutrons are within a cone in the forward direction (< 62 degrees for a $E_{CM} = 1.5$ MeV neutron). This should be contrasted with the C-Fe case where the neutron emission is spread over a much wider angular range. The solid angle subtended by the n-wall at the target as a fraction of the maximum solid angle subtended by the evaporation neutrons was calculated using simple two-body kinematics. This fraction is plotted in fig. 5.5 as a function of the neutron wall to target distance. The three arrows labelled A, B and C show the positions where the n-wall experiments were carried out. Also shown in the figure is the fraction of 4π subtended by the n-detector. By inverting the reaction, the figure shows that the effective solid angle subtended by the neutron wall at position B (where the main data-taking run was performed) is increased from 6 % to 30 % for a 1 MeV (laboratory frame) neutron. The laboratory energies of the neutrons in

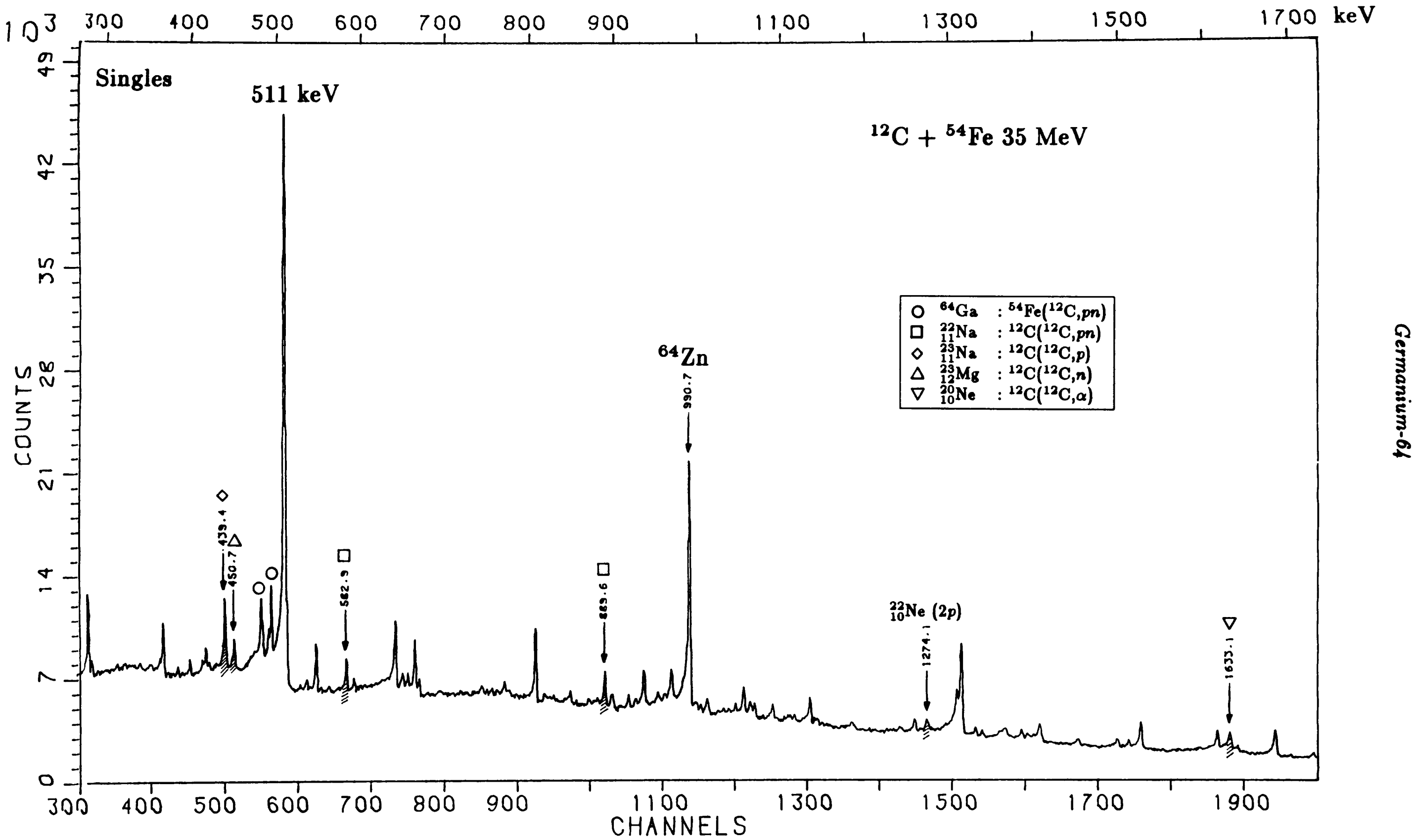


Fig.5.1 : Singles γ-ray spectrum from the reaction $^{12}C + ^{54}Fe$ at 35 MeV. Contaminant lines from reactions on carbon in the target are indicated.

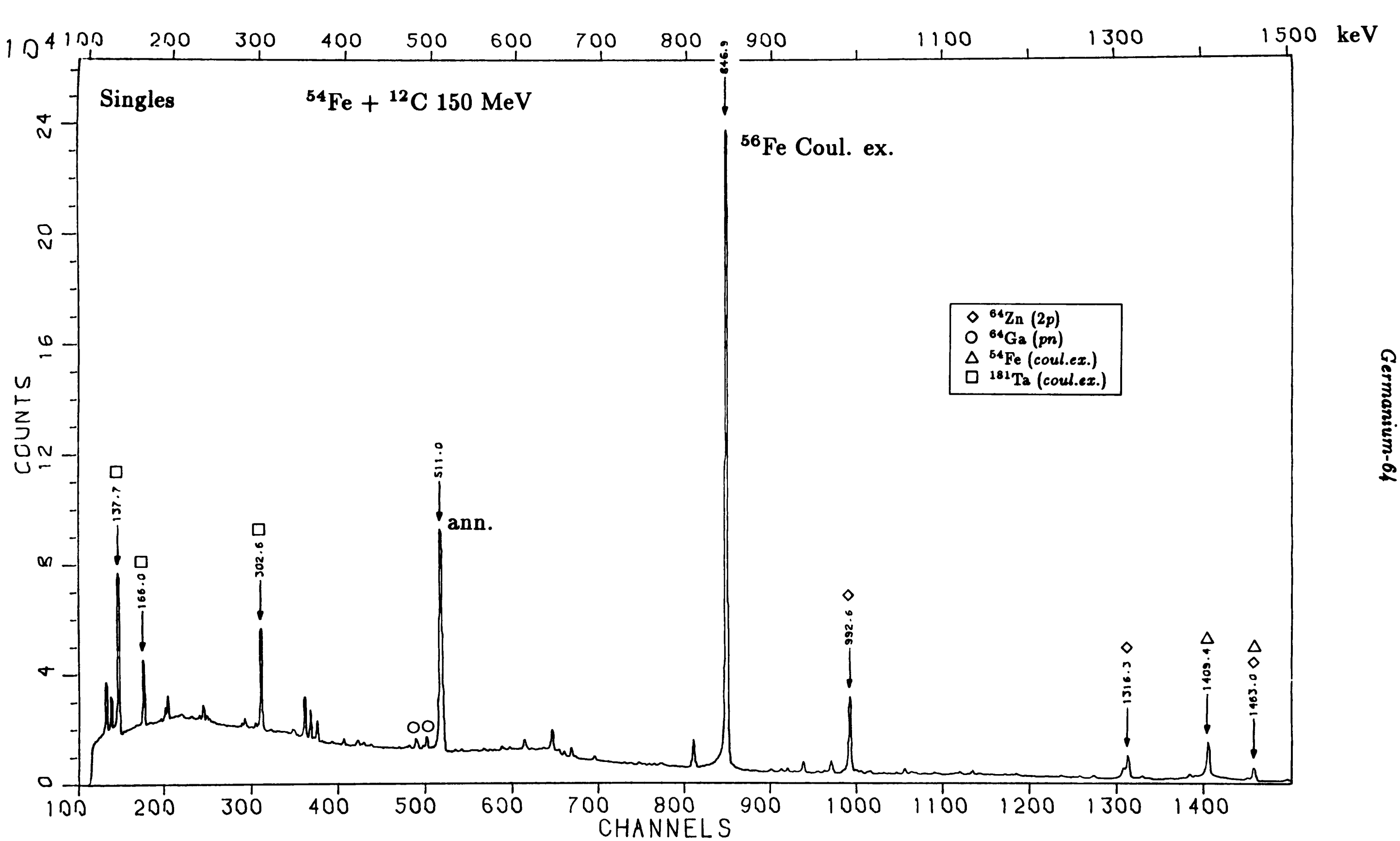


Fig.5.2 : Singles γ-ray spectrum from the reaction ^{54}Fe + ^{12}C at 150 MeV. This spectrum is free from the contaminant lines present in the previous spectrum and demonstrates the advantage of using the inverse reaction.

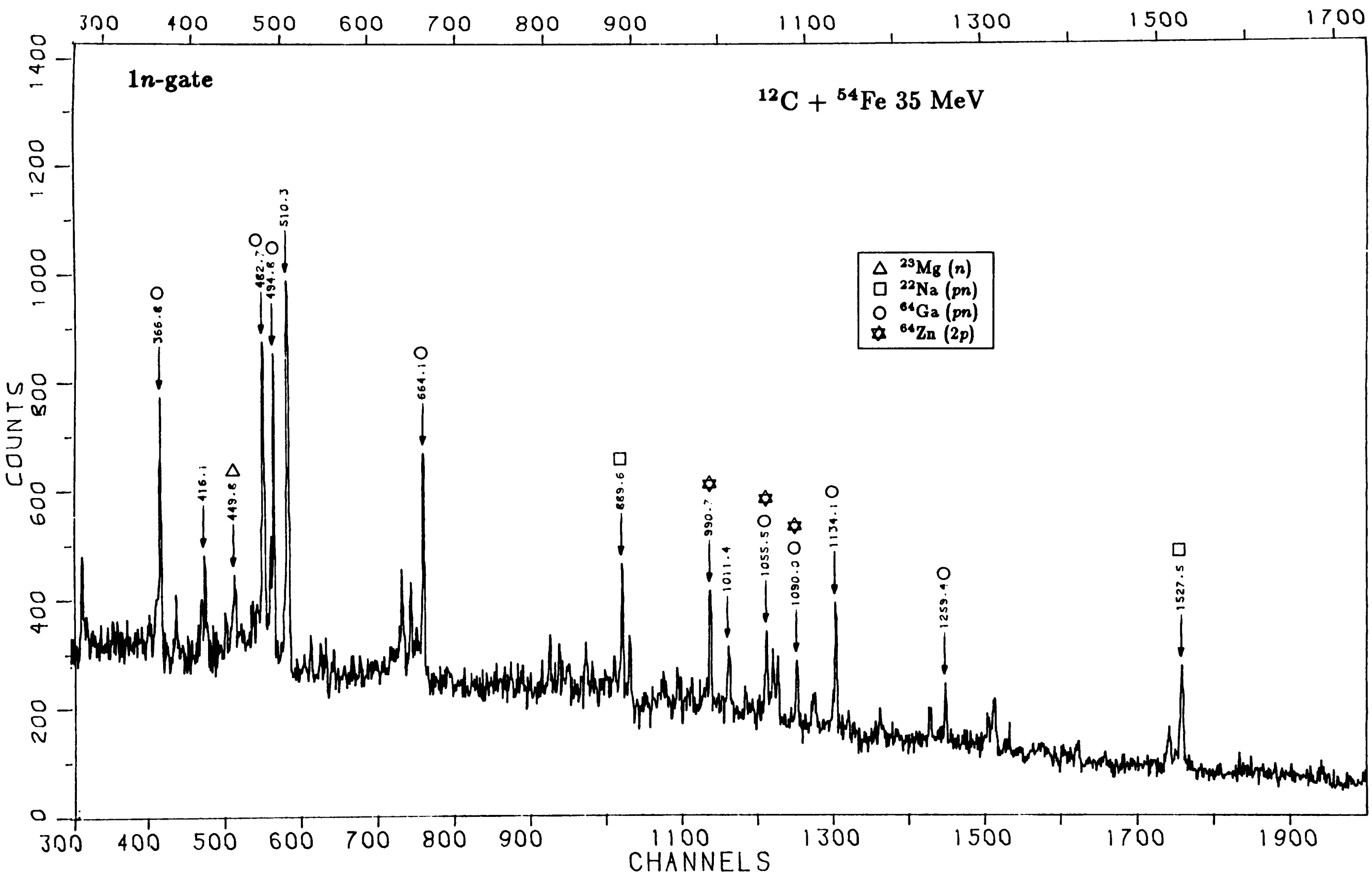


Fig.5.3 : Neutron gated spectrum from the reaction $^{12}C + ^{54}Fe$ at 35 MeV.

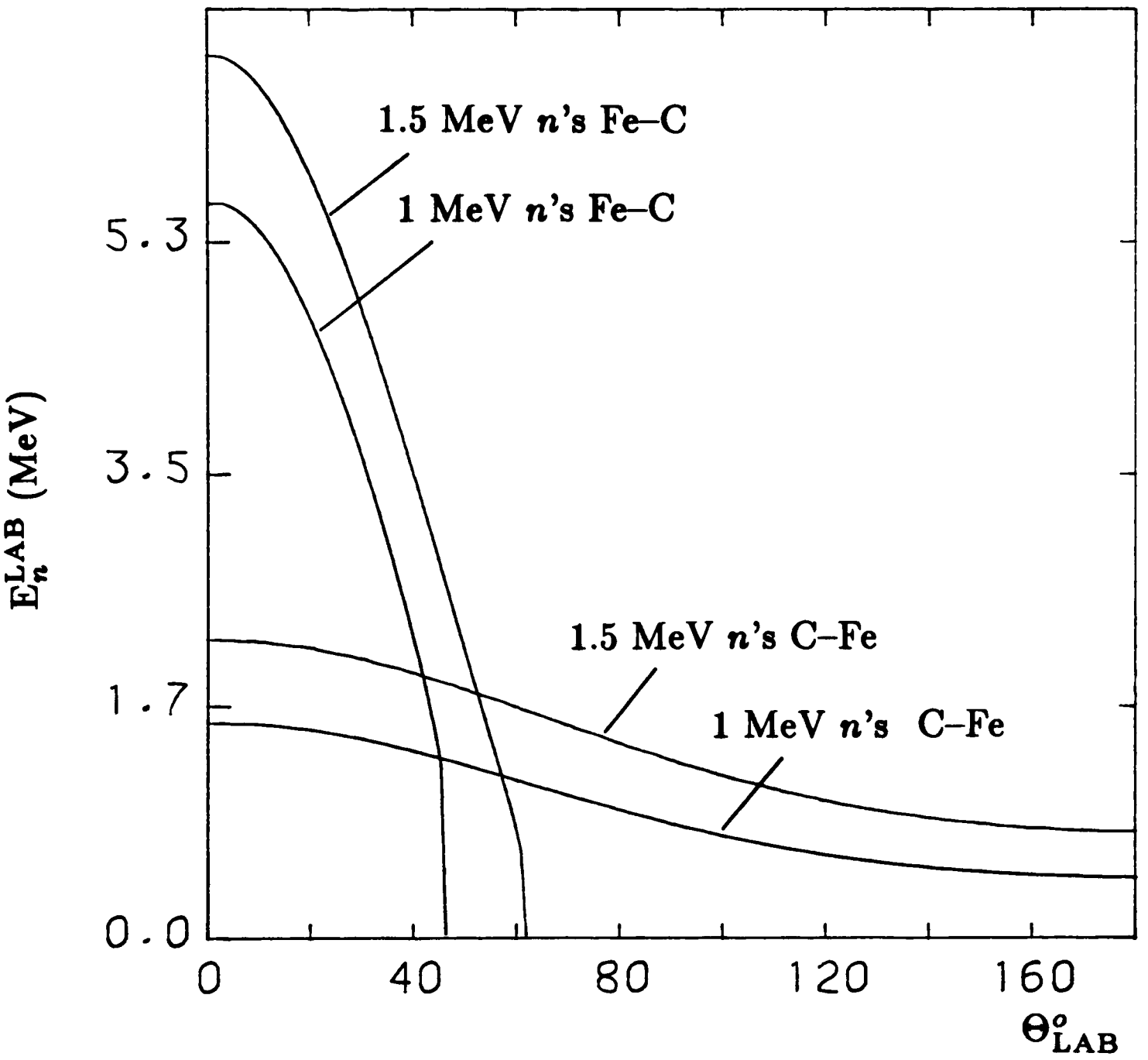


Fig.5.4 : Energy of evaporated neutron vs. angle of emission. Energy and angles are in the lab. frame.

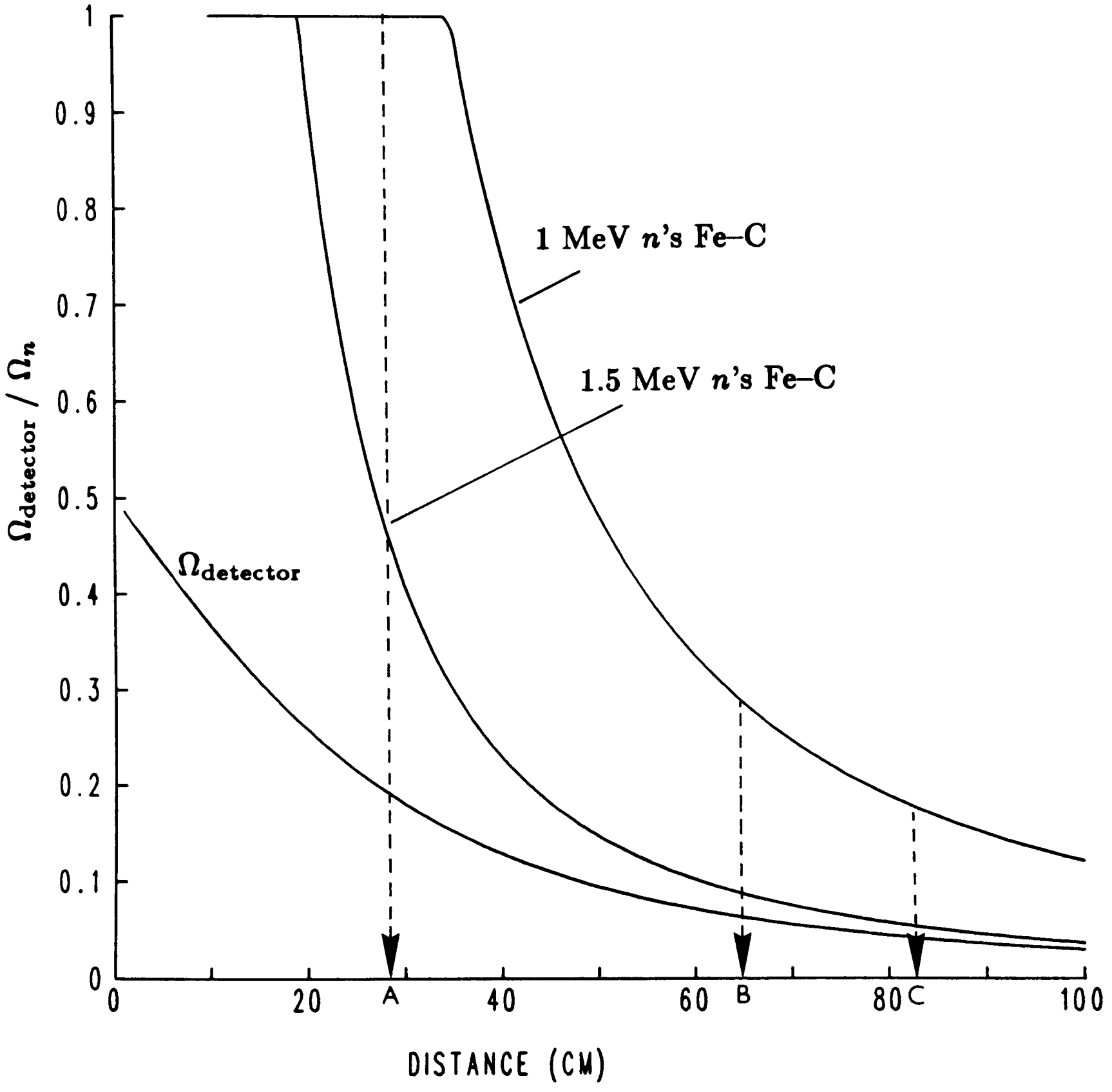


Fig.5.5 : Solid angle subtended by the neutron wall as a fraction of the maximum solid angle subtended by the evaporation neutrons plotted as a function of the target-neutron wall distance. A,B and C are the 3 positions at which the experiments were conducted. The solid angle subtended by the neutron wall as a fraction of 4π is given by the curve marked $\Omega_{detector}$.

the Fe-C reaction are also considerably higher than the C-Fe case. It is a common problem with pulse shape discrimination that low energy neutrons (< 500 keV) are hard to discriminate from γ-rays [AHM77, KAL70, chapter 5 of ENG74, BIR64 and references therein]. This is because the light emission is smaller for low energy neutrons and so the pulse shape differences between neutron and gamma induced scintillations in the detector are correspondingly smaller. As the neutrons in the Fe-C reaction are higher in energy, their larger signals make them easier to detect and discriminate from γ-rays. Unfortunately, the disadvantage we found in inverting the reaction was that the beam current was much lower than the C-Fe case† and hence the counting rate was correspondingly reduced. Typically, in the C-Fe experiment, a beam current of 20 particle-nA was obtained while the beam current in the Fe-C experiment was only about 2 particle-nA — 10 times smaller. However, this is outweighed by the increase‡ in the effective solid angle and the reduction of contaminant reactions in the Fe-C reaction. A summary of the advantages and disadvantages of adopting the Fe-C over the C-Fe combination is listed in table 5.2

Advantages	Disadvantages
1. Kinematics – focus n's	1. Low beam current
2. Reduced σ for reactions on light impurities	
3. n energy raised – easier to detect – easier for PSD hence good n-γ separation	

Table 5.2 : Advantages and disadvantages of using the Fe-C reaction over the C-Fe reaction.

Doppler broadening of lines as a result of the larger momentum in the Fe-C reaction was not a problem as thick targets (100 μg/cm^2 ^{12}C on 20 μm natural iron

† The accelerator was used at its maximum working voltage of 10 MV for the Fe-C reaction.

‡ By a factor of 5 for $1n$ and 25 for $2n$ events.

backing) were used and the states of interest (the first few excited states) should have decayed from a stopped nucleus.

The Fe-C reaction was adopted for the primary data collecting experiments where the kinematic focusing of the neutrons into the detector was important. In experiments where a high reaction rate was required, the C-Fe reaction was used.

5.3 Excitation Function

An experiment was carried out to determine the excitation function of reaction lines from $^{12}C + ^{54}Fe$ for a range of bombarding energies between 30 and 45 MeV. A ^{12}C beam was used as we required a rate high enough (Ge(Li) rate ~3.5 kcts/s) to enable sufficient data to be collected at each angle. As the intention was to obtain the excitation function of known and intense γ-ray lines from the reaction, the presence of contaminant γ-rays from $^{12}C + ^{12}C$ was not important. By knowing how the yields of the dominant γ-rays varied with energy, the optimum energy at which unwanted γ-rays could be minimized was found. An angular distribution experiment was also carried out but, as no new information was obtained, these data are not reported.

5.3.1 Experimental Details

In the excitation function experiment, a Compton-suppressed Ge(Li) detector (CSG) was used. This reduces significantly the Compton background of the γ-ray peaks and so improves the peak to background ratio of the γ-ray lines. The CSG was positioned 23 cm from the target and at an angle of 0° to the beam axis to obtain maximum yield (the wall of the chamber was thinnest at 0 degrees). A ^{12}C beam at 7 energies in the interval between 30 and 45 MeV (listed in table 5.3) was used to bombard a 1 mg/cm^2 ^{54}Fe target (enriched to 95.6 %) on a 50 mg/cm^2 gold

backing. In order to correct for dead-time losses, a pulser, strobed by the digitized beam current, was fed into the Ge(Li) 'test' input. This digitized current was also fed into a scalar and so the value recorded by this scalar, relative to the pulser peak area in the spectrum, was indicative of the dead-time losses of the system and was used to correct for these losses. The arrangement of the electronics is shown in fig. 5.6.

5.3.2 Analysis - Excitation Function

The yield of the various γ-rays was normalized to the yield of the 279 keV transition from the Coulomb Excitation (CE) of $\frac{3}{2}^+$ ground state to the $\frac{5}{2}^+$ state in ^{197}Au since this was the strongest transition in ^{197}Au. Although the cross-section for the CE process is not constant over the energy range (30 – 45 MeV), it is a smoothly varying function of energy and thus the gold CE line was a suitable candidate for normalizing purposes. Table 5.3 shows the calculated cross-sections for CE at the various energies integrated over the target thickness (see Appendix I for the derivation).

E_{kin}	$\sigma_{CE}(^{197}Au;279\ keV)$
30	17.9
32.5	22.2
33.3	23.4
35	26.5
37.5	30.8
40	35.2
45	44.0

Table 5.3 : Thick target cross-sections (mb) for Coulomb excitation of ^{197}Au by ^{12}C. The projectile energy, E_{kin}, is in MeV.

The yield curves presented below have all been corrected for the gold CE variation as well as for dead-time losses. Figs. 5.7(b) to (d) show the excitation functions

KEY TO FIGURE 5.6

ADC - Analog-to-Digital Converter [Tennelec TC205A]

AMP - Linear Amplifier [Tennelec 205A]

CF - Constant Fraction Discriminator [Ortec 583]

G&D - Gate and Delay generator [Ortec 416A]: Used to convert the NIM fast negative logic pulses to positive logic pulses

GELI - Germanium (lithium-drifted) gamma-ray detector

INT ENC - Interrupt Encoder: Oxford designed CAMAC unit which controls the servicing of interrupt requests by any CAMAC module and generates software controlled logic pulses as strobe for external units

I/R - Input register - A module which accepts data via a multiway front panel connector and transfers this to the CAMAC dataway.

LE - Leading Edge discriminator [LeCroy 380A]

LU - Logic unit [Phillips 755]: A coincidence unit but coincidence requirement set to unity (=1). Upper LU used as a pulse stretcher to increase pulse width to 200ns while lower LU used as a gate to veto timing signals in coincidence with signals from the Compton Suppressor.

TFA - Timing Filter Amplifier [Ortec 474, Ortec 454]

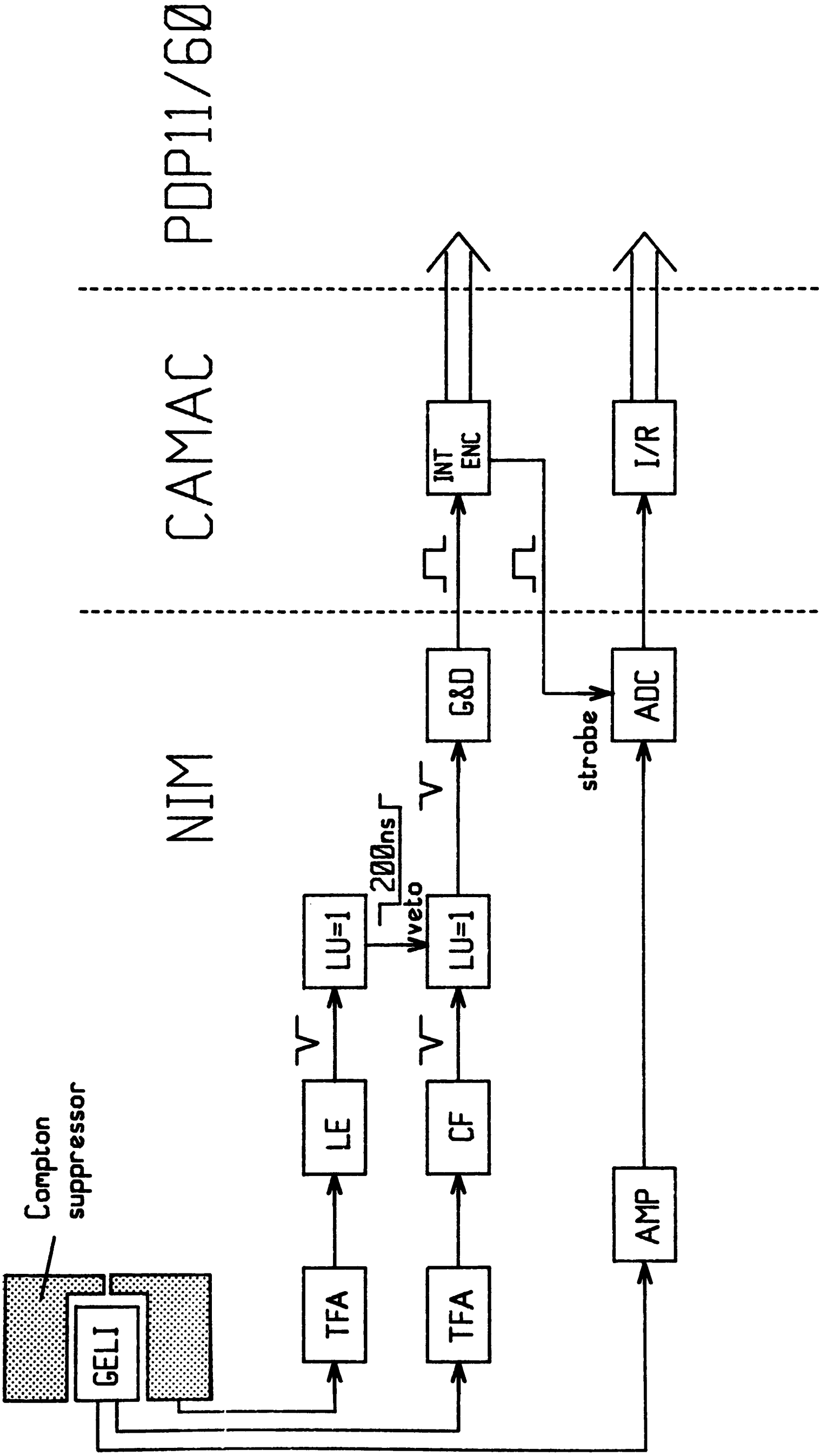


Fig.5.6 : Electronic layout for the Excitation Function experiment using a Compton-suppressed Ge(Li).

of several γ-rays from the reaction. Part (b) shows the γ-rays from the first 3 transitions of the ground state band in ^{64}Zn. The yields have been normalized to the 30 MeV yield of the 2→0 (992 keV) transition. The yield curves of a few γ-rays from ^{63}Zn are shown in part (c). Here, the 650, 413 and 640 keV γ-rays represent one cascade to the ground state (g.s.). The yields of the 413 and 640 keV lines have been normalized to the 35 MeV yield of the 650 keV ground state transition. The 193 keV line that has also been included is the strongest ^{63}Zn line observed in the spectrum and is one of the g.s. transitions in this nucleus. The yield curves of two strong transitions in ^{64}Ga are shown in part (d). The yields of these γ-rays should reflect the cross-sections for the production of their parent nuclei and so the cross-sections calculated by CASCADE have been included in part (a) for comparison. We see that the experimental yield curves follow the trend predicted by CASCADE. As the experiment results agree with the theoretical predictions, the optimum energy range quoted in chapter 2 (32-38 MeV ^{12}C beam) can be used as a reliable guide in choosing the bombarding energy to use. Table 5.4 shows the details of the γ-ray transitions considered in these figures.

Figure	Channel	Nucleus	E_γ (keV)	Transition
5.7(b)	$2p$	^{64}Zn	992	$2^+ \rightarrow 0^+$
			1315	$4^+ \rightarrow 2^+$
			1687	$6^+ \rightarrow 4^+$
5.7(c)	$2pn$	^{63}Zn	193	$\frac{5}{2}^- \rightarrow \frac{3}{2}^-$
			650	$\frac{5}{2}^- \rightarrow \frac{3}{2}^-$
			413	$\frac{7}{2}^- \rightarrow \frac{5}{2}^-$
			640	$\frac{9}{2}^+ \rightarrow \frac{7}{2}^-$
5.7(d)	pn	^{64}Ga	367	$4^+ \rightarrow 3^+$
			495	$4^+ \rightarrow 2^+$

Table 5.4 : Gamma-ray energies of the yield curves shown in fig.5.7

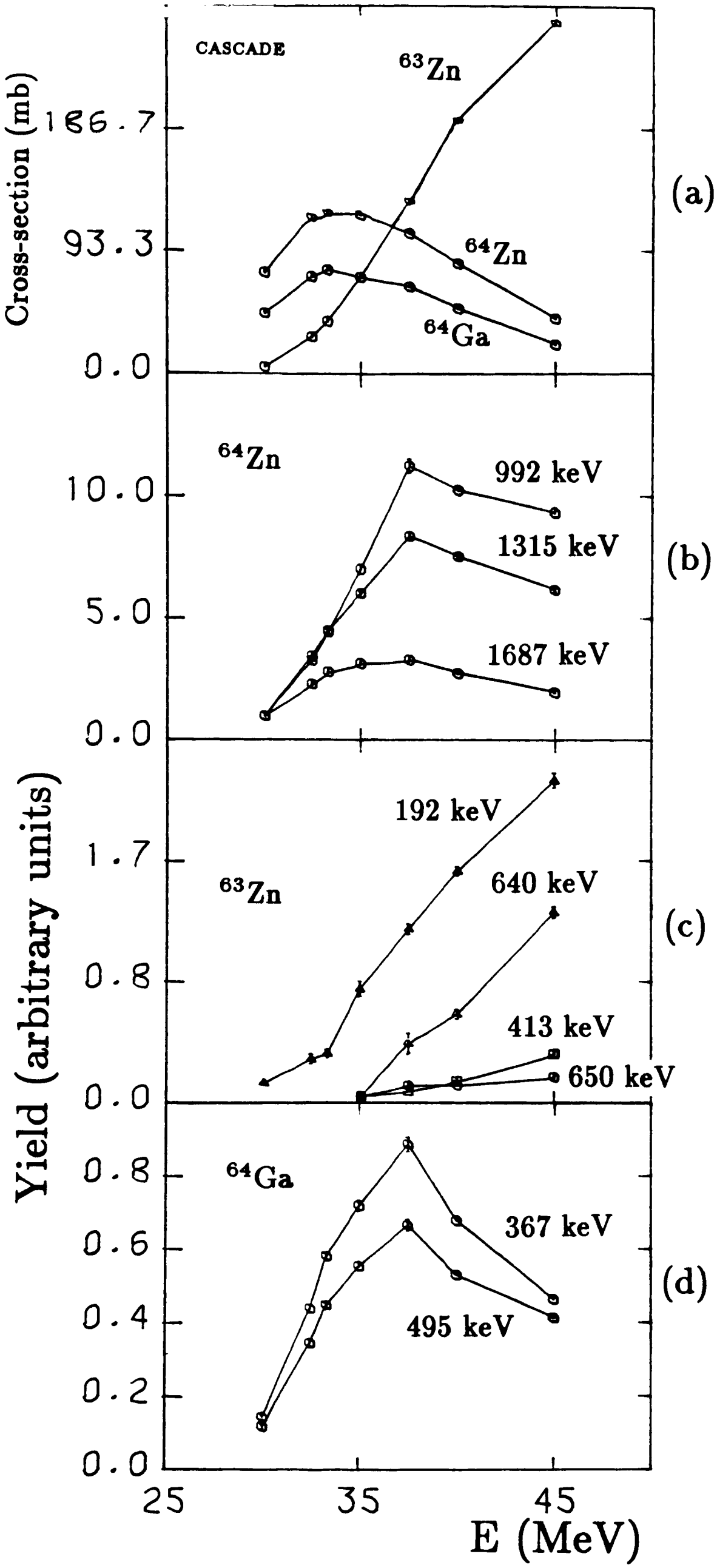


Fig.5.7 : Yield curves for a few prominent γ-rays from the reaction $^{12}C + ^{54}Fe$. (a) is the CASCADE yield curves for 3 evaporation channels from which the γ-rays have been derived. The excitation functions for the γ-rays correspond to : (b) ^{64}Zn, (c) ^{63}Zn and (d) ^{64}Ga. Energies are the projectile energies in the lab. frame

5.4 Relative Cross-sections

The runs with the neutron wall (§5.6.3) provided data from which the relative cross-sections of the pn and $2n$ channels could be extracted. However, no singles spectra were collected during the run — to reduce the dead-time loss of the system — and so the ratio of these cross-sections to the cross-section of the largest channel, the $2p$ channel, was not known. To remedy this, a separate experiment was performed in which the singles data were collected. A ^{54}Fe beam at 150 MeV was used to bombard a 100 μg/cm^2 ^{12}C target on a 20 μm natural iron backing. The inverse reaction with the same centre-of-mass energy was also performed where a ^{12}C beam at 33.3 MeV struck a target of 1 mg/cm^2 ^{54}Fe target on a 50 mg/cm^2 gold backing. In both these reactions, a Compton-suppressed Ge(Li) detector was placed at ~55° to the beam axis and γ-ray singles data were collected.

For a particular nucleus, if the intensity of the ground state transition is measured, then the relative cross-section for its production can be deduced. Two problems were encountered: firstly, for the odd-A or odd-odd nuclei, there are several parallel paths feeding the ground state (g.s.) and it was difficult to ensure that all the strengths were included in the sum of the intensities. Secondly, the detector efficiency for low energy γ-rays (typically < 250 keV) was much harder to determine due to the change in the slope of the efficiency curve around this energy (fig.5.8). Because of this, nuclei with low energy transitions have an added uncertainty in their final sums.

The relative production cross-sections of ^{64}Zn and ^{64}Ga were calculated from the experimental results. Other prominent channels like ^{63}Zn and ^{61}Zn were not considered as they have very many parallel ground state transitions and also many low energy γ-rays in their γ-decay. This makes the extraction of a reliable and consistent relative cross-section for these nuclei an impractical exercise. Table 5.5(a) shows the intensities of the various γ-rays used in each nucleus to calculate the relative cross-sections. Part (b) summarizes the results. As mentioned above, the

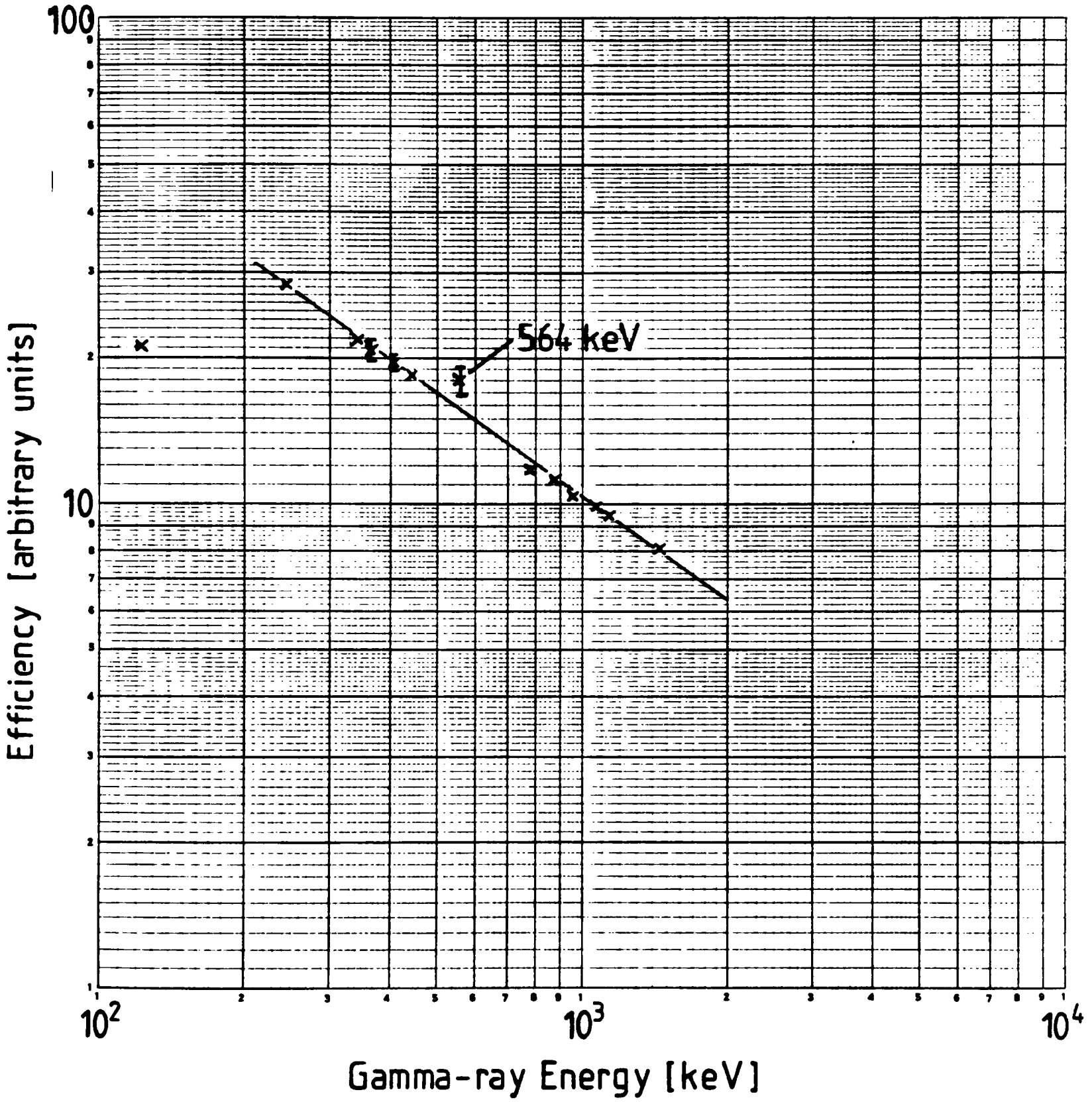


Fig.5.8 : Detection efficiency curve for a typical Ge(Li) using a ^{152}Eu source.

intensities for many parallel γ-decay paths in an odd-odd nucleus like $^{64}_{31}$Ga have to be added together to obtain the total intensity of the γ-decay. This total intensity can then be regarded as being representative of the relative cross-section for the production of the nucleus. In the decay scheme of ^{64}Ga, (fig. 5.15), the decay of the 43 keV state was not observed in our spectrum and so the sum of the intensities of the transitions feeding this level had to be taken. The 128 keV transition, however, lies in the energy range at which the Ge(Li) efficiency is uncertain. To get around this problem, the intensities of the transitions feeding this line were summed. Hence, the first 7 rows of table 5.5(a) show the γ-ray lines used to obtain the intensity of the 128 keV line. In the 4th. column, the intensities of the transitions to the first excited state are given and their sum is given in column 5. For $^{64}_{32}$Zn, the situation is simpler as only the intensity of the 992 keV line was required as almost all the γ-ray decay strength is channelled into this ground state transition. These intensities were taken from the Fe-C data. This was because the use of an identical beam and target combination as the neutron wall experiment allowed us to compare the intensities from the two experiments without much worry about possible contaminant lines (as would have been the case for the C-Fe reaction). Unfortunately, the intensity of the 850 keV line from ^{64}Ga overlapped with the Coulomb excitation line (847 keV) of the ^{56}Fe backing, and so was difficult to measure. Hence, the intensity of the 495 keV line relative to the 850 keV line was obtained from the C-Fe data (the Fe target had a gold backing) and this ratio was used to estimate an intensity for the 847 keV line in the Fe-C case. The intensities quoted here have been corrected for the Ge(Li) detector efficiencies. For the relative cross-sections, the entry in table 5.5(b) for ^{64}Zn has been corrected for the β-decay of ^{64}Ga to ^{64}Zn. This has been done by using the total intensity of the ^{64}Ga γ-decay and the known value* of the transition intensity of the 992 keV line from β-decay to determine the percentage of the 992 keV γ-rays that have come from the β-decay of ^{64}Ga. As the cross-section

* Nucl. Data Sheets **28**, 179 (1979).

for the production of ^{64}Ge was very small, the analogous correction for the lines in ^{64}Ga from the β-decay of ^{64}Ge was ignored.

The errors in the normalized intensities are a combination of errors in the peak efficiency and in calculating the peak area [HEL75]. The former comes from uncertainty in the efficiency interpolation (ϵ_{eff}) and the lack of reproducibility of the source geometry (ϵ_{src}). As these errors and the error in determining the peak area (ϵ_{area}) are uncorrelated, they can be summed in quadrature to obtain the net error. These net errors are quoted in square brackets [ ] in the following tables.

Nucleus	γ-ray energy (keV)	Efficiency corrected intensity‡		Total Intensity
^{64}Ga	367+364¶	262(7)		
	152	~0		
	537	56(6)		
	850†	51(10)		
	1109	21(8)		
	1186	~0		
	1514	25(4)		
		→	415(16)	
	280		45(3)	
	492+495¶		298(11)	
	665		213(9)	
			→	971(22)
^{64}Zn	992		→	2448(28)

Table 5.5(a) : γ-ray intensities used for the determination of the relative cross-sections of the evaporation channels. All the data (except †) have been taken from the Fe-C reaction at 150 MeV.
†derived from the C-Fe reaction at 33.3 MeV.
¶The intensities of doublets or close-lying lines have been added together.
‡Corrected for Ge(Li) detection efficiencies.

Nucleus	Channel	Total Relative intensity	Norm. Relative intensity
^{64}Zn	$2p$	1994(26)[216]	100[11]
^{64}Ga	pn	971(22)[107]	49[5]

Table 5.5(b) : Intensities of several evaporation channels from table 5.5(a). The error in ( ) is the error in the peak intensity while the error in [ ] is the net error (using ϵ_{src} = 4 % and ϵ_{eff} = 10 %). Column 4 shows the experimental intensities normalized to the ^{64}Zn line.

5.4.1 Absolute Cross-sections

An approximate estimate of the absolute cross-sections can be made in the following way. The Coulomb excitation line of the ^{56}Fe backing of the ^{12}C target is clearly evident in the singles spectrum. The Coulomb excitation process is well understood and so the integrated cross-section for the Coulomb excitation of the backing by the ^{54}Fe beam can be calculated. From this, the integrated beam current can be deduced and hence the cross-sections for the production of the other nuclei can be determined from the intensities of their γ-rays. The integrated Coulomb excitation cross-section of the 847 keV $0^+ \rightarrow 2^+$ transition in ^{56}Fe for a 146.7 MeV† ^{54}Fe beam stopping in a ^{56}Fe target is 110 mb. This was calculated using a modified version of the de Boer and Winther Coulomb excitation program [ALD66] where the modification allowed the cross-section for a thick target to be obtained. A full discussion of the calculation is given in Appendix I. The percentage of the the incident ^{54}Fe beam that is Coulomb excited is 0.00076 %. Table 5.6 shows the intensities of the 847 keV Coulomb excitation line of ^{56}Fe and the 992 keV $2^+ \rightarrow 0^+$ (ground state) transition in ^{64}Zn. A correction has been made for the different γ-ray detection efficiencies of these lines. The calculated cross-sections have also been included in the table.

Nucleus	Channel	Relative Intensity	σ (mb)
^{56}Fe	coulex	104022 (379) [11210]	110 (1)
^{64}Zn	$2p$	23125 (307) [2509](2)	338 [37]
^{64}Ga	pn	–	164 [18]

Table 5.6 : Cross-sections for three exit channels from the reaction ^{54}Fe + ^{12}C (^{56}Fe backing). The pn cross-section has been calculated using values from table 5.5(b). See table 5.5(b) for an explanation of the errors.
(1) calculated cross-section.
(2) corrected for ^{64}Ga β-decay.

† This takes into account the 3.3 MeV loss through the 100 μg/cm^2 carbon target.

Several assumptions have been made in this approach and they are as follows:

i) The ^{12}C thickness is 100 $\mu g/cm^2$.

ii) Decay of the ^{64}Zn goes entirely through the 992 keV transition.

iii) The angular distribution effects of the γ-rays are minimized by having the Ge(Li) detector at 55°.

Fig. 5.9 shows the singles spectrum from which the data have been taken. The lower spectrum is the same spectrum but magnified by 8 in the y-direction to show the smaller peaks. The 847 keV line is seen to dominate the spectrum. By far the largest source of uncertainty is the target thickness. The error in this quantity is not known and the thickness quoted is the nominal value. It is not unreasonable to expect this thickness to vary by up to 20 % although a more pessimistic view might expect a factor of two in the uncertainty. It is clear that these cross-sections are by no means precise but they provide a good order-of-magnitude estimate of the cross-sections we are dealing with and provide us with an idea of the sizes of the channels we are considering. Of particular interest is the approximate size of the $2n$ channel as this will indicate the sensitivity of our pure neutron multiplicity detection system. Therefore, these values will be used again when the cross-section of the $2n$ channel making ^{64}Ge is calculated in order to determine an absolute, albeit approximate, cross-section for this channel.

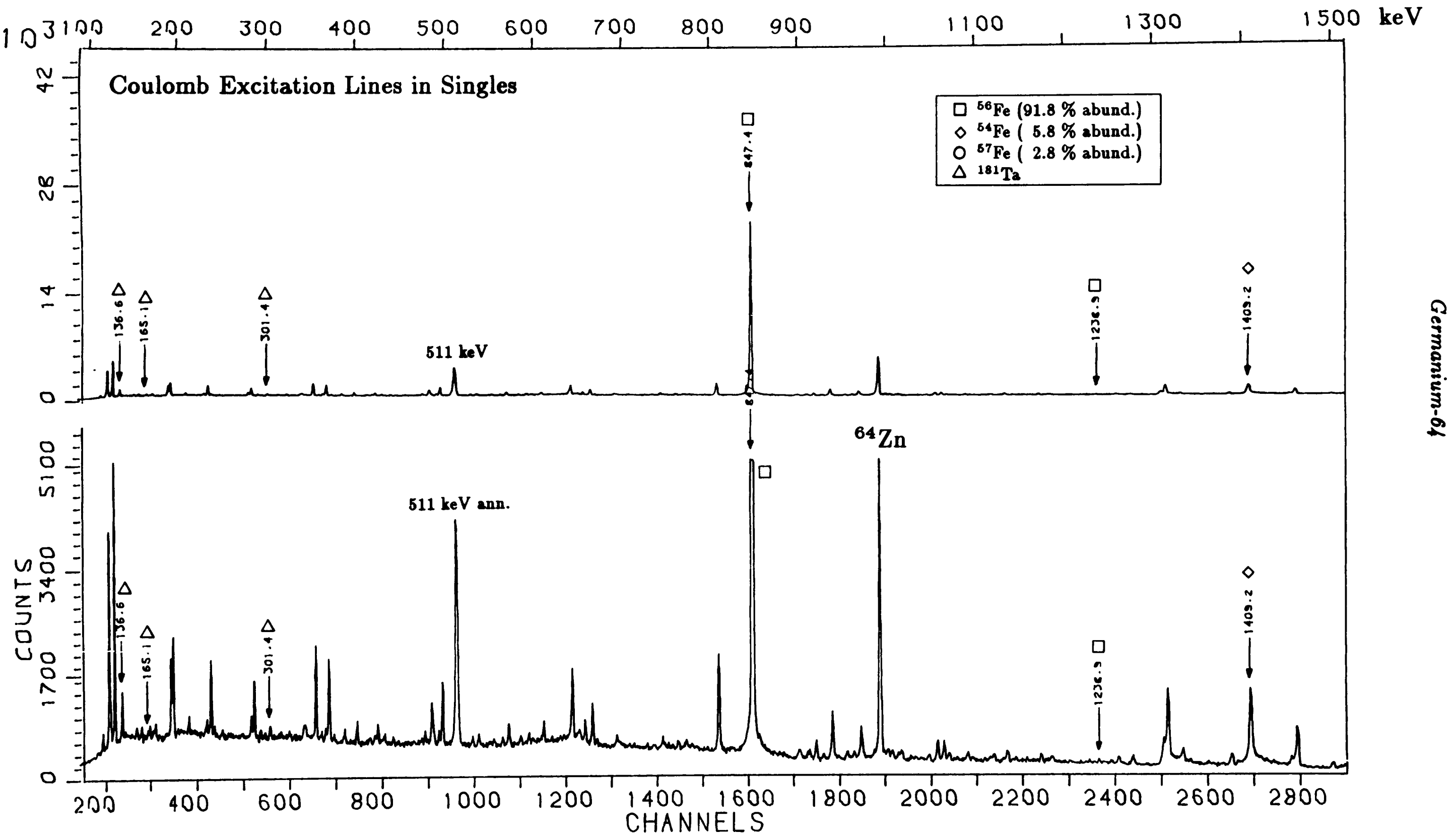


Fig.5.9 : Singles spectrum from which the relative intensities of the γ-rays from the different residual nuclei have been taken. The Coulomb excitation lines have been labelled. The lower spectrum is the upper spectrum magnified to show the weaker lines.

5.5 ^{64}Ge β-decay

An experiment was performed to collect the β-decay spectrum of ^{64}Ge using the reaction ^{12}C + ^{54}Fe at 35 MeV†. The target was a 1 mg/cm^2 ^{54}Fe target on a 50 mg/cm^2 gold backing. This experiment furnished a value for the cross-section for the production of ^{64}Ge relative to the other residual nuclei. The relative cross-sections for the production of the various nuclei were determined by measuring γ-decay intensities in the daughter nuclei of their β-decay. Although the decay of ^{64}Ge to ^{64}Ga generates several γ-rays (fig. 5.10), only the 427 keV line was present with sufficient intensity to be seen.

The experiment used a mechanical chopper to generate periodic pulses of beam. The beam was switched on for 1 minute and then switched off for 2 minutes and this 3 minute cycle was continuously repeated for 5 hours. Fig. 5.11 shows schematically the cycle. This cycle allowed ~75 % of the ^{64}Ge ($T_{1/2}$ = 64 s) to decay before producing a fresh batch. An in-beam γ-ray spectrum was collected and when the beam was off, the activity spectrum was collected. Two activity spectra were collected: one for the first 60 s and the other for the second 60 s. The activity spectrum collected in the first minute is shown in fig. 5.12. This experiment was subsequently repeated with the duration of the run increased to 16 hours. In second experiment, the out-of-beam period was divided into six 20 s time slots instead of the 60 s time slots used before. The activity in the first 60 s (i.e. the sum of the first 3 time slots) is shown in fig. 5.13 where the 427 keV peak looks much more convincing. The results of this latter experiment will be discussed in the following sections.

5.5.1 Relative Cross-sections

The relative cross-sections of the various channels of the reaction can be obtained by observing the β-decay of product nuclei that are radioactive. Consider the

† This is approximately the same energy used by [DAV73], which was 36 MeV, to study ^{64}Ge using this reaction.

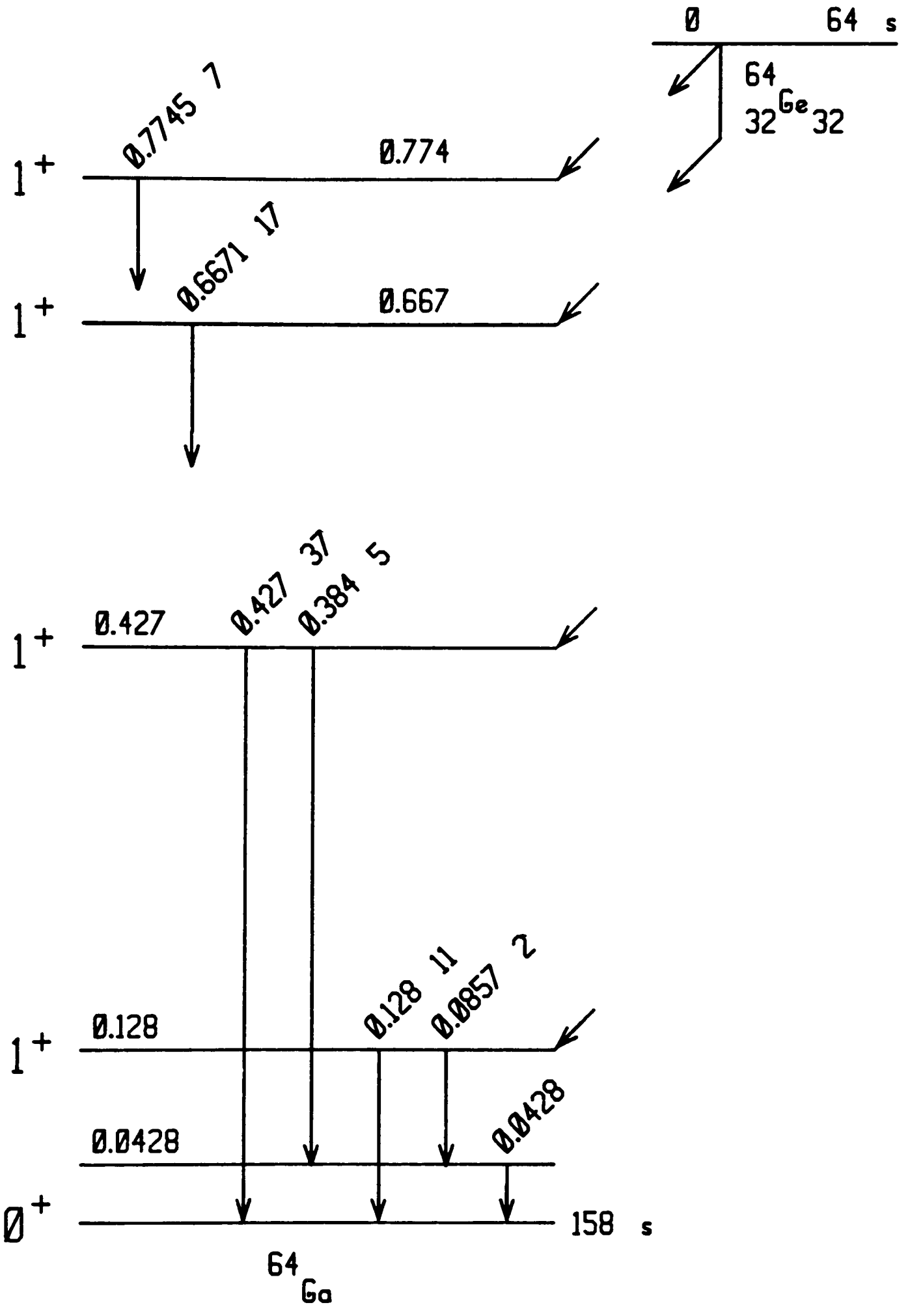


Fig.5.10 : Decay scheme of ^{64}Ge taken from [ROB74]. Nucl. Data Sheet nomenclature adopted. All the energies are in MeV.

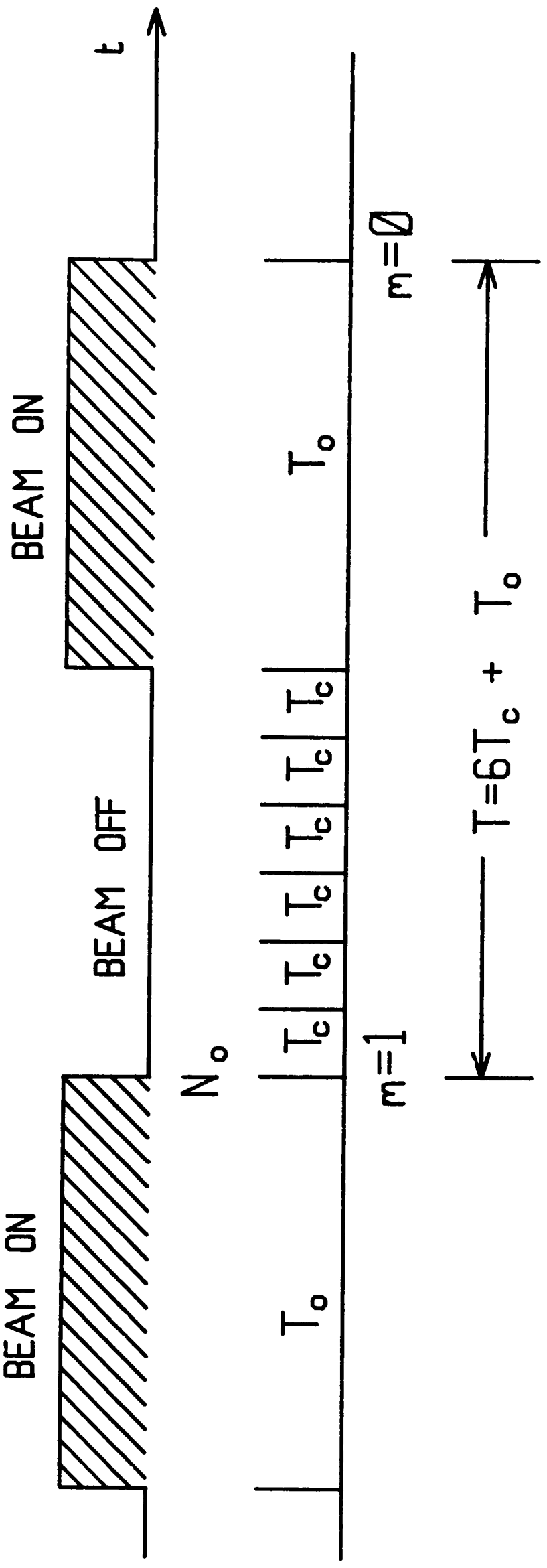


Fig.5.11 : Beam cycle and collection times (T_c) for the activity spectra. T_o is the irradiation period.

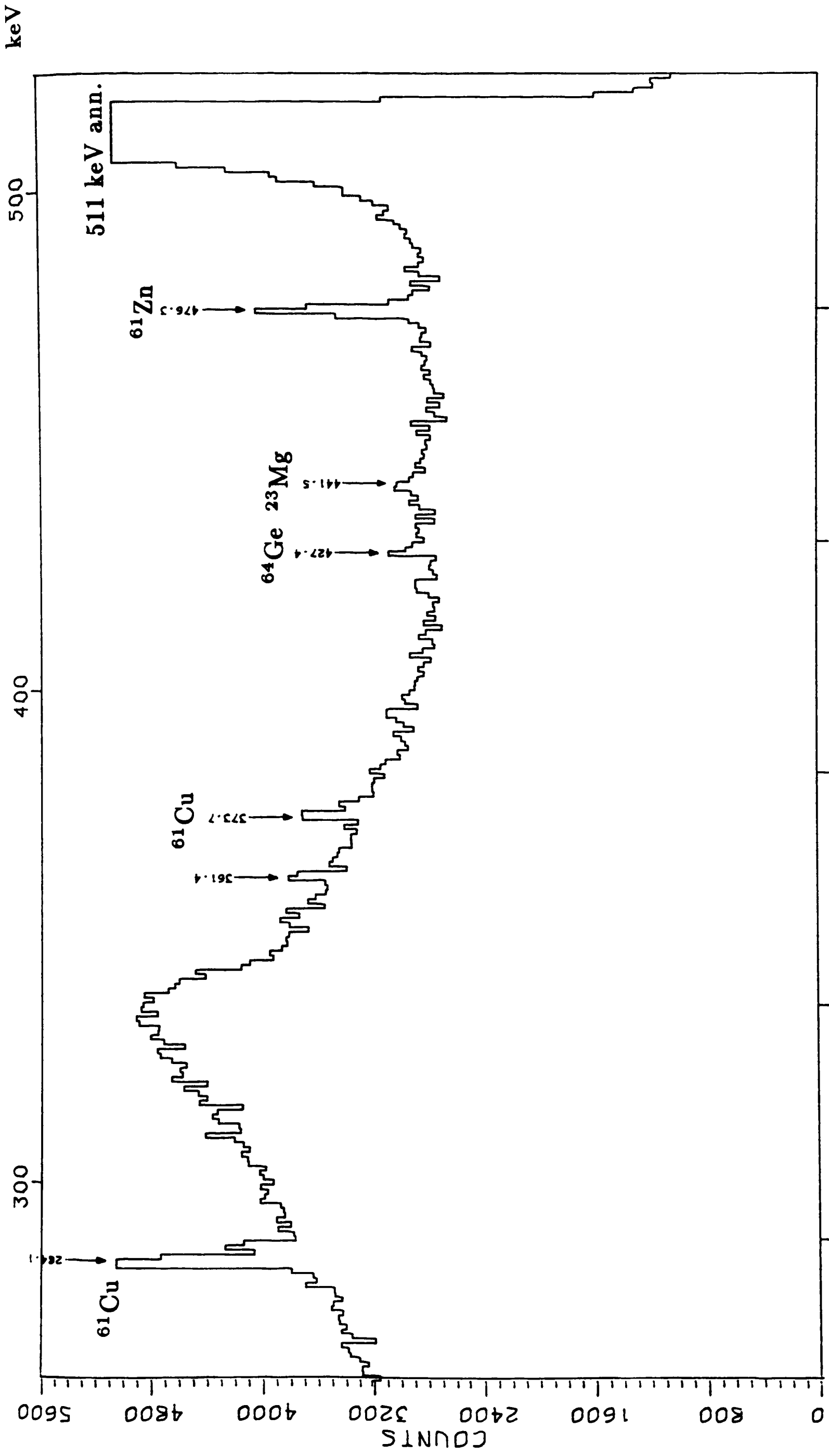


Fig.5.12 : Activity spectrum in the 1st 60s for ^{12}C + ^{54}Fe at 35 MeV. Collection time : 5 hours.

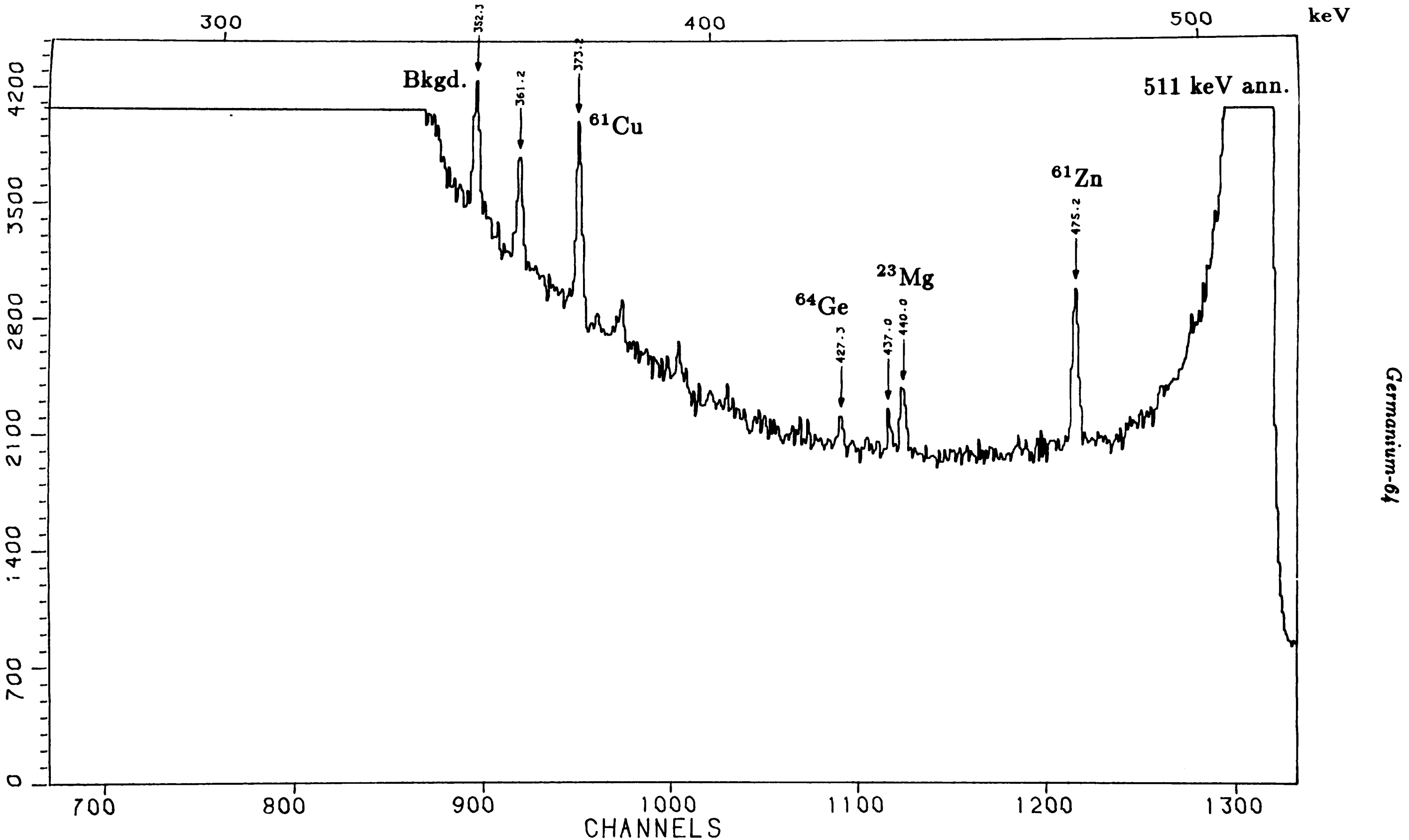


Fig.5.13 : Activity spectrum in the 1st 60s for $^{12}C + ^{54}Fe$ at 35 MeV. Collection time : $\sim$ 16 hours.

beam impinging on the target for an interval T_o and consider a particular channel which produces a radioactive nucleus X. For a period T_c after that, the β-decay spectrum is collected with the beam off. If n of these nuclei are created per second ($n \sim \sigma_{chan}/\sigma_T$ where σ_{chan} is the cross-section of the channel and σ_T is the total cross-section) during T_o and this rate is assumed constant, the number of these nuclei at the start of data collection will be

$$N_o(X) = \int_0^{T_o} n(X)\mathrm{e}^{-t/\tau}dt, \qquad \tau = \text{mean life of the nucleus}$$
$$= n(X)\tau(1-\mathrm{e}^{-T_o/\tau})$$

The total number of decays in the interval T_c will be

$$N(X) = N_o(X)(1-\mathrm{e}^{-T_c/\tau})$$
$$= n(X)\tau(1-\mathrm{e}^{-T_o/\tau})(1-\mathrm{e}^{-T_c/\tau})$$

So, using the mean lives of ^{64}Ge and ^{64}Ga of 92(4) [ROB74] and 227(2) [DAV73] seconds respectively, $N(X)/n(X)$ can be calculated (Table 5.7).

$T_c(s)$	$N(Ge)/n(Ge)$	$N(Ga)/n(Ga)$
20	8.6 (0.2)	4.45 (0.03)
40	15.5 (0.3)	8.52 (0.06)
60	21.1 (0.4)	12.25 (0.07)

Table 5.7 : The number of decays of nucleus X per creation rate.

As the experiment was carried out continuously in 3 minute cycles (one minute with beam on followed by six 20s intervals of data collection with the beam off), we have to consider the build up of radioactive nuclei with time. This is given by

$$f_b = \sum_{m=0}^{\infty} \mathrm{e}^{-mT/\tau}$$

where T is the total time of the cycle i.e. 3 minutes. This factor for ^{64}Ge and ^{64}Ga is given in table 5.8.

	$\mathbf{X} = {}^{64}\mathbf{Ge}$		$\mathbf{X} = {}^{64}\mathbf{Ga}$	
T_c (s)	I	I'(X)	I	I'(X)
20	261 (88)	705 (238)	25601 (166)	59527 (386)
40	281 (120)	759 (324)	48719 (229)	113300 (532)
60	417 (143)	1127(386)	70146 (275)	163130 (640)
%	37[ROB74]		43[RAM75]	
$f_b(X)$	1.165		1.826	
$\epsilon(E_\gamma, X)$	9.0(2)		4.6(20)	
E_γ	427 keV		991 keV	

Table 5.8 : β-decay of ^{64}Ga and ^{64}Ge. I is the intensity of the line at E_γ, % is the number of photons per 100 parent decays, ϵ is the gamma-ray efficiency factor and I'(X) is the number of decays of the parent X.

The 427 keV transition in ^{64}Ga, populated by the β-decay of ^{64}Ge, was observed in the experiment (fig. 5.13). Using the intensity of this line and the branching factor, % (see caption of table 5.8), the number of decays of the parent can be determined. Similarly, for the *pn* channel, the intensity of the 991 keV transition can be used to calculate the number of decays of ^{64}Ga. These numbers are tabulated in table 5.8.

The ratio of the *pn* to 2*n* cross-section is given by

$$\frac{\sigma_{pn}(^{64}Ga)}{\sigma_{2n}(^{64}Ge)} = \frac{I'(Ga)}{I'(Ge)} \left(\frac{n(Ga)}{N(Ga)}\right) \left(\frac{N(Ge)}{n(Ge)}\right) \frac{f_b(Ge)}{f_b(Ga)} \frac{\epsilon(E_\gamma, Ge)}{\epsilon(E_\gamma, Ga)}$$

where the last factor takes into account the efficiency of the Ge(Li) detector with respect to γ-ray energy. The relative cross-sections thus calculated are presented in table 5.9.

$T_c(s)$	σ_{pn}/σ_{2n}
20	204 (69)
40	290 (78)
60	349 (120)

Table 5.9 : Ratio of the cross-sections of the pn to $2n$ channels for various collection times T_c

The pn cross-section is seen to be two orders of magnitude larger than the $2n$ cross-section. In order to compare with the other channels, the normalized counts

$$I''(X) = I'(X)\left(\frac{n(X)}{N(X)}\right)\frac{1}{f_b(X)}\frac{1}{\epsilon(E_\gamma, X)}$$

were calculated. The results, using data from the first 20 seconds of activity, is summarized in table 5.10. CASCADE cross-sections have been included for comparison and they show that the theoretical predictions differ at most by approximately a factor of two from the experimental results.

X	E_γ (keV)	$I''(X)$	$\sigma_{CAS}(X)$ (mb)	$\sigma(X)$ (mb)
^{64}Ga	992	1590 (40) [176]	79	164 [26]
^{64}Ge	427	6 (3) [3]	0.8	0.6 [3]
^{63}Zn	670,962	561 (15) [62]	40	58 [9]
^{61}Zn	475	119 (8) [15]	10	12 [2]
^{61}Cu	283,373	915 (39) [106]	71	95 [15]

Table 5.10 : $I''(X)$ is the number of β-decays of the parent nucleus X, $\sigma_{CAS}(X)$ is the CASCADE cross-section and $\sigma(X)$ is the cross-section normalized to the ^{56}Fe Coulomb excitation line (see section 4). E_γ is the γ-ray line(s) used to determine the yields. For an explanation of the errors quoted in [ ], see table 5.5(b).

5.6 ^{64}Ge Reaction Study

In this section, the data obtained from the study of the γ-rays from the reaction ^{54}Fe + ^{12}C at 150 MeV is presented. This energy corresponds to the maximum operational voltage of 10 MV for the Oxford Folded Tandem accelerator and brings in approximately 1 MeV less energy in the centre-of-mass system than the C-Fe reaction. However, this difference should not alter the $2n$ cross-section (which makes ^{64}Ge) by much (see §2.5.3). The plan of this section is to identify all the γ-rays from the reaction and to show the method by which the relevant data are extracted.

The data are reduced progressively to filter out the γ-ray lines from 'contaminant channels' i.e. any channel other than the $2n$ channel. This is achieved by imposing stricter and stricter coincidence requirements on the data. At each stage, stock is taken of the γ-rays lines left in the spectrum and these are traced back to their parent nuclei. For each γ-ray peak, its intensities in the different coincidence spectra are compared and the presence of other γ-rays from the same nucleus feeding it, or are fed by it, is noted. This then allows us to deduce the probable source of the γ-ray. A catalogue of the γ-ray lines from the reaction is given in table 5.13. Ultimately, only one γ-ray peak remains at the end of the data reduction and this is shown to be a good candidate for the $2n\gamma$ channel.

Having established this, the possibility of observing γ-rays from contaminant $2n$ channels is explored and shown to be unlikely. The γ-ray is thus shown to correspond to a transition in ^{64}Ge and arguments associating this γ-ray with the γ-decay of the first excited state is given.

The relative cross-sections for the production of ^{64}Ga and ^{64}Ge are determined from the intensities of their γ-ray lines in the neutron gated spectrum. The absolute cross-sections are then obtained by normalizing on the ^{56}Fe Coulomb excitation cross-section given in §5.4.1 and a summary of the experimental results of this chapter is given.

5.6.1 Experimental Details

Three separate experiments were carried out in the search for ^{64}Ge and table 5.11 lists the details of each individual run.

Run	Events[1] ($\times 10^3$)	Ge(Li)[2]	Target	L[3]	d[4] (cm)	Ω[5] (sr)
20	4130	1	100 μg/cm^2 ^{12}C on 15.7 mg/cm^2 Fe	L3	83	0.6
21[6]	14063	4	100 μg/cm^2 ^{12}C on 15.7 mg/cm^2 Fe	L4	65	0.9
24[7]	34238	4	300 μg/cm^2 ^{12}C on 18.9 mg/cm^2 Au	L5	29	4.6

Table 5.11 : Details of the 3 runs in which the search for ^{64}Ge was conducted. Runs 20 and 21 used the same target but run 24 had a different target.
(1) Number of events collected.
(2) Number of Ge(Li) detectors used.
(3) Experimental arrangement used (see §3.6).
(4) Distance between neutron wall and the target.
(5) Solid angle subtended by the neutron wall.
(6) 1 Freiburg PSD, 4 Oxford *composite* PSD's.
(7) All 5 Freiburg PSD's.

Although the greatest amount of data were collected in run 24, the 300 μg/cm^2 ^{12}C target consisted of three 100 μg/cm^2 ^{12}C layers stuck together which, unfortunately, came apart during the experiment. As a result, many of the lines were found to have significant Doppler peaks present resulting in a noticeable deterioration of the γ-ray spectrum. The data presented in this section thus, come predominantly from run 21. However, data from the other two runs will be shown to support the existence of the ^{64}Ge peak observed in run 21.

The block diagram representing the electronics used for run 21 was shown in fig 3.4. The physical layout of the experiment was L4 in §3.6. This arrangement consisted of one Ge(Li) detector at 0° and three other Ge(Li) detectors at $\sim$ 55° to

the beam axis. In chapter 3, plate 3.6 showed the top view of the target chamber surrounded by the Ge(Li) detectors.

A partially depleted surface barrier (SB) detector was positioned at zero degrees and as close as possible to the target (~2 mm). The SB detector was 0.95 mm thick with a surface area of $\approx$ 115 mm^2. A logic signal was derived from the output of this SB detector and this was recorded for each event. The data were sorted for events with and without charged particles and the spectra obtained are shown in fig. 5.14. The Coulomb excitation lines of ^{54}Fe, ^{56}Fe and ^{181}Ta are enhanced in the $\gamma 0p$ spectrum over the $\gamma 1p$ spectrum as these γ-rays should not be coincident with any charged particles. By comparing the intensities of *pn* (^{64}Ga) lines in the $1p$ spectrum with the intensities of the lines in the total spectrum (i.e. sum of $0p$ and $1p$), the efficiency of the SB detector was determined. Table 5.12 shows the intensities of a few prominent *pn* lines and their corresponding efficiencies which give a value of ~57 % for detecting protons from the target. The slightly lower efficiency (55 %) of the 128 keV line is the result of poor timing of the electronics for this low energy γ-ray . The $1p$ condition also includes α-particles as the target was thin enough to allow alpha particles to go through the target and into the SB detector. The target holder and mount for the SB detector were shown in Plates 3.1 to 3.3 in chapter 3.

E_γ (keV)	$\gamma 0p$	$\gamma 1p$	Efficiency (%)
128	68322(374)	84344(399)	55.2(4)
235	19917(280)	27602(309)	58 (1)
367	34691(273)	44977(306)	56.4(6)
483	24682(292)	33027(330)	57 (1)
495	32377(263)	29528(284)	57 (1)
665	22592(250)	29528(284)	57 (1)
1136	8655(160)	11332(191)	57 (1)
1261	5542(132)	7361(161)	57 (2)

Table 5.12 : Intensities (uncorrected for Ge(Li) efficiency) of *pn* lines in the $0p$ and $1p$ spectrum. The efficiency quoted in column 4 is the ratio of the $1p$ intensity to the total intensity ($0p$ + $1p$)

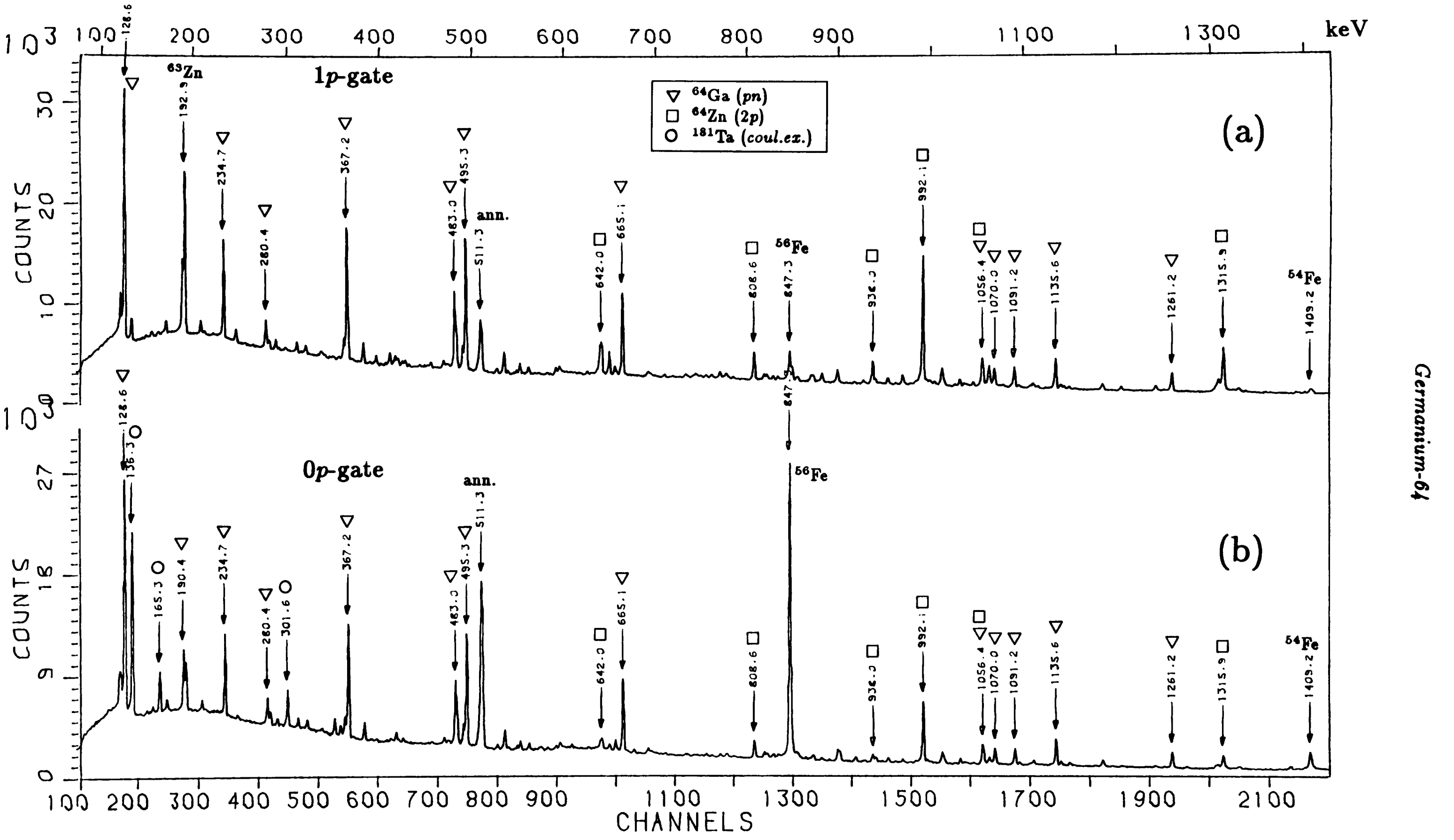


Fig.5.14 : γ-ray spectrum in coincidence with charged particles (a) and in anti-coincidence with charged particles (b).

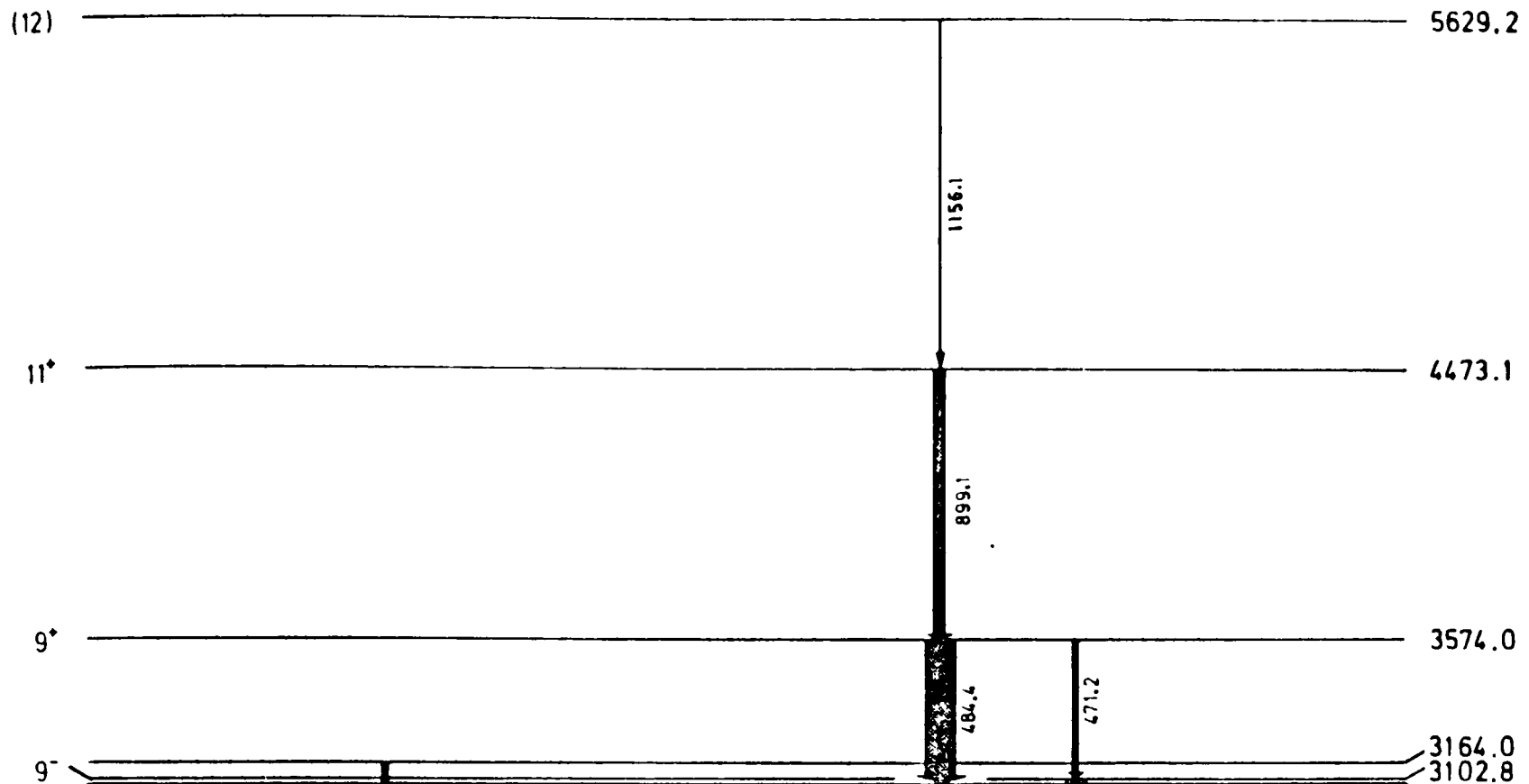
5.6.2 Results & Analysis

The *pn* channel from $^{12}C + ^{54}Fe$ at 35 MeV making ^{64}Ga has been studied and reported by Schmal *et al* [SCH84]. They used a similar quadrant neutron detector to the one used in the present work but placed it at 90° to the beam axis [ROT81]. However, no charged particle detector was used in their experiment. Their level scheme for ^{64}Ga was used to help identify many of the γ-rays observed in the present experiment and this level scheme has been reproduced in fig. 5.15. As can be seen, the level scheme of this odd-odd nucleus is quite complex with many parallel paths de-exciting the nucleus. This proved to be a problem when the total strength of the γ-ray decay was determined as many different γ-ray intensities had to be taken into account and summed.

In this section the corresponding sorting programme is included on the page following the figure of each spectrum. This is to show the exact sorting and co-incidence requirements placed on each spectrum. As was shown in §3.9, TOF n-γ discrimination alone was inadequate to reject all of the non-n events. In order to do so, a n event was made to satisfy both PSD and TOF conditions before being accepted.

The neutron gating was found to be very effective in removing events that had no coincident neutrons present. In fig. 5.16, the singles spectrum is shown in the top half while the n-gated spectrum is shown in the lower half. The lines from Coulomb excitation: ^{181}Ta (137, 166, 302 keV), ^{54}Fe (1409 keV), ^{56}Fe (847 keV) and ^{57}Fe (353 keV) while visibly present in the singles spectrum, have disappeared in the n-gated spectrum. The $2p$ lines from ^{64}Zn have also been effectively suppressed. The ratio of the intensities of the 992 keV line from ^{64}Zn in the n-gated spectrum and the singles spectrum indicate that the breakthrough of non-neutron events is at the one per cent level.

Events in which charged particles were detected were identified by sorting for γ-rays in coincidence with signals from the SB detector. By applying a n-gate



^{64}Ga

Fig.5.15 : Level scheme of ^{64}Ga from [SCH84]. The many parallel paths seen in this odd-odd nucleus made the determination of the gamma decay strength difficult.

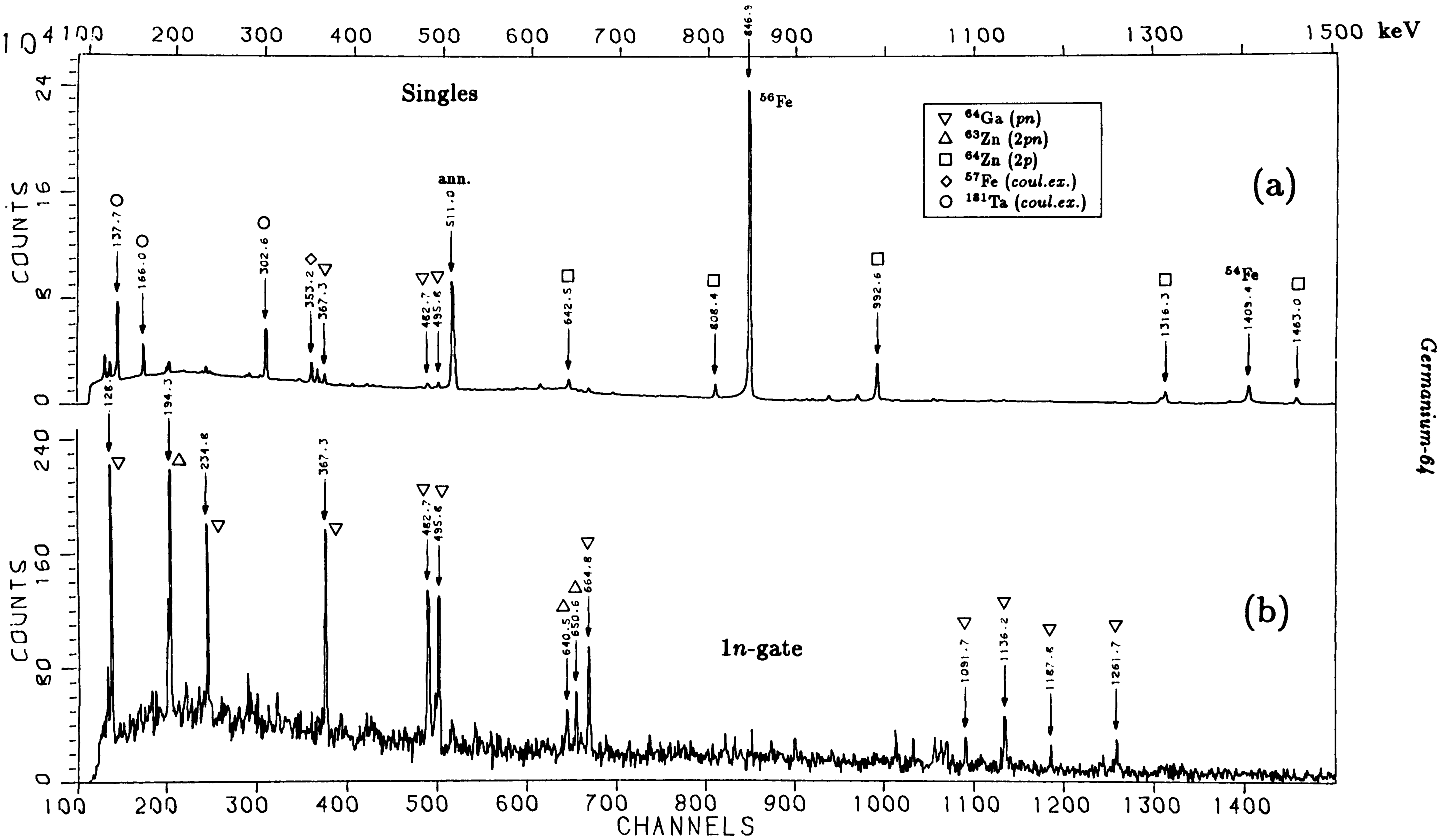


Fig.5.16 : This figure shows the effect of n gating on the data. (a) shows the singles spectrum while (b) shows the n gated spectrum. Many of the strong lines (from Coulomb excitation or charged-particle-only channels) in the singles spectrum disappear in the gated spectrum.

as well provided us with a $1n1p$ spectrum of $n\gamma p$-coincidence events. Conversely, the $1n0p$ spectrum was obtained by vetoing charged particle related events during sorting.

A study was made of all the γ-ray lines from the reaction. This study included γ-ray lines in the singles spectrum and the $1n$, $1n0p$, $2n$ and $2n0p$ spectra. These spectra are shown in figs. 5.17, 5.18, 5.19, 5.20 and 5.21. A list of the γ-rays is given in table 5.13.

For each γ-ray , this list shows whether it is present or absent in the different coincidence spectra studied and this forms a guide to the possible sources of the γ-ray . Comparison with other work allows us to follow through the possible γ-decay paths in the tentative source nucleus to ensure that the other γ-rays in the paths are observed in our spectra. These paths are indicated in the table. No paths are listed for the ^{64}Ga data and the reader is referred to fig. 5.15 for this information. The ratio of the intensities in the $1n1p$ and $1n0p$ spectra were also used to help identify some of the γ-rays. A plot of this ratio is shown in fig. 5.22. The ratios of the γ-rays from ^{63}Zn can be seen to be well separated from the ^{64}Ga and ^{61}Zn γ-rays. The reason is that ^{63}Zn is made via the $2pn$ channel and so is enhanced in the $1n1p$ spectrum over the other two (pn for ^{64}Ga and αn for ^{61}Zn). This fact was used in assigning the ^{63}Zn γ-rays. For instance, for the 1013 and 1091 keV γ-rays, although their energies correspond to ground state transitions in ^{63}Zn (as well as transitions in ^{64}Ga), the intensity ratios indicate that their main components come from transitions in ^{64}Ga.

Figs. 5.23(b) and (a) show the spectra obtained by gating on neutrons with and without charged particles respectively. The $1n0p$ spectrum is seen to contain many pn lines. In order to remove these lines, the difference between the $1n0p$ and $1n1p$ spectra, normalized to the 367 keV line from ^{64}Ga, was taken (fig. 5.23(c)). Two peaks remained after subtraction: one at 128 keV and the other at 903 keV. The peak at 128 keV comes from the difference between the large ^{64}Ga line in both the $1n0p$ and $1n1p$ spectra and is the result of poor timing. The timing for low

Fig.5.17(a) : Singles spectrum

Singles (part b)

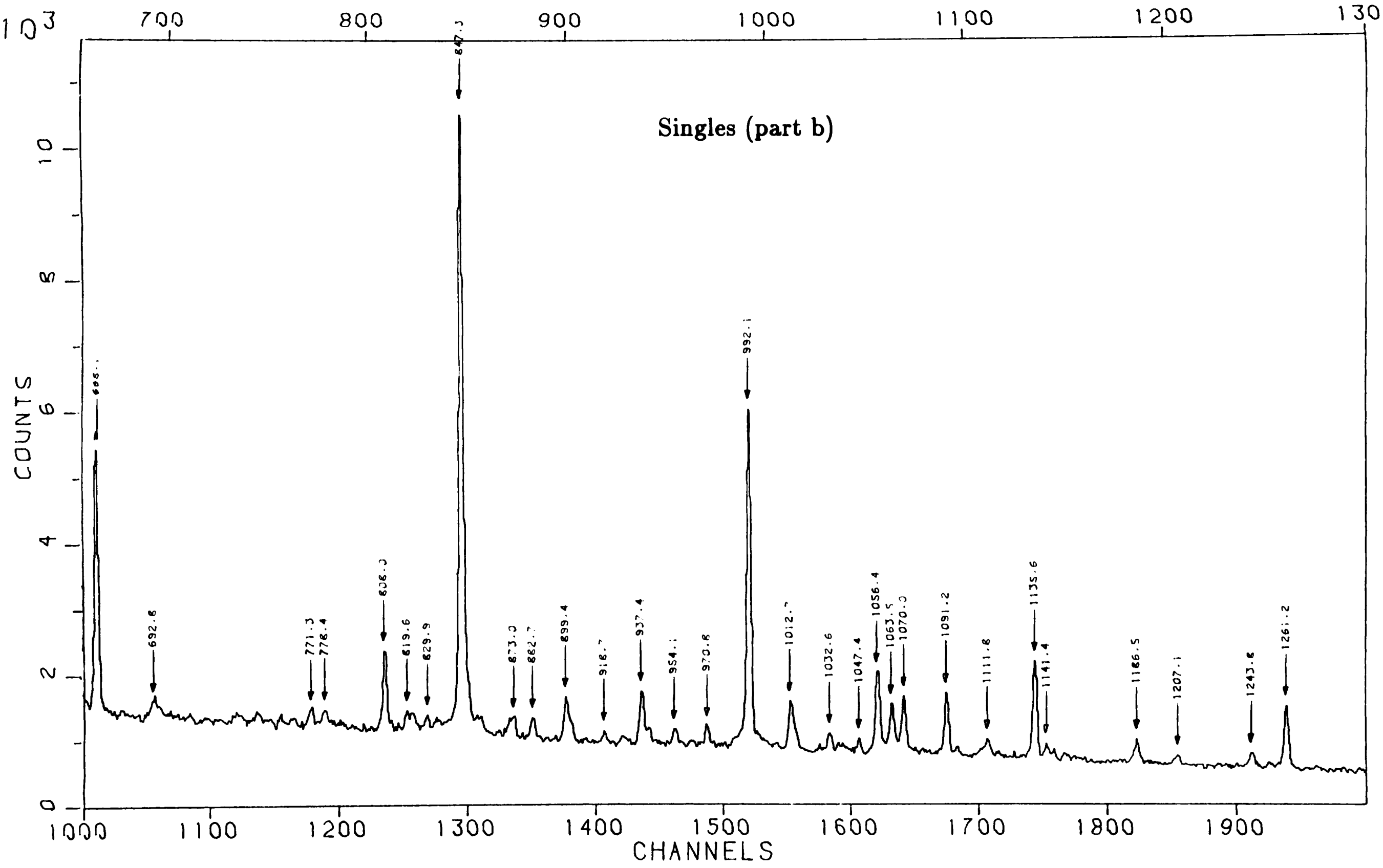


Fig.5.17(b) : Singles spectrum

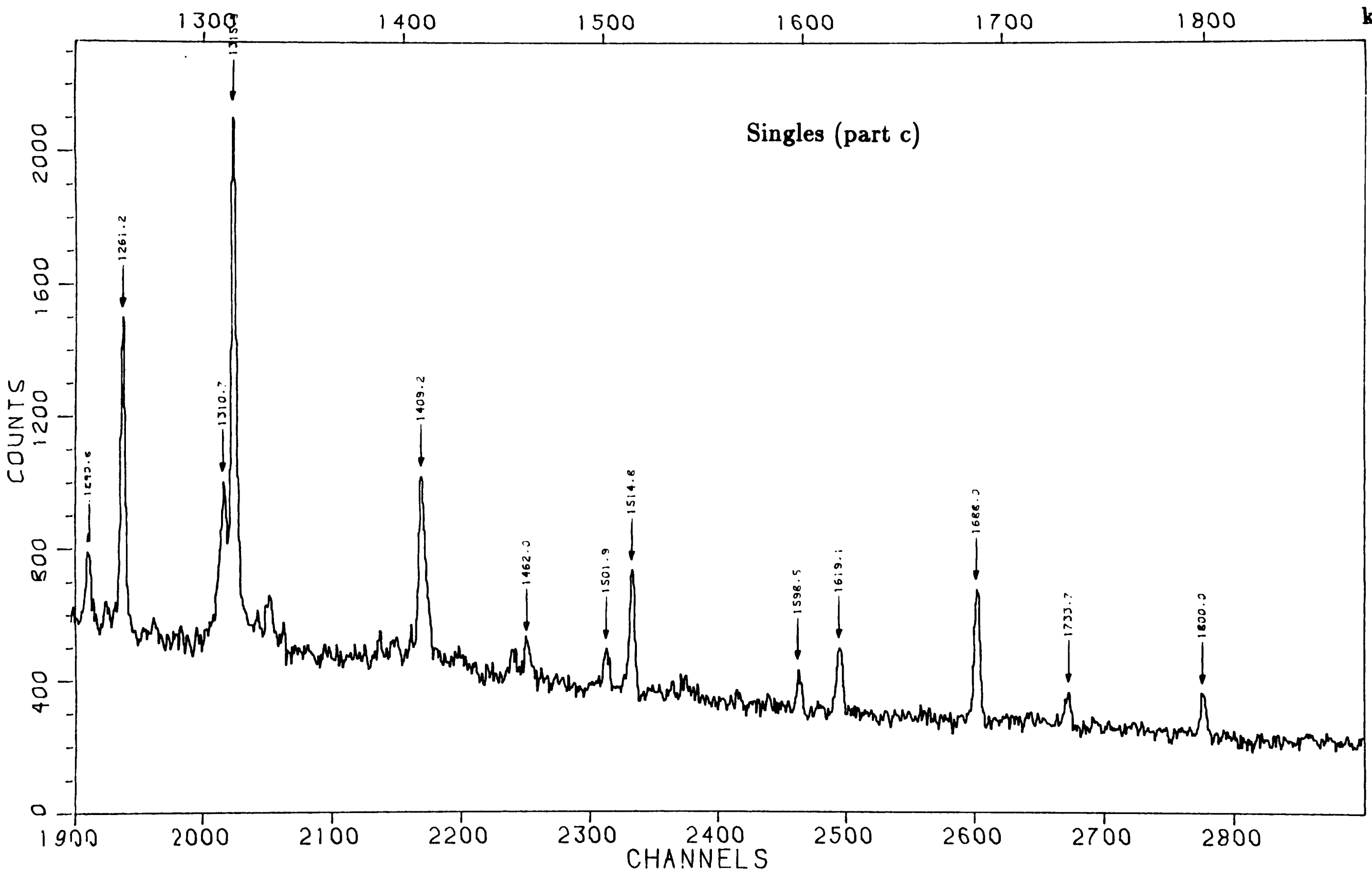


Fig.5.17(c) : Singles spectrum

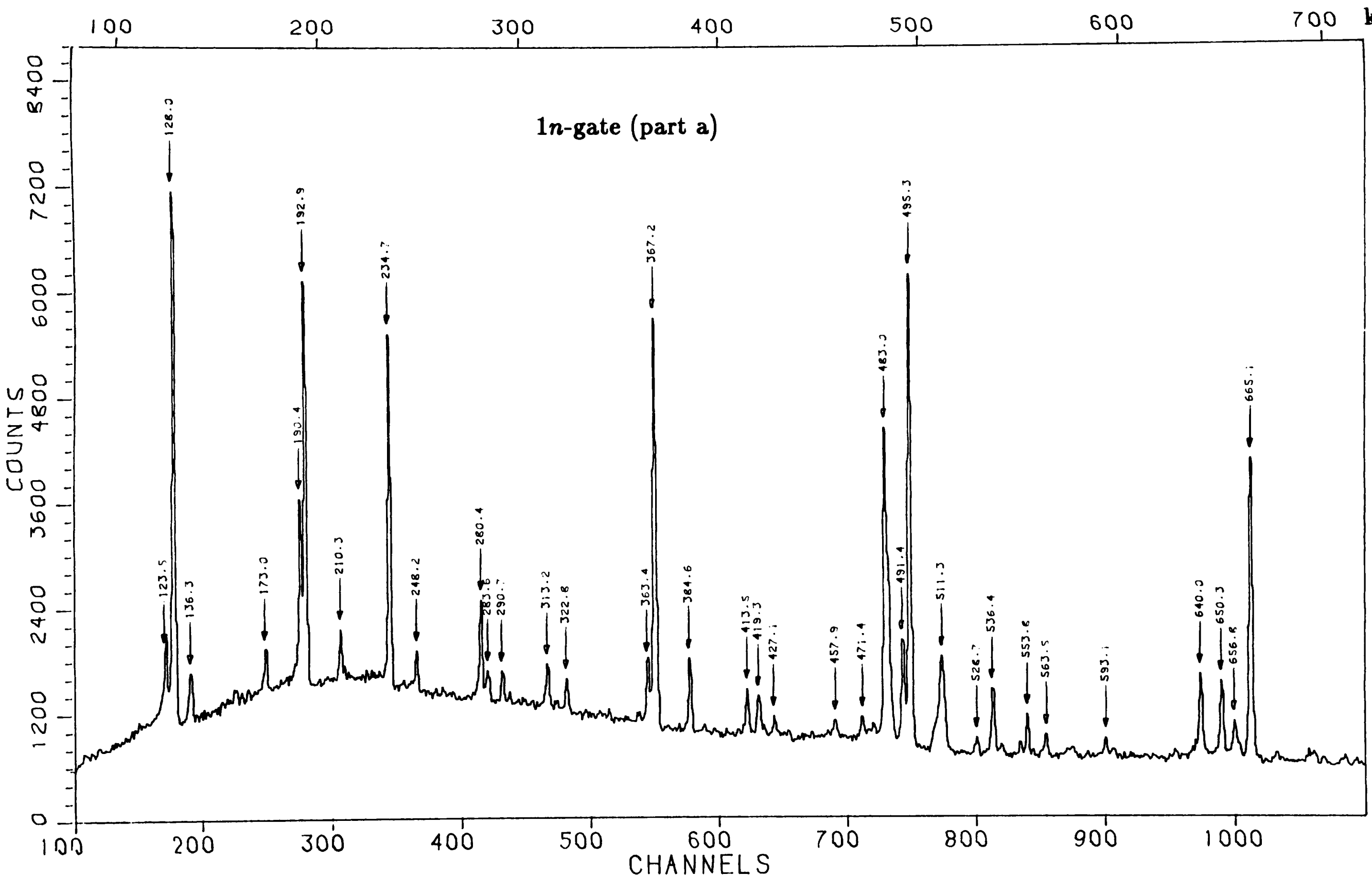


Fig.5.18(a) : 1n spectrum

1*n*-gate (part b)

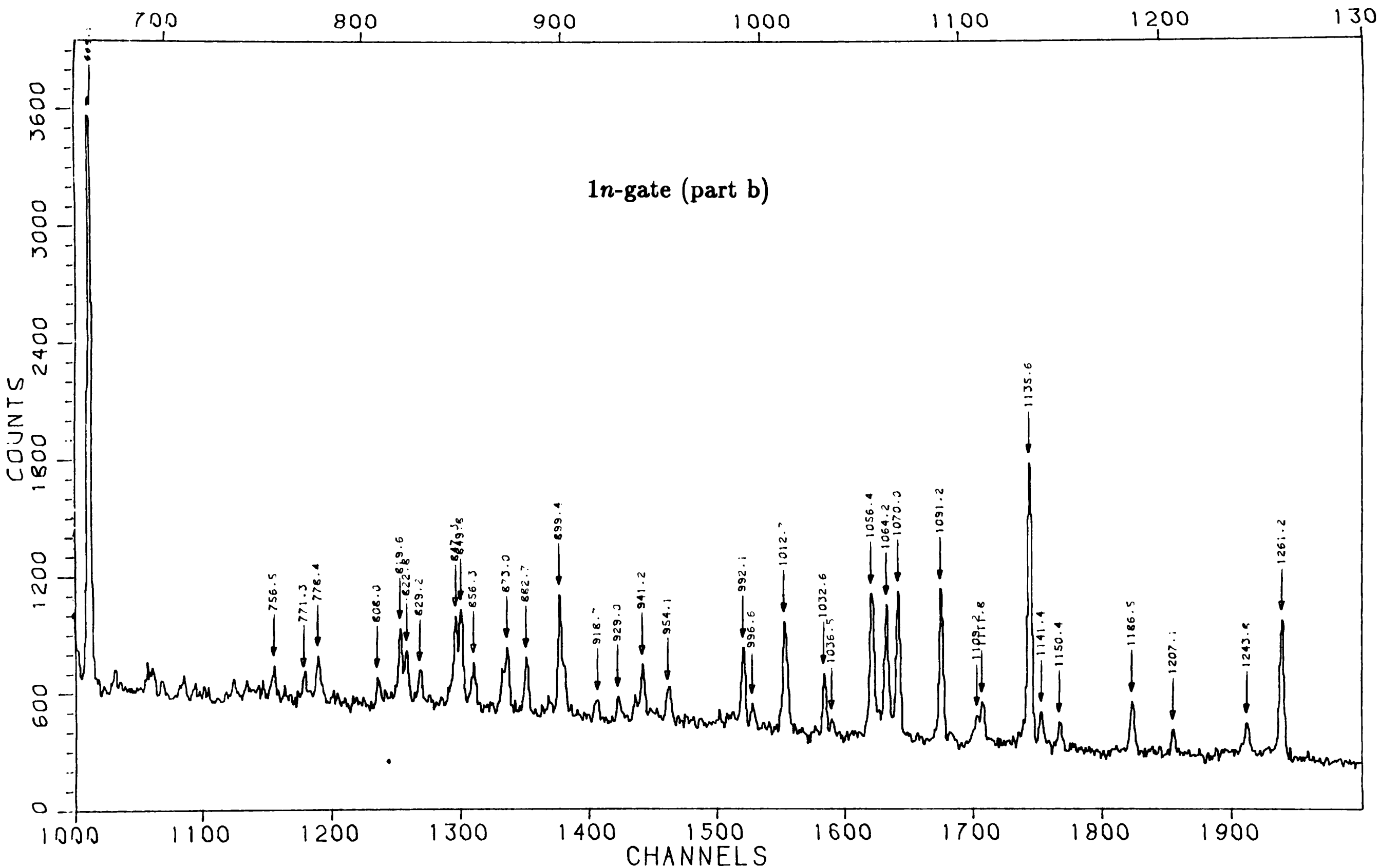


Fig.5.18(b) : 1n spectrum

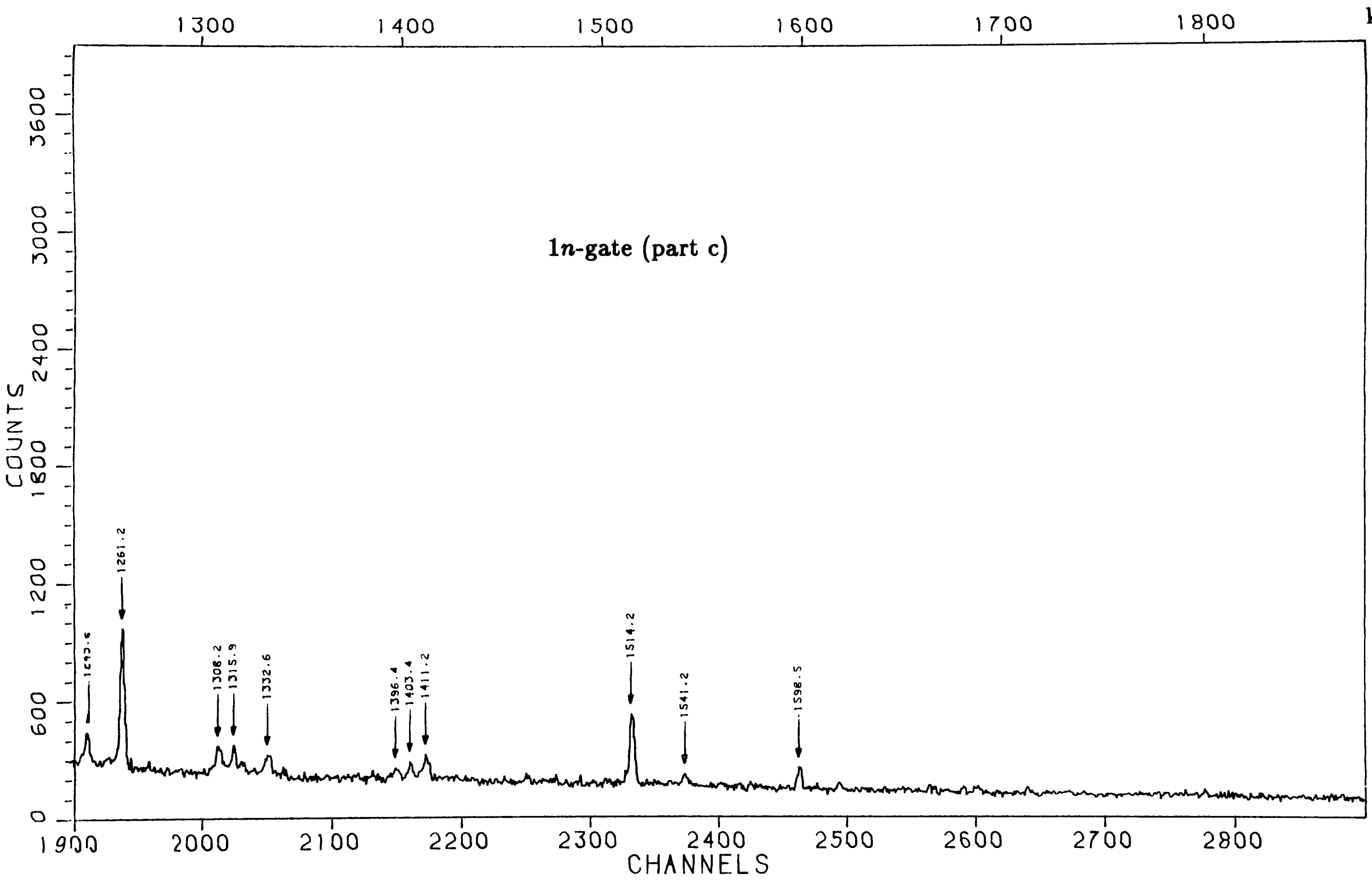


Fig.5.18(c) : 1n spectrum

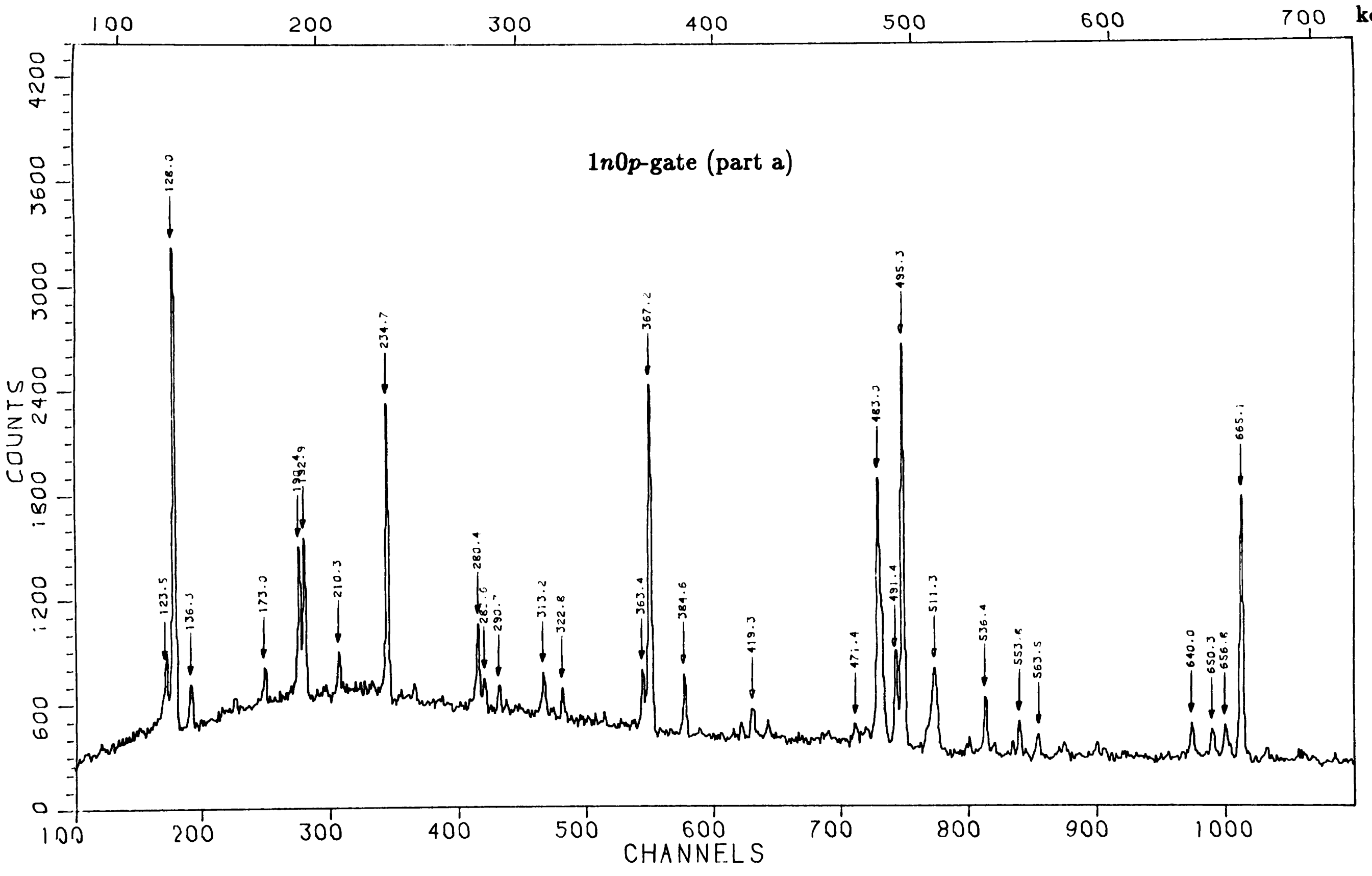


Fig.5.19(a) : 1n0p spectrum

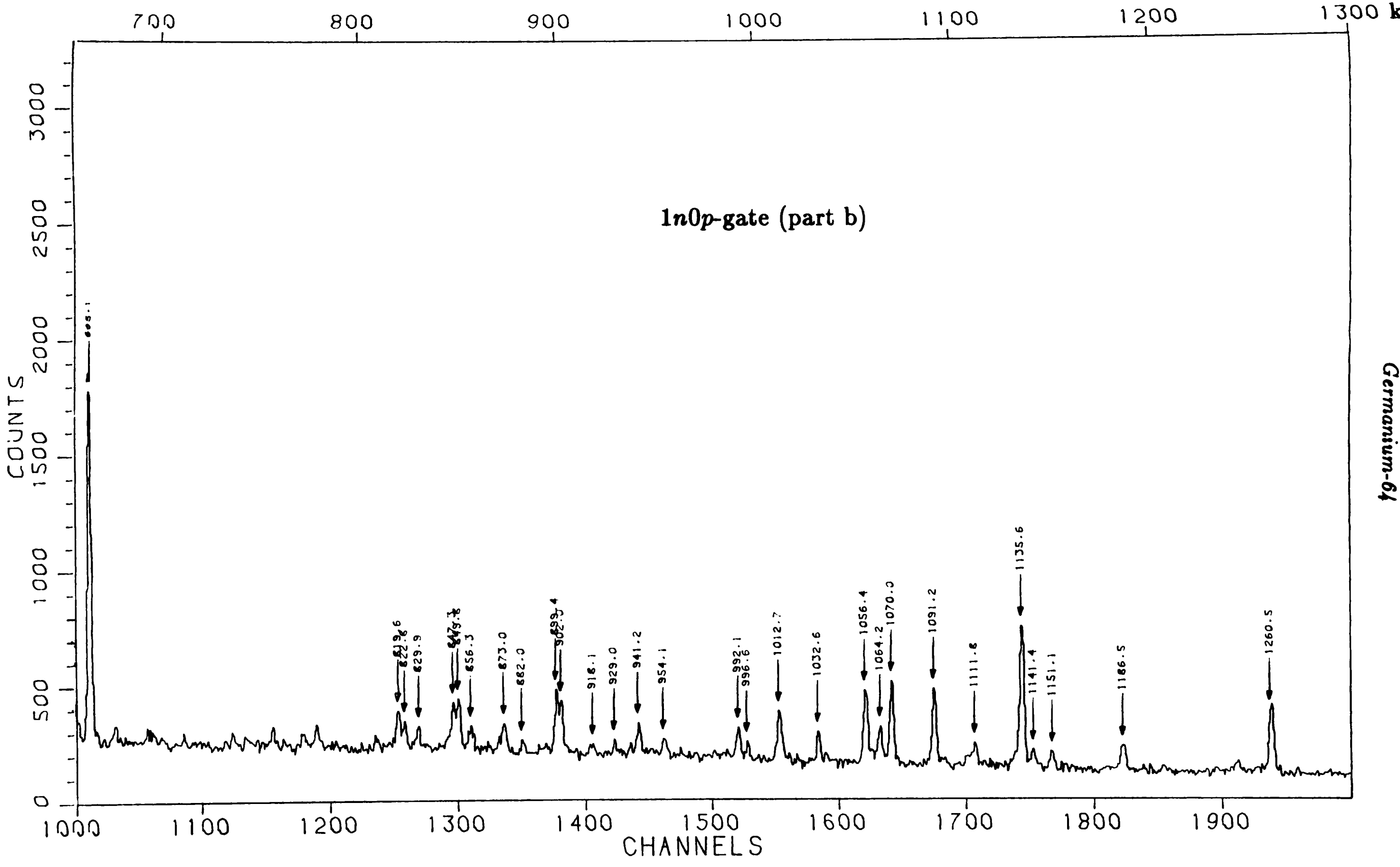


Fig.5.19(b) : 1n0p spectrum

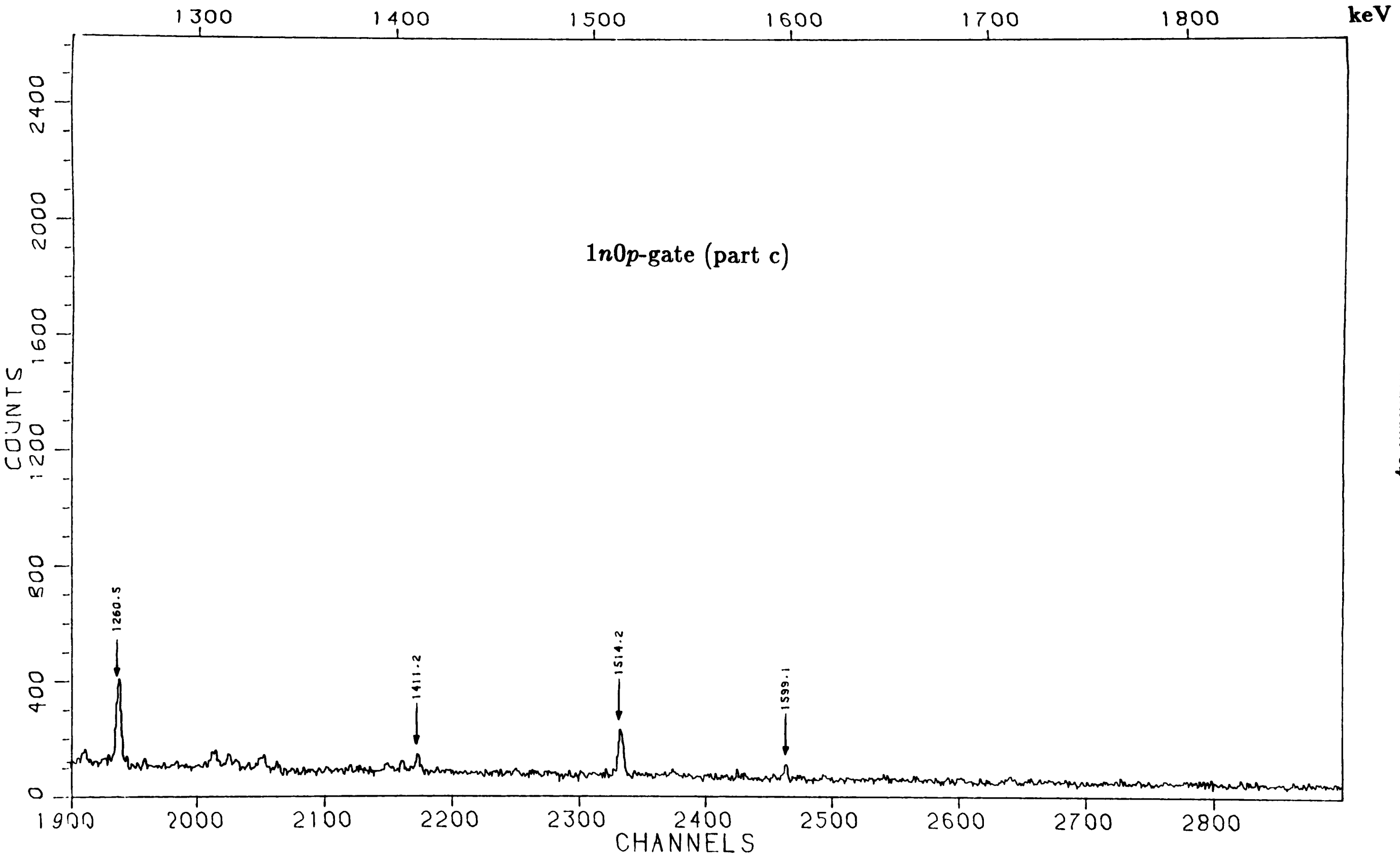


Fig.5.19(c) : 1n0p spectrum

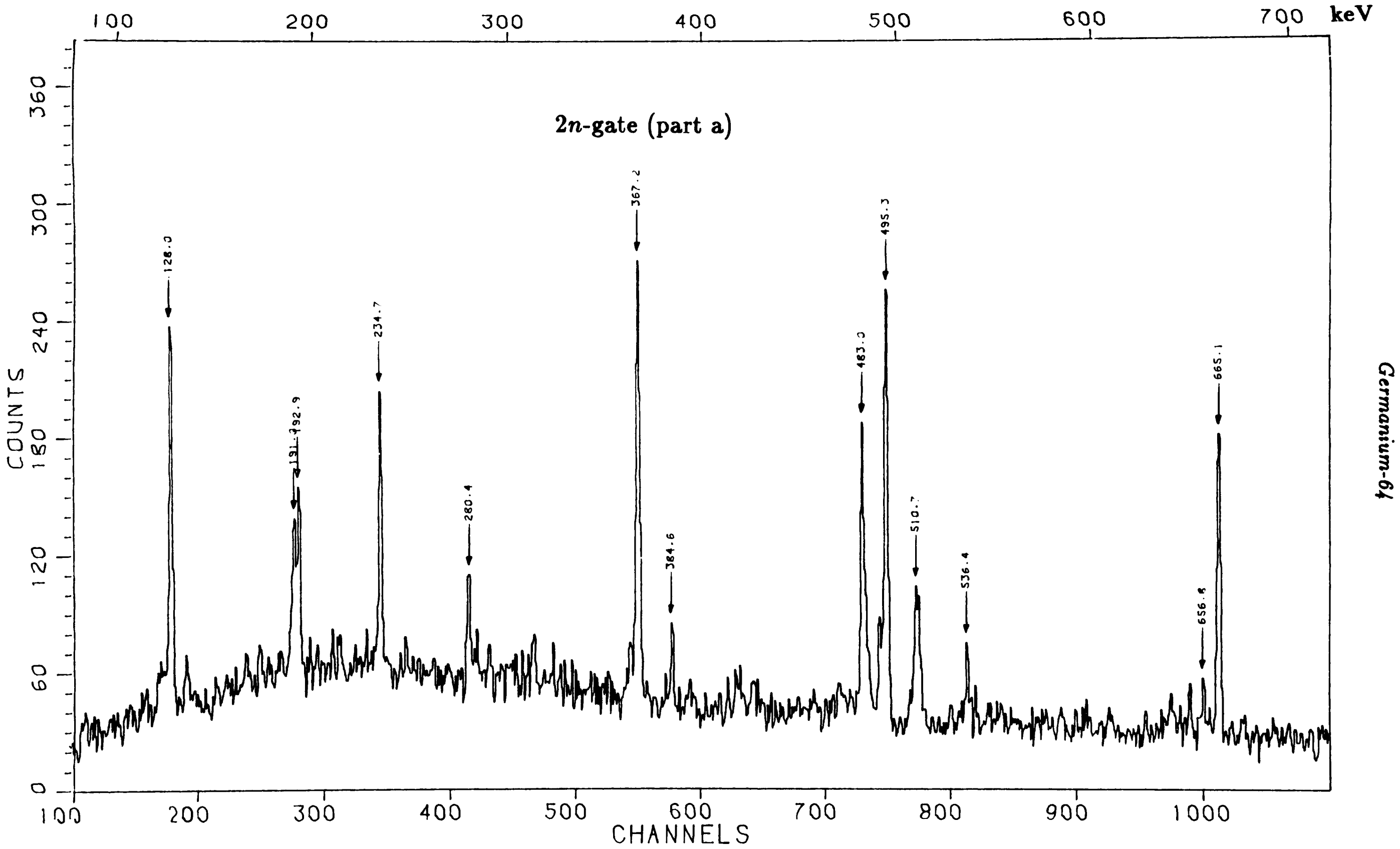


Fig.5.20(a) : 2n spectrum

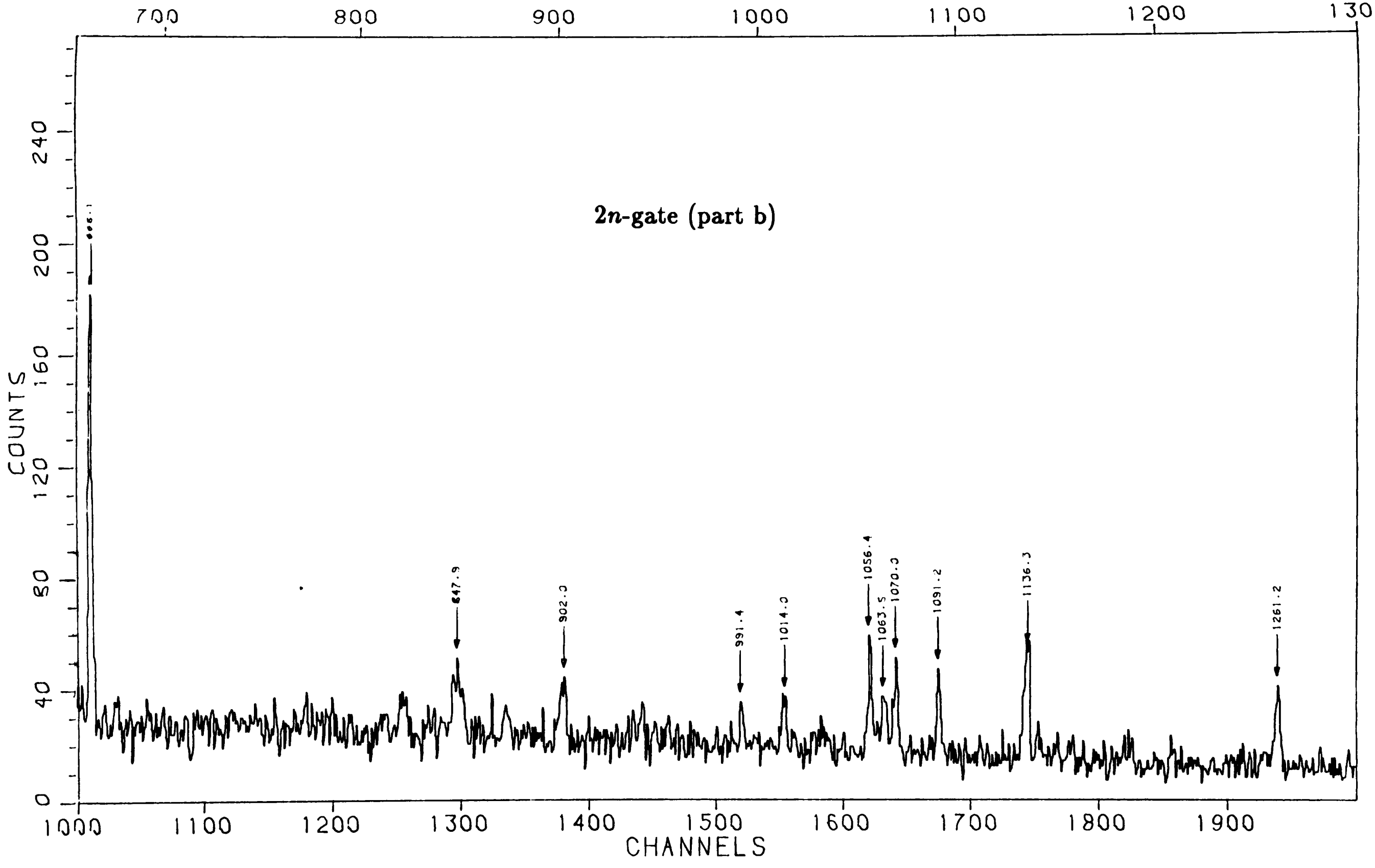


Fig.5.20(b) : 2n spectrum

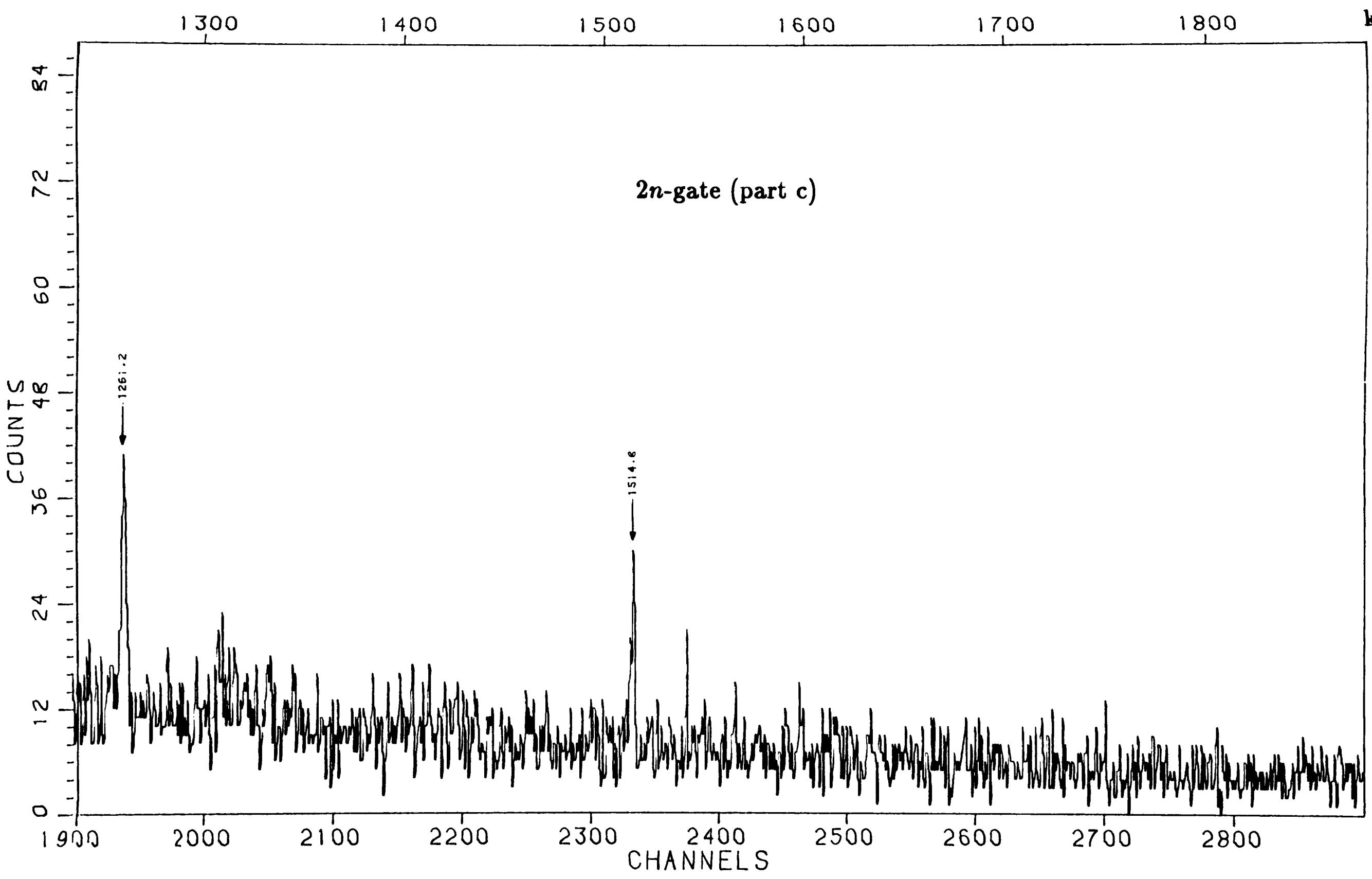


Fig.5.20(c) : 2n spectrum

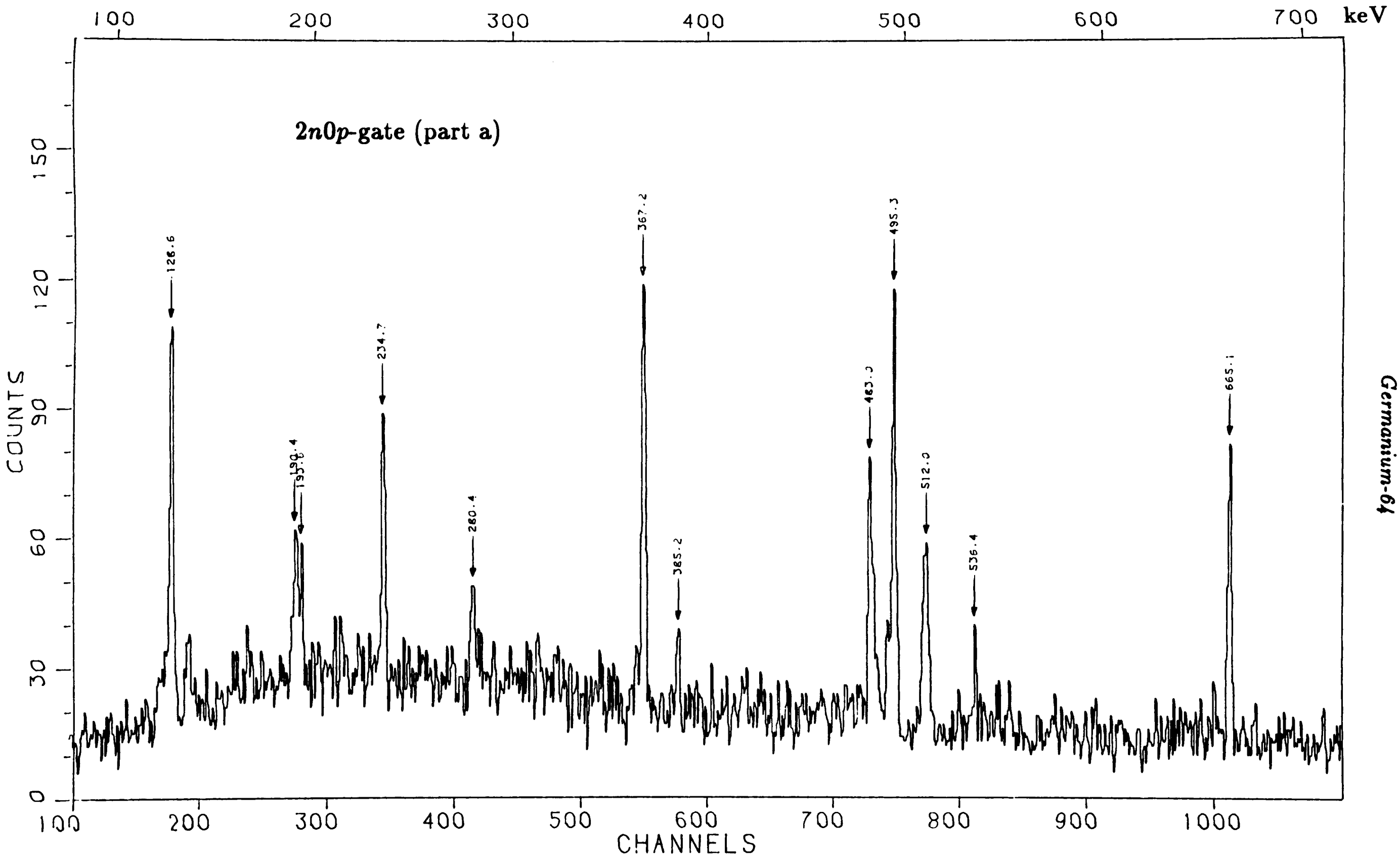


Fig.5.21(a) : 2n0p spectrum

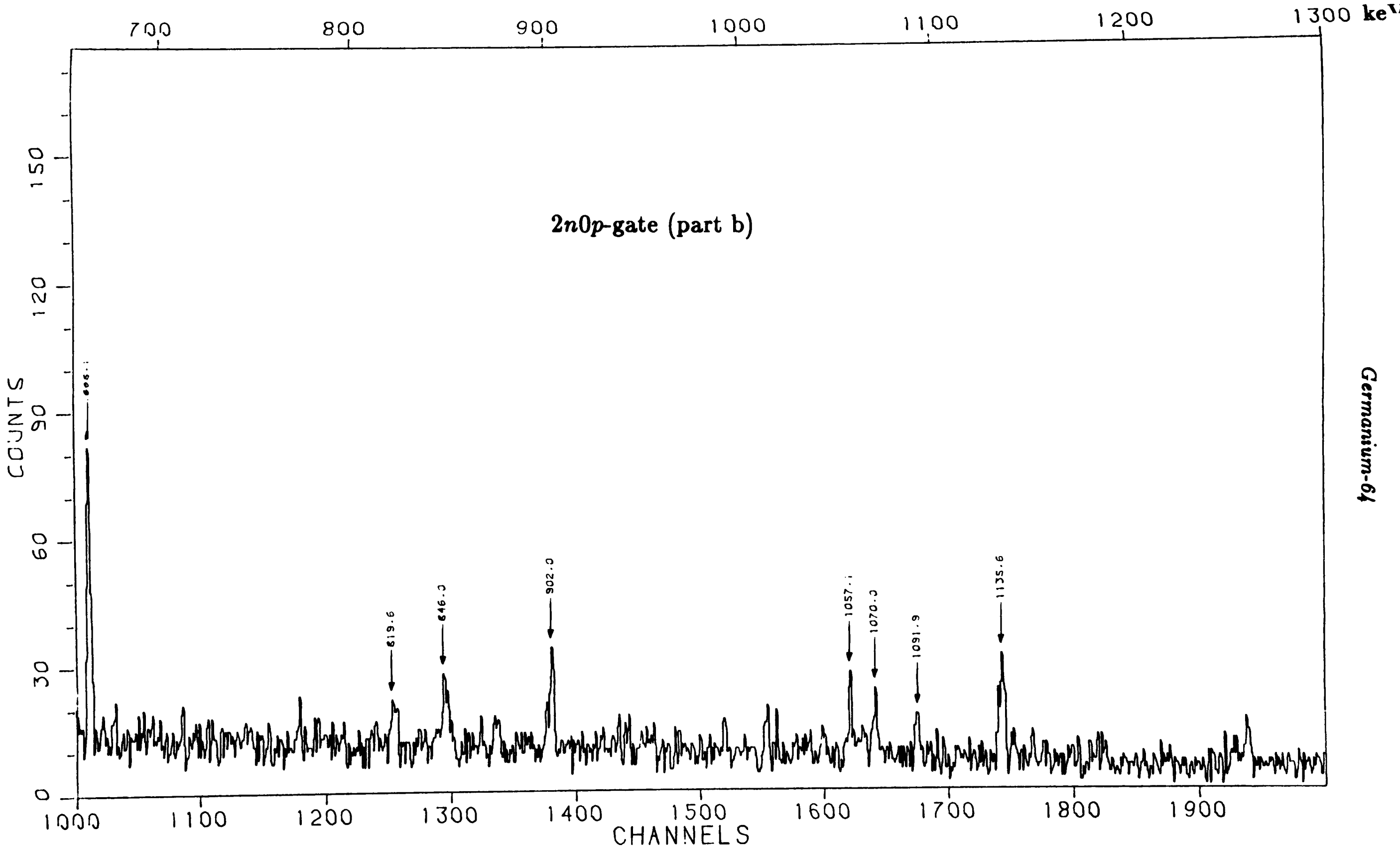


Fig.5.21(b) : 2n0p spectrum

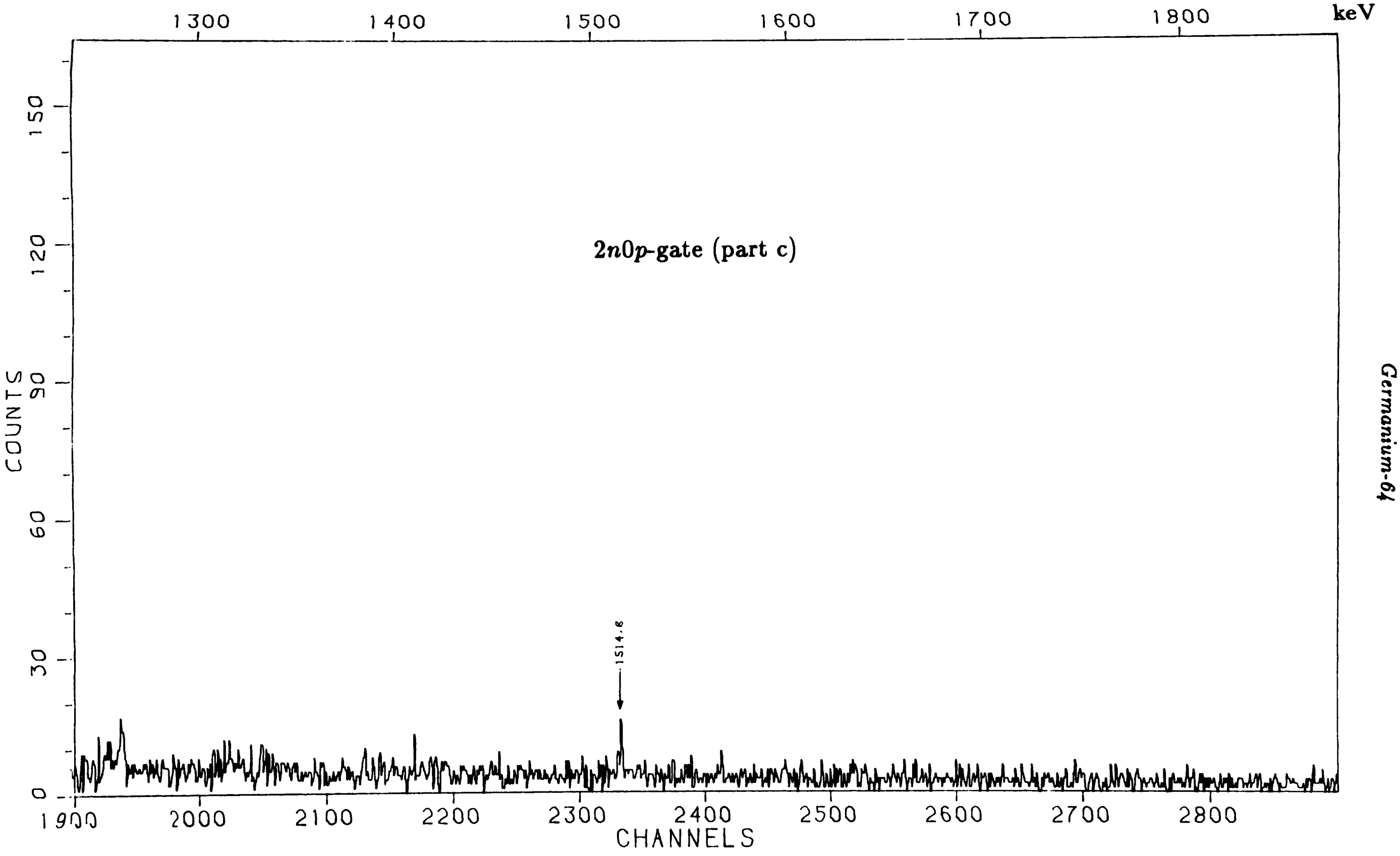


Fig.5.21(c) : 2n0p spectrum

#	E_γ	Nucleus	Ref.	Comments
1)	123.9 *abc*	^{61}Zn	NDS 123.6	→gs {2}
		^{57}Fe	NDS 122	→(14)
2)	128.3 *abcde*	^{64}Ga	NDS 128.1	
			COL 128.1	
3)	136.1 *abcd*	^{181}Ta	NDS 136.1	prob *n* component as well as it is present in *n*-gated spectra →gs {1}
		^{57}Fe	NDS 136	→gs
4)	165.3 *a*	^{181}Ta	NDS 165.4	→3
5)	173.2 *abc*	^{64}Ga	COL 173.0	
6)	190.7 *abcde*	^{64}Ga	COL 190.4	
7)	193.2 *abcde*	^{63}Zn	NDS 192.9	→gs {7}
8)	210.4 *abc*	^{64}Ga	COL 210.1	
		^{61}Cu	NDS 209.6	→102 {1}
9)	234.8 *abcde*	^{64}Ga	COL 234.7	
10)	248.0 *abc*	^{63}Zn	TOI 248.0	→gs
11)	280.1 *abcd*	^{64}Ga	COL 280.1	
12)	283.6 *abc*	^{64}Ga	COL 282.1	
13)	290.8 *abc*	^{64}Ga	COL 290.9	
14)	301.7 *a*	^{181}Ta	NDS 301.5	→gs
15)	313.2 *abc*	^{64}Ga	COL 313.3	
16)	322.9 *abc*	^{64}Ga	COL 323.1	
17)	339.3 *a*	^{61}Cu	NDS 340	→68 {1}
18)	352.5 *a*	^{57}Fe	NDS 352.4	→(14)
		^{61}Cu	NDS 352.4	→8→102
19)	359.1 *a*	^{64}Zn	NDS 359	feeds 1276, 1387, 2195 & 3188 keV γ-rays which are not seen in the spectra →(1387)→103 | →(1387)→51→69 etc.
20)	363.8 *abc*	^{64}Ga	COL 363.5	
21)	367.2 *abcde*	^{64}Ga	NDS 367.06	
			COL 367.0	
22)	384.6 *abcde*	^{64}Ga	COL 384.5	
23)	398.4 *a*	^{64}Zn	NDS 398.2	→96→65→103 | →96→65→51→69
24)	413.5 *ab*	^{63}Zn	TOI 415	→44 {2}
25)	419.4 *abc*	^{64}Ga	COL 419.2	
26)	427.2 *b*	^{64}Ga	NDS 427.0	populated in our β-decay expt. →gs
27)	457.8 *ab*	^{63}Zn	NDS 457.9	→7
28)	471.1 *abc*	^{64}Ga	COL 471.2	
29)	483.0 *abcde*	^{64}Ga	COL 482.8	
30)	484.8 *abcde*	^{64}Ga	COL 484.4	
31)	491.8 *abcde*	^{64}Ga	COL 491.6	
32)	495.3 *abcde*	^{64}Ga	NDS 495.15	
			COL 495.1	
33)	511.2 *abcde*	e^+e^-		annihilation γ-ray
34)	* 528.7 *ab*			
35)	536.5 *abcde*	^{64}Ga	COL 536.5	
36)	550.2 *abc*	^{64}Ga	COL 550.4	
37)	552.8 *abc*	^{64}Ga	COL 553.5	
38)	563.0 *abc*	^{64}Ga	COL 563.0	
39)	583.5 *a*	^{64}Ga	COL 584.3	very weak in *b* & *c*
		^{61}Cu	NDS 583.5	→17→68→69

Table 5.13 (continued)

#	E_γ	Nucleus	Ref.	Comments
40)	592.7 *ab*	^{64}Ga	COL 592.4	
41)	* 596.6 *a*			
42)	640.3 *abc*	^{63}Zn	NDS 640	→76 | →58→7 | →24→44 {1}
43)	642.0 *a*	^{64}Zn	NDS 641.4	→101→90→69 {1}
44)	650.5 *abc*	^{63}Zn	NDS 650.2	→gs {4}
45)	* 656.8 *abc*			
46)	664.8 *abcde*	^{64}Ga	NDS 663.89	
			COL 664.6	
47)	693.1 *a*	^{64}Ga	COL 693.2	
48)	* 756.4 *b*			
49)	771.4 *ab*	^{64}Ga	COL 771.2	
		^{64}Zn	NDS 770.7	→90→69
50)	778.3 *ab*	^{64}Ga	COL 777.7	
51)	808.3 *ab*	^{64}Zn	NDS 807.85	→69 {5}
52)	819.5 *abcde*	^{64}Ga	COL 819.1	
53)	822.6 *b*	^{64}Ga	COL 822.0	
54)	* 829.5 *ab*			
55)	847.1 *abcde*	^{56}Fe	TOI 846.8	→gs {2}
56)	849.9 *bc*	^{64}Ga	COL 849.8	
57)	856.1 *bc*	^{64}Ga	COL 856.2	
58)	870.8 *abcd*	^{63}Zn	NDS 871	→7
59)	873.1 *abcd*	^{61}Zn	NDS 873	→1
60)	882.7 *ab*	^{63}Zn	NDS 881	→42→76 | →42→58→7 | →24→44
61)	899.4 *abcd*	^{64}Ga	COL 899.1	
62)	901.9 *abcde*	^{64}Ge	OOI	→gs
63)	918.8 *abc*	^{64}Zn	NDS 918.9	→69; present in *b* & *c* as well thus probably *n* component. Poss. ^{64}Ga using ($1n1p/1n0p$)
64)	929.0 *b*	^{64}Ga	COL 928.7	
65)	937.5 *a*	^{64}Zn	NDS 937.1	→103 {2}
			NDS 936.9	→51→69
66)	941.2 *bcd*	^{64}Ga	COL 940.7	
67)	* 954.4 *abc*			
68)	970.5 *a*	^{61}Cu	NDS 970.0	→gs {2}
		^{64}Ga	COL 969.6	
69)	991.9 *abcd*	^{64}Zn	NDS 991.54	→gs {14}
70)	* 996.6 *bc*			*n*-related channel; no definite assignment.
71)	1013.2 *abcde*	^{64}Ga	NDS 1012.4	→29→21→2; more likely (using $n1p/n0p$)
		^{63}Zn	NDS 1013	→7
72)	1032.5 *abc*	^{64}Ga	COL 1032.1	
73)	* 1036.4 *bc*			*n*-related channel; no definite assignment.
74)	1047.4 *a*	^{64}Zn	NDS 1046	→43→101→90→69
75)	1056.7 *abcde*	^{64}Zn	NDS 1056.0	→100→90→69
		^{64}Ga	COL 1056.3	
76)	1063.9 *abcd*	^{63}Zn	TOI 1065.2	→gs {2}
77)	1070.0 *abcde*	^{64}Ga	COL 1069.5	
78)	1091.3 *abcd*	^{63}Zn	NDS 1091.6	→7
		^{64}Ga	COL 1091.0	more likely (using $n1p/n0p$).
79)	1109.3 *abc*	^{64}Ga	COL 1108.8	
80)	1112.1 *abcd*	^{64}Ga	COL 1111.0	
81)	1135.6 *abcde*	^{64}Ga	COL 1135.3	
82)	1141.9 *ab*	^{61}Zn	NDS 1141	→1; not conclusive as ($n1p/n0p$) large.

Table 5.13 (continued)

#	E_γ	Nucleus	Ref.	Comments
83)	1150.7 *bc*	^{64}Ga	OOI	using (1*n*1*p*/1*n*0*p*)
84)	1186.6 *abc*	^{64}Ga	COL 1186.1	
85)	1206.7 *ab*	^{63}Zn	NDS 1206.8	→gs
86)	1243.9 *ab*	^{63}Zn	NDS 1245	→7
87)	1260.9 *abcde*	^{64}Ga	COL 1260.5	
88)	* 1308.2 *b*			
89)	1310.7 *a*	^{61}Cu	NDS 1310.54	→gs
90)	1315.9 *ab*	^{64}Zn	NDS 1315.2	→69 {5}
91)	1332.8 *abc*	^{64}Ga	COL 1332.8	
92)	* 1403.6 *b*			possibly ^{64}Ga; using (1*n*1*p*/1*n*0*p*)
93)	1409.4 *a*	^{54}Fe	NDS 1408.1	→gs
94)	1411.9 *abc*	^{64}Ga	COL 1411.5	
95)	1461.9 *a*	^{64}Zn	NDS 1462	→103 | →51→69
96)	1501.7 *a*	^{64}Zn	NDS 1500.4	→65→103 | →65→51→69 {1}
97)	1514.7 *abcde*	^{64}Ga	COL 1514.1	
98)	1541.2 *b*	^{64}Ga	OOI	using (1*n*1*p*/1*n*0*p*)
99)	1598.9 *abc*	^{63}Zn	NDS 1599.5	→44
100)	1619.1 *a*	^{64}Zn	NDS 1618.2	→69 {1}
101)	1688.0 *a*	^{64}Zn	NDS 1686.5	→90→69 {2}
102)	1733.1 *a*	^{61}Cu	NDS 1732.7	→gs {2}
103)	1800.2 *a*	^{64}Zn	NDS 1799.4	→gs {5}

KEY to the table:

NDS	–	Nuclear Data Sheets.
COL	–	Cologne data [SCH84].
TOI	–	Table of Isotopes, 1978.
OOI	–	present work.
→gs	–	ground state transition.
→88	–	transition feeding # 88.
→(432)	–	transition to state which decays via a 432 keV γ-ray not listed in this table.
|	–	the vertical bar separates the different γ-decay paths listed.
{n}	–	number of other γ-rays in this table feeding this γ-ray.
*	–	unidentified.
a	–	observed in ningles.
b	–	observed in *n* spectrum.
c	–	observed in *n*0*p* spectrum.
d	–	observed in 2*n* spectrum.
e	–	observed in 2*n*0*p* spectrum.

Table 5.13 : Catalogue of all the γ-ray lines observed in the ^{64}Ge experiment.

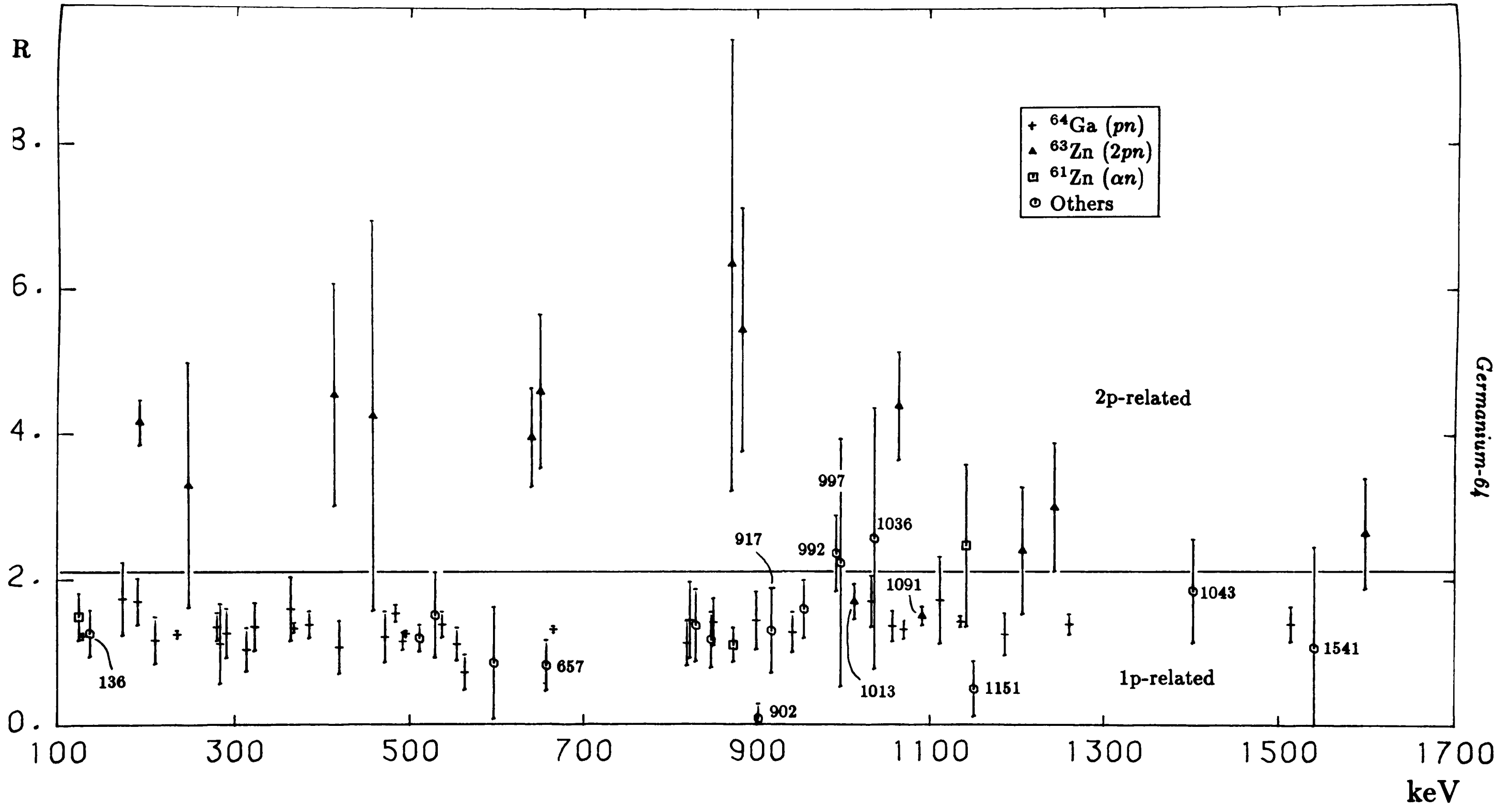


Fig.5.22 : Ratio (R) of the intensities of the γ-ray peaks in the $1n1p$ to those in the $1n0p$ spectrum for selected peaks. The line separating the p and $2p$-related points is mainly to guide the eye.

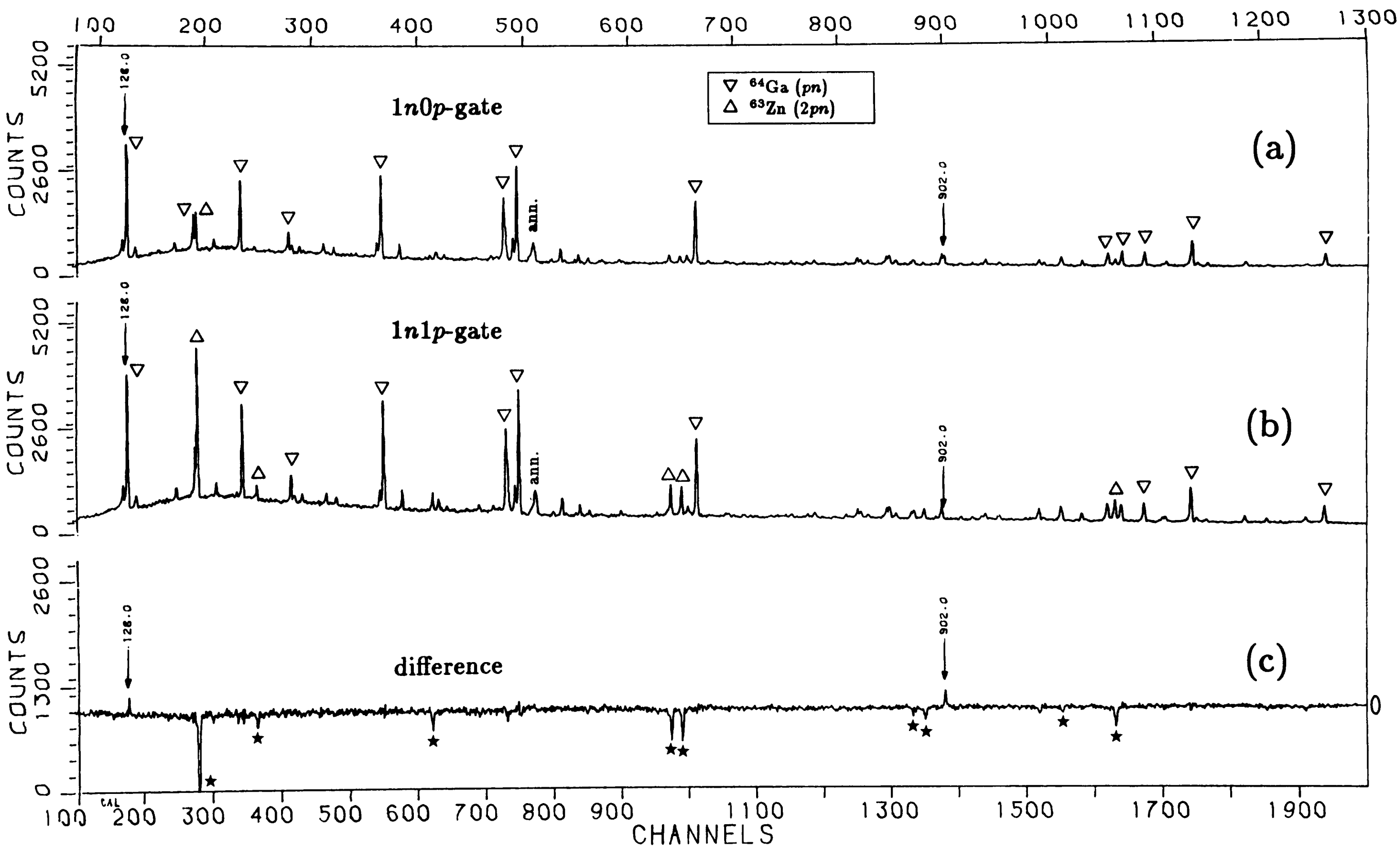


Fig.5.23 : *n*-gated spectra with and without charged particles : (a) 1*n*0*p* (b) 1*n*1*p* and (c) their difference (the spectra were normalized to the 367 keV line before subtraction). A constant level is added to show the oversubtraction but the true zero is indicated.

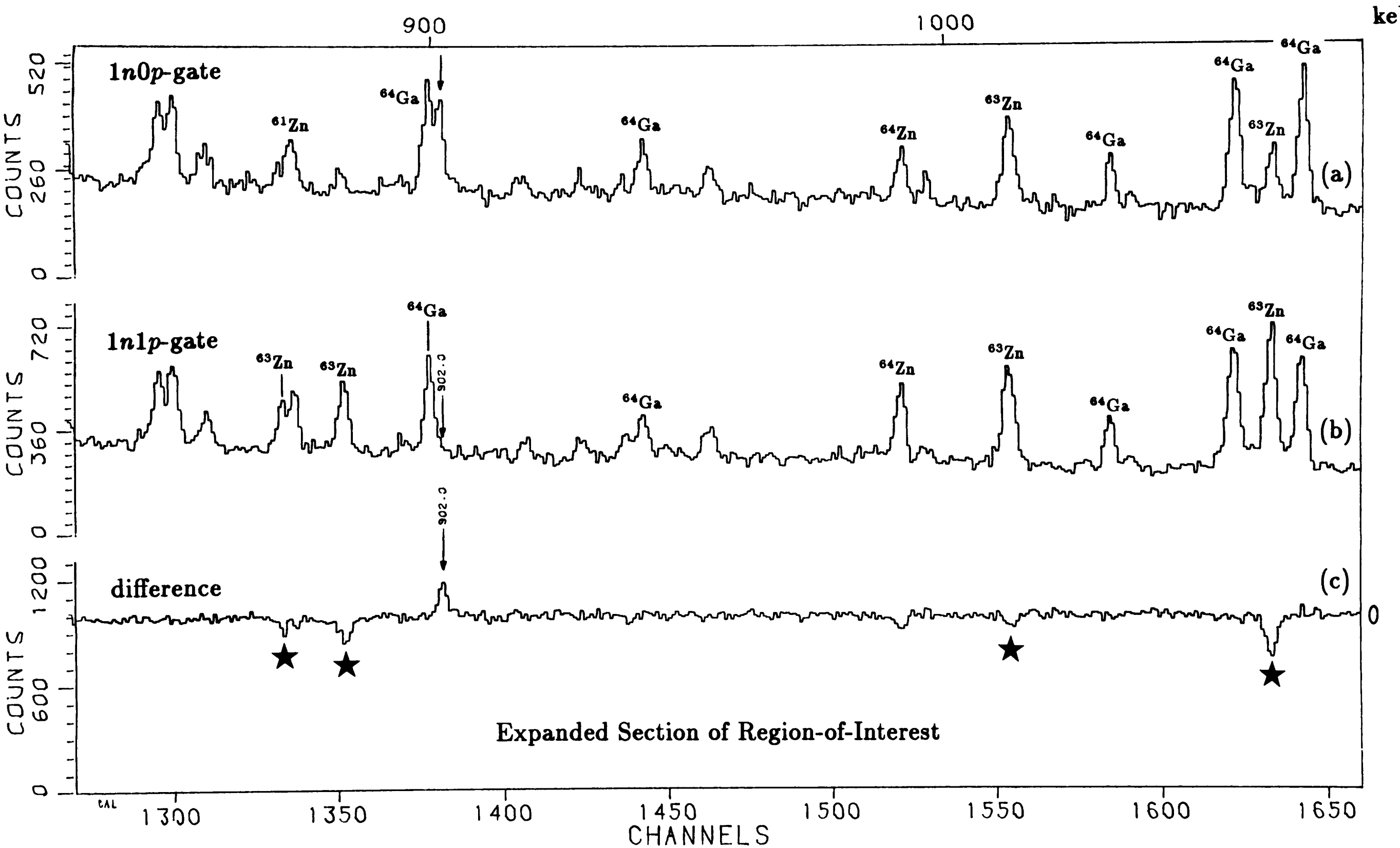


Fig.5.24 : Expanded section of the (a) 1*n*0*p* and (b) 1*n*1*p* spectra and (c) their difference normalized to the 367 keV line.

```
001  !      Sorting programme to look for 1n channel
002  !      with/without protons.
003  !
004  !      Window 0 - TOF1
005  !      Window 1 - TOF2
006  !      Window 2 - TOF3
007  !      Window 3 - TOF4
008  !      Window 4 - TOF5
009  !      Window 5 - PSD1
010  !      Window 6 - PSD2
011  !      Window 7 - PSD3
012  !      Window 8 - PSD4
013  !      Window 9 - PSD5
014  !      Window 10 - 1N0P
015  !      Window 11 - 1N1P
016  !
017   TITLE S903
018   OR 10 11 R1              !check to see that it's 1n
019   IF R1
020    AND 0 5 R2              !check to see that
021    AND 1 6 R3              !they satisfy BOTH
022    AND 2 7 R4              !TOF and PSD
023    AND 3 8 R5
024    AND 4 9 R6
025    OR R2 R3 R4 R5 R6 R7    !check that it's at least 1n
026    IF R7
027      IF 10                 !W#10=1N0P
028        INC 0 P15 0 1       !gamma 1
029        INC 1 P16 0 1       !gamma 2
030        INC 2 P17 0 1       !gamma 3
031        INC 3 P18 0 1       !gamma 4
032      ENDIF
033      IF 11                 !W#11=1N1P
034        INC 4 P15 0 1       !gamma 1
035        INC 5 P16 0 1       !gamma 2
036        INC 6 P17 0 1       !gamma 3
037        INC 7 P18 0 1       !gamma 4
038      ENDIF
039    ENDIF
040   ENDIF
041   END
```

Fig.5.23.SOL : Sorting programme for 1*n*-gated spectra.

energy γ-rays is substantially worse than the higher energy ones because of the limited dynamic range of the constant fraction circuits used for time pick-off. Additional evidence for this poor timing is shown by the slightly lower proton detection efficiency for the 128 keV line (discussed in the previous section). Although the efficiency was not significantly reduced, the large intensity of the peak implied that even a small change in the efficiency was noticeable in the subtracted spectrum. When the TOF data were gated by different γ-rays from the *pn* channel, the resulting spectra showed that the number of counts under the TOF peak for the 128 keV line was about a factor of 3 down when compared with the TOF peaks gated by the other lines. This is indicative of the loss of data for the 128 keV line through poor timing.

The peak at 902 keV comes from a peak which forms a doublet with the 899 keV line from ^{64}Ga. An expanded section of the region of interest is shown in fig. 5.24. There is a clear doublet in the $1n0p$ spectrum but only one peak in the $1n1p$ spectrum. The 902 keV line does not correspond to any known transition in any of the evaporation residues from ^{54}Fe + ^{12}C. It is not consistent with a *pn* channel as all the γ-ray peaks from the *pn* channel disappear on subtraction. Its noticeable absence in the $1n1p$ spectrum strongly suggest that its exit channel is free of charged particles.

The subtracted spectrum also shows several negative peaks (marked with a *) which come from the $2pn$ channel leading to ^{63}Zn. These lines over-subtract due to the higher charged particle detection probability of this channel.

With reference to the 128 keV line in the subtracted spectrum, if instead of normalizing the $1n0p$ and $1n1p$ spectra to the 367 keV line, we were to normalize the spectra to the 128 keV line, then the subtracted spectrum has only one peak remaining in it. In this case, however, some of the *pn* lines begin to over-subtract, as seen in fig. 5.25. This figure shows the subtracted spectra with the $1n0p$ and $1n1p$ spectra normalized to the 128 keV (part (a)) and 367 keV (part (b)) γ-rays.

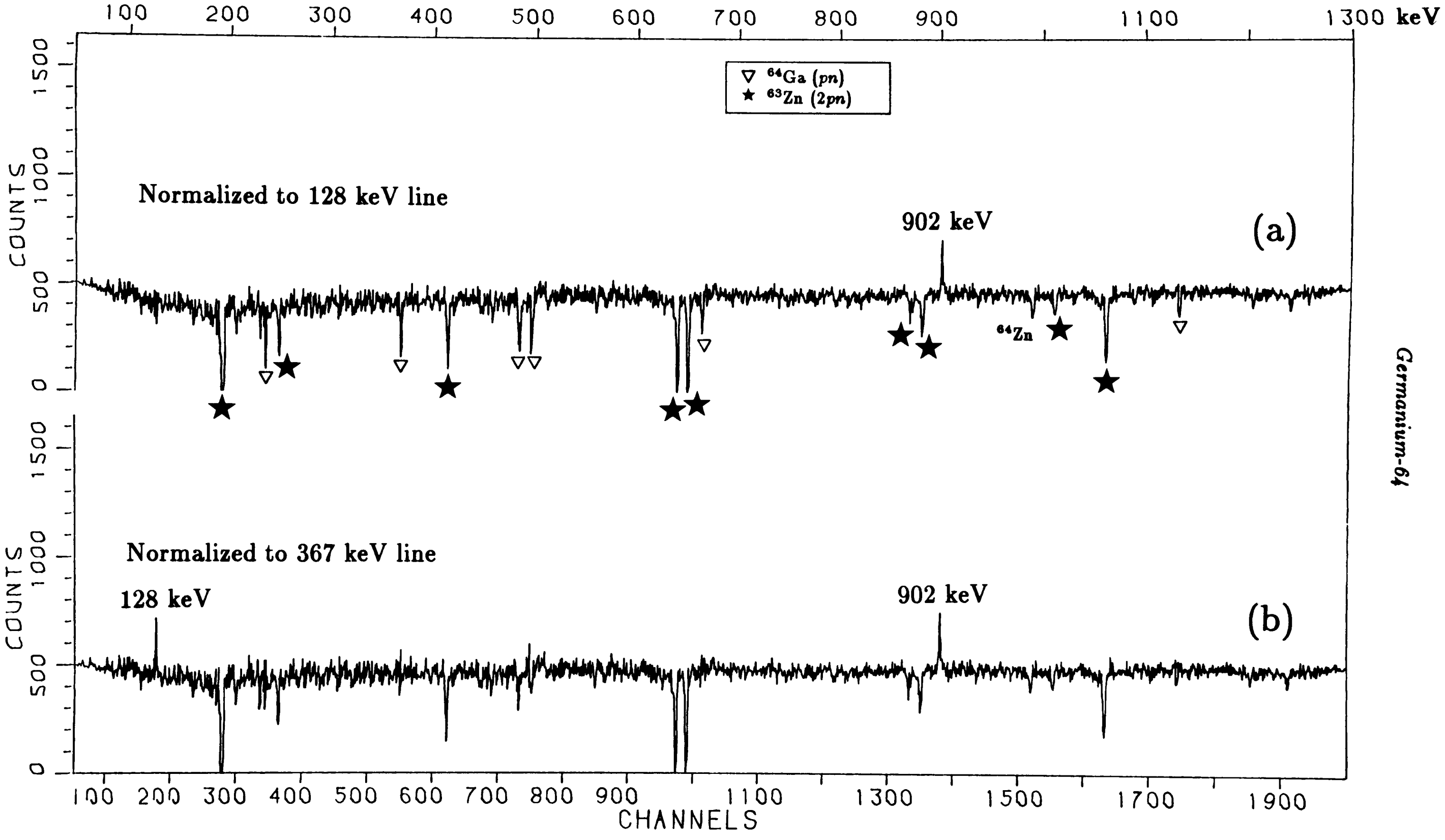


Fig.5.25 : Subtracted spectra ($1n0p - 1n1p$) normalized to (a) the 128 keV line and (b) the 367 keV line both from ^{64}Ga.

The 902 keV line still remains in part (a) which suggests that it is a genuine γ-ray peak arising from a charged-particle-free channel.

Having established that this γ-ray comes from n-only events, the multiplicity of the neutrons was investigated. The data were sorted for events in which neutron signals were detected in two (or more) neutron detectors. When the $2n$ spectrum was examined, it was found to be dominated by lines from ^{64}Ga which must have arisen from single neutrons being recorded twice (see fig. 5.26). This is a common problem with n-multiplicity experiments [LIS85] as the neutrons tend to scatter off one detector into another, thereby introducing cross-talk into the system. In this $2n$ spectrum, the 902 keV line is enhanced with respect to the ^{64}Ga lines by a factor of about 4. To enhance the pure n evaporation lines, the $0p$ requirement is switched on to produce the $1n0p$ and $2n0p$ spectra as shown in figs. 5.27(b) and (a) respectively. When the $1n0p$ spectrum, normalized to the 367 keV line in the $2n0p$ spectrum, is subtracted from the $2n0p$ spectrum, the only γ-ray peak remaining in the subtracted spectrum (apart from the 511 keV annihilation γ-ray) is the 902 keV peak, showing that the presence of this peak is enhanced by the $2n$-gate. When the $2n0p$ and $2n1p$ spectra are compared and the difference between them taken (fig. 5.28), we find that the 902 keV line is the only γ-ray peak left in the subtracted spectrum.

The cross-talk between n-detectors can be reduced by accepting $2n$ events from non-adjacent detectors only. The probability for cross-scattering in this case is considerably lower than before but the statistics are commensurately poorer. As there were 5 detectors altogether (4 large quadrants and a small central cylinder), the non-adjacent neutron events were defined to be events in which signals from non-adjacent quadrants were received, with the small central detector ignored. Fig. 5.29 shows the effect of this coincidence requirement. The 902 keV line is again the only γ-ray peak in the spectrum which again suggests that this γ-ray comes from a pure neutron channel of multiplicity two.

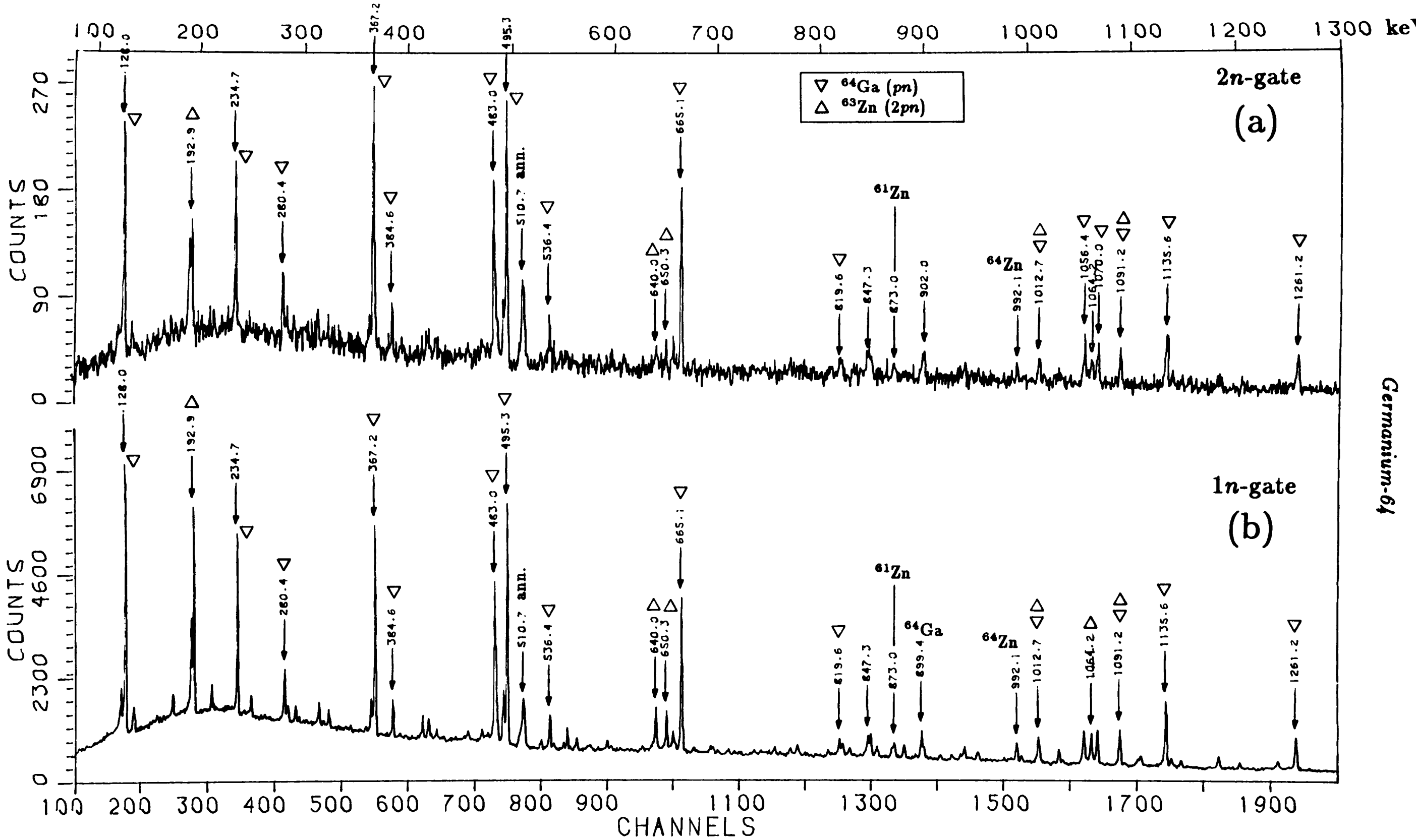


Fig.5.26 : Spectra gated on (a) two neutrons and (b) one neutron.

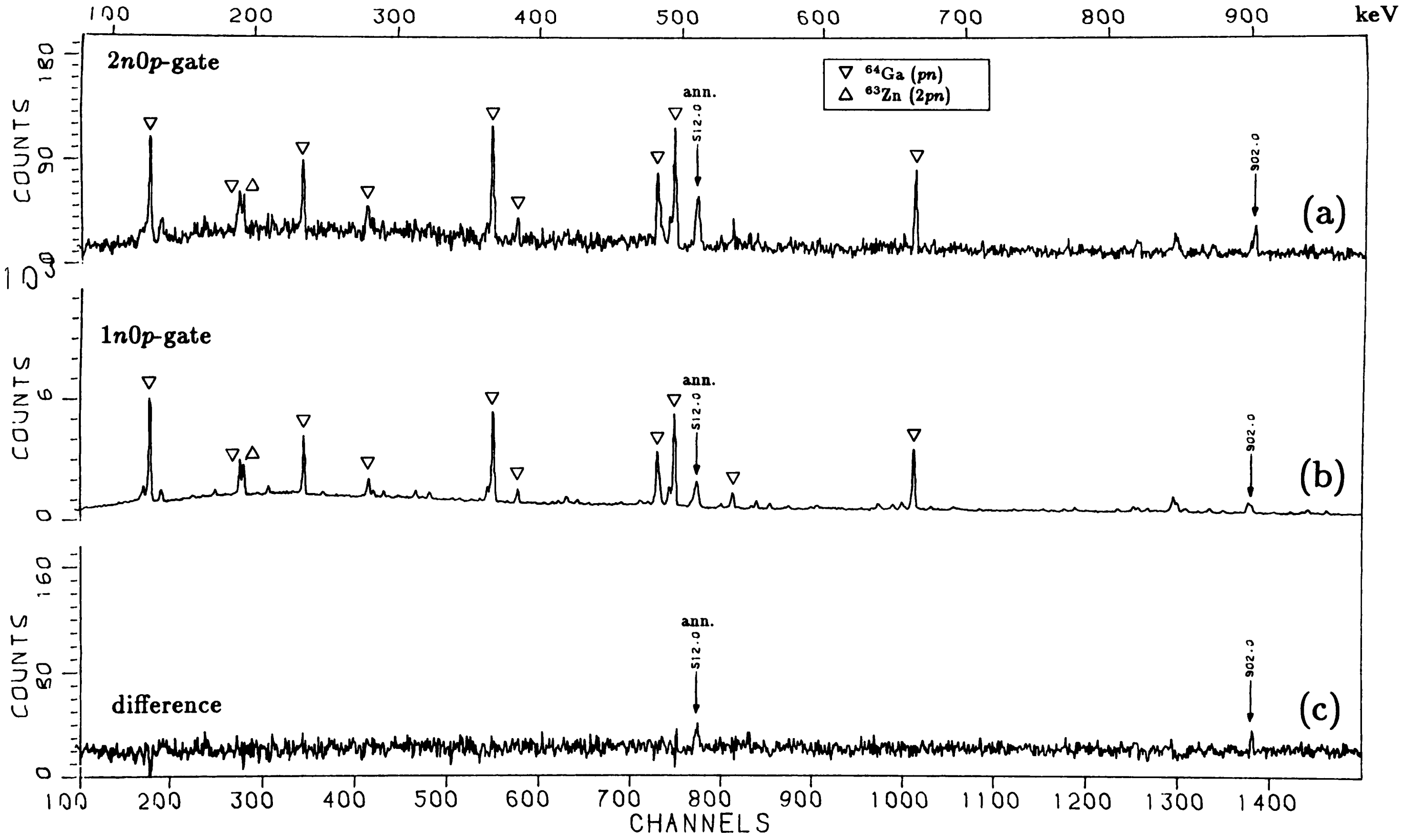


Fig.5.27 : (a) $2n0p$ (b) $1n0p$ and (c) $2n0p - const. \times 1n0p + const.$

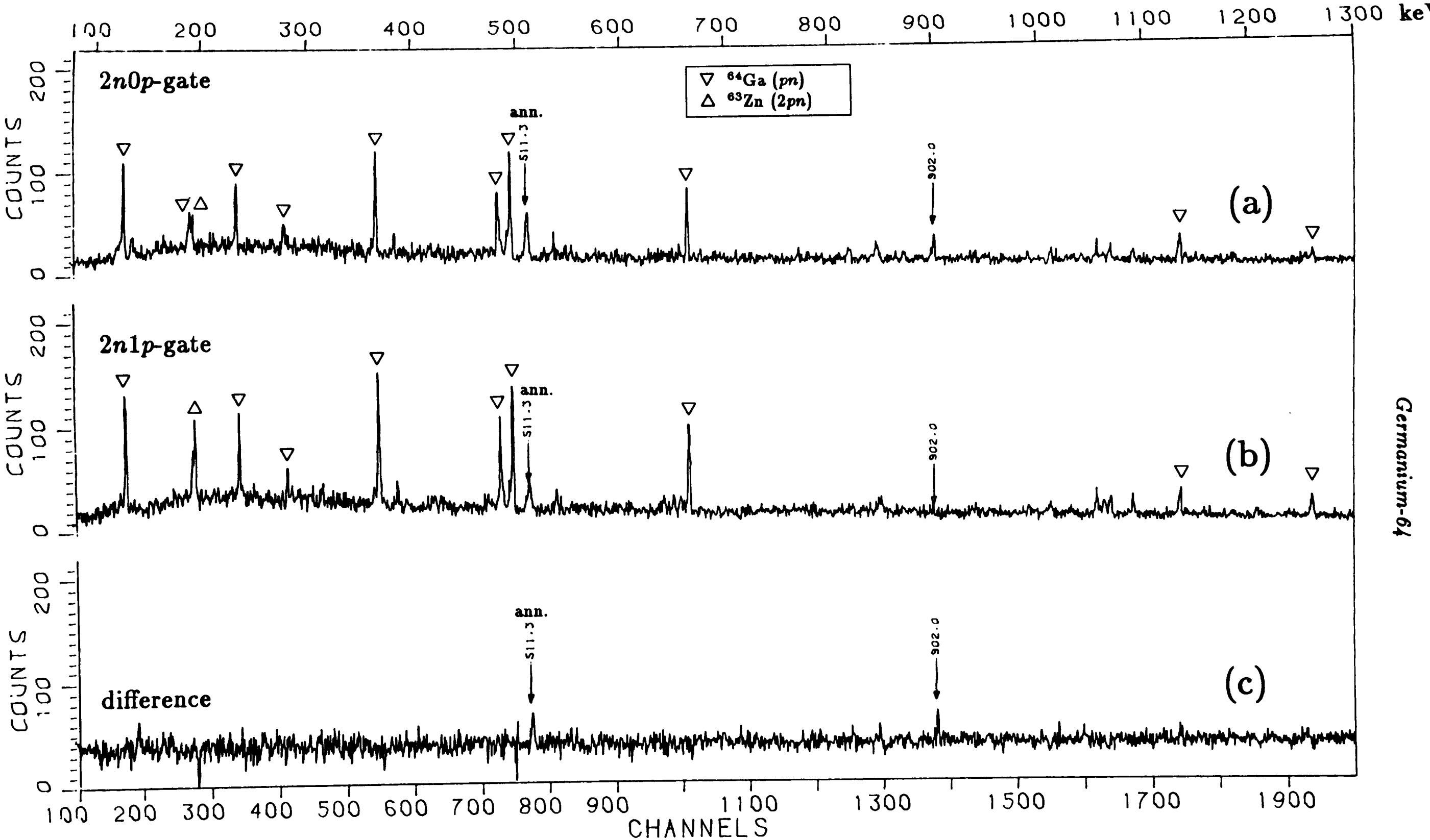


Fig.5.28 : (a) $2n0p$ (b) $2n1p$ (c) $2n0p - 2n1p \times (210/251) + const.$

```
001  !
002  !    Sort programme to look for 1n channel with/without protons
003  !    Using 2d windows
004  !
005  !    Window 0 - W2D 1
006  !    Window 1 - W2D 2
007  !    Window 2 - W2D 3
008  !    Window 3 - W2D 4
009  !    Window 4 - W2D 5
010  !    Window 12 - 2n0p
011  !    Window 13 - 2n1p
012  !
013   TITLE S922
014   OR 12 13 R1              !check to see that it's 2"n"
015   IF R1
016      AND 0 1 R2             !see if any 2 true neutron events
017      AND 0 2 R3             !between any of the detectors.
018      AND 0 3 R4
019      AND 0 4 R5
020      AND 1 2 R6
021      AND 1 3 R7
022      AND 1 4 R8
023      AND 2 3 R9
024      AND 2 4 R10
025      AND 3 4 R11
026      OR R2 R3 R4 R5 R6 R7 R8 R9 R10 R11 R12     !check for 2n
027      IF R12
028         IF 12                 !W#12=2N0P
029            INC 0 P15 0 1        !GAMMA 1
030            INC 1 P16 0 1        !GAMMA 2
031            INC 2 P17 0 1        !GAMMA 3
032            INC 3 P18 0 1        !GAMMA 4
033         ENDIF
034         IF 13                 !W#13=2N1P
035            INC 4 P15 0 1        !GAMMA 1
036            INC 5 P16 0 1        !GAMMA 2
037            INC 6 P17 0 1        !GAMMA 3
038            INC 7 P18 0 1        !GAMMA 4
039         ENDIF
040      ENDIF
041   ENDIF
042   END
```

Fig.5.28.SOL : Sorting programme for $2n$-gated spectra.

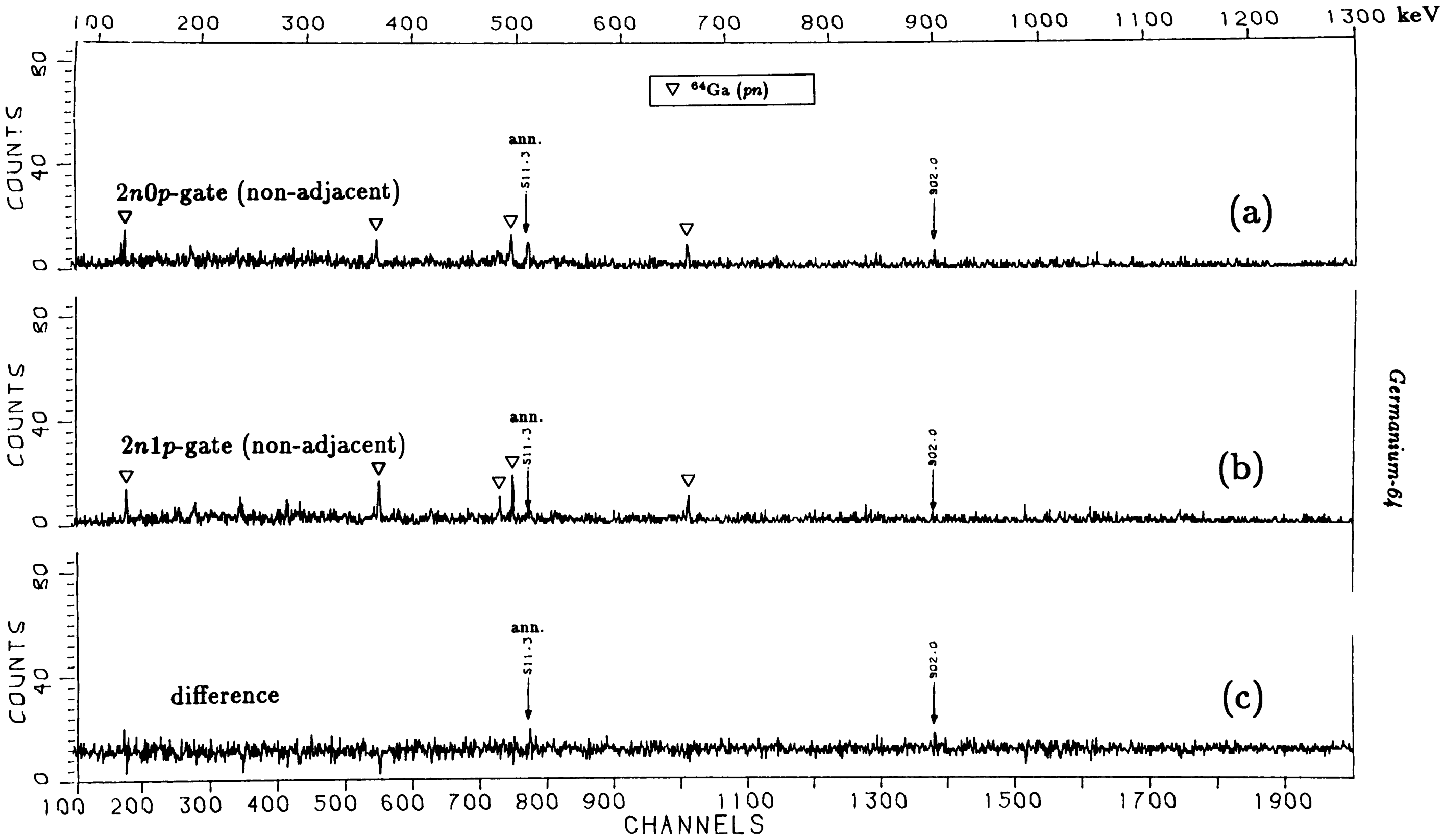


Fig.5.29 : Spectra of events gated by non-adjacent neutron detectors : (a) $2n0p$ (b) $2n1p$ (c) difference between (a) and (b)

```
001  !
002  !    Sort programme to look for 1n channel with/without protons
003  !    Using 2d windows
004  !    Taking non-adj detectors only
005  !
006  !    Window 0 - W2D 1
007  !    Window 1 - W2D 2
008  !    Window 2 - W2D 3
009  !    Window 3 - W2D 4
010  !    Window 4 - W2D 5
011  !    Window 12 - 2n0p
012  !    Window 13 - 2n1p
013  !
014   TITLE S925
015   OR 12 13 R1              !check to see that it's 2"n"
016   IF R1
017    AND 0 2 R3              !between any of the detectors.
018    AND 0 4 R5
019    AND 1 3 R7
020    AND 1 4 R8
021   AND 2 4 R10
022   AND 3 4 R11
023   OR R3 R7 R12                !check for 2n for non-adj detectors
024   OR R3 R5 R7 R8 R10 R11 R13 !check for 2n with l'll detector included
025   IF R12
026    IF 12              !W#12=2N0P
027     INC 0 P15 0 1          !GAMMA 1
028     INC 1 P16 0 1          !GAMMA 2
029     INC 2 P17 0 1          !GAMMA 3
030     INC 3 P18 0 1          !GAMMA 4
031    ENDIF
032    IF 13              !W#13=2N1P
033     INC 4 P15 0 1          !GAMMA 1
034     INC 5 P16 0 1          !GAMMA 2
035     INC 6 P17 0 1          !GAMMA 3
036     INC 7 P18 0 1          !GAMMA 4
037    ENDIF
038   ENDIF
      ⋮
      ⋮
039   IF R13
040    IF 12              !W#12=2N0P
041     INC 8 P15 0 1          !GAMMA 1
042     INC 9 P16 0 1          !GAMMA 2
043     INC 10 P17 0 1         !GAMMA 3
044     INC 11 P18 0 1         !GAMMA 4
045    ENDIF
046    IF 13              !W#13=2N1P
047     INC 12 P15 0 1         !GAMMA 1
048     INC 13 P16 0 1         !GAMMA 2
049     INC 14 P17 0 1         !GAMMA 3
050     INC 15 P18 0 1         !GAMMA 4
051    ENDIF
052   ENDIF
053  ENDIF
054  END
```

Fig.5.29.SOL : Sorting programme for 2*n*-(non adj.)-gated spectra.

Fig. 5.30 shows the $1n0p$ and $1n1p$ spectra from run 20 and their difference (normalized to the 367 keV γ-ray peak). The ^{64}Ga lines disappear in the subtracted spectrum and the 902 keV γ-ray peak is the only remaining peak in the subtracted spectrum. As before, the over-subtracted peaks come from the $2pn$ channel making ^{63}Zn. The $2n0p$ and $2n1p$ spectra from run 24 are shown in fig.5.31. Again we see a marked difference in the intensities of the 902 keV γ-ray peak in the two spectra while the pn lines (665 and 1136 keV) are present with similar intensities in both spectra. The data from these two runs support the existence of this γ-ray at 902 keV and further support the assertion that this γ-ray is associated with a pure $2n$ evaporation channel.

As a recapitulation of the data reduction employed in this section to extract the pure neutron channel, fig. 5.32 has been included to show the spectra (from run 20) with increasing coincidence requirements going from top to bottom. Part (a) shows the singles spectrum. The ^{64}Zn($2p$) lines and the massive ^{56}Fe Coulomb excitation line (whose tail is just seen in the figure) form the dominant peaks in this spectrum. When the n-coincidence is switched on, these lines disappear to leave a spectrum dominated by lines from n-related channels (part (b)). If charged particle anti-coincidence is demanded, the charged particle related channels are significantly reduced (part c). The ^{63}Zn($2pn$) lines are removed completely but the ^{64}Ga(pn) lines still remain. However, the latter lines can be removed by subtracting off a normalized $1n1p$ spectrum and the resulting spectrum is shown in part d where the only remaining γ-ray peak is the 902 keV line.

From the analysis of the coincidence spectra presented, we find that the 902 keV line is enhanced over every other line as the data were successively reduced to extract pure n events. Thus, we can conclude that this γ-ray comes from a pure n evaporation channel. Its enhancement over the pn lines when a $2n$-gate is applied strongly suggests that the channel is a $2n$ channel. It remains for us to determine the nucleus associated with this channel.

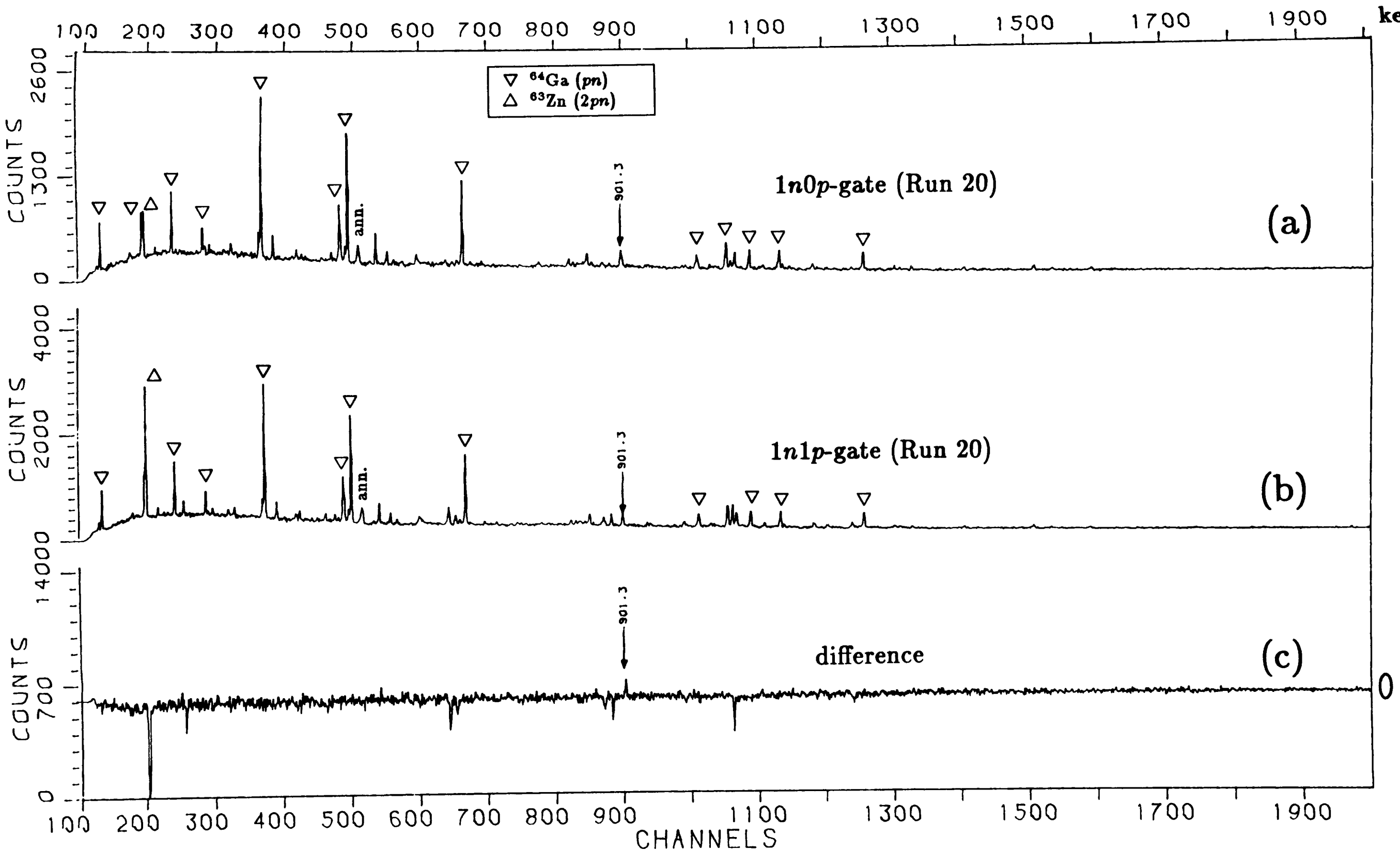


Fig.5.30 : n-gated spectra with and without charged particles from run 20 : (a) $1n0p$ (b) $1n1p$ and (c) their difference (the spectra were normalized to the 367 keV line before subtraction).

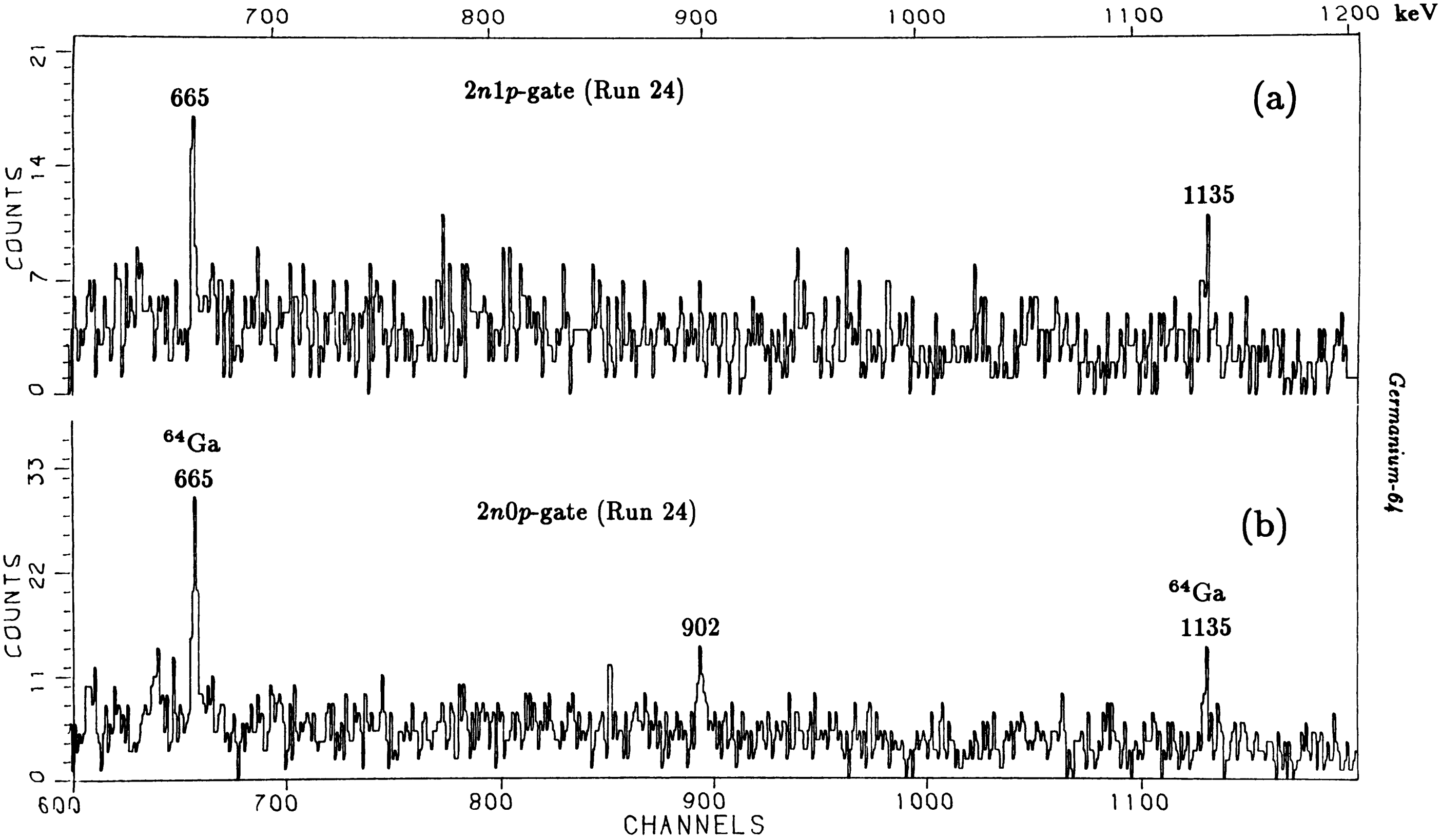


Fig.5.31 : Spectra from run 24 gated by (a) $2n1p$ and (b) $2n0p$ showing the presence of the 902 keV line in the latter spectrum but not in the former.

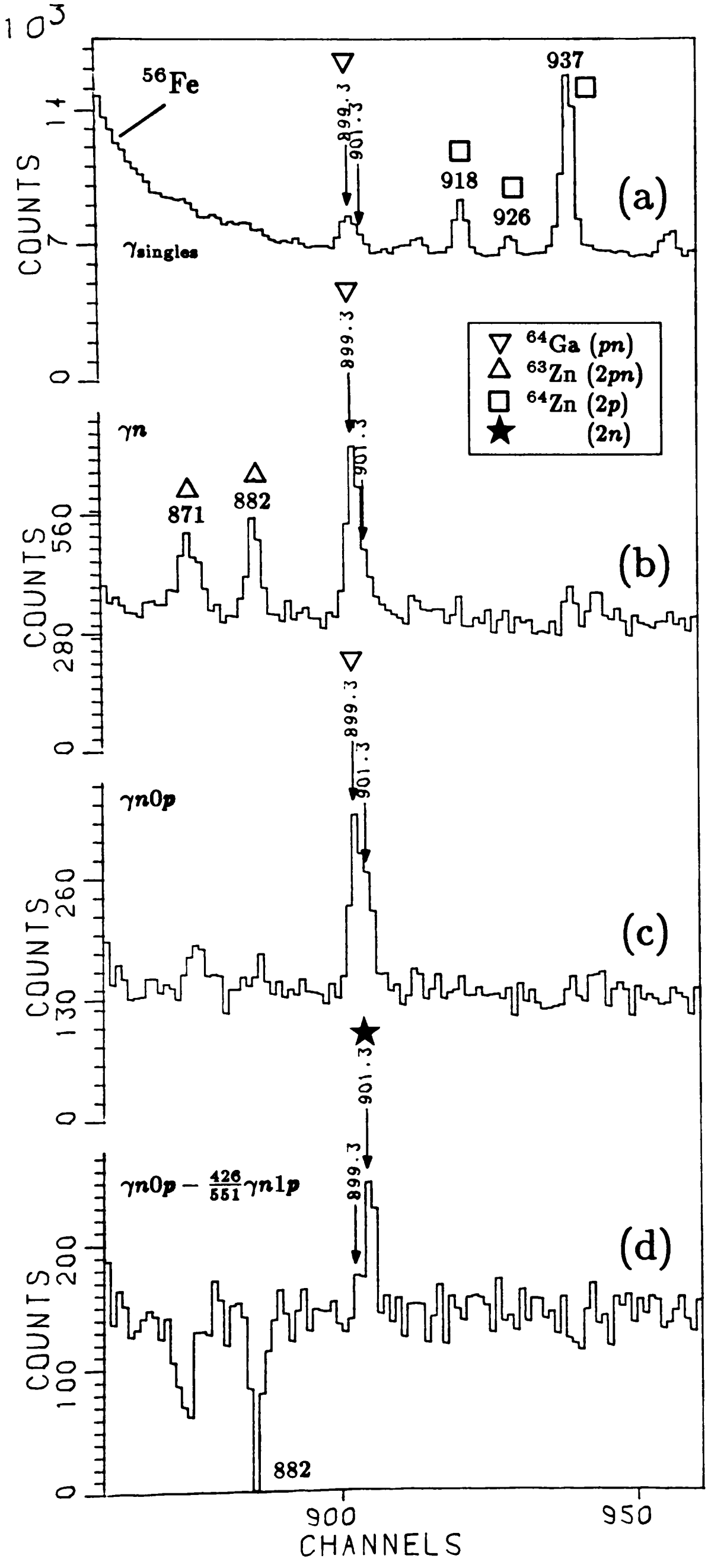


Fig.5.32 : Effect of progressively adding coincidence requirements to reduce the data : (a) singles, (b) 1*n* gate, (c) 1*n*0*p* gate (d) $|\ (1n0p) - N \times (1n1p)\ |$ where N, the normalizing factor = (426/551).

Almost all the lines (except for a few weak ones) from the reaction have been identified and a catalogue of these γ-rays has been given above. None of these γ-rays were found to be associated with exit channels from reactions other than ^{54}Fe + ^{12}C. The ^{12}C target was enriched to 99.9 % and so reactions on ^{13}C was unlikely. Moreover, the $2pn$ (^{64}Zn) channel from ^{54}Fe + ^{13}C formed 50 % of the total cross-section (using CASCADE) and this channel was not seen (the ^{64}Zn lines were found to be effectively suppressed by the n-gating). This channel is two orders of magnitude larger than the $2n$ channel and hence the probability of observing γ-rays from the latter without observing substantial γ-ray peaks from ^{64}Zn in the n-gated spectrum is extremely small. Similarly, reactions on other possible impurities can be ruled out as the majority of the lines in the spectra have been accounted for and the ones that have not been identified are considerably weaker than the norm. Table 5.14 shows the CASCADE cross-sections for reactions on possible impurities and we see that no $2n$ channel forms a significant fraction of the total cross-sections in any of the reactions. Therefore, we can conclude that the 902 keV γ-ray is a $2n$ channel from the ^{54}Fe + ^{12}C reaction and so must come from a transition in ^{64}Ge.

Target	Largest Cross-section			$2n$ channel	
	Chan.	Nucl.	σ	Nucl.	σ
$^{13}_{6}$C	$2pn$	^{64}Zn	236	^{65}Ge	2.4
$^{14}_{7}$N	$2pn$	^{65}Ga	144	^{66}As	0.0
$^{16}_{8}$O	$3p$	^{67}Ga	85	^{68}Se	0.3
$^{27}_{13}$Al	$2pn$	^{78}Rb	65	^{79}Y	0.0
	$3p$	^{78}K	64		
$^{28}_{14}$Si	$3p$	^{79}Rb	49	^{80}Zr	0.0

Table 5.14 : Cross-sections in mb (using CASCADE) for reactions of ^{54}Fe at 150 MeV on various targets. The largest cross-section is given and the channel and residual nuclei associated with this is included.

5.6.3 Relative Intensities of the Reaction Lines

The intensities of the γ-rays were used to obtain the relative cross-sections for the production of ^{64}Ga and ^{64}Ge. The intensities quoted here have been corrected for the γ-ray detection efficiency of the γ-ray detector. These intensities have been taken from the $1n$ spectrum where the n-related channels are enhanced over the other channels. Table 5.15 shows the intensities of the γ-rays from transitions in ^{64}Ga and ^{64}Ge and uses a layout similar to table 5.5(a). As stated before, the decay scheme of the odd-odd nucleus, ^{64}Ga, is complex and contains many parallel de-excitation paths and so many different γ-ray transitions have to be added to obtain the total γ-decay strength. ^{64}Ge is made via the $2n$ channel and so its γ-rays have a higher probability of being detected in coincidence with neutrons. The intensity of this γ-ray has to be corrected for this difference. The efficiency for detecting $2n$ events is

$$2\epsilon(1-\epsilon)+\epsilon^2$$

where ϵ is the efficiency for detecting one neutron. The first term is the efficiency for detecting just one of the two neutrons while the second term is the efficiency for detecting both neutrons. For small efficiencies, the first term dominates. The efficiency for detecting $2n$ events relative to $1n$ events is simply $(2-\epsilon)$ and using $\epsilon \approx 10$ % (§3.8.2), the correction factor for the 902 keV becomes 1.9. In table 5.16, the cross-sections from β-decay, together with the results obtained in this section, are given. Both cross-sections have been normalized to the ^{56}Fe Coulomb excitation cross-section which was calculated in section 4. The cross-sections for the production of ^{64}Ge from the β-decay experiment (0.6 ± 0.3 mb) and the in-beam experiment (1.1 ± 0.4 mb) are consistent. The cross-sections predicted by CASCADE have also been included in this table and these show that the predictions come within a factor of two of the experimental results. We can also compare these cross-sections with the cross-sections of Roberston and Austin [ROB74] who made

^{64}Ge using the ^{64}Zn(^{3}He,3n)^{64}Ge reaction at 37.6 MeV and see that both methods give similar magnitudes for the production of ^{64}Ga and ^{64}Ge.

Nucleus	γ-ray energy (keV)	Efficiency corrected intensity		Total Intensity
^{64}Ga	367+364†	51(1)		
	537	9.8(8)		
	850	7(2)		
	1109	2.8(9)		
	1514	12.7(8)		
		→	83(3)	
	280		8.9(8)	
	492+495†		81(2)	
	665		56(2)	
			→	229(4)
^{64}Ge	902		→	3(1)

Table 5.15 : γ-ray intensities used for the determination of the relative cross-sections of the evaporation channels in the following table. The intensities were extracted from the 1n spectrum.
†The intensities of doublets or close-lying lines have been added together.

Nucleus	Chan.	β-decay	In-beam	CASCADE	RA
^{64}Ga	pn	164[26]	164[28]	79	100($p2n$)
^{64}Ge	2n	0.6[3]	1.1[4]	0.8	0.1(3n)

Table 5.16 : Relative cross-sections for the pn and 2n lines from ^{12}C + ^{54}Fe. The cross-sections have been normalized to the ^{56}Fe Coulomb excitation cross-section. The errors quoted are a combination of the statistical error, ϵ_{src} (5 %) and ϵ_{eff} (5 %). The column 'RA' shows the experimental cross-sections from the reaction ^{3}He + ^{64}Zn at 37.6 MeV laboratory energy [ROB74]. The derivation of the errors in [ ] are explained in §5.4. (ϵ_{src} = 4 % and ϵ_{eff} = 5 %).

5.6.4 Summary

In summary, the arguments for assigning the 902 keV γ-ray to ^{64}Ge are as follows:-

i) The β-decay of ^{64}Ge has been studied using the reaction ^{12}C + ^{54}Fe at 35 MeV.

- Other workers have detected ^{64}Ge produced with the same reaction [DAV73].
- the cross-section was found to be 0.6 ± 0.3 mb.

ii) The inverse reaction has been used at 150 MeV† to study the γ-rays from the decay of ^{64}Ge.

- $1n0p$, $1n1p$, $2n0p$ and $2n1p$ spectra indicate a $2n0p$ γ-ray at 902 keV.
- possible background reactions (e.g. ^{54}Fe + ^{13}C) have been ruled out.
- the cross-section, 1.1 ± 0.4, is consistent with the β-decay results.

iii) Two other in-beam experiments (one with a different ^{12}C target) performed in this work showed a consistent presence of a $2n0p$ γ-ray at this energy.

It can, therefore, be concluded that the 902 keV line comes from ^{64}Ge. In the next section, we discuss the justifications for assigning this γ-ray to the decay of the first excited state in ^{64}Ge.

---

† The inverse of 35 MeV viz. 157.5 MeV was not used due to the limitations imposed by the available accelerator. However, the $2n$ cross-sections were not expected to vary by much between these two energies (see §2.5.3).

5.7 Conclusion

In this section, we shall consider the results presented in the preceding sections and address three outstanding questions:

i) Why have other studies not observed the ^{64}Ge $2 \rightarrow 0$ transition ?

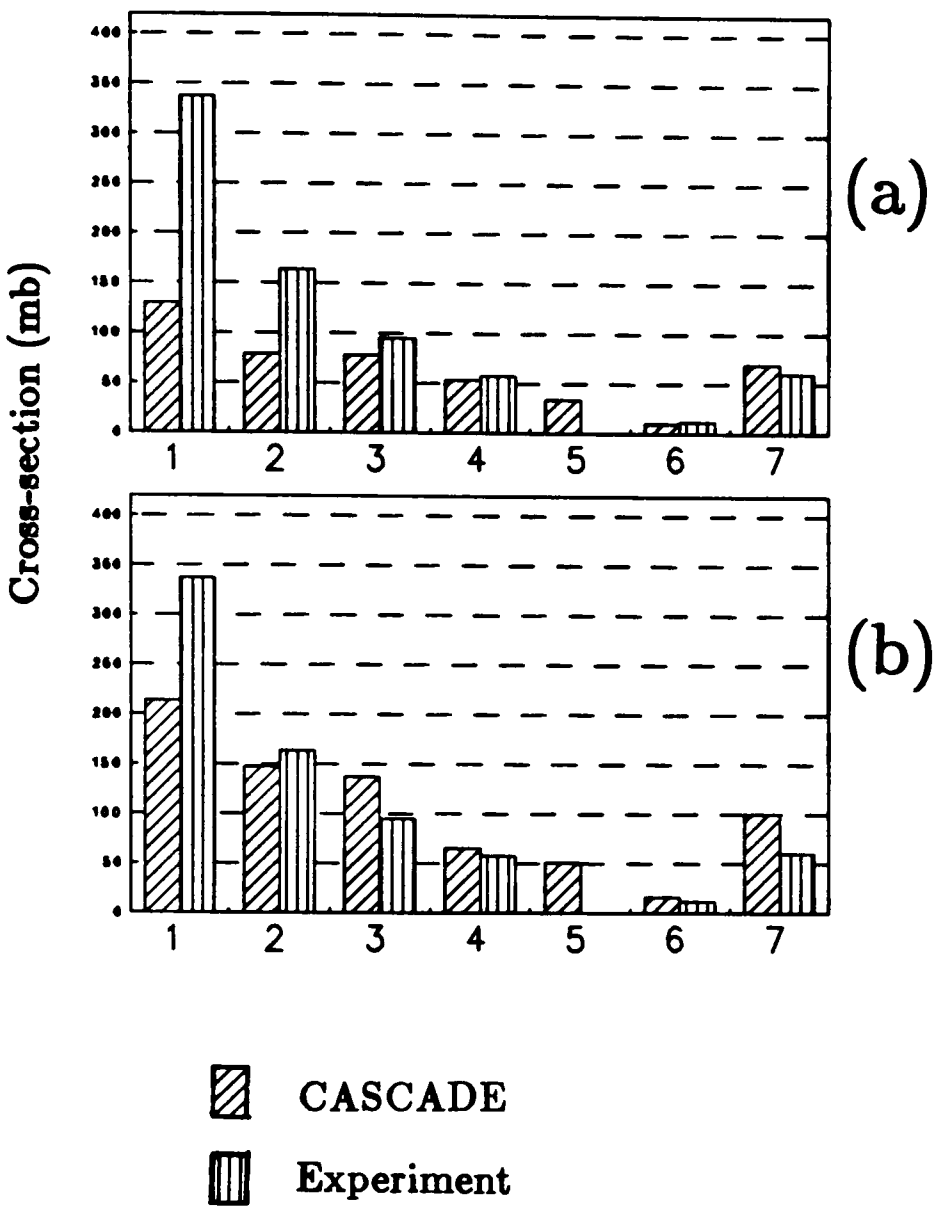
ii) How reliable has CASCADE been ? Is it reliable for predicting low cross-sections ?

iii) Is the 902 keV γ-ray transition correctly assigned to the γ-decay of the first excited state ?

(i) It is not surprising that previous searches for this nucleus have been unsuccessful. In our case, the yield of the 902 keV line in the $1n$ spectrum would only be ~23 % of the yield of the nearby 899 keV line from ^{64}Ga without the charged particle veto. In previous work, a carbon beam was used on a ^{54}Fe target and there was a strong contaminant line from ^{22}Na at 891 keV (from reactions on carbon on and in the target). Our success was due to higher neutron detection efficiency, fewer contaminant lines from the inverted reaction and effective discrimination against the *pn* channel through the use of charged particle detection.

(ii) The experimental and CASCADE cross-sections for the various evaporation channels from ^{12}C + ^{54}Fe at 35 MeV are shown in fig. 5.33(a). The experimental cross-sections have been taken mainly from the β-decay experiment (except for ^{64}Zn which has been taken from the singles data in section 4). We see that there is good general agreement and that the relative cross-sections are reproduced‡. Some of the channels (e.g. the $2p$ and the *pn*) seem to be underestimated by the code. As shown in Appendix V, the theoretical cross-sections are sensitive to the fusion cross-section (or equivalently the maximum angular momentum, L_o, brought into the compound

‡ The $3p$ (^{63}Cu) experimental cross-section is not available because ^{63}Cu is a stable nucleus and therefore no data are available from the β-decay experiment. Furthermore, the many parallel γ-decay paths in this nucleus make the determination of the total γ-decay intensity from the in-beam experiment difficult.



1 – $2p$
2 – pn
3 – αp
4 – $2pn$
5 – $3p$
6 – αn
7 – $2n$

Note : $2n$ channel has been multiplied by 100

Fig.5.33 : Comparing experimental cross-sections (σ) with (a) CASCADE σ using default input parameters and (b) CASCADE σ with $r_{oLDM} = 1.5$ and $L_o = 15\ \hbar$ (see text).

nucleus) and the liquid drop radius parameter, r_{oLDM}, which determines the yrast line at high (> 20 MeV) excitation energy. If these parameters are varied, we can obtain a much better agreement with the experimental values. Fig. 5.33(b) shows the CASCADE cross-sections using values: $L_o = 15\ \hbar$ (the CASCADE default is 11.2 $\hbar$) and $r_{oLDM} = 1.5$ (increased from 1.26). The former reflects the fusion cross-section for the reaction and at the energy used (which is just ~1.5 MeV above the Coulomb barrier in the centre-of-mass frame), the assumption of two rigid colliding spheres (used to calculate the default value) no longer holds true. At these low energies, the diffuse nature of nuclear boundaries become important and the quantum tunnelling of the barrier may account for a larger fusion cross-section (and hence L_o) than predicted with the simple model.

The liquid drop radius, r_{oLDM}, will affect the shape of the yrast line and consequently the level densities. The assumption made is that the nucleus behaves like a deformed liquid drop at high excitation energies. The level densities in this high excitation region are not known and the extrapolated values may not be correct. In fact, the ratio of the decay probabilities has been suggested as a possible probe of the yrast shape at high energies [PUH77a]. However, we must bear in mind that the error in the thickness of our target is not known and as the thickness is used to calculate the absolute values of the experimental cross-sections, the latter will be affected by any inaccuracies in the target thickness.

In conclusion, we have shown that the relative magnitudes for the cross-sections predicted by CASCADE are borne out by experimental results. The design and nature of the experiment were not intended as a test for CASCADE nor to obtain precise measurements of the relative cross-sections of the reaction channels and so no special effort was made to reduce the possible errors. However, the order and magnitude of CASCADE's predictions agree well with our experiment and its comparison with experiments in the mass 80 region also show good agreement†. The predicted cross-section of ~1 mb for the $2n$ channel has also been verified

† C.J.Lister, private communication.

by our experiment and so its predictions for small cross-sections has been shown to be reasonably accurate. Nevertheless, work should be done on a systematic analysis of the evaporation cross-sections for different reactions producing nuclei in this region and the results compared with CASCADE values. From this, a better understanding of CASCADE's virtues and limitations could be obtained. However, CASCADE is a useful tool for its general predictive qualities and is a convenient method by which untried reactions can be selected.

(iii) Turning now to the question of 902 keV being the energy of the first excited state in ^{64}Ge, there are four possible cases where the 902 keV line might NOT be the first excited state in ^{64}Ge and these are shown in fig. 5.34.

Case a : γ-rays below ~100 keV would have been below our Ge(Li) detector thresholds. Using the empirical relationship between the energy of the first 2^+ state and the quadrupole deformation parameter (§2.5.1), a superdeformed ground state shape ($\epsilon = 0.6$) would have a 2_1^+ state at ~200 keV and so an energy lower than this is unlikely. However, assuming that the energy *is* lower than this — which corresponds to a very superdeformed nucleus — we should expect to observe parts of the rotational sequence (with transition energies > 100 keV) built on the ground state but we do not. It is therefore unlikely for this situation to be the case.

Case b †: The existence of a 0^+ state lower in energy than 902 keV cannot be ruled out. Here, we have to rely on the systematics of the periodic table to decide how likely this occurrence is. There are *very few* cases in the periodic table where the first excited state of an even-even nucleus does not have a spin and parity of 2^+ and these exceptions have been listed in table 5.17

---

† It is worth pointing out that the shape prediction using the energy of the 2_1^+ state would not be affected by the existence of a 0_2^+ state lower in energy.

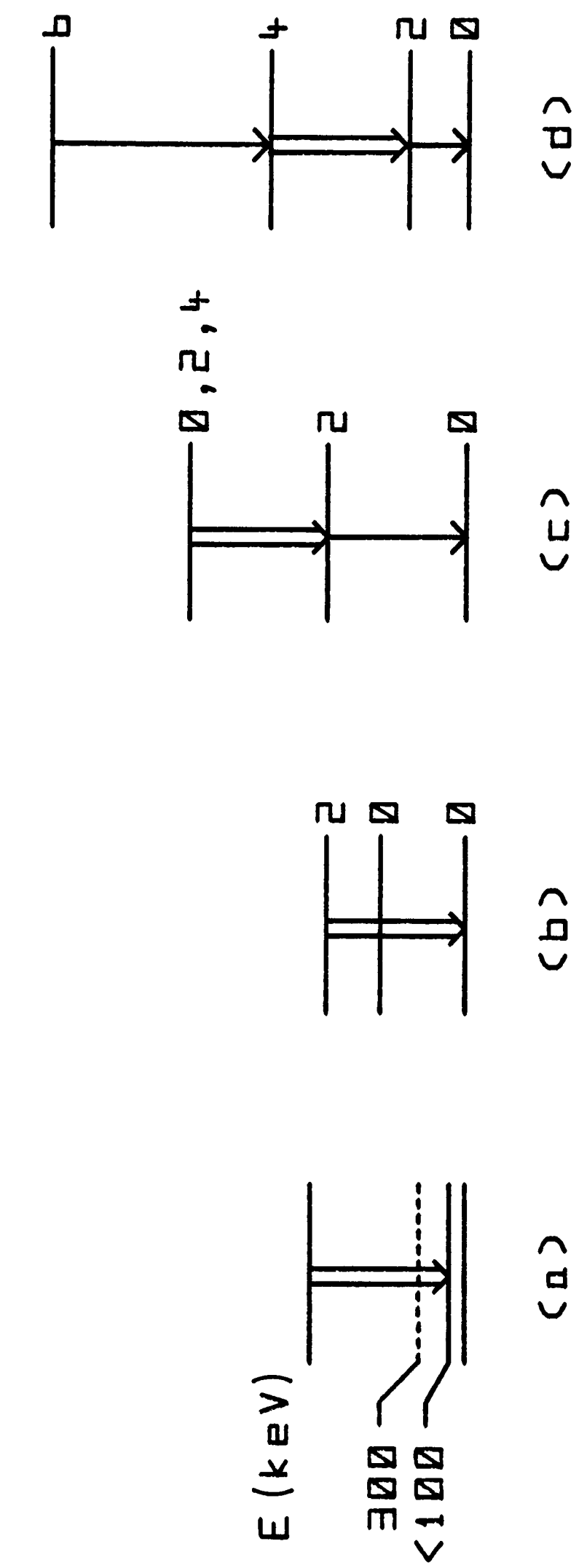


Fig.5.34 : Four possible cases where the 902 keV transition may have been misidentified as the γ-decay of the first excited state in ^{64}Ge. The double arrow shows where the 902 keV transition may be instead.

#	Nucleus	J^π
1.	$^{16}_{8}$O	0^+
2.	$^{40}_{20}$Ca	0^+
3.	$^{72}_{32}$Ge	0^+
4.	$^{90}_{40}$Zr	0^+
5.	$^{96}_{40}$Zr	0^+
6.	$^{98}_{40}$Zr	0^+
7.	$^{98}_{42}$Mo	0^+
8.	$^{146}_{64}$Gd	3^-
9.	$^{208}_{82}$Pb	3^-

Table 5.17 : Spin and parity (other than 2^+) of the first excited states of even-even nuclei.

These anomalous spins occur for special reasons. In the doubly-magic nuclei, they are described as p-h excitations built on spherically symmetric closed shells [GRE65]. Thus the 0_2^+ states in ^{16}O and ^{40}Ca are 4p-4h states [ZUK68, GER67] while the 3^- state in ^{208}Pb is a p-h octupole vibrational state [GIL66]. ^{146}Gd is also another doubly-closed shell nucleus [KLE78] and has an octupole excitation as the first excited state. From the systematics of 0^+ states, we find that a low-lying 0^+ state in a sequence of isotopes is characteristic of a change in the ground state shapes of the nuclei from a spherical to a deformed shape [VER79, CAS72]. The other nuclei in table 5.17 belong to such a class as they are situated on the boundary of a region of deformed nuclei in the N≈64, Z∼40 region [ARS69]. Calculations in which excited states in a five-dimensional quadrupole oscillator were obtained [GNE71] showed that a nuclear shape with two minima in the potential energy surface (one spherical, the other triaxial) could reproduce the low-lying sequence of levels in ^{72}Ge and ^{98}Mo (including the 0_2^+ level as the first excited state). This suggests a co-existence of two shapes in these nuclei and so strengthens the argument that the low-lying 0^+ is related to shape transitions. ^{64}Ge is not expected to fall

into either of the above two categories and so we would not expect a low-lying 0^+ state to be present in this nucleus.

Cases c & d : Case c assumes a vibrational excitation sequence while case d assumes a rotational sequence for the excited states. In these two cases, we would expect to observe the J=2 → J=0 transition as well but we do not. Table 5.18 shows the relative photon intensities of the the two (or three) most intense γ-ray lines from nuclei in this region and show that the 2 → 0 transition is approximately twice as large as the next intense transition and, in some cases, by almost a factor of five.

It is inconceivable that this transition could have been missed as there is no evidence for another γ-ray peak for energies up to 2.5 MeV (see fig. 5.35). With the Ge(Li) efficiency taken into account, a γ-ray peak of the same intensity as the 902 keV line should be visible in the spectrum for energies up to 2.5 MeV.

If we compare the γ-ray energy with the energies of the first 2^+ state in this region, we see that a state at 902 keV fits remarkably well with the observed trend (fig. 5.36). Fig. 5.37 shows the systematic behaviour of the the low-lying states in the Ge isotopes and the state at 902 keV is consistent with the systematics.

Another question to which we should address ourselves is whether we expect to have observed any other transitions in ^{64}Ge and whether it is reasonable that we do not.

Fig. 5.38(a) and (b) show the $1n0p$, $1n1p$ and the subtracted spectra. From the singles spectrum, the intensities of the $2^+ \rightarrow 0^+$ and $4^+ \rightarrow 2^+$ transitions in ^{64}Zn can be determined. Table 5.19 shows the intensities (corrected for Ge(Li) efficiency) of these two transitions.

E_γ (keV)	FWHM (channels)	I_γ
991(2 → 0)	3.6	389
1315(4 → 2)	4.1	148

Table 5.19 : Intensities (corrected for Ge(Li) efficiency) of the two transitions in ^{64}Zn.

Nucleus	Reaction	Energy (MeV)	$E_2(J_2^\pi) \rightarrow E_1(J_1^\pi)^{(1)}$	$E_\gamma^{(2)}$ (keV)	$I_\gamma^{(3)}$	Ref.	$T_{1/2}^{(4)}$ (ps)	B(E2)$^{(4)}$ (w.u.)
^{66}Ge	^{58}Ni(^{10}B,$pn\gamma$)	29	$957(2^+) \rightarrow g.s.$	957	100	WAD79	3.7	12
			$2174(4^+) \rightarrow 957(2^+)$	1217	48.5		< 1.5	> 8.9
^{68}Ge	^{58}Ni(^{12}C,$2p\gamma$)	39	$1016(2^+) \rightarrow g.s.$	1016	100	LIM81	2.1	15
			$2268(4^+) \rightarrow 1016(2^+)$	1252	59		0.8	14
^{70}Ge	^{68}Zn(α,$2n\gamma$)	30	$1040(2^+) \rightarrow g.s.$	1040	100	MOR76	1.27	21.5
			$2153(4^+) \rightarrow 1040(2^+)$	1114	64			
^{60}Zn	^{58}Ni(^{3}He,$n\gamma$)	10	$1004(2^+) \rightarrow g.s.$	1004	100	KAM74		
			$3504(0^+) \rightarrow 1004(2^+)$	2500	23			
			$2194(4+) \rightarrow 1004(2^+)$	1189	18			
^{62}Zn	^{62}Ni(α,$2n\gamma$)	30	$954(2^+) \rightarrow g.s.$	954	100	NDS$^{(5)}$	1.7	28
			$2186(4^+) \rightarrow 954(2^+)$	1232	50		1.0	14
^{64}Zn	^{61}Ni(α,$n\gamma$)	8	$992(2^+) \rightarrow g.s.$	992	100	CHA76	1.8	22
			$1799(2^+) \rightarrow 992(2^+)$	808	26		1.8	30
			$2307(4^+) \rightarrow 992(2^+)$	1315	17		≈ 0.5	≈ 20
^{66}Zn	^{64}Ni(α,$2n\gamma$)	27	$1039(2^+) \rightarrow g.s.$	1039	100	BRU75	1.65	18.2
			$2450(4+) \rightarrow 1039(2^+)$	1411	62		0.19	34

Table 5.18 : Relative photon intensities of the two (or three) most intense lines from nuclei in the A=60 region.
(1) Initial and final level with the spin and parity in brackets. (*g.s.* = ground state)
(2) Gamma-ray energy.
(3) Relative photon intensity. Normalized to the g.s. transition (100).
(4) Nucl. Data Sheets. (5) Nucl. Data Sheets **26**, 71 (1979).

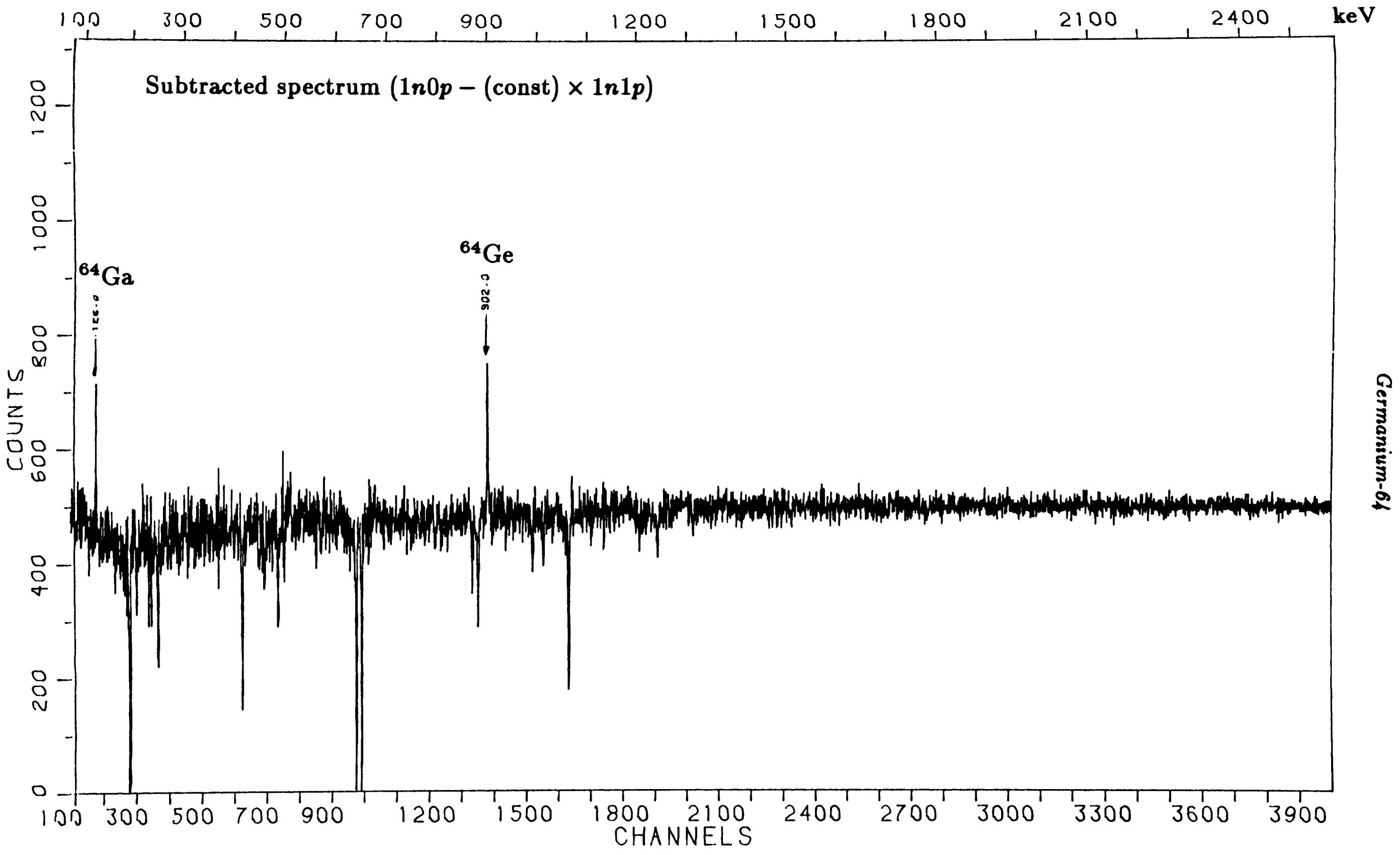


Fig.5.35 : Subtracted 1*n* spectrum (i.e. 1*n*0*p* - const. ×1*n*1*p*, where *const* was obtained by normalizing the two spectra to the 367 keV *pn* line.

SYSTEMATICS OF THE A=60 REGION

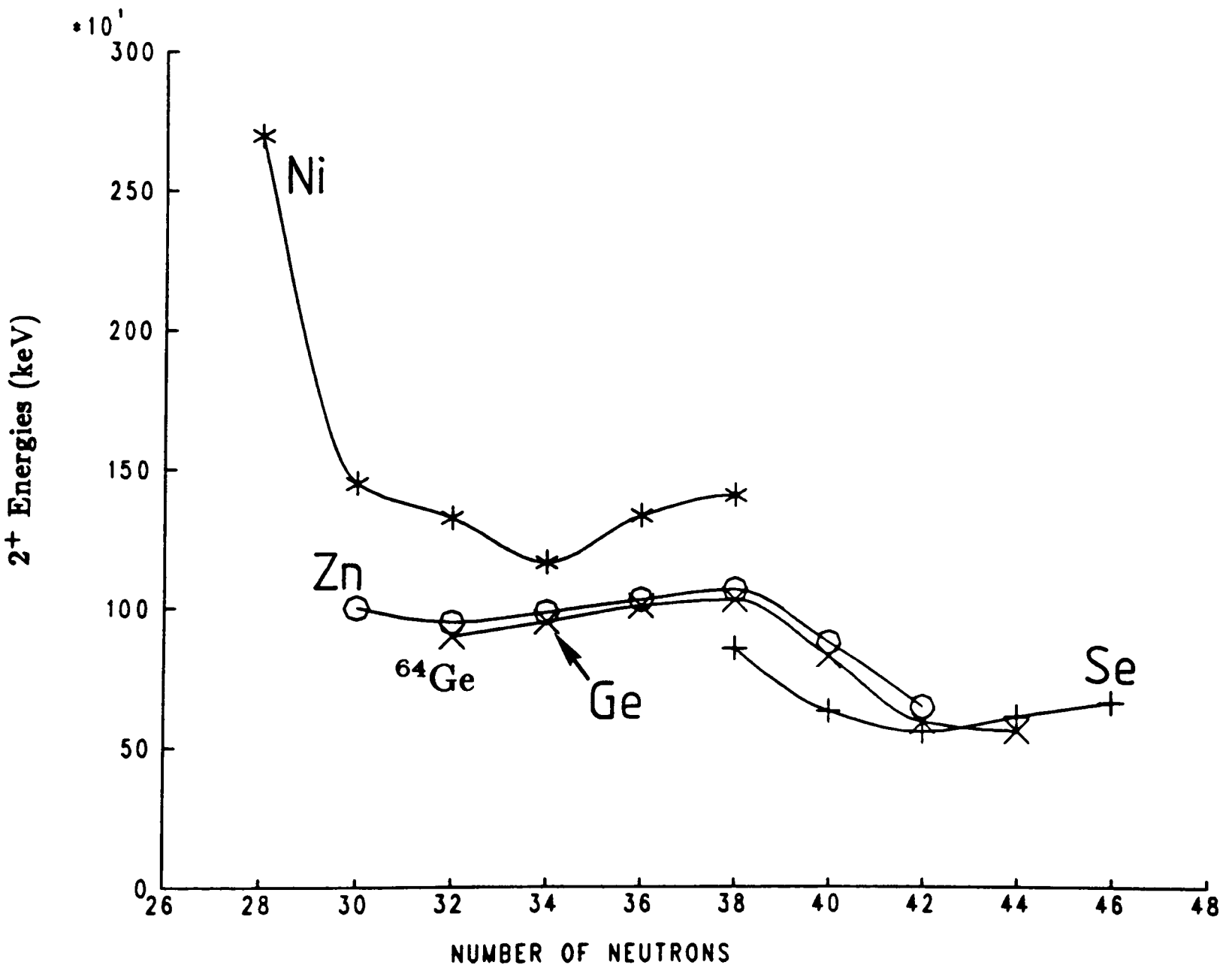


Fig.5.36 : Systematics of first 2^+ states in the A=60 mass region.

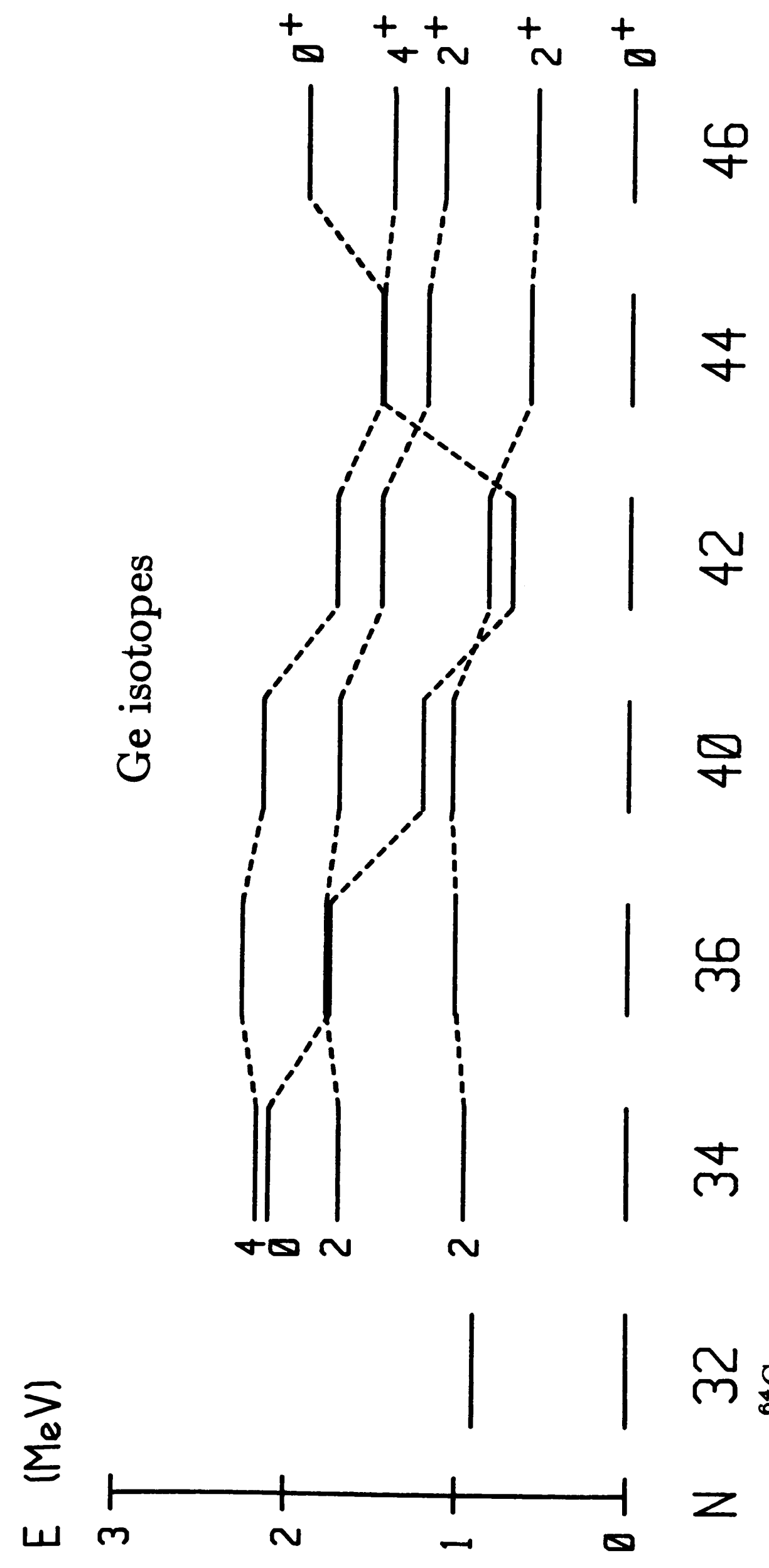


Fig.5.37 : First four excited states in the Ge isotopes.

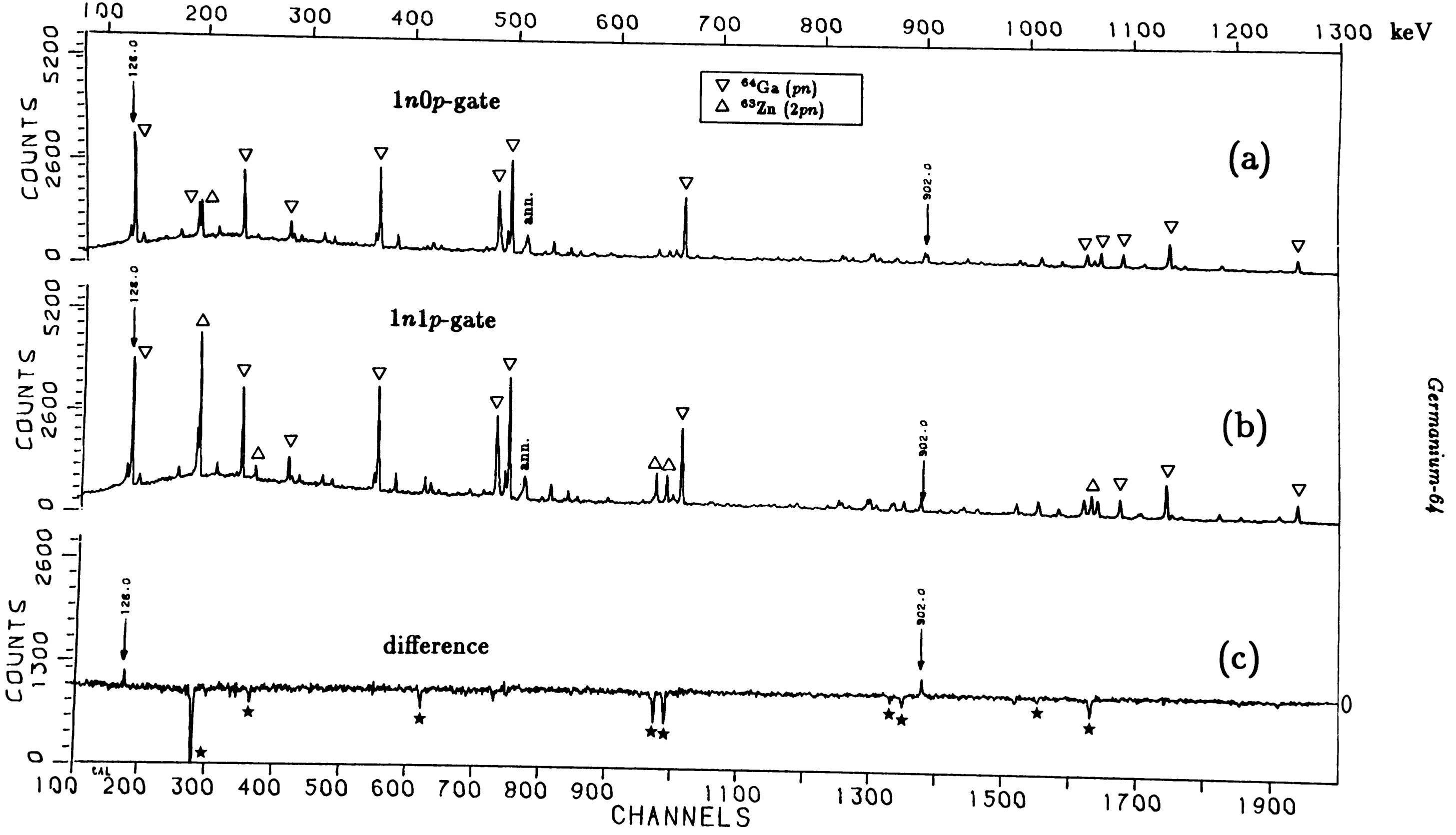


Fig.5.38 : (a) $1n0p$ (b) $1n1p$ (c) $1n0p - const. \times 1n1p$.

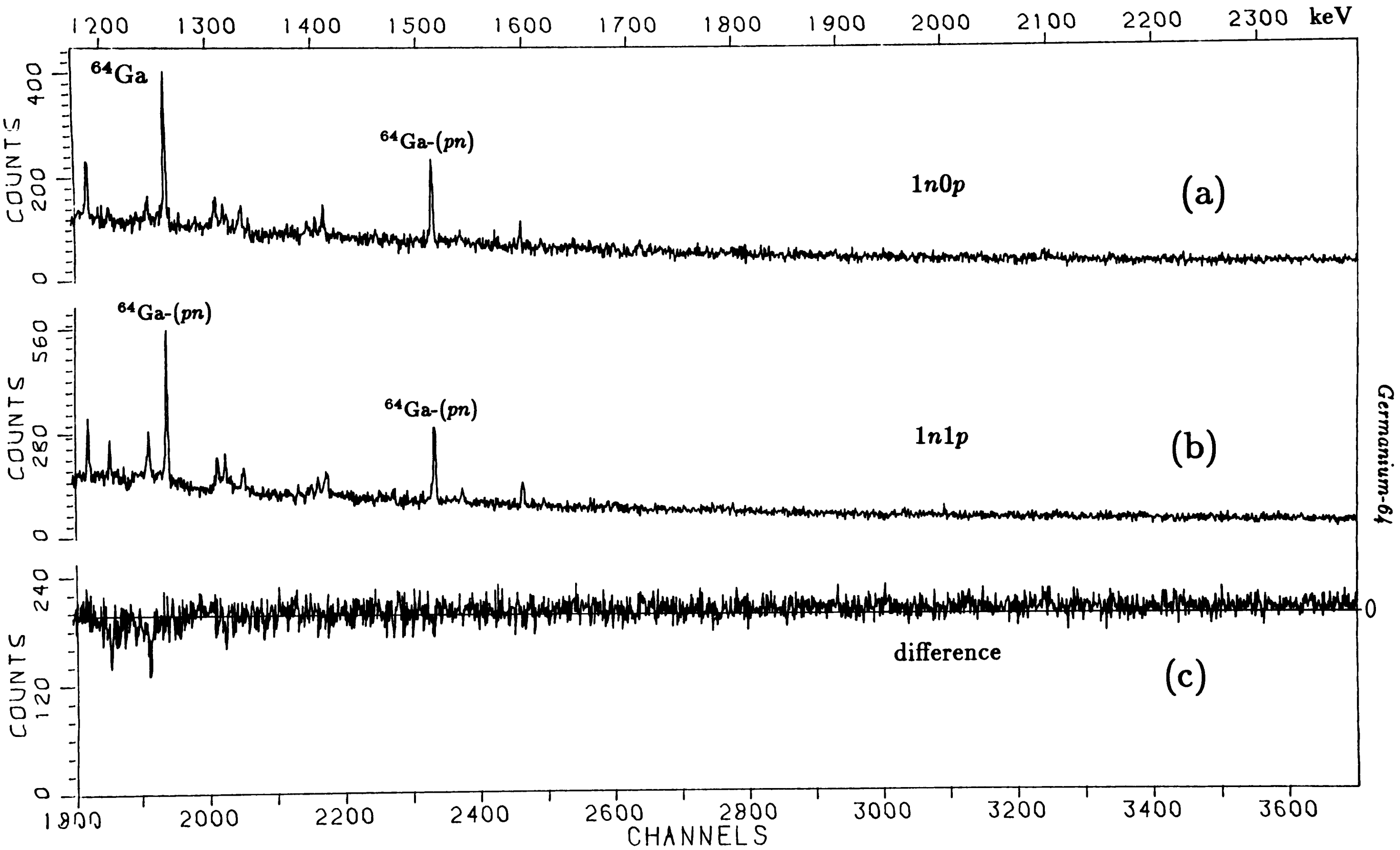


Fig.5.38 : (a) 1*n*0*p* (b) 1*n*1*p* (c) 1*n*0*p* − *const.* × 1*n*1*p*.

The intensity of the 902 keV line in the $1n$ spectrum is 600 ± 115 counts (uncorrected for Ge(Li) efficiency). Assuming that the $(4 \rightarrow 2)/(2 \rightarrow 0)$ ratio in ^{64}Zn is similar to ^{64}Ge, we would thus expect a peak with ≈ 190 counts over 5 channels at approximately 1500 keV. This implies a peak height of ~35 counts and we see in fig. 5.38 that this is easily hidden in the background noise.

Using the empirical formula relating the quadrupole deformation parameter, ϵ, and the energy of the first 2^+ state (§2.5), we obtain $\epsilon = 0.28$ for ^{64}Ge. Superdeformation can thus be ruled out for the ground state of this nucleus. The empirical formula has been shown in §2.5 to employ certain generalizations, e.g. an axially symmetric nuclear shape, that may not always be true. Hence, although the prediction of ϵ by [RAG78] is seen to be the closest to the experimental value, more states in this nucleus must be known before a sensible comparison with the different model predictions can be made.

In summary, we believe that we have observed γ-rays from a transition in ^{64}Ge following $2n$ evaporation from a compound nucleus. From systematics and an absence of any other γ-ray peak in the subtracted $1n$ spectrum (as well as the subtracted $2n$ spectrum), we conclude that this transition corresponds to the ground state transition from the (presumably 2^+) first excited state in ^{64}Ge. Other transitions have not been observed but we have shown that these γ-rays can be hidden in the background and, futhermore, the strength may (like ^{60}Zn) be distributed amongst several γ-rays. In this chapter, we have demonstrated that the observation of pure neutron evaporation from channels with cross-sections less than or in the order of 1 mb is possible with the technique developed in this work. This technique has enabled the first observation of γ-rays from ^{64}Ge to be made.

6

CHAPTER 6

Conclusion

"Oh, I've had such a curious dream"

The aim of the work reported in this thesis has been to determine whether the ground state shape of ^{64}Ge is *superdeformed*. The method selected to do so was the γ-ray spectroscopy of its low-lying states populated with a pure neutron ($2n$) channel. In order to separate this very small channel from a large background of charged particle related channels, a pure neutron multiplicity detection system was designed and developed.

In our system, we were able to determine the neutron multiplicity of an event and, using a charged particle detector, were able to reduce events in coincidence with charged particles. *Ningles* data were collected event-by-event and the data rejection and extraction were performed off-line. To this end a sorting language **SOL** was defined and an interpreter written.

The acid test of the system was the investigation of γ-rays from ^{64}Ge. The data were progressively reduced by applying more and more stringent coincidence requirements. In the resulting spectrum, only one γ-ray peak at 902 keV remained. The systematics of the region suggest that this energy corresponds to the first excited (presumably 2^+) state in ^{64}Ge. This energy implies a quadrupole deformation

parameter $\epsilon = 0.28$ and so a superdeformed shape ($\epsilon = 0.6$) can be rejected. The integrated beam current of the experiment was determined from the intensity of the ^{56}Fe Coulomb excitation line from the backing of the ^{12}C target by using the theoretically calculated Coulomb excitation cross-section. The absolute cross-sections of the different evaporation channels could then be calculated using this integrated beam current. Notwithstanding the many uncertainties in this treatment, estimates of the absolute cross-sections of various channels were obtained and the cross-section for the production of ^{64}Ge was calculated to be $\sim$1 mb.

Using the techniques we have developed, it should be possible to study other exotic nuclei in the very neutron deficient regions of the periodic table; e.g. the heavier self-conjugate nuclei should be accessible by this method. A crucial point in this approach is the use of a heavy projectile and light target in order to kinematically focus the evaporated neutrons into the neutron wall downstream. The Oxford Folded Tandem accelerator was operating at its maximum working voltage for our ^{64}Ge experiment and, although the system is capable of investigating other exotic nuclei, the correspondingly higher energies required would necessitate the use of a higher voltage accelerator.

* * * *

"The time has come," the Walrus said,
"to talk of many things:
Of shoes — and ships — and sealing-wax —
Of cabbages — and kings —
And why the sea is boiling hot —
And whether pigs have wings."

APPENDIX I

Coulomb Excitation

I.1 Introduction

The cross-sections of the Coulomb excitation of ^{56}Fe and ^{197}Au were required in the analyses of the experiments described in chapter 5. The Coulomb excitation of the $0^+ \rightarrow 2^+$ transition in ^{56}Fe was calculated using the de Boer and Winther Coulomb excitation program [ALD66]. For the $3/2^+ \rightarrow 5/2^+$ transition in ^{197}Au, only the relative cross-sections were of interest as they were used for normalizing the γ-ray yield curves and so a formula for the cross-section was used instead. These two methods are discussed separately.

I.2 Iron-56

The de Boer and Winther program provides the differential cross-section for Coulomb excitation and a curve for ^{54}Fe + ^{56}Fe at 150 MeV is shown in fig. I.1. The program was modified to calculate the integrated cross-section. This modified program calculates the total cross-section at the incident energy and the stopping power in the medium for the incident ion (using the formulae quoted by Ziegler in [AND77,ZIE80,ZIE77]). The program then steps through the backing in a pre-set interval (0.1 mg/cm^2 was chosen), calculates the percentage of the beam lost in that

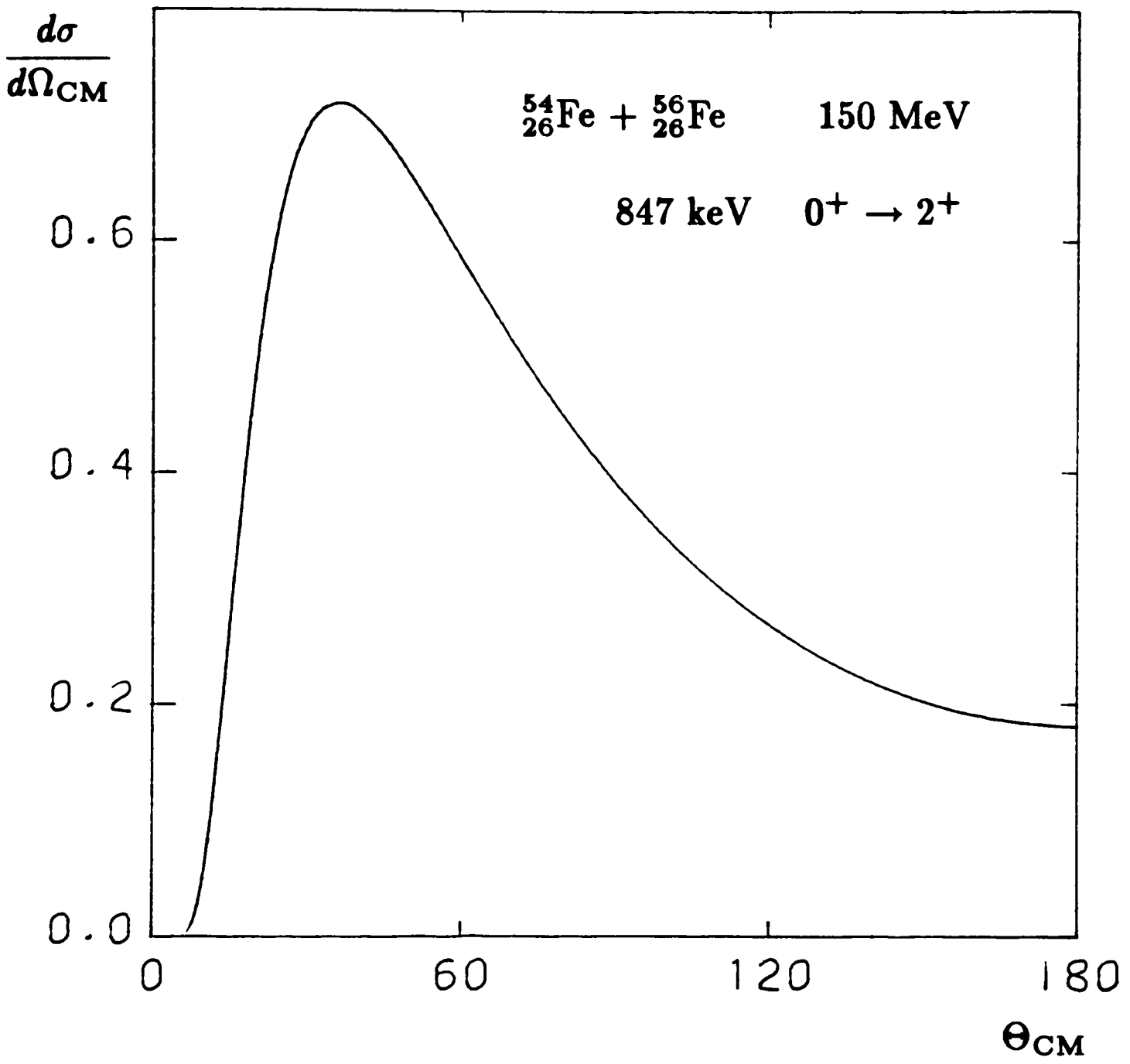


Fig.I.1 : Differential cross-section as a function of angle calculated by the de Boer and Winther program.

section through Coulomb excitation and reduces the energy of the incident beam according to the stopping power calculated. This is repeated until a lower limit for the beam energy is reached (10 MeV was found to be a good value as the Coulomb excitation had, to all intents and purposes, disappeared). The range of the heavy-ion in the backing is taken to end where the Coulomb excitation cross-section is less than 10^{-4} mb. Listed in part 4 of this appendix are the standard equations used to calculate the matrix elements used by the program.

I.3 Gold-197

The cross-section for the Coulomb excitation of ^{197}Au is calculated using the formulae [ALD66]

$$\sigma_{E\lambda} = C_{E\lambda} E_{\mathrm{MeV}}^{\lambda-2} (E_{\mathrm{MeV}} - \Delta E'_{\mathrm{MeV}})^{\lambda-1} B(E\lambda) f_{E\lambda}(\eta_i, \xi)$$

$$C_{E\lambda} = \frac{Z_1^2 A_1}{40.03} [0.07199(1 + \frac{A_1}{A_2}) Z_1 Z_2]^{-2\lambda+2} \qquad \text{barns}$$

$$\Delta E' = (1 + A_1/A_2)\Delta E$$

$\Delta E =$ excitation energy

$A_1 =$ projectile mass

$A_2 =$ target mass

$E_{\mathrm{MeV}} =$ projectile energy in MeV

$B(E\lambda) =$ reduced transition probability

$\lambda =$ multipolarity (=2 in our case)

The classical $f_{E\lambda}$ function is obtained using a function which interpolates the graph given on page 460 of [ALD66]. The resulting curve is shown in fig. I.2. As for the ^{56}Fe case, the beam here is stepped through the backing in 0.1 mg/cm^2 intervals until its energy drops below 10 MeV. The integrated cross-section is then calculated by knowing the percentage of the beam that has been Coulomb excited.

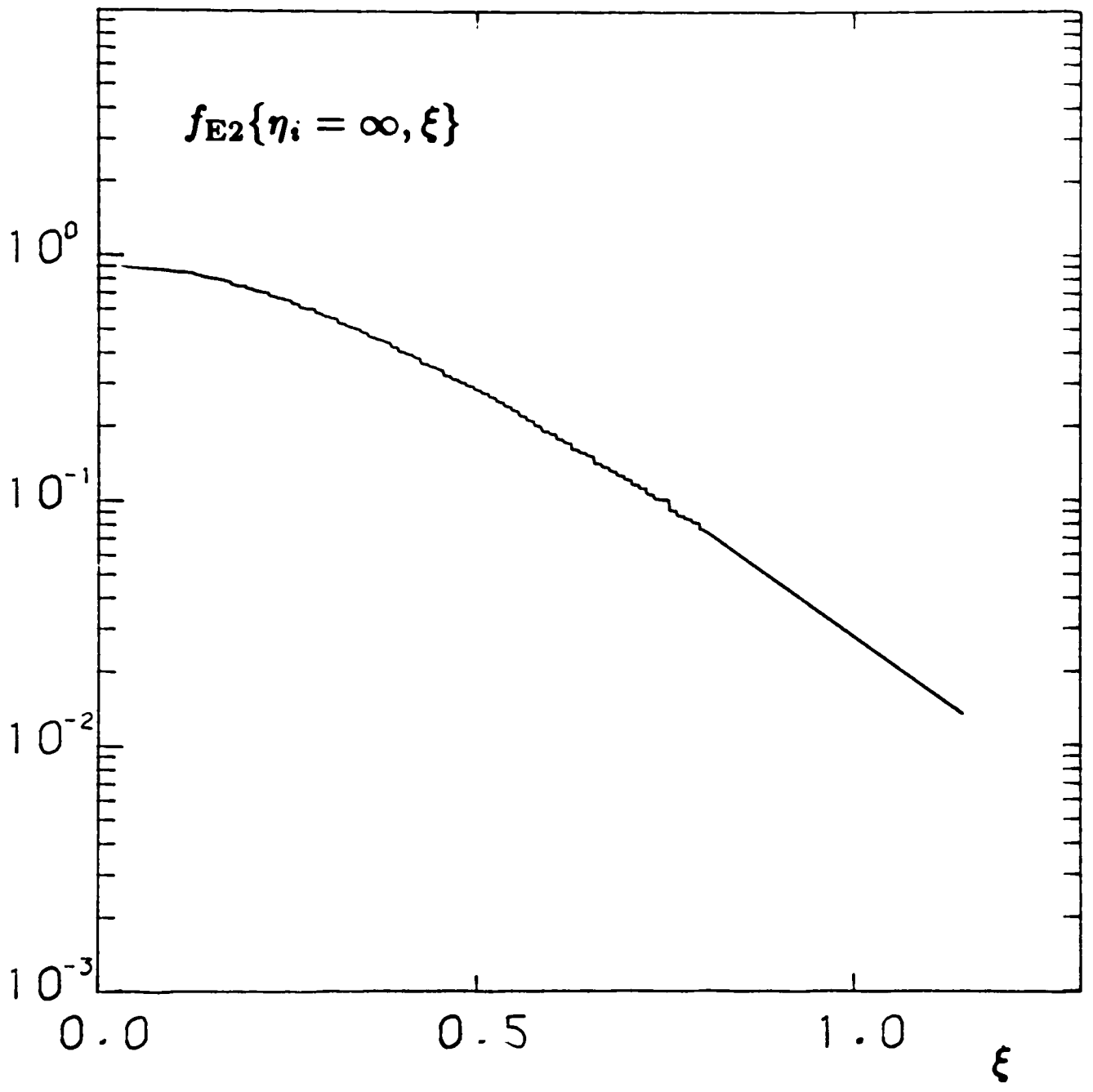


Fig.I.2 : Classical f_{E2} function used in the Coulomb excitation program for ^{197}Au.

I.3 Some Useful Formulae

From Bohr and Mottleson [BOH69] chapters 3.3 and 4.3, we obtain the following relationships for transition probabilities and quadrupole moments.

$$B(E2; I_1 \rightarrow I_2) = (2I_1+1)^{-1} | < I_2 \| M(E2) \| I_1 > |^2 \tag{1}$$

$$eQ = \left(\frac{16\pi}{5}\right)(2I+1)^{-1/2}(II20|II) < I \| M(E2) \| I > \tag{2}$$

$$Q = \frac{3K^2 - I(I+1)}{(I+1)(2I+3)} Q_o \tag{3}$$

$$B(E2; KI_1 \rightarrow KI_2) = \left(\frac{5}{16\pi}\right) e^2 Q_o^2 (I_1 K 20 | I_2 K)^2 \tag{4}$$

where

$B(E2)$ = reduced transition probability.

Q = spectroscopic quadrupole moment.

Q_o = intrinsic quadrupole moment.

K = projection of I on the intrinsic 3-axis.

$M(E2)$ = E2 moment.

For a $2 \rightarrow 0$ transition, equations (3) and (4) reduce to

$$Q = -\frac{6}{21} Q_o = -\frac{6}{21} \sqrt{\frac{16\pi}{2} B(E2) \uparrow}$$

Using a value of $B(E2, 0 \rightarrow 2) = 0.0877$ e^2b^2 [HEI71], the matrix elements were calculated to be $< 0 \| M(E2) \| 2 > = < 2 \| M(E2) \| 0 > = 0.296$ and $< 2 \| M(E2) \| 2 > = -0.35$.

The formulae used to calculate the stopping powers are [ZIE77]

$$S = S_{HI}^{nucl} + S_{HI}^{elec} \quad [\text{ eV / } (10^{15} \text{ atoms / cm}^2) \text{ }]$$

where S_{HI}^{nucl} is the nuclear stopping power given by

$$S_{HI}^{nucl} = s_n (8.462 Z_1 Z_2 M_1) / \left[(M_1 + M_2)(Z_1^{2/3} + Z_2^{2/3})^{1/2} \right]$$

$$s_n = 0.5 \ln(1+\epsilon) / (\epsilon + 0.10718 \epsilon^{0.37544})$$

$$\epsilon = 32.53 \, M_2 E[\text{keV}] / \left[Z_1 Z_2 (M_1 + M_2)(Z_1^{2/3} + Z_2^{2/3})^{1/2} \right]$$

where the subscipts 1 and 2 denote the ion and target respectively and the electronic stopping power is given by

$$S_{HI}^{elec} = S_H^{elec} < S > Z_{HI}^2$$

where S_H^{elec}, the electronic stopping power of protons in a medium, is given in [AND77] and $< S >$ is given by

$$< S > = \left[1 - \exp(-A)\left(1.034 - 0.1777\exp(-0.08114 Z_1)\right)\right]^2$$

$$A = B + 0.0378 \sin\left(\frac{\pi B}{2}\right)$$

$$B = 0.886\left(\frac{E[\text{keV}]}{25 M_1}\right)^{1/2} Z^{-2/3}$$

The following values have been used in the calculations:

$B(E2\downarrow, {}^{197}\text{Au}\ 5/2^+ \rightarrow 3/2^+)$ $= 0.209\ \text{e}^2\text{b}^2$ [BOL79]

^{56}Fe mass density $= 7.866 \times 10^3\ \text{mg/cm}^3$

^{56}Fe number density $= 8.483 \times 10^{22}\ \text{Atoms/cm}^3$

^{12}C mass density $= 2.266 \times 10^3\ \text{mg/cm}^3$

^{12}C number density $= 1.136 \times 10^{23}\ \text{Atoms/cm}^3$

APPENDIX II

The Neutron Wall

II.1 Setting up the Neutron Wall

Threshold of the detectors

The voltage of the photomultipliers should be adjusted so that the γ-rays from a ^{241}Am source are observed by the detector. This γ-ray source (59.5 keV) has been empirically determined to be equivalent to a 500 keV neutron. This was done using a p beam on a ^{7}Li target which produced monoenergetic neutrons (Chapter I.E of [MAR60]; see also [KAL70]). The pulse height from the liquid scintillator in-beam was monitored and compared with the signals obtained from the source to obtain the said relationship. The optimum voltage for the photomultipliers was found to be ~ -2200V. The gains of each tube should be adjusted for maximum signal.

Deoxygenated NE213

The presence of oxygen in the liquid scintillator has the effect of quenching the light output [PRI53]. To reduce this effect, dry Argon gas (or Nitrogen gas) should be bubbled through the liquid scintillator. Other ways of removing oxygen can be found in Chapter 8 of [BIR64].

II.2 The Neutron Wall at a glance

Ref : JOH71, CAR72

Quadrants

Dimensions : Inner radius 8 cm

: Outer radius 35 cm

: Thickness 16 cm

Central detector 125 cm (diameter) × 125 cm encapsulated liquid scintillator (NE213).

Quadrant Tanks

- constructed of aluminium.
- interior coated with white reflector paint (NE561).
- two glass viewing ports (11 cm in diameter) cut into the tank.
- each port optically coupled (using NE587) to a Mullard 11 cm XP1040 photomultiplier tube.
- each tank is filled with ~14.6 litres of NE213 liquid scintillator.

Photomultipliers

- Mullard 11 cm diameter XP1040 tubes.
- Each pair of photomultiplier tubes is powered by a Fluke 423A regulated high voltage power supply.

II.3 Setting up the Composite PSD (see fig. 3.3)

1) Connect the DYNODE output (positive signal) of the photomultiplier to a Timing Filter Amplifier (TFA) and the ANODE signal to a fast Leading Edge (LE) discriminator. Trigger oscilloscope with the output from the LE discriminator.

2) Place a ^{241}Am source against the n-detector and adjust the gain of the TFA for a reasonable pulse size e.g. a gain of 10 with an ORTEC 474 TFA.
   - a bipolar pulse should be seen with a large positive component and a small negative swing.
   - the zero cross-over for the γ's observed in the oscilloscope should be at the same position.
   - adjust the INT and DIFF time constants to obtain a clean cross-over (20 ns & 100 ns were found to be optimal).
3) Connect the start and stop signals of the Time-to-Amplitude Converter (TAC) as shown in fig. 3.3.
4) Place a reasonably strong γ-ray source next to the detector.
5) The TAC spectrum on a Multichannel Analyser (MCA) should show a symmetric Gaussian-like peak — if not, adjust the 'walk' of the Constant Fraction Discriminator (CFD) to obtain such a peak.
6) Place a n-source (e.g. Am-Be) near the n-detector — preferably behind some lead shielding (~5 cm) to reduce the γ-rays.
7) A double humped TAC spectrum should be observed in the MCA.
8) The following should be adjusted to achieve good n-γ discrimination.
   - gain of the TFA
   - INT & DIFF of the TFA
9) When the optimum setting has been achieved, repeat 4) and 5) to ensure γ-ray TAC peak is still symmetric. γ-ray sources with different line energies should be tried to ensure the stability of the system to pulse amplitude walk.
10) Repeated iteration of steps 4 – 9 should be performed until a satisfactory n-γ discrimination is achieved (or until your patience runs out).

II.4 Setting up the Freiburg PSD (see Plate II.1)

1) Connect ANODE signal from the photomultiplier (negative signals) to the 'INPUT' of the unit.
2) Look at the signal from the 'TEST' output (with a lemo socket). Adjust the 'DISC' potentiometer until the signals are just above the noise.
3) The 'MONITOR' switch should be on the left (as shown in the photograph (plate II.1)).
4) Connect the 'START' signal to the the start input of a TAC and the 'MONITOR' signal to the stop input.
5) With a γ-ray source next to the n-detector, adjust the 'WALK' potentiometer to get a symmetric peak.
6) If a neutron source (e.g. Am-Be) is brought up to the detector (preferably shielded by ~5 cm of lead to attenuate the γ-rays), then a double humped peak should be observed.
7) The 'GAMMA' and 'NEUTRON' outputs provide positive logic pulses depending on the setting of the 'LATCH' potentiometer. This can be used if a hardware n-γ discrimination is required. In this case, if the 'MONITOR' switch is switched over to the right side: the TAC spectrum will show a cutoff depending on the setting of the 'LATCH' potentiometer. The logic signals coming out of the 'GAMMA' and 'NEUTRON' outputs then depend on whether the input signal generates a pulse shape signal that is inside or outside the 'LATCH' setting.
8) The 'DELAY' potentiometer allows us to introduce a delay into the output of the 'GAMMA' and 'NEUTRON' logic pulses.

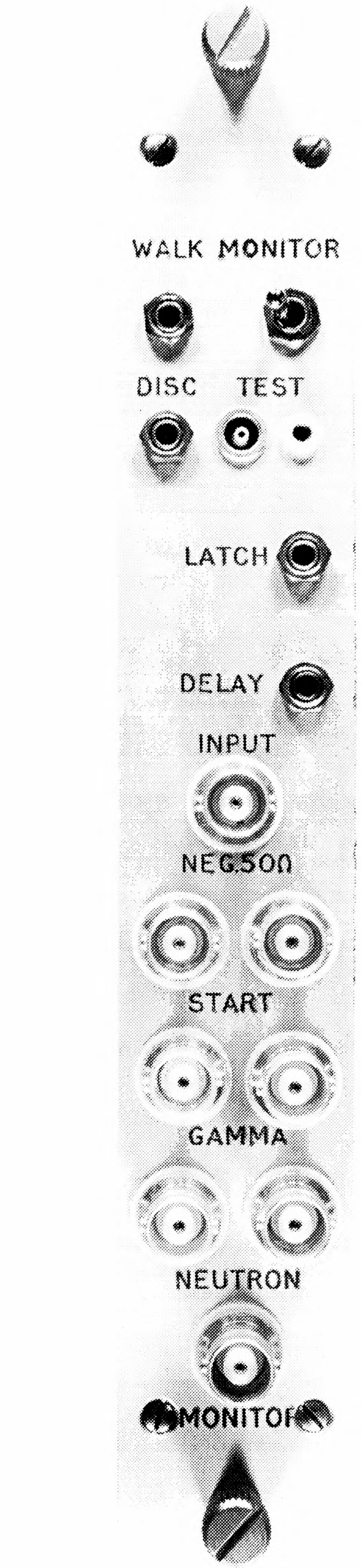


Plate.II.1 : Front panel of the Freiburg Pulse Shape Discriminator.

APPENDIX III

Pulse Shape Discrimination with Liquid Scintillators

III.1 Liquid Scintillators [KIN66, BRO79, BIR64]

In a liquid scintillator, the neutrons elastically scatter off the protons and transfer a fraction of their energy to the protons whilst a γ-ray transfers its energy to the electrons via Compton scattering (and photoabsorption).

In passing through the scintillator, a charged particle will induce ionization in its path (forming a track of high excitation density) and produce secondary electrons (δ-rays) which will cause ionization and excitation in small localized regions known as 'spurs' (fig. III.1). For the electrons, only the spurs will be formed and no track is produced (fig. III.2). Very heavily ionizing particles will create a large number of spurs around the track which merge to form a larger cylindrical track of high excitation density.

Transitions of the π-electronic states of the liquid molecule produce the scintillations. These states are excited in the ionization process. The singlet states excited ($^1X^*$,$^1X^{**}$...etc.) promptly decay to the ground state (^1X) both radiatively and non-radiatively. The triplet states ($^3X^{**}$,$^3X^{***}$ ...etc.) similarly undergo a rapid, mainly non-radiative, transition to the lowest triplet state ($^3X^*$) which cannot decay to the ^1X state as a result of the LS coupling selection rule†. However, this

† Spin-flip transitions are forbidden by this selection rule.

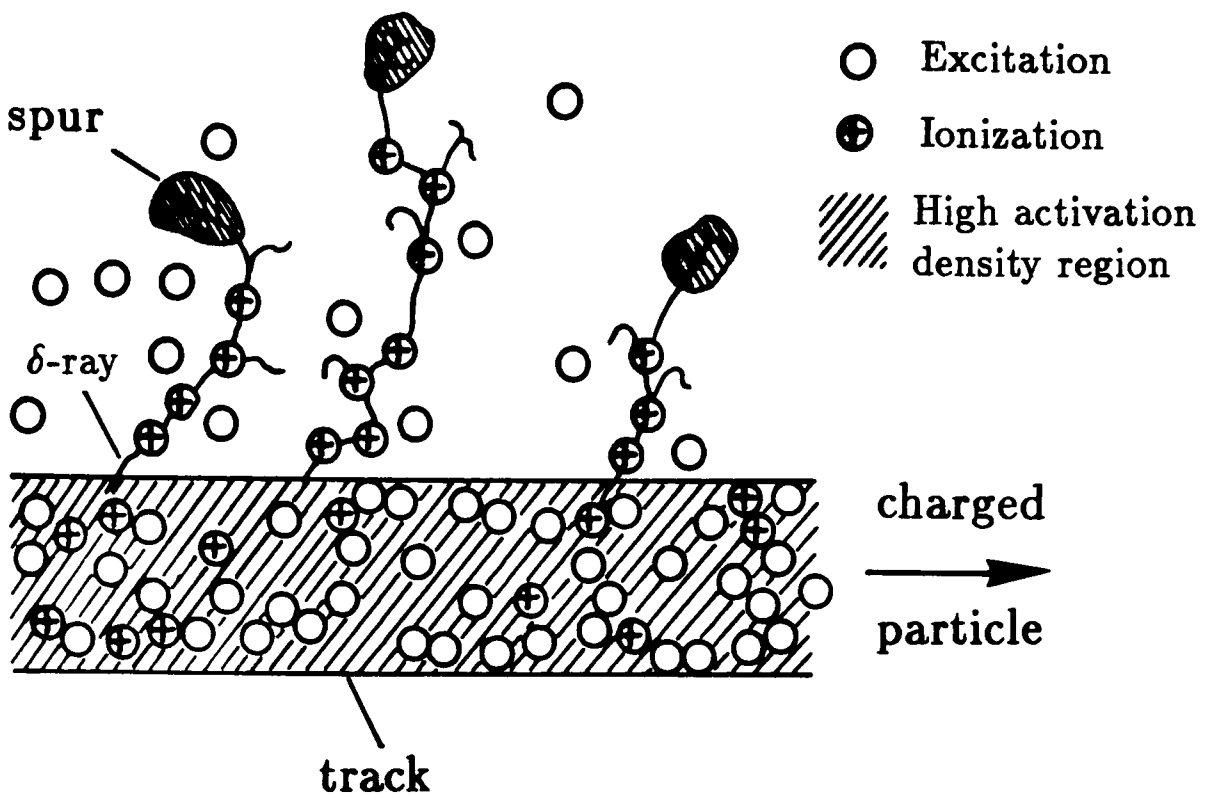


Fig.III.1 : Ionization in a scintillator caused by a heavily ionizing charged particle [BRO79 and reference therein].

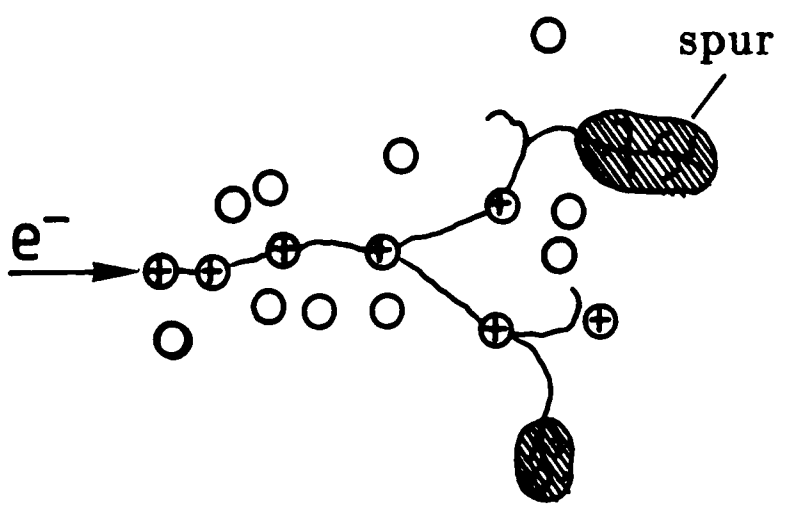


Fig.III.2 : Ionization in a scintillator caused by an electron.

state can decay by triplet annihilation viz.

$$^3X^* + ^3X^* \rightarrow ^1X^* + ^1X + \text{phonons}$$

This process is delayed and so produces a delayed component in the light output.

It is found experimentally [BIR64] that the prompt scintillation component is dependent on dE/dx, the rate of energy loss of the ion through the medium while the slow component is not. The relative intensities of the fast and slow component thus depend on dE/dx and therefore on the nature of the ionizing particle. This is reflected in the dependence of the scintillation pulse shape on the type of the incident particle.

For a large volume detector, the self-absorption of the emitted photon is high enough to warrant the addition of a solute which has its lowest singlet and triplet excitations correspondingly lower than those of the solvent. This will permit a one-way energy transfer from the solvent to the solute which has to be chosen so that this energy transfer will compete favourably with the other modes of de-excitation. The amount of solute added has to be weighed against the degradation of timing resolution of the medium.

In large detectors, light of a longer wavelength is more efficiently transmitted through the liquid and so a secondary solute is often added to shift the spectrum towards lower energy.

Secondary solvents can also be added to facilitate the energy transfer between solvent and solute, in particular the tertiary states. However, the timing resolution will suffer as a result.

The liquid scintillator used in the experiment was NE213 which uses xylene as the primary solvent and naphthalene as the secondary solvent. This scintillator posseses reasonable timing resolution and good pulse shape properties enabling reasonable n-γ discrimination to be achieved.

This section is meant to provide a flavour of the useful properties of liquid scintillators but for an in-depth discourse on this fascinating subject, the reader is referred to [BIR64].

III.2 Freiburg Pulse Shape Discriminator - *modus operandi*

The shape of the signal from the liquid scintillator is dependent upon the ratio of the prompt and delayed components of the scintillation light. The light output from neutrons contain a higher proportion of the delayed component and so a method of determining the pulse shape provides the discrimination required between neutrons and gamma-rays (fig. III.3).

The light from the liquid scintillator is collected by an XP1040 photomultiplier tube and the dynode chain, shown in fig. III.5, provides a working voltage of -2.5 kV and draws a current of 2.5 mA. A negative bias is used to dispense with the use of a decoupling capacitor at the anode. Signals appearing at the anode thus suffer less distortion.

The anode signal is fed into a Pulse Shape Discriminator (PSD) built on a design by P.Betz *et al* [BET74]. The input signal is split up (fig. III.6) and channelled into a Constant Fraction Discriminator (CFD) and an integrator (INT). The function of the integrator is to convert the pulse shape information from the decay time (fig. III.3) to the rise time (fig. III.4) of the signal. This integrated signal is then converted to a bipolar signal by the Double Delay Line Amplifier (DDLA). The zero-crossing point of the output signal from the DDLA depends on the rise time of the integrated signal. This crossing point is then determined by a Zero-Crossing Discriminator (ZCD) which generates a fast negative logic pulse. The CFD output is used to start a Time-to-Amplitude Converter (TAC) and the output from the ZCD to stop it.

In tests with a 10 mCi Am-Be source, the TAC spectrum obtained is shown in fig. III.7(a). The peak (P_γ) to valley ratio is 8. The response of the PSD to a ^{60}Co source is shown in Fig III.7(b) for comparison.

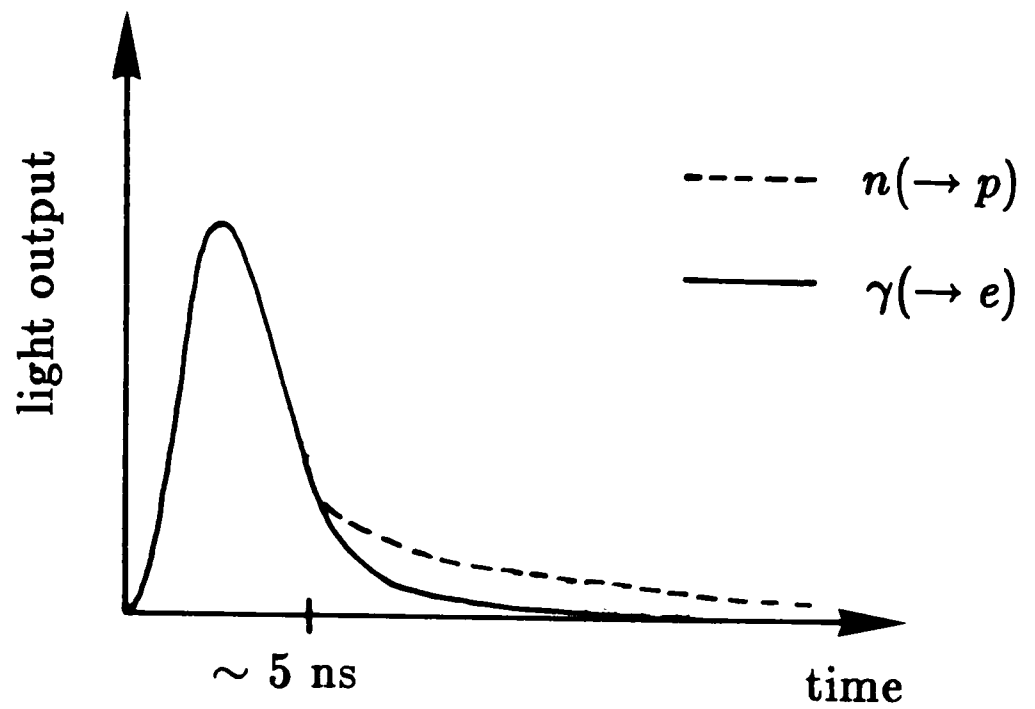


Fig.III.3 : Light output from the scintillator as a function of time for different incident particles.

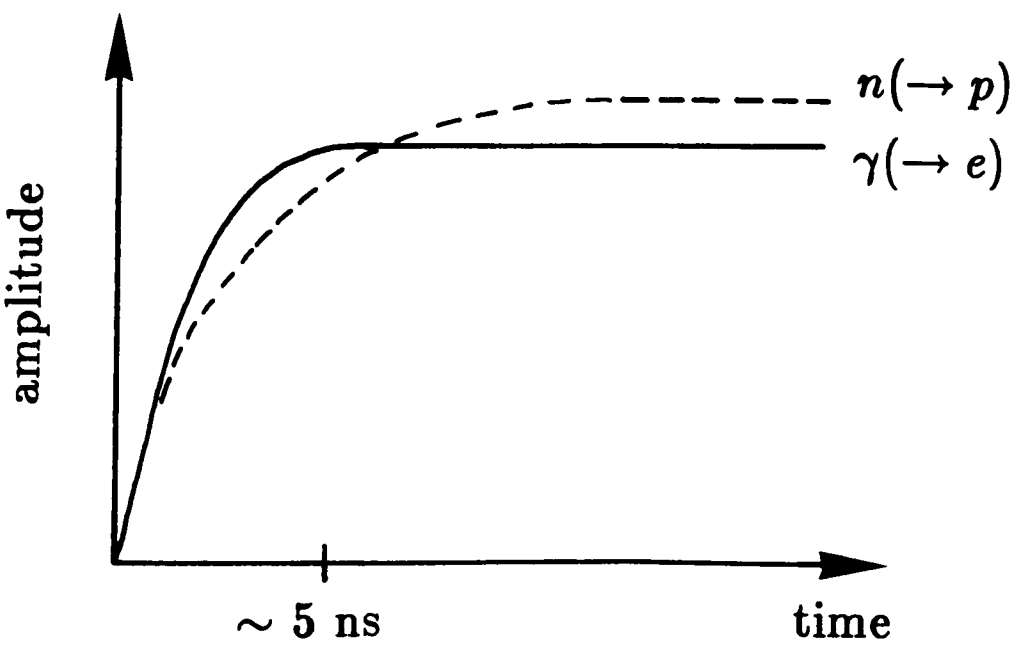


Fig.III.4 : Output from an integrator for signals from different incident particles.

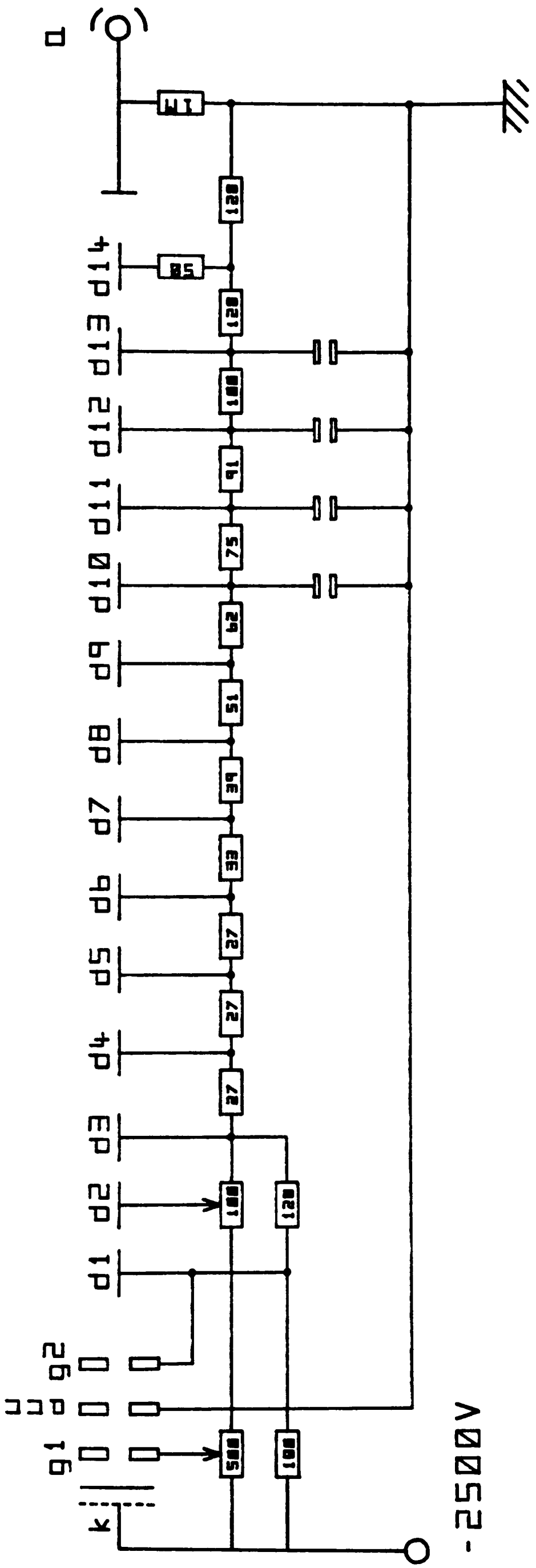


Fig.III.5 : Dynode chain used to power the photomultiplier.

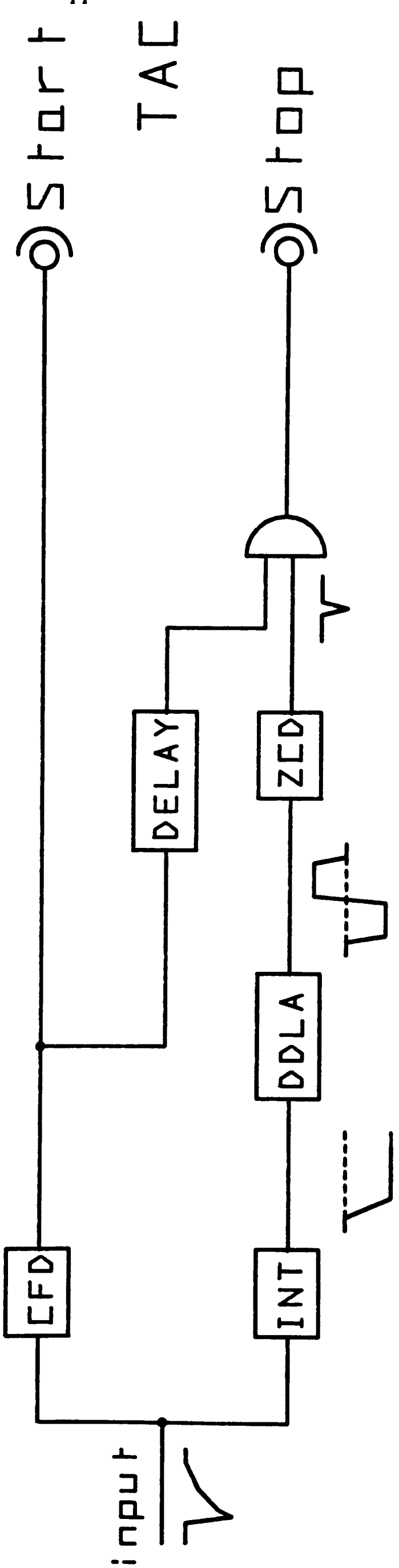


Fig.III.6 : Schematic electronic block diagram for the Freiburg PSD.

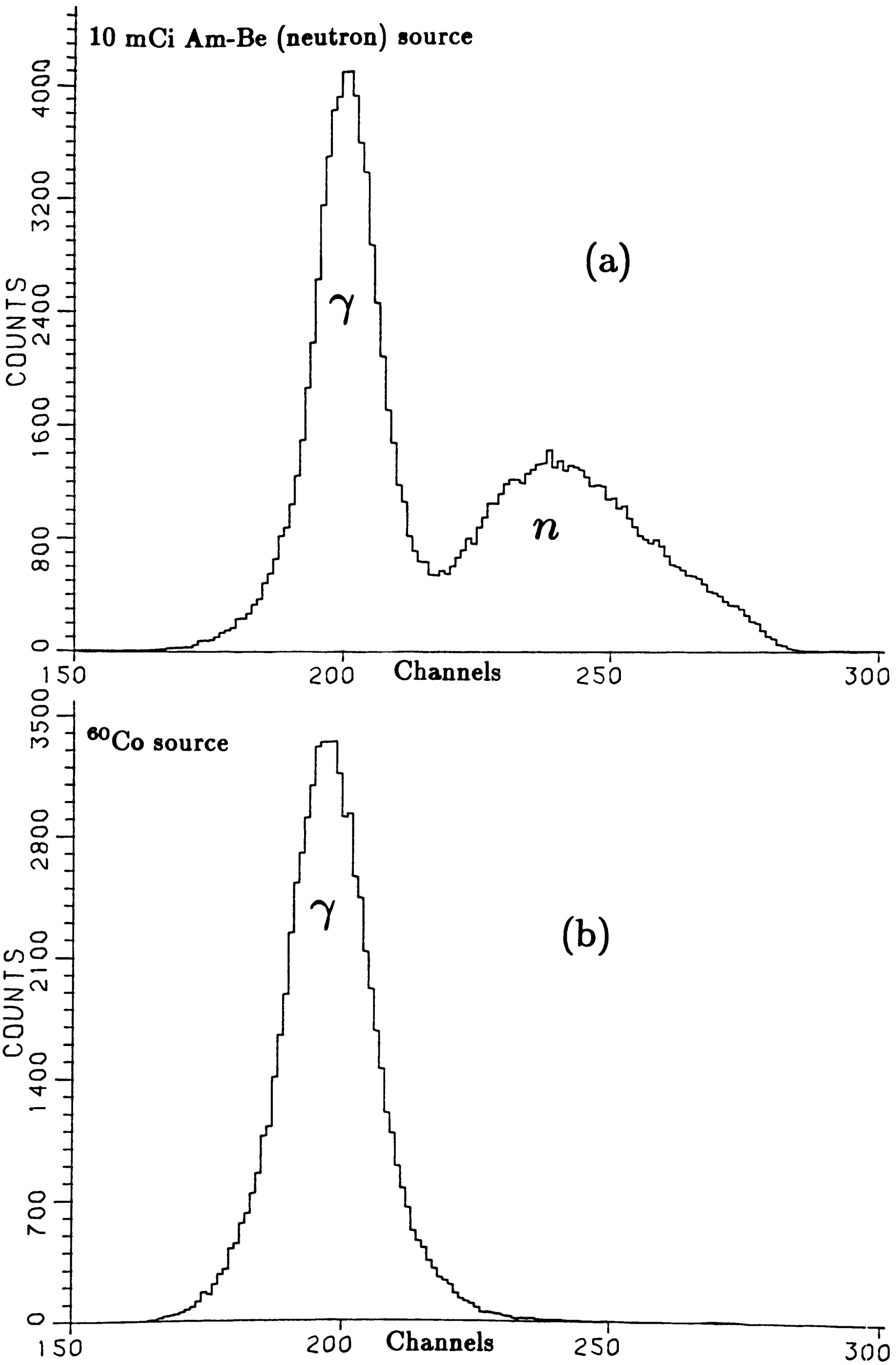


Fig.III.7 : TAC spectrum of Freiburg PSD output for (a) neutron source and (b) γ-ray source.

APPENDIX IV

The Sorting Routine

IV.1 A Sorting Language SOL

"Contrariwise," continued Tweedledee, " if it was so,
it might be; and if it were so, it would be:
but as it isn't it ain't. That's logic.

The data had to be sorted into different spectra depending on the logical relationship between the signals from the various detectors, so a minimal sorting language **SOL** was defined and implemented. In section 3, the syntax of this language is given but in this section, the various logical operations and bit-wise manipulations are introduced and explained.

In the off-line analysis program, GENDAT, up to 32 windows (0...31) can be defined. A window can take one of two values viz. 1, which is *true* or 0, which is *false*. The status of each window is set, for each event, in a double precision integer consisting of 4 bytes (32 bits). Bit 0 (the least significant bit) corresponds to window 0, bit 1 to window 1 and so on. If a window is satisfied (i.e. *true*) the corresponding bit is then set to 1, otherwise, it is left as 0.

SOL is incorporated in GENDAT and operates on *logical lists* and *registers*. The registers are similar to the windows i.e. there are up to 32 of them and the

status of each is defined by a bit in a 32 bit word. The registers take the values 0 (*false*) or 1 (*true*). A *logical list* is a list of windows and registers to which logical operations are performed and whose result is placed in one of the registers (which shall be termed the *output register*). The logical operations include:–

• OR - the logical list is checked and if one element of the list is *true* then the output register is *true*.

• AND - the *output register* is *true* ONLY if every element of the list is *true*. For instance, in the following statement

```
AND 0 2 3 R4 R3 9 R5
```

will set the *output register* R5 to *true* iff. windows 0,2,3 and 9 and registers R3 and R5 are all *true*. The *output register* always comes after the logical list.

• Individual bits of a parameter word (2 bytes long) can be tested and, if found set to 1, an *output register* can be set to *true* using TBIT e.g.

```
TBIT 4 5 R7
```

will check the 6th bit (as the first bit is bit number 0) of parameter 4 and set register 7 to *true* if the bit is 1.

• The value of a register can be logically negated by NOT e.g.

```
NOT R15
```

will set register 15 to *false* if the value is *true* and vice versa.

• **Program control** is achieved via IF..ENDIF or IF..ELSE..ENDIF structures where a logical list is tested to decide the subsequent flow of the program. E.g.

```
IF 0 R1 2 R5
<block 1>
ELSE
<block 2>
ENDIF
```

The instructions within <block 1> are executed if 0,2,R1 and R5 are *true*, otherwise, <block 2> is executed. The IF-structure can be nested e.g.

```
IF ...
```

```
        IF ...
        :
        ENDIF
    ELSE
    :
    ENDIF
```

• Ultimately, a spectrum is updated if a specified logical relationship between the various windows (and registers) is satisfied. The spectrum can either be incremented (INC) or decremented (DEC). For the former, the appropriate channel in the spectrum will be increased by 1 whilst the latter will reduce the channel by 1 e.g.

```
INC 6 3 100 4
```

will increment spectrum 6 with parameter 3, P(3), using a back-bias of 100 and a compression factor of 4 i.e.

$$Y_6(x) = Y_6(x) + 1$$

$$\text{where} \qquad x = \frac{P(3) - 100}{4}$$

There are two logical counterparts LINC and LDEC which will update the spectrum if the logical list is satisfied e.g.

```
LINC 6 3 100 4 0 R3 1 2 R20
```

will be carried out only if 0,1,2,R3 and R20 are *true*.

For each event, the registers are cleared and then set according to the dictates of the current **SOL** programme. The instructions are executed sequentially. For speed, the program has to be assembled (or *tokenized* — which is the replacement of the verbose, but easy to understand, syntax with a series of numbers which can be interpreted with greater speed by the analysis program). A title can be added to each programme using

```
TITLE string
```

which allows an alphanumeric string to be attached to each programme thus allowing easier identification after assembly. (Source files have the extension .SOR while

assembled files have .BIN as an extension). All characters after the symbol ! are ignored during assembly and so comments can be added to the source file this way. The end of every **SOL** programme must have the statement

END

IV.2 An Example SOL Programme

As an example, consider the hypothetical situation where we have 4 parameters per event on a data tape corresponding to:–

P0	–	γ-ray energy
P1	–	TOF data
P2	–	PSD data
P3	–	Router bit pattern

and bit number 6 is set in P3 if a charged particle is detected. Further, assume window 0 to be set if the TOF parameter indicates a neutron and, similarly, window 1 for a PSD neutron. To obtain the following spectra:–

Spectrum #	Comment
0	γ's in coincidence with TOF n
1	γ's in coincidence with TOF n and PSD n
2	γ's in coincidence with TOF n and PSD n and charged particle
3	γ's NOT in coincidence with TOF n or PSD n

the corresponding **SOL** programme is (next page):–

```
! Listed below is an example of a typical SOL programme. The
! syntax of the language is flexible enough to allow us to
! achieve a similar end in many different ways. The program is
! in a file 'EXAMPLE.SOR' and when assembled with the command
! ASM EXAMPLE EXAMPLE, will produce another file 'EXAMPLE.BIN'
! with the tokenized programme.
! Back bias = 200, Compression factor = 2
!
TITLE EXAMPLE PROGRAM      ! title of EXAMPLE.SOR
IF 0                       ! check TOF n
  INC 0 0 200 2            ! increment spectrum 0
  IF 1                     ! check if also PSD n
          INC 1 0 200 2    ! if so increment spectrum 1
          TBIT 3 5 R0      ! check bit 6 of P3 for charged ptcle. event
          LINC 2 0 200 2 R0  ! inc. sp. 2 if with charged particle
 ENDIF
ELSE                       ! NOT TOF n
  OR 1 R1                  ! copy window 1 to R1
  NOT R1                   ! invert R1
  LINC 3 0 200 2 R1        ! if R1 true (i.e. PSD n false) then inc.
ENDIF
END                        ! indicate end of prog. to assembler
```

IV.3 Syntax of SOL

For brevity, the syntax of the minimal sorting language, **SOL**, is listed below in BNF‡ notation.

```
<programme>        ::= <expression>
                       END
<expression>       ::= <or>|<and>|<inc>|<linc>|<dec>|<ldec>|<if>|<lbl>
                       |<tbit>|<not>|<title>
<or>               ::= OR <logical list> <output register>
<and>              ::= AND <logical list> <output register>
<inc>              ::= INC <spectrum> <parameter> <backbias> compression.>
<linc>             ::= LINC <spectrum> <parameter> <backbias> <comp.>
                           <logical list>
<dec>              ::= DEC <spectrum> <parameter> <backbias> <compression>
<ldec>             ::= LDEC <spectrum> <parameter> <backbias> <comp.>
                           <logical list>
<if>               ::= IF <logical list>
                           <expression>
                       ENDIF
                       | IF <logical list>
                           <expression>
                       ELSE
                           <expression>
                       ENDIF
<tbit>             ::= TBIT <parameter> <bitnumber> <output register>
<not>              ::= NOT <register>
<title>            ::= TITLE <string>
<logical list>     ::= <log. param.> | <log. param.> <logical list>
<log. param.>      ::= <window> | <register>
<output register>  ::= R<integer>
<register>         ::= R<integer>
<window>           ::= <integer>
<parameter>        ::= <integer>
<spectrum>         ::= <integer>
<backbias>         ::= <integer>
<compression>      ::= <integer>
<bitnumber>        ::= <integer>
<string>           ::= <char> | <char><string>
<integer>          ::= <number> | <number><integer>
<char>             ::= a|b|...|z|A|B|...Z
<number>           ::= 0|1|2|...|9
```

---

‡ Backus Naur Form - J.W.Backus, Proc. Zürich ACM-GAMM Conf, ICIP Paris 1959.

APPENDIX V

CASCADE Input

In order to select suitable reactions to produce the nuclei studied in this thesis, an evaporation code, CASCADE, was used. The theory of evaporation calculations has been discussed in §2.3 and in this appendix we address ourselves to the more practical aspects of running the code. This code was modified to run on a VAX11/780†. The code accepts 16 input cards which allow the user to change various parameters used by the program. A brief summary of the input cards is given in table V.1. For detailed description of the meaning of each variable, the reader is referred to the documentation supplied with the program [PUH79]. A typical input used by our calculations is shown in fig. V.1. Most of the input parameters have been set to zero. In such a situation, the program substitutes default values for the input parameters and fig. V.2 shows the CASCADE output with the default input parameters chosen by the program.

According to Pühlhofer [PUH77a, PUH79], the parameters that may be important are CL0, R0LDM and KOPTEB. We varied these parameters as well as a few others to see what effect they had on the calculated cross-sections. Table V.2 shows the cross-sections for the different input parameters where the numbers in [...] are the default values used by the program. This table is displayed in pictorial form in fig. V.3 in which the percentage variation from the default values are plotted. We see from the table that the cross-sections do not vary by more than a factor of 2 and the $2n$ cross-section stays at $\sim$1 mb. The largest variation comes from varying CL0,

† E.F.Garman, Nucl. Physics Laboratory, Oxford, 1982.

the maximum angular momentum brought into the compound nucleus. As shown in §2.3, the cross-sections are dependent on the angular momentum and so we see that the fusion cross-section, σ_F, varies as we vary CL0. The relative cross-sections, however, hardly vary at all. The default value for CL0 is calculated using a formula from [COH74]. We find that the liquid drop radius parameter, R0LDM, alters the relative cross-sections of the evaporating channels. This variable changes the shape of the yrast line used by the program and this, in turn, affects the level densities and hence the transmission coefficients of the evaporating particles. The default value of R0LDM has been taken from [MYE73]. KOPTEB, the option for the liquid drop mass formula used also changes the relative cross-section by a noticeable amount. This parameter chooses one of 7 different formulae of the liquid drop mass formula and the default one is from [MYE66].

This investigation into the dependence of the cross-section on the input parameters is by no means exhaustive. Not all the parameters have been varied but the ones left out have been indicated not to be crucial to the result of the calculations [PUH77a, PUH79]. However, we have shown that in most cases, even for the critical parameters, the cross-sections do not change by more than a factor of two when the parameters are varied. To use CASCADE as a tool for selecting suitable reactions, we require only order-of-magnitude accuracy for the predictions and so the default values were used in our calculations.

1	title	
2	entrance channel	IZP,IAP,IZT,IAT,ELAB
3	spins	JP,JT,IP12,JCN
4	decay cascade	KOPTK,IPS1,IPSMAX,NNX,NPX,NAX
5	4th decay, fission	IZE4,IAE4,JE4,IZFF,DAF,FB
6	CN angular momentum	CL0,DIFF,SIGMACN
7	level dens. parameters	FTHETA,KOPTLD
8	level dens. high excit.	DALDM,UTR,ULDM,UITR,UILDM,KOPTLQ,KOPTEB
9	yrast line	R0LDM,DEF,DEFS
10	γ-decay	ξE1,ξM1,ξE2,CJG1,CJG2,ξENH,GMIN
11	cut-offs	WGR,CGR,CVCBE,CVCB,VK,CVK
12	cut-offs	EXR0,EXH,CJC,LC0
13	output options	KOUTW,KOUTL,KEVAP,KGAMMA
14	individual level density parameters (or blank card)	
15	individual spectra (or blank card)	
16	new run or two blank cards	

Table V.1 : Brief description of the CASCADE input cards.

Input	Comments
54Fe + 12C at 150 MeV	Card 1
26,54,6,12,150.	Card 2
0,5,0,0,	Card 3
0,0,0,0,0,0,	Card 4
0,0,0,1,0.,0.,	Card 5
0.,0.,0.,	Card 6
0.,2,	Card 7
0.,0.,0.,0.,0.,0,0,	Card 8
0.,0.,0.	Card 9
0.,0.,0.,0.,0.,0.,0.,	Card 10
0.,0.,0.0,0.,0.,0.,	Card 11
0.,0.,0.,0,	Card 12
0,0,0,0,	Card 13
	Card 14
	Card 15
	Card 16

Fig V.1 : Typical input cards to CASCADE.

```
C A S C A D E  I  54Fe + 12C at 150 MeV

ENTR.CHANNEL, CN  ZP,AP,ZT,AT,ELAB,ZCN,ACN,EXCN 26  54   6   12 150.0 32   66   32.6
SPINS             JP,JT,IP12,JCN                    0        0      0        0
DECAY CASCADE     OPT,IPS1,IPSMAX,NN,NP,NA          3   10   20    3    3    3
4.DECAY, FISSION  Z4,A4,J4, IZFF,DAF,FFB            0    0    0      1   8.00   1.00
ANGULAR M. IN CN CL0,DIFF,(SIGMACN)                11.18   2.00  (    0.0)
LEVEL DENS. PARM  FTHETA,OPTION,PARM/LEVLS IN      0.00     2    —
LEVEL DENS. LD    DA,UTR/LDM,UJTR/LDM,OPT,OPTEB    8.00 10.0 20.0 10.0 20.0    0    0
YRAST LINE        R0LDM,DEF,DEFS                   1.26 0.31E-04 0.35E-07
GAMMA DECAY       E1,M1,E2(WEISSK.U),ENH,GMIN      0.00010 0.030    5.0   0. 0.   0.   1.0000
CUTOFFS           WGR,CGR,CVCBE,CVCB,VK,CVK        0.0030 0.0008 0.10 0.04 0.33 0.05
CUTOFFS           EX-RANGE,EXH,CJC,L-CUTOFF        32.0   30.0   3.0       19
OUTPUT OPTIONS    KOUTW,KOUTL,KEVAP,KGAMMA           1     1     1     1
```

A	-1	0	1	2	3	4	5	6	7	8	9	(N-Z)
38		0.0		0.0		0.0		0.0		0.0		0.00 0
39	0.0		0.0		0.0		0.0		0.0		0.0	0.00 0
40		0.0		0.0		0.0		0.0		0.0		0.00 0
41	0.0		0.0		0.0		0.0		0.0		0.0	0.00 0
42		0.0		0.0		0.0		0.0		0.0		0.00 0
43	0.0		0.0		0.0		0.0		0.0		0.0	0.00 0
44		0.0		0.0		0.0		0.0		0.0		0.00 0
45	0.0		0.0		0.0		0.0		0.0		0.0	0.00 0
46		0.0		0.0		0.0		0.0		0.0		0.00 0
47	0.0		0.0		0.0		0.0		0.0		0.0	0.00 0
48		0.0		0.0		0.0		0.0		0.0		0.00 0
49	0.0		0.0		0.0		0.0		0.0		0.0	0.00 0
50		0.0		0.0		0.0		0.0		0.0		0.00 0
51	0.0		0.0		0.0		0.0		0.0		0.0	0.00 0
52		0.0		0.0		0.0		0.0		0.0		0.00 0
53	0.0		0.0		0.0		0.0		0.0		0.0	0.00 0
54		0.0		0.0		0.0		0.0		0.0		0.00 0
55	0.0		0.0		0.0		0.0		0.0		0.0	0.00 0
56		0.0		0.0		0.0		0.0		0.0		0.00 0
57	0.0		0.0		0.0		0.0		0.0		0.0	0.00 0
58		0.0		1.0		0.0		0.0		0.0		1.03 0
59	0.0		0.0		0.0		0.0		0.0		0.0	0.00 0
60		0.0		0.5		2.3		0.0		0.0		2.83 0
61	0.0		9.6		71.4		0.0		0.0		0.0	81.01 000000
62		0.0		0.4		0.0		0.0		0.0		0.45 0
63	0.0		0.0		40.2		30.7		0.0		0.0	70.85 000000
64		0.8		79.2		124.0		0.0		0.0		203.89 000000000000000
65	0.0		0.2		1.0		0.0		0.0		0.0	1.12 0
66		0.0		0.1		0.0		0.0		0.0		0.06 0

```
RESIDUE CROSS S.        361.24 MB
FISSION CROSS S.          0.00 MB
FUSION  CROSS S.        363.07 MB

LOST CROSS SECTIONS       3.32 MB CN.GT.JMAX
```

Fig.V.2 : CASCADE output giving the cross-section for the various channels.

#	2p	pn	αp	2pn	3p	αn	2n	$\sigma_F^{(1)}$	Comments
1	124.0	79.2	71.4	40.2	30.7	9.6	0.8	363.1	default
2	124.0	79.2	71.4	40.1	30.7	9.6	0.8	363.1	card 5 diproton
3	124.0	79.2	71.4	40.2	30.7	9.6	0.8	363.1	card 5 deuteron
4	124.0	79.2	71.4	40.2	30.7	9.6	0.8	363.1	card 5 IZFF=0 [1]
5	124.0	79.2	71.4	40.2	30.7	9.6	0.8	363.1	card 5 FB=0.5 [1.0]
6	52.9	34.4	28.1	24.3	17.8	4.7	0.4	167.1	card 6 CL0=6 [11.2]
7	67.0	43.3	36.1	28.6	21.2	5.8	0.5	206.3	card 6 CL0=7 [11.2]
8	82.5	53.0	45.1	32.3	24.2	6.9	0.6	250.3	card 6 CL0=8 [11.2]
9	100.7	64.4	56.2	36.4	27.5	8.1	0.7	299.2	card 6 CL0=9 [11.2]
10	120.2	76.8	68.9	39.6	30.2	9.4	0.7	352.9	card 6 CL0=10 [11.2]
11	137.8	86.5	77.9	43.1	33.1	10.5	0.8	396.1	card 6 CL0=11 [11.2]
12	161.3	101.1	94.4	45.5	35.2	11.9	0.9	458.8	card 6 CL0=12 [11.2]
13	211.4	136.1	136.0	49.7	38.7	14.8	0.9	598.8	card 6 CL0=13 [11.2]
14	111.0	80.4	88.3	35.3	28.1	11.6	0.6	363.1	card 6 CL0=15 [11.2]
15	119.2	99.3	74.1	30.7	25.8	7.0	0.4	363.1	card 7 FTHETA=0.5 [0.85]
16	119.3	87.5	74.7	36.8	26.0	11.2	0.9	363.1	card 7 KOPTLD=0 [1]
17	123.2	78.6	68.6	41.3	33.0	10.4	1.0	363.1	card 8 UTR,ULDM=15,20[10,20]
18	120.5	80.0	69.3	43.7	31.3	10.3	0.9	363.1	card 8 UTR,ULDM=5,30[10,20]
19	124.0	79.2	71.4	40.2	30.7	9.6	0.8	363.1	card 8 UTR,ULDM=10,30[10,20]
20	119.4	77.2	62.2	48.9	38.0	9.8	0.9	363.1	card 8 KOPTEB=0 [0]
21	105.6	89.9	64.8	52.8	28.7	12.8	1.3	363.1	card 8 KOPTEB=1 [0]
22	124.1	77.7	64.7	44.3	35.5	9.2	0.8	363.1	card 8 KOPTEB=2 [0]
23	110.8	90.3	68.2	46.8	26.5	12.1	1.2	363.1	card 8 KOPTEB=3 [0]
24	125.5	73.8	64.6	44.3	38.6	8.8	0.7	363.1	card 8 KOPTEB=4 [0]
25	110.7	87.6	69.1	47.3	27.9	12.1	1.1	363.1	card 8 KOPTEB=5 [0]
26	120.5	71.1	81.7	45.4	25.0	10.5	0.6	363.1	card 8 KOPTEB=6 [0]
27	121.9	75.6	74.3	41.7	31.0	10.0	0.7	363.1	card 9 R0LDM=1.1 [1.26]
28	125.4	76.7	67.1	45.7	30.7	9.5	0.8	363.1	card 9 R0LDM=1.2 [1.26]
29	124.5	76.9	65.3	47.4	31.8	9.5	0.9	363.1	card 9 R0LDM=1.4 [1.26]
30	122.3	79.5	64.0	45.0	34.0	10.0	0.9	363.1	card 9 R0LDM=1.5 [1.26]
31	122.1	75.9	63.7	51.3	32.1	10.0	0.9	363.1	card 9 R0LDM=1.6 [1.26]
32	118.1	77.5	64.0	49.8	35.6	10.2	1.0	363.1	card 9 R0LDM=1.7 [1.26]
33	118.4	74.8	63.6	55.1	32.5	10.5	1.0	363.1	card 9 R0LDM=1.8 [1.26]
34	123.9	79.1	71.3	40.2	30.7	9.6	0.8	363.1	card 9 R0LDM=1.9 [1.26]
35	124.0	79.2	71.4	40.2	30.7	9.7	0.8	363.1	card 11 WGR=0.005 [0.003]
36	124.0	79.2	71.4	40.2	30.7	9.6	0.8	363.1	card 11 WGR=0.001 [0.003]
37	124.0	79.2	71.4	40.2	30.7	9.6	0.8	363.1	card 11 CGR=0.0001 [0.0003]
38	124.0	79.2	71.4	40.2	30.7	9.6	0.8	363.1	card 11 CGR=0.001 [0.0003]
39	124.0	79.2	71.4	40.2	30.7	9.6	0.8	363.1	card 12 EXR0=5 [32]
40	124.0	79.2	71.4	40.2	30.7	9.6	0.8	363.1	card 12 EXR0=20 [32]
41	124.0	79.2	71.4	40.2	30.7	9.6	0.8	363.1	card 12 EXR0=50 [32]
42	124.2	79.4	71.8	39.7	30.4	9.6	0.8	363.1	card 12 EXR0=100 [32]
43	124.6	79.3	71.9	39.9	30.2	9.6	0.8	363.1	card 12 EXH=1 [30]

Table V.2 (continued)

#	2p	pn	αp	2pn	3p	αn	2n	$\sigma_F^{(1)}$	Comments
44	124.0	79.1	71.4	40.0	30.5	9.6	0.8	363.1	card 12 EXH=10 [30]
45	124.2	79.5	71.6	40.4	30.9	9.7	0.8	363.1	card 12 EXH=20 [30]
46	124.2	79.5	71.6	40.4	30.9	9.7	0.8	363.1	card 12 EXH=30 [30]
47	124.2	79.5	71.8	40.4	30.9	9.7	0.8	363.1	card 12 EXH=100 [30]
48	123.9	79.2	71.5	40.1	30.7	9.6	0.8	363.1	card 12 EXH=500 [30]
49	123.9	79.2	71.2	40.3	30.8	9.6	0.8	363.1	card 12 CJC=1.0 [3.0]
50	123.7	79.3	71.3	41.0	31.2	9.7	0.8	363.1	card 12 CJC=5.0 [3.0]
51	118.6	75.0	65.4	40.3	30.9	9.4	0.8	347.2	card 12 CJC=10.0 [3.0]
52	124.4	79.9	72.1	40.4	30.8	9.7	0.8	364.3	card 12 LC0=15 [19]
53	124.3	80.8	73.1	40.4	30.8	9.7	0.8	366.4	card 12 LC0=20 [19]
54	124.0	80.5	72.9	40.1	30.6	9.7	0.8	366.4	card 12 LC0=30 [19]

Table V.2 : Cascade cross-sections (mb) for ^{54}Fe + ^{12}C at 150 MeV for different input parameters. An accompanying plot shows the percentage variations from the 'default' values for the various parameters. The values quoted in [...] are the default values assumed by the code if no input value is given.
(1) Fusion cross-section (in mb).

CASCADE: Variations on a theme

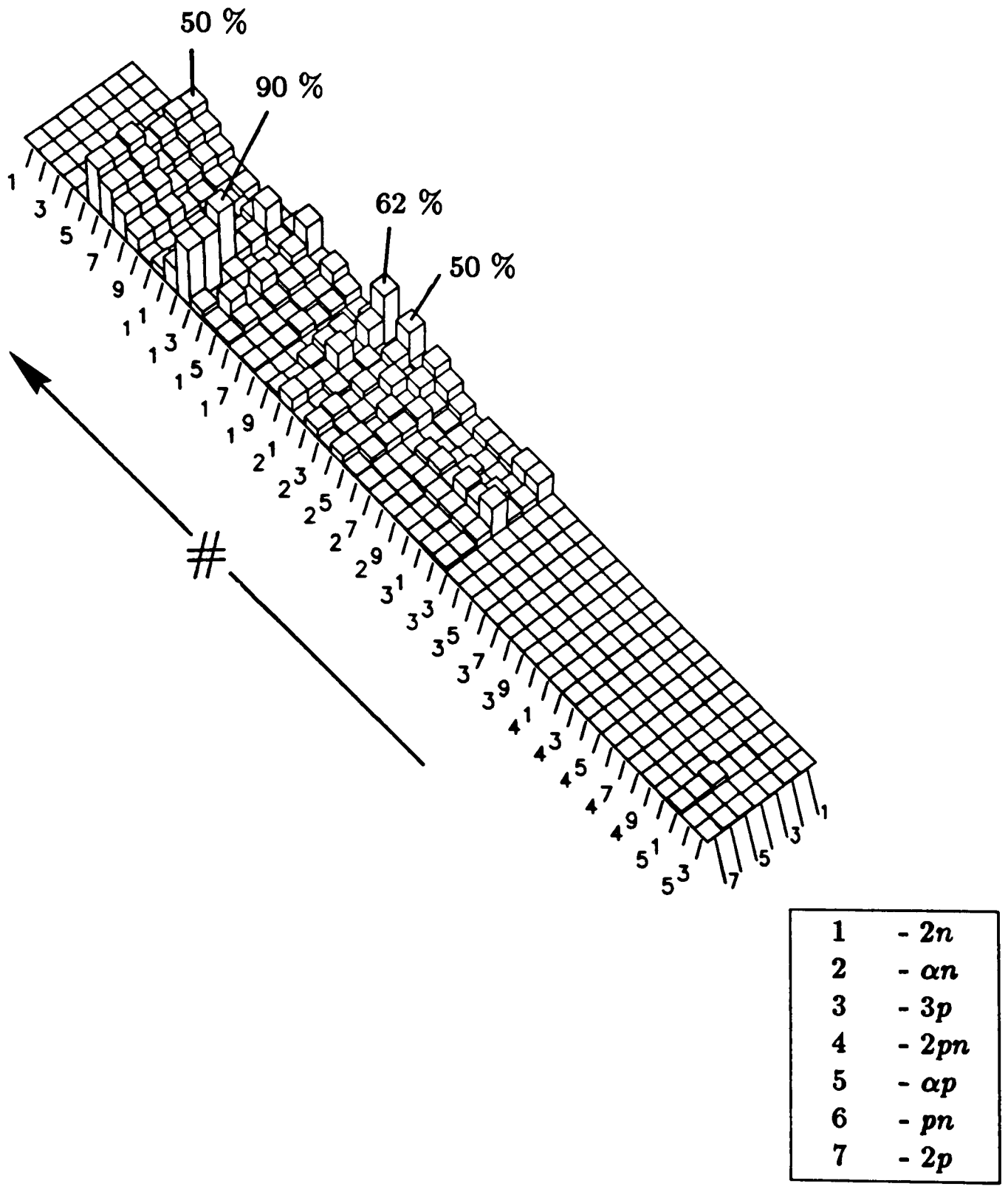


Fig.V.3 : Pictorial representation of table V.2. The z-direction represents the percentage (%) variation of the cross-section from the default value and these percentages are indicated for a few peaks.

APPENDIX VI

List of Runs

Run No.	Date	Reaction	Energy (MeV)	Machine (line)	Comments
1	Jan 1983	^{12}C+Ni	–	EN(B4)	experimenting with timing, TAC and ARC timing
2^M	Jan 1983	^{12}C+^{54}Fe	35	EN(B4)	3 n-detectors, 2 Ge(Li)'s, e-by-e, also ran at 33 MeV
3	Feb 1983	^{12}C+^{54}Fe	35	EN(B4)	γ-γ ,^{64}Ga data, 2 Ge(Li)'s, 1 ptcle. telescope, e-by-e
4^M	Mar 1983	^{12}C+^{54}Fe	35	FT(C1)	12 n-detectors, 2 Ge(Li)'s, CPVD(V1), hardware sort
5	May 1983	^{12}C+^{54}Fe p+^{7}Li	35 3	EN(B4)	test CPVD(V2), 1 n-detector, 1-2 Ge(Li)'s
6*	May 1983	^{29}Si+^{54}Fe	90	FT(C1)	test CPVD(V3,V4), 2 n-detectors, 2 Ge(Li)'s, ^{80}Sr
7	Jul 1983	^{12}C+^{54}Fe	35	FT(C1)	test TOF with neutrons
8	Dec 1983	p+^{7}Li	3	EN(B4)	new target chamber, test TOF
9	Dec 1983	^{12}C+^{54}Fe p+^{7}Li	35 3	EN(B4)	test TOF, used 1 Ge(Li)
10	Dec 1983	^{12}C+^{56}Fe p+^{7}Li	 3	EN(B4)	test out NORMAN and used 2 photomultipliers in coincidence
11	Jan 1984	^{12}C+^{54}Fe	35	FT(C1)	1st. run using NORMAN as well as the big plastic scintilators

(continued)

Run No.	Date	Reaction	Energy (MeV)	Machine (line)	Comments
12	Feb 1984	$^{12}C+^{54}Fe$	35	EN(B4)	1st. set up on B4
14	Mar 1984	$^{12}C+^{54}Fe$	35	EN(B4)	lead wall added, CPVD(V4) has collimator added to stop the beam hitting it
15	May 1984	Various		EN(B4)	$^{12}C+^{12}C$, $^{12}C+^{28}Si$, $^{10}B+^{56}Fe$, excit. fn. for $^{12}C+^{54}Fe$. β-decay expt. I
16	Jun 1984	$^{12}C+^{54}Fe$	35	EN(B4)	*Composite* PSD, 11/60-VAX connection tested under experimental conditions, changed NORMAN to run negatively
17	Jul 1984	$^{28}Si+^{40}Ca$	70	FT(A3)	test using SB telescope to detect α's at 60°
18	Aug 1984	$^{54}Fe+^{12}C$	148/150	FT(C1)	cryopump tested, inverse reaction used
19	Sep 1984	$^{54}Fe+^{12}C$	150	FT(C1)	little n-detector at 0°, Freiburg PSD added
20	Nov 1984	$^{54}Fe+^{12}C$	150	FT(C1)	using SB detector instead of CPVD, collect true singles
21	Feb 1985	$^{54}Fe+^{12}C$	150	FT(C1)	using 4 Ge(Li)'s, 5 neutron detectors, target chamber much closer to n-detector (54.5 cm from lead wall), previously, it was ~ 83 cm from the wall NORMAN on rollers and 65cm from target, Ge(Li)'s at 0°, 125°, −45°, −125°
22	Apr 1985	$^{12}C+^{54}Fe$	35	FT(A2)	β-decay expt. II. 2 Ge(Li)'s, one with an anti-Compton shield, both at 90°, target at 45°
23	Jul 1985	$^{24}Mg+^{27}Al$	62-72	FT(C1)	NORMAN ~ 30 cm from target, 4 Ge(Li)'s at ±90° and ±125°, 5 Freiburg PSD's installed
24	Aug 1985	$^{54}Fe+^{12}C$	150	FT(C1)	4 Ge(Li)'s as in run 23, new large area SB detector
25	Jan 1986	$^{54}Fe+^{12}C$ $^{12}C+^{54}Fe$	150 30-45	FT(A1)	Singles run with Compton Suppressor. Angular Distribution. Excitation function

"...what is the use of a book," thought Alice,
"without pictures or conversations† ?"

---

† or references — S. ?

REFERENCES

AHM77 M.Ahmed
A comparative study of n-γ discrimination properties of scintillators NE213, C_6H_6, C_6D_6 and Stilbene
Nucl. Instr. Meth. **143**, 255 (1977)

ALD66 K.Alder and A.Winther
Coulomb excitation
Academic Press (1966)

AND77 H.A.Anderson and J.F.Ziegler
Hydrogen stopping powers and ranges in all elements. Vol. 3 of the Stopping and Ranges of Ions in Matter
Pergamon Press (1977)

ARN71 W.D.Arnett, J.W.Truran and S.E.Woosley
Nucleosynthesis in supernova models II. The ^{12}C detonation model
Astrophys. J. **165**, 87 (1971)

ARS69 D.A.Arseniev, A.Sobiczewski and V.G.Soloviev
Equilibrium deformations of neutron-rich nuclei in the A≈100 region
Nucl. Phys. **A139**, 269 (1969)

BAT61 R.Batchelor, W.B.Gilboy, J.B.Parker and J.H.Towle
The response of organic scintillators to fast neutrons
Nucl. Instr. Meth. **13**, 70 (1961)

BEN84 R.Bengtsson, P.Möller, J.R.Nix and Jing-ye Zhang
Nuclear shapes and shape transitions
Phys. Scripta **29**, 402 (1984)

BET74 P.Betz, G.Braun, G.Hammel and J.Urban
A fast neutron-gamma discriminator
Nucl. Instr. Meth. **119**, 199 (1974)

BET84 R.R.Betts
Recent progress in the study of heavy-ion resonances
Proc. 4th. Int. Conf. on Clustering Aspects of Nucl. Struct. and Nucl. Rxns., Chester, UK, p. 133 (1984)

BIR64 J.B.Birks
The theory and practice of scintillation counting
Pergamon Press (1964)

BOH69 A.Bohr and B.R.Mottelson
Nuclear structure Vol. I — Single-particle motion
W.A.Benjamin Inc. (1969)

BOH75 A.Bohr and B.R.Mottelson
Nuclear structure Vol. II — Nuclear deformations
W.A.Benjamin Inc. (1975)

BOL72 M.Bolsterli, E.O.Fiset, J.R.Nix and J.L.Norton
New calculation of fission barriers for heavy and superheavy nuclei
Phys. Rev. **C5**, 1050 (1972)

BOL79 H.H.Bolotin, D.L.Kennedy, B.J.Linard, A.E.Stuchbery, S.H.Sie, I.Katayama and H.Sakai
Measured lifetimes of states in ^{197}Au and a critical comparison with the weak-coupling core-excitation model
Nucl. Phys. **A321**, 231 (1979)

BRI72 C.E.Brient, C.E.Nelson and R.L.Young
Pulse shape analyzer for fast neutron-gamma discrimination
Nucl. Instr. Meth. **98**, 329 (1972)

BRO79 F.D.Brooks
Development of organic scintillators
Nucl. Instr. Meth. **162**, 477 (1979)

BRU75 J.F.Bruandet, M.Agard, A.Giorni, J.P.Longequeue, C.Morand and T.U.Chan
High-spin states in ^{66}Zn
Phys. Rev. **C12**, 1739 (1975)

CAN79 M.J.Canty, P.A.Gottschalk and F.Pühlhofer
Shell model level densities in evaporation calculations
Nucl. Phys. **A317**, 495 (1979)

CAR72 J.M.G.Caraça
Electromagnetic properties of light proton-rich nuclei
D.Phil. Thesis, unpublished (1972)

CAS72 R.F.Casten, E.R.Flynn, O.Hansen and T.J.Mulligan
A study of the neutron-rich isotopes near A=100 by means of the (t,p) reaction
Nucl. Phys. **A184**, 357 (1972)

CHA76 A.Charvet, R.Duffait, T.Negadi, A.Emsallem, G.Marguier and R.Chery
Lifetimes of levels in ^{64}Zn from Doppler shift measurements via the $^{61}Ni(\alpha,n)^{64}Zn$ reaction
Phys. Rev. **C13**, 2237 (1976)

COH74 S.Cohen, F.Plasil and W.J.Swiatecki
Equilibrium configurations of rotating charged or gravitating liquid masses with surface tension. II
Ann. Phys. **82**, 557 (1974)

COO78 B.Cooke
GENDAT - a general data acquisition program
Oxford University Nucl. Phys. Lab. Internal Report 87/78 (1978)

DAV73 C.N.Davids and D.R.Goosman
Mass of ^{64}Ge and its rôle in nucleosynthesis
Phys. Rev. **C7**, 122 (1973)

DEH73 W.Dehnhardt, O.C.Kistner, W.Kutschera and H.J.Sann
Recoil-distance lifetime measurements in ^{46}Ti and ^{50}Cr
Phys. Rev. **C7**, 1471 (1973)

EKS79 L.P.Ekström, G.D.Jones, F.Kearns, T.P.Morrison, O.M.Mustaffa, D.N.Simister, H.G.Price, P.J.Twin, R.Wadsworth and N.J.Ward
Gamma-ray spectroscopy on ^{48}Cr
J.Phys. G **5**, 803 (1979)

ENG74 J.B.A.England
Techniques in nuclear structure physics
MacMillan Press (1974)

FOR76 G.Fortuna, R.B.Huber, W.Kutschera, M.Morando, H.Morinaga, R.A.Ricci and C.Signorini
High-spin states in ^{48}Ti and ^{46}Ti
Il Nuovo Cimento **34A**, 321 (1976)

GED68 D.A.Gedcke and C.W.Williams
High resolution time spectroscopy
ORTEC Application note (August 1968)

GER67 W.J.Gerace and A.M.Green
The effect of deformed states in the Ca isotopes
Nucl. Phys. **A93**, 110 (1967)

GIL65 A.Gilbert and A.G.W.Cameron
A composite nuclear-level density formula with shell corrections
Can. J. Phys **43**, 1446 (65)

GIL66 V.Gillet, A.M.Green and E.A.Sanderson
Particle-hole excitations in ^{208}Pb
Nucl. Phys. **88**, 321 (1966)

GNE71 G.Gneuss and W.Greiner
Collective potential energy surfaces and nuclear structure
Nucl. Phys. **A171**, 449 (1971)

GRE65 A.M.Green
Collective vibrations in nuclei
Rep. Prog. Phys. XXVIII, 113 (1965)

GR062 L.Grodzins
The uniform behaviour of electric quadrupole transition probabilities from first 2^+ states in even-even nuclei
Phys. Lett. **2**, 88 (1962)

HAA75 B.Haas, P.Taras, J.C.Merdinger and R.Vaillancourt
Yrast states in ^{48}Cr and reaction mechanism of the $^{34}S + ^{16}O$ reaction at E_{lab} = 30 - 36 MeV
Nucl. Phys. **A238**, 253 (1975)

HAL68 I.Halpern, B.J.Shepherd and C.F.Williamson
Angular-momentum distributions of residual nuclei in compound-nuclear reactions
Phys. Rev. **169**, 805 (1968)

HAN79 H.Hansen, P.Hornshøj and N.Rud
High-spin states in the $N = Z$ nuclide ^{48}Cr populated in the reaction $^{40}Ca(^{10}B, np)^{48}Cr$
Nucl. Phys. **A327**, 193 (1979)

HAU52 W.Hauser and H.Feshbach
The inelastic scattering of neutrons
Phys. Rev. **87**, 366 (1952)

HEI71 J.Heisenberg, J.S.McCarthy and I.Sick
Inelastic electron scattering from several Ca, Ti and Fe isotopes
Nucl. Phys. **A164**, 353 (1971)

HEL75 R.G.Helmer, J.E.Cline and R.C.Greenwood
Gamma-ray energy and intensity measurements with Ge(Li) spectrometers
The Electromagnetic Interaction in Nuclear Spectroscopy, p. 775, ed. W.D.Hamilton, North-Holland Publ. Co. (1975)

HUG55 D.J.Hughes and J.A.Harvey
Neutron cross sections
BNL 325, Assoc. Universities Inc. (1955)

IEE75 IEEE
IEEE Standard modular instrumentation and digital interface system (Computer Automated Measurement and Control IEEE Std. 583-1975 in *CAMAC Instrumentation and Interface Standards*
IEEE Inc. (1975)

JOH71 P.B.Johnson, J.M.G.Caraça, J.N.Pihl, R.D.Gill and H.J.Rose
An associated gamma ray time of flight spectrometer with high neutron efficiency
Nucl. Instr. Meth. **93**, 417 (1971)

KAL70 J.Kalyna and I.J.Taylor
Pulse shape discrimination: An investigation of n-γ discrimination with respect to size of liquid scintillator
Nucl. Instr. Meth. **88**, 277 (1970)

KAM74 R.Kamermans, H.W.Jongsma, J.van der Spek and H.Verheul
γ-ray transitions in ^{48}Cr and ^{60}Zn
Phys. Rev. **C10**, 620 (1974)

KIN66 T.A.King and R.Voltz
The time dependence of scintillation intensity in aromatic materials
Proc. Roy. Soc. **A289**, 424 (1966)

KLE78 P.Kleinheinz, S.Lunardi, M.Ogawa and M.R.Maier
The 3^- state in the doubly closed shell nucleus $^{146}_{64}Gd_{82}$
Z. Physik **A284**, 351 (1978)

KUM66 H.Kümmel, J.H.E.Mattauch, W.Thiele and A.H.Wapstra
A new mass law with shell and deformation corrections
Nucl. Phys. **81**, 129 (1966)

KUT73 W.Kutschera, R.B.Huber and C.Signorini
Gamma-ray spectroscopy of ^{48}Cr
Nucl. Phys. **A210**, 531 (1973)

KUT74 W.Kutschera, R.B.Huber, C.Signorini and H.Morinaga
Observations of a high-spin yrast cascade in ^{50}Cr
Phys. Rev. Lett. **33**, 1108 (1974)

KUT78 W.Kutschera, B.A.Brown and K.Ogawa
The empirical $(1f_{7/2})^n$ model
La Rivista del Nuovo Cimento **1**, N.12 (1978)

LAR76 S.E.Larsson, G.Leander, I.Ragnarsson and N.G.Alenius
Collective motion and deformed shell structure in the doubly even fp shell nuclei
Nucl. Phys. **A261**, 77 (1976)

LIM81 A.P.de Lima, A.V.Ramayya, J.H.Hamilton, B.Van Nooijen, R.M.Ronningen, H.Kawakami, R.B.Piercey, E.de Lima, R.L.Robinson, H.J.Kim, L.K.Peker, F.A.Rickey, R.Popli, A.J. Caffrey and J.C.Wells
Multiple band structures in ^{68}Ge
Phys. Rev. **C23**, 213 (1981)

LIS85 C.J.Lister and B.J.Varley
New regions of nuclear deformation
Conference on Nucl. Struct. with Heavy Ions, Bologna, Italy, p. 53, Italian Phys. Soc. (1985)

LOB70 K.E.G.Löbner, M.Vetter and V.Hönig
Nuclear intrinsic quadrupole moments and deformation parameters
Nucl. Data Tables **A7**, 495 (1970)

MAR60 J.B.Marion and J.L.Fowler
Fast neutron physics Parts I & II
Interscience Publishers, Inc., NY (1960)

MIL67 R.G.Miller and K.W.Kavanagh
Masses and excitation energies of some proton-rich nuclei
Nucl. Phys. **A94**, 261 (1967)

MOL81 P.Möller and J.R.Nix
Nuclear mass formula with a Yukawa-plus-exponential macroscopic model and a folded-Yukawa single-particle potential
Nucl. Phys. **A361**, 117 (1981)

MOR76 C.Morand, M.Agard, J.F.Bruandet, A.Giorni, J.P.Longequeue and T.U.Chan
^{70}Ge high-spin levels via the $^{68}Zn(\alpha,2n\gamma)^{70}Ge$ reaction
Phys. Rev. **C13**, 2182 (1976)

MYE60 W.D.Myers and W.J.Swiatecki
Nuclear Masses and Deformations
Nucl. Phys. **81**, 1 (1960)

MYE66 W.D.Myers and W.J.Swiatecki
Anomalies in nuclear masses
Proc. Int. Symp. on Nuclides far off the Stability line, Lysekil, Sweden; Arkiv för Fysik **36**, 343 (1966)

MYE73 W.D.Myers
Geometric properties of leptodermous distributions with applications to nuclei
Nucl. Phys. **A204**, 465 (1973)

NAT66 O.Nathan and S.G.Nilsson
Collective nuclear motion and the unified model
Alpha-, Beta- and Gamma-ray spectroscopy, Vol. 1, p. 601, ed. K.Siegbahn, North-Holland Publishing Co. (1966)

NIL55 S.G.Nilsson
Binding states of individual nucleons in strongly deformed nuclei
Mat. Fys. Medd. Dan. Vid. Selsk. **29**, no. 16 (1955)

PRI53 R.W.Pringle, L.D.Black, B.L.Funt and S.Sobering
A new quenching effect in liquid scintillators
Phys. Rev. **92**, 1582 (1953)

PUH77a F.Pühlhofer
On the interpretation of evaporation residue mass distributions in heavy-ion induced fusion reactions
Nucl. Phys. **A280**, 267 (1977)

PUH77b F.Pühlhofer, W.F.W.Schneider, F.Busch, J.Barrette, P.Braun-Munzinger, C.K.Gelbke and H.E.Wegner
Isotope and element distributions of the evaporation residues from fusion of 160 MeV ^{32}S with $^{24,25,26}Mg$ and ^{27}Al
Phys. Rev. **C16**, 1010 (1977)

PUH79 F.Pühlhofer
CASCADE - A nuclear evaporation code
CASCADE documentation, unpublished (1979)

RAG78 I.Ragnarsson, S.G.Nilsson and R.K.Sheline
Shell structure in nuclei
Phys. Rep. **45**, 1 (1978)

RAG84 I.Ragnarsson and R.K.Sheline
Systematics of nuclear deformation
Phys. Scripta **29**, 385 (1984)

RAI50 J.Rainwater
Nuclear energy level argument for a spheroidal nuclear model
Phys. Rev. **79**, 432 (1950)

RAM75 S.Raman, N.B.Gove and T.A.Walkiewicz
Isospin impurity of ^{64}Ga ground state
Nucl. Phys. **A254**, 131 (1975)

RIN80 P.Ring and P.Schuck
The nuclear many-body problem
Springer-Verlag New York Inc. (1980)

ROB74 R.G.H.Robertson and S.M.Austin
Neutron-deficient isotopes ^{64}Ge and ^{65}Ge
Phys. Rev. **C9**, 1801 (1974)

ROG69 V.C.Rogers, L.E.Beghian and F.M.Clikeman
The energy level structure of ^{45}Sc from the $(n, n'\gamma)$ reaction
Nucl. Phys. **A137**, 85 (1969)

ROT81 J.Roth, L.Cleemann, J.Eberth, T.Heck, W.Neumann, M.Nolte, R.B.Piercey, A.V.Ramayya and J.H.Hamilton
A neutron multiplicity technique for in-beam γ-spectrscopy on neutron deficient nuclei
Proc. 4th. Int. Conf. on Nucl. Far from Stability, Helsingør, Denmark, p. 680 (1981)

SCH84 N.Schmal, L.Cleemann, J.Eberth, P.W.M.Glaudemans and D.Zwarts
Shell model states in the odd-odd nucleus ^{64}Ga
Proc. Int. Symp. on In-beam Nucl. Spectroscopy, Debrecen, Hungary, p. 121 (1984)

SHE72 J.R.Shepard, R.Graetzer and J.J.Kraushaar
The level structure of ^{48}Cr and ^{68}Ge from the (p, t) reaction at $E_p = 27\ MeV$
Nucl. Phys. **A197**, 17 (1972)

SHE76 R.K.Sheline
Spectroscopy of nuclei far from stability
Proc. 3rd. Int. Conf. on Nucl. Far from Stability, Cargèse, Corsica, France, p. 351, CERN 76-13 (1976)

STE72 F.S.Stephens, R.M.Diamond, J.R.Leigh, T.Kammuri and K.Nakai
Decoupled yrast states in odd-mass nuclei
Phys. Rev. Lett. **29**, 438 (1972)

STR67 V.M.Strutinsky
Shell effects in nuclear masses and deformation energies
Nucl. Phys. **A95**, 420 (1967)

STR68 V.M.Strutinsky
"Shells" in deformed nuclei
Nucl. Phys. **A122**, 1 (1968)

SUG79 E.Sugarbaker, F.W.N.de Boer, P.A.Smith C.A.Fields, L.E.Samuelson, and D.Cline
The $^{54}Fe(^{12}C, xn\gamma)$ reactions
University of Colorado Annual Report p. 103, NPL-845 (1979)

TH064 T.D.Thomas
The analysis of nuclear evaporation spectra
Nucl. Phys. **53**, 558 (1964)

TWI83 P.J.Twin, P.J.Nolan, R.Aryaeinejad, D.J.G.Love, A.H.Nelson and A.Kirwan
TESSA : A multi-detector γ-ray array designed to study high-spin states
Nucl. Phys. **A409**, 343 (1983)

VER79 M.Vergnes
Survey of even-even nuclei in the Ge region
Proc. 6th. European Phys. Soc. Nucl. Div. Conf. on the Struture of Medium-heavy Nucl., Rhodes, Greece, p. 25 (1979)

WAD79 R.Wadsworth, L.P.Ekström, G.D.Jones, F.Kearns, T.P.Morrison, O.M.Mustaffa, H.G.Price, P.J.Twin and N.J.Ward
A study of the neutron-deficient isotope ^{66}Ge
J. Phys. G **5**, 1761 (1979)

WAK69 Y.Wakuta, H.Tawara, M.Hyakutake and M.Sonoda
A fast neutron time-of-flight spectrometer with neutron-gamma ray discrimination
Nucl. Instr. Meth. **71**, 133 (1969)

ZIE77 J.F.Ziegler
The electronic and nuclear stopping of energetic ions
App. Phys. Lett. **31**, 544 (1977)

ZIE80 J.F.Ziegler
Stopping cross-sections for energetic ions in all elements. Vol. 5 of the Stopping and Ranges of Ions in Matter
Pergamon Press (1980)

ZUK68 A.P.Zuker, B.Buck and J.B.McGrory
Structure of ^{16}O
Phys. Rev. Lett. **21**, 39 (1968)

ZUR83 R.W.Zurmühle, P.Kutt, R.R.Betts, S.Saini, F.Haas and O.Hansen
Resonances in elastic and inelastic scattering of $^{24}Mg + ^{24}Mg$
Phys. Lett. **129B**, 384 (1983)

